# Development of An Inverse FE Modelling Method for Material Parameters Identification Based on Indentation Tests

**Bing Li**

**A thesis submitted in partial fulfilment of the requirement of the Liverpool John Moores University for the degree of Doctor of Philosophy**

**School of Engineering, Liverpool John Moores University**

**March 2009**

# ACKNOWLEDGEMENTS

I would like to take this opportunity to express my deepest gratitude and sincerest thanks to my supervisors Dr James Ren, Dr Russell English, Dr Glynn Rothwell for their inspiring supervision of my study and guidance during the production of this thesis.

Many other academic. secretarial and technical members of staff have facilitated the realization of this thesis and I express them all my gratitude. I would like to thank Mr. Clive Eyre and Mr. Steven Gotts for their invaluable technical support with material testing and funny jokes.

I acknowledge the Liverpool John Moores University and the School of Engineering for the facilities and support provided.

Special thanks also to my group mates, Dr Peter Kong, Mr. Mohammad Shariatmadari, Mr. Jarema Krywonos, Mr. Yaodong Gu and Mr. Yousheng Li for their friendship and sharing the experience of being a postgrate student. I am also grateful of the help of my friends, who gave me help in many ways and shared a great time in my studies and life at Liverpool John Moores University.

Finally, I would like to thank my family for sustained encouragement that gave me motivation during my studies, continuous and unselfish love and support.

Bing Li

# ABSTRACT

In this work, an inverse FE modelling program based on the Kalman filter technique has been developed and used to study three material models (linear elastic, hyperelastic and hyper foam). Two error treatment methods have been developed and implemented in the program and their feasibilities for different material systems were systematically investigated. FE models simulating the indentation process of three typical material behaviours have been developed and some important factors including mesh sensitivity, frictional conditions and material properties have been systematically studied to validate the FE models. The use of single indenter and dual indenters have been comparatively studied in terms of accuracy, convergence and robustness of the inverse program, which are important for materials characterisation. The program was evaluated with blind tests using numerical experimental data of known material properties. The validated method was then successfully used to study the properties of EVA foams for midsole of sport shoes and human heel pad using a newly develop continuous indentation testing system.

Blind tests have been successfully used to establish the validity, efficiency and robustness of the program with different material models, error treatment and selection of indenters. The results showed that the double indenters method is better than the single indenter method, which is initial value dependent for some materials. The results also showed that the new random error treatment method is applicable to all the three material models while the converged results based on the program with constant error distribution was initial values dependent. The blind test results showed that Kalman filter is a feasible method and the random error treatment is more practical approach for characterisation material and can be universally applied to different materials models. Sensitivity test with perturbation in the indentation force demonstrated that the program is robust against potential experimental noise/errors.

The framework established has been successfully used to characterise the properties of EVA foams in comparison with conventional compression, and compression-shear methods. The prediction from indentation tests showed comparable accuracy to the standard combined compression-shear tests, while pure compression could not predict

the parameters accurately describing the material at complex situations. The parameters inversely predicted can be directly used in the product design and simulation process. A new *in vivo* test machine has been developed and performed on human subject with good accuracy and repeatability. The inverse method has been used to predict the elastic and nonlinear parameters of the heel pad. The predict elastic and hyperelastic properties showed good correlation for all the subjects tested. However the nonlinear model is more accurate in describing the stiffening effect of the heel pad. This method would provide a practical way for detecting the property change of the heel pad with different conditions.

# Contents

# Symbols (In Order of Appearance)

## 2.3 Mechanical testing of the human heel pad

- $T_f$ **The heel pad thickness at a given force**
- $T_U$ **The unloaded heel pad thickness**
- $\varepsilon$ **Strain**

## 2.4 Linear and Nonlinear elastic material behaviours

- $E$ **The Young's modulus**
- $\sigma_x$ **The tensile stress**
- $\varepsilon_x$ **The tensile strain**
- $\nu$ **Poisson's ratio**
- $G$ **The shear modulus**

## 2.5 The basics of non-linear continuum mechanics for finite element analysis

- $K^0$ **Reference/initial configuration**
- $K^t$ **Deformed configuration**
- $X$ **Position of a particle in the reference/initial configuration**
- $x$ **Position of a particle in the deformed (current) configuration**
- $u(X)$ **A deformation** $f = x(X)$ **is a mapping of a closed bounded region into another closed bounded region**
- $\varphi$ **The transfer function between reference configuration and deformed configuration**
- $F$ $F_{iA} = \varphi_{i,A}$ **The deformation gradient tensor,**
- $J$ **The Jabobian matrix of the deformation,** $J = \det F$
- $F^T$ **Transpose of a matrix** $F$
- $V_0$ **The volume in initial configuration**
- $V$ **The volume in deformed configuration**
- $\rho_0$ **The density in initial configuration**
- $\rho$ **The density of the body in the deformed configuration and**
- $C$ **The right Cauchy-Green deformation tensor,** $C = F^T F$
- $B$ **The left Cauchy-Green deformation tensor,** $B = FF^T$
- $\lambda_1, \lambda_2, \lambda_3$ **Principle stretches**
- $tr$ **Trace of a matrix (i.e.,** $trC = C_{11} + C_{22} + C_{33}$ **)**
- $I_1$ **The first invariant of** $C$, $I_1 = trC$
- $I_2$ **The second invariant of** $C$, $I_2 = (trC)^2 - trC^2$
- $I_3$ **The third invariant of** $C$, $I_3 = \det C$
- $\delta_{ij}$ **The Kronecker delta function**
- $I$ **Identity tensor**
- $E$, $E_{ij}$, $\varepsilon_{ij}$ **Green-Lagrange strain tensor**
- $P$ **First Piola-Kirchhoff stress tensor,** $P = JF^{-1}T$
- $S$ **Second Piola-Kirchhoff stress tensor,** $S = JF^{-1}TF^{-T} = PF^{-T}$

- $T$ **Cauchy stress**
- $W, \tilde{W}$ **Strain energy function**
- $U$ **Strain energy density**

## 2.6 Strain energy functions for rubber, foams and biological materials

- $C_1, C_2, C_{01}, C_{10}$ **constants**
- $J^{el}$ **The elastic volume ratio**
- $J^{th}$ **The thermal volume ratio**
- $J$ **The total volume ratio**
- $\overline{\lambda}_i$ ( $i = 1,2,3$ ) **The deviatoric stretches**, which are related to principal stretches $\lambda_i$ ,

  $i = 1,2,3 \quad \overline{\lambda}_i = J^{-1/3}\lambda_i$
- $\lambda_i$ ($i = 1,2,3$ ) **The principal stretches**
- $\hat{\lambda}_i$ ($i = 1,2,3$ ) **The deviatoric stretches**, which are related to principal stretches $\lambda_i$ ,

  $i = 1,2,3$ , $\hat{\lambda}_i = (J^{th})^{-1/3}\lambda_i$
- $\mu_0$ **The initial shear modulus**
- $K_0$ **The initial bulk modulus**
- $\alpha_i$ , $\mu_i$ **The temperature-dependent material parameters**
- $\beta_i$ **The temperature-dependent material parameters, which is related to the Poisson's ratio**
- $\varepsilon^{th}$ **The linear thermal expansion**
- $\nu$ **Poisson's ratio**
- $\varepsilon_1$, $\varepsilon_2$, $\varepsilon_3$, **The logarithmic principal strains.**
- $D_1$ **The temperature-dependent constant**
- $B$ **The left Cauchy-Green deformation tensor**
- $b_1, b_2, b_3$ **The principle values of** $B$
- $f$ **Constant**

## 2.8 Inverse problems and its application in material properties prediction

- $O(x)$ **Objective function**
- $l_q, u_q$ **The lower and upper bounds of the unknown vector**
- $\Phi^{Exp}$ **Experiments**
- $\Phi^{Mod}$ **Model value**
- $\Omega(x)$ **The regularization operator**
- $p$ **Probability**
- $\Delta O(x)$ **Difference in the value of the objective function between two iterations**
- $T$ **Temperature**
- $r$ **Reduction factor**
- $f(x)$ **Target function /Objective function**
- $f^2(x)$ **The least-square-function/Objective function**
- $\nabla f$ **The first order differential**
- $\nabla\nabla f$ **The second order differential**
- $b$ , $A$ **Matrix related to least-square-function**
- $\lambda$ **Scaling parameter**

- $x_0, x_1, x_2 \ldots$ **Unknown parameters**
- $w_0, w_1, w_2 \ldots$ **Weights of** $x_0, x_1, x_2 \ldots$
- $\sum$ **Sum**
- $Y[k]$ **Output**
- $T[k]$ **Target value**
- $e[k]$ **The difference between the target output and the actual output**
- $\alpha, \mu, \delta$ **Const**

## 3.2 Parameter estimation model based on the extended Kalman filter technique

- $x_{k+1}$, $x_k$ **Unknown state parameter vector at time** $k$ **and** $k+1$ **respectively**
- $w_k$ **Process noise vector at time** $k$
- $z_k$ **The measurement parameter vector at time** $k$
- $v_k$ **The measurement noise vector at time** $k$
- $h(x_k)$ **The measurement prediction vector at time** $k$
- $p(w_k)$ **Probability of error** $w_k$
- $p(v_k)$ **Probability of error** $v_k$
- $\hat{x}_k$ **Posterior estimation** $k$
- $\hat{x}_k^-$ **Prior estimation at time** $k$
- $K_k$ **Kalman gain matrix at time** $k$
- $h(\hat{x}_k^-)$ **The measurement prediction at time** $k$
- $H_k$ **The Jacobian matrix of partial derivatives of '** $h(x_k)$ **' with respect to '** $x_k$ **'**
- $P_k$ **The posterior estimate error covariance at time** $k$
- $I_n$ **Identity matrix of size** $n$
- $R_k$ **Standard deviation of measurement error**
- $Q_k$ **Standard deviation of process error**
- $w_i^T$ **Transpose of vector** $w_i$
- $i$ **Time sequence** $i = 1,2,3,\cdots,k,\cdots$
- **Standard deviation of normal distribution**
- $\mu$ **Mean value of normal distribution**

## 3.3 Inverse FE indentation modelling based on the Kalman filter method

- $\sigma$ **Standard deviation of normal distribution**
- $\mu$ **Mean value of normal distribution**
- $F$ **Reaction force of indentation**
- $\Delta F$ **The difference of** $F$ **between measurement and prediction**

## 3.4 Application of the inverse FE modelling approach to different material systems

- $\mu_i, \alpha_i, \beta_i, D_i$ **Temperature-dependent material parameters**

# List of Figures

## Chapter 1



## Chapter 2

**Chapter 3**

**Chapter 4**

**Chapter 5**

# CHAPTER ONE

# INTRODUCTION

## 1.1 Introduction

For over a century, indentation test has been employed to probe the mechanical behavior of materials for a wide range of engineering applications. In the indentation test, an indenter is pressed onto the sample surface and the resistance of the material is represented by the size of the residual impression on the surface or the force-indentation depth data (Figure 1.1). The main reason for its ubiquitous use is its intrinsic experimental simplicity in terms of facilities and sample requirements. Indentation tests can be performed with minimal specimen preparation and/or mounting and can be conducted several times on a single specimen at different locations. Indentation tests can also be performed within different environments (e.g. temperatures or humidity) with complicated loading histories *(Ren et al, 2002; Petre et al, 2005)*. In addition, recent developments of advanced instruments have made possible the application of forces from kilo-Newtons down to piconewtons, and local displacements down to nanometers. Indentation tests are used for many types of materials such as metals, ceramic and plastic and recently, biological entities *(Petre et al, 2005)*. Traditionally, indentation tests have been mainly used to measure the hardness of materials, which is a good indicator to compare materials for a particular application. However, it could not provide the constitutive law or parameters of the materials. This has limited its applications in particular for those with complex constitutive stress-strain relationships such as polymer foams and biological materials. It is very important to develop a more thorough approach to predict the material parameters in order to establish the constitutive material law, which is essential to simulate the material/structure behaviors in services (Figure 1.1).

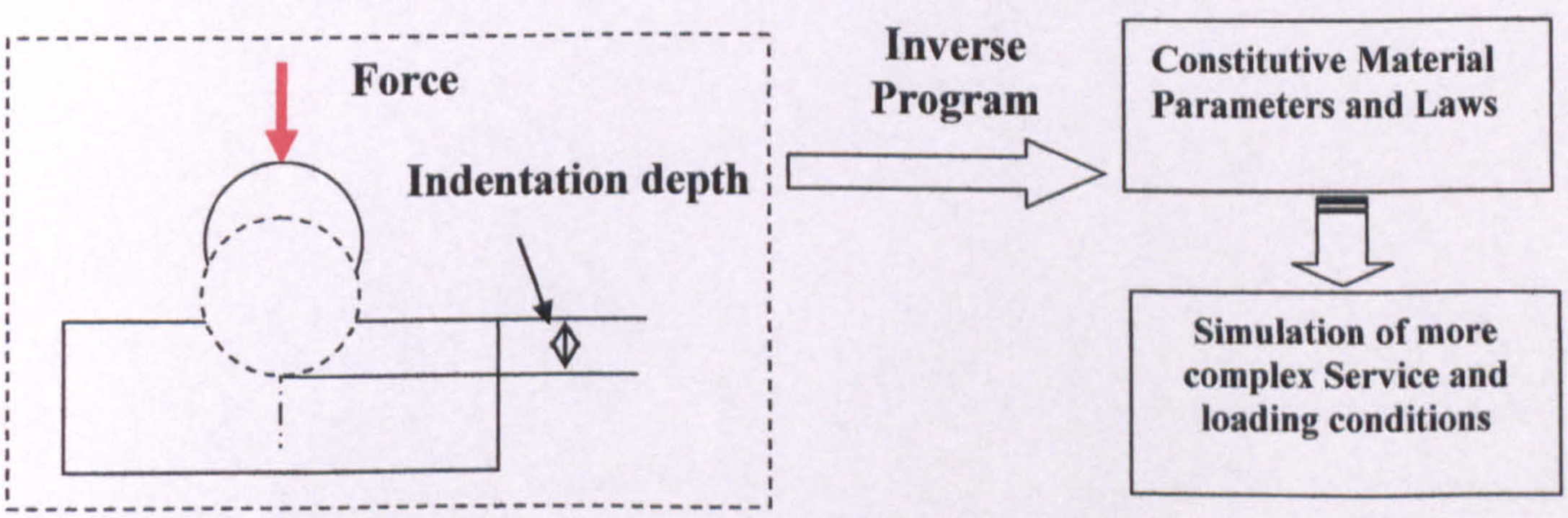


**Figure 1.1** Schematic to show an indentation process.

One viable way to predict the material properties from indentation tests are to use so called inverse finite element (FE) modelling method combining indentation tests, FE simulation and inverse parameter identification. Recently, inverse FE modelling methods have been developed extensively to deal with situations where the material parameters (as input in the FE models) could not be directly determined from an experimental tests *(Dao et al, 2001; Ren et al, 2006; Delalleau et al, 2006).* The most common method is the interactive inverse FE method. In this process, an optimisation algorithm is coupled with finite element modelling to find the optimal values for a set of target parameters, which produce numerical results matching the experimental results (minimising the objective function). In the interactive inverse processes, the FE simulation has to be repeated with changing material parameters until an optimum combination of material properties has been found. Recently, a new post modelling approach has been proposed in material parameters characterisation *(Nakamura et al, 2000; Gu et al, 2003; Delalleau et al, 2006).* This method does not require the repeat of FE analysis during the optimisation process, which could be a significant advantage for practical application as it does not rely on the complex modelling program and resources. In this approach, a simulation space is developed based on finite element modelling data within which parameters searching process is to be performed. Among the approach currently available for engineering applications, a potentially useful program for material parameters identifications based on the indentation tests is the Klaman filter method. This technique was initially developed for optimisation of electronic/control systems (signal-processing algorithm) *(Grewal and Andrews, 2001).* The capacity of the program in dealing with noises in the input made it potentially suitable for characterising material tests data with a certain level of error or noise. This is particularly important for *in vivo* tests on human subjects as it is difficult to control due to the nature of the testing *(Ren et al, 2005).*

According to Tikhonov and Arsenin *(Tikhonov and Arsenin, 1977),* ill-posed problems can yield stable solutions if sufficient priori information about the true solution is available. An inverse modelling technique is not effective unless they satisfy convergence and consistency conditions. This requires an accurate FE model of the system, an effective estimation mechanism and proper experimental setup. In many cases, direct applications of inverse analysis techniques would not yield

accurate solutions since many problems are ill-condition (i.e. difficult to converge to a unique solution). In some cases, some pre-known or presumed conditions must be prescribed to establish a robust procedure for individual cases. These are particular important for material parameters identifications as there are many factors which may potentially influence the results when a complex material model is involved such as rubber, foams and biological tissues. Therefore, it is essential, for both research and industrial applications, to develop a practical approach applicable to these materials.

## 1.2 Aims and Objectives

This work aims to develop a new inverse FE modelling method to accurately predict material parameters for three main material models for sport and biological materials and use the developed program to characterise the properties of ethylene vinyl acetate (EVA) foams and the human heel pad *in vivo*.

**Main objectives are:**

- To develop an inverse FE indentation technique based on the Kalman filter method to predict material parameters accurately;
- To investigate the feasibility of the approach to three typical material models (i.e. linear elastic, hyperelastic and hypefoam models) using blind tests; and establish factors affecting the accuracy and robustness of the inverse FE indentation approach;
- To develop a new continuous indentation testing system for foam and *in vivo* human heel pad tests;
- To perform indentation tests on EVA foams and inversely predict the material parameters in comparison with other conventional test methods;
- To test the human heel pad *in vivo* with different spherical indenters and inversely predict the material parameters using the program developed.

Detailed studies of the EVA foams and the human heel pad *in vivo* are very important for many product developments in particular in sport technology. EVA foams are widely used in sport footwear and equipments such as the midsole of sport shoes, providing the shock absorbing and cushioning capacity *(Mills 2003; Ruiz-Herrero et al, 2005)*. The properties of EVA foams are highly nonlinear and viscoelastic *(Verdejo and Mills, 2004)*. Determination of the material parameters is important to provide data for the simulation of their service performances, product design and quality control. The Human heel pad is an important part of the human body. A detailed knowledge of its mechanics is indispensable to understand its functions as well as treatment of injury and medical conditions. *In vivo* characterisation of heel-pad deformation can also provide insight into tissue properties changes that may occur in diseases such as diabetes rheumatoid arthritis *(Rome, 1998; Hsu et al, 2000; 2002)*. In

addition, quantitative characterisation of the properties of the heel pad is also of great importance to sport shoe design due to its wide usage as the midsole materials.

## 1.3 Outline of the thesis

In Chapter 2, background information and current researches on indentation tests, inverse modelling and their applications in materials characterisation are reviewed. It covers different types of indentation tests and their applications in studying various materials. A summary of current testing methods of polymer foams and mechanical testing of biological materials (the heel pad) is presented in the first section. The basic theories of nonlinear mechanics and strain energy functions are reviewed with the key controlling materials discussed. The theoretical frame of different inverse FE modelling methods and optimisation programs are compared. The difficulties and challenges for the inverse FE modelling approach based the indentation tests are reviewed and discussed.

In Chapter 3, an inverse FE modelling program based on the Kalman filter technique is developed and applied to study three commonly used material models (linear elastic, hyperelastic and hyperfoam) in blind tests. Two error treatment methods are developed and implemented in the program and their feasibility for different material systems is systematically investigated. The use of single indenter and dual indenter method are comparatively studied in terms of accuracy, convergence and robustness of the predicted results, which are important for materials characterisation. The program is evaluated using blind tests with numerical experimental data to investigate their validity, efficiency and robustness of the program with different material models. The sensitivity of the estimated mechanical properties to variations of the input parameters (e.g. potential perturbation of the load) is also established.

In Chapter 4, the inverse FE program developed is used to predict the material properties of EVA foams and the human heel pad *in vivo*. A new continuous indentation testing system is designed and constructed. The accuracy of the systems is validated on a silicone rubber material with known material properties and assessed by comparing the testing results with the data from a standard tensile testing machine. In the second part of the chapter, two EVA foams used in sport shoes are systematically tested. The material parameters are then predicted using the framework of the hyperfoam model established in Chapter 3. The inversely predicted results are

compared to the values determined from the conventional compression and compression-shear test methods. In the third part of the chapter, the properties of the human heel pad are studied using the indentation tests and inverse FE modelling program. The repeatability and effect of experimental conditions on *in vivo* testing are systematically assessed. Tests with different indenter sizes are performed on three human subjects, and then the linear elastic and nonlinear elastic material parameters of the human heel pad are identified from the indentation test data.

Chapter 5 discusses the application of inverse FE modelling techniques in material parameters identification based on the indentation method and factors affecting the FE modelling and inverse modelling results. The accuracy and sensitivity of the inverse FE modelling program developed in this study are compared to other approaches. The advantages and disadvantages of using the dual indenter method against the conventional single indenter method are also discussed. The constitutive stress-strain curves of the materials are determined from the parameters predicted and compared to some published results. The elastic and nonlinear properties of the human heel are compared and their suitability for describing the material is compared and discussed.

In Chapter 6, overall conclusions were given and future works are highlighted.

# CHAPTER TWO

# LITERATURE REVIEW

## 2.1 Introduction

In this chapter, the main types of indentation tests and their applications in testing a wide range of materials are reported. The current testing methods of foam materials and biological materials (e.g. the human heel pad) *in vivo* are compared and the importance of parameter identification is highlighted. The nonlinear mechanics and strain energy functions of materials are presented. The theoretical frame and current researches on the inverse FE modelling method and optimisation programs are critically reviewed and potential improvement is discussed. The difficulties and challenges for inverse FE modelling approach based on the indentation tests to predict the nonlinear material properties are reviewed and discussed.

## 2.2 Indentation method and its applications in characterising materials

For over a century, the indentation test has been employed to probe the mechanical behavior of materials for a wide range of engineering/medical applications *(Ren et al, 2002; Gerard, 2005)*. In the test, an indenter is pressed onto the sample surface and the force-indentation depth data was used to represent the resistance of the material. Many different types of indenters with various shapes have been developed as schematically shown in Figure 2.1. Sharp indenters such as cone, sharp pyramidal tip indenter (trilateral or quadrilateral) and spherical indenter are normally used for harder materials such as metal or ceramic or plastics. Many hardness systems have been developed based on the average pressure underneath the indenters *(Dao et al, 2001)*. Softer materials such as foams and biological tissues are normally tested using flat indenter and spherical indenters. Conventional foam tester (shore hardness) requires a large sample (at least 6 mm thick) and the method only provides information about the hardness of a sample, which could not be directly used to model the detailed material behaviours in service (*Petre et al, 2007*).

Recently, instrumented indentation is increasingly being used to probe the dynamic mechanical response of materials *(Taljat and Zacharia, 1998; Giannakopoulos, 2006)*. In the test, the force and indentation depth is continuously monitored and the indentation resistance of the material is represented by the whole loading unloading curve rather than a single value. Figure 2.2 shows, schematically, a typical continuous indentation curve of EVA foams, which is normally used for making the midsole of running shoes. The whole loading curve can be used to represent the resistance of the material over different indentation depth, therefore provide a more realistic representation of the loading condition in service. This could be a distinctive advantage of continuous indentation over static indentation tests. The additional levels of control, sensitivity, and data acquisition offered by instrumented indentation systems have resulted in numerous advances in materials science, particularly regarding fundamental mechanisms of mechanical behaviour.

A number of studies have used continuous indentation to study the loading response of both isolated and bulk soft tissue. It is convenient to use and does not require large

specimen. In addition the loading mode in an indentation is directly relevant to some service condition of these materials, such as foams, heel pad etc. This made it an attractive method in testing these materials. However, the strain fields under an indenter are very complex even for an isotropic material and a robust data analysis method is very essential. For more complicated materials systems (e.g. thin films, small volumes, porous structures, biomaterials), indentation response is tied to specific aspects of material behavior yet effective interpretation requires expertise in both indentation mechanics and the physics of the system being indented. *(Gouldstone et al, 2007).* Another difficulty in analyzing indentation test data is associated with the material behaviors, which are often described by complex nonlinear material models *(Lanir, 1979; Oomens et al, 1987; Keeve et al, 1998; Hendriks et al, 2006).* Most of these models have multiple parameters that could not be directly obtained from the indentation tests. A thorough approach to predict these properties has to be developed. This is particularly important for sport materials such as foam (e.g. midsole EVA foams) and biological tissue (e.g. the human heel pad) (Figure 2.3), as these materials could be under very complex loading conditions in service.

## 2.3 Mechanical testing of the human heel pad

Heel pad testing and its interaction with the supporting structure (shoe) is an important research field for sport or medical applications. Figure 2.3 shows the structure of the human foot within an assembly of a running shoe. The human heel pad is uniquely designed to enable pain-free weight bearing and locomotion *(Rome, 1998)*. It also has the ability to attenuate impact forces at heel strike of the gait cycle so as to protect the underlying calcaneum bone *(Noe et al, 1993; Narvaez et al, 2000)*. All these functions are directly linked to the mechanical behavior of the foot and detailed knowledge of the heel pad mechanics is indispensable, in order to understand its roles as well as injury and medical condition. In addition, the properties of the heel pad also have great importance in product design in terms of providing stability and comfort for sport shoes and protection equipments. All these require detailed investigation with a proper testing and analysis method.

Examinations of the mechanical properties of the human heel pad have been taken two routes: *in vitro* testing and *in vivo* testing. An *in vitro* biological study is carried out on tissues in isolation from a living organism. An *in vivo* biological study is the one taking place within a living biological organism. Both methods have been widely used in many biological systems such as skin and internal organs. The testing method mode can be indentation, compression, tension or torsion depends on the condition of the biological system and the physiological condition of the organ *(Serup and Jemec, 1999; Ren et al, 2005, 2006)*.

### *In vitro* tests of the human heel pad

Figure 2.4(a) shows the setup of an *in vitro* compression test on the human heel pad *(Ker, 1996)*. The heel specimen with skin, fatty tissue and calcareous are separated from the subject and loaded with a metal plate attached to an actuator. The pad is covered by plastic cling film to avoid risk of drying. This approach was also used by other researchers*(Aerts et al, 1995)*. As shown in the Figure 2.4(a), the skin of the heel impacts against a horizontal circular plate of 64 mm diameter. The load and displacement are monitored representing the resistance of the heel to the compression

loading. A typical force displacement data is shown in Figure 2.4 (b). Both the loading and unloading curves are highly nonlinear with significant stiffening at high strain level and hysteresis loop. The *in vitro* tests is similar to conventional material tests once the sample is ready, however, one major problem with *in vitro* studies lies that the tissue no longer has the same physiological properties as *in vivo* situation due to the loss of water etc.

**<u>*In vivo* tests of the human heel pad</u>**

*In vivo* tests are performed on biological tissue in its natural state with the material behavior close to the real physiological condition. It has been increasingly used to study the deformation of biological tissue such as human skin, biological organs, heel as well some internal organs. The most frequently encountered techniques included tension tests, compression tests, torsion tests, suction tests or indentation tests *(Gunner et al, 1979; Ohura et al, 1980; Wijn, 1980; Berardesca et al, 1986; Sugihara et al, 1991; Warren et al, 1991; Clark et al, 1996; Tong et al, 2003; Pailler-Mattei and Zahouani, 2006).* Two most suitable methods for heel tests are the compression and indentation tests.

Figure 2.5 shows a typical set-up of *in vivo* compression testing of the human heel pad *(Tong et al, 2003).* The test rig used includes a base plate, a support frame with a see-through Perspex foot mount plate attached to it, a foot rest jig incorporating a linear lead screw slide unit with a rotating handle at the end of it and a L-shaped plate which supports the probe holder with the ultrasound transducer probe. A force transducer and linear variable displacement transducer (LVDT) measured the compression force and displacement. Velcro straps are used to restrain patient foot movement relative to the test rig. The heel pad thickness at unloaded condition ($T_U$) and loaded condition ($T_L$) is measured using Ultrasound. The compressibility index (CIndex), which determines the resilience of the heel pad, is calculated according to equation:

$$CIndex(\%) = \left(\frac{T_L}{T_U}\right)100 \qquad (2.3.1)$$

Where a higher CIndex denotes a higher heel pad resilience.

Strain ($\varepsilon$) in the heel pad is estimated (calculated) according to

$$\varepsilon = 1 - \left( \frac{T_f}{T_U} \right) \tag{2.3.2}$$

where $T_f$ denotes the heel pad thickness at a given force and $T_U$ is the unloaded heel pad thickness. When $\varepsilon = 0$, there is no compression; and when $\varepsilon = 1$, there is full compression. This semi-quantitative index allows direct comparison of the effect of factors such as age, sex, weight, height of all subjects on their heel mechanical strength *(Tong et al, 2003)*.

Klaesner *et al (2001)* used a portable indenter device to determine the force-displacement data on soft tissue in a clinical setting. In the test, the foot is stabilised using clay to minimise movement of the metatarsals and the stiffness can be measured using the indentation test (r=4mm indenter was used). The data is then used to calculate the effective Young's modulus for the tissue using equations derived by Zheng *et al (1999)*. The test is convenient to perform, however, the results of the approach are in a wide range of values dependent upon the portion of the curve used as shown in Figure 2.6. This clearly shows that the stiffness is strongly strain level dependent, which made the interpretation of indentation data more difficult. This made it difficult to directly compare results from different sources. A more thorough approach has to be used to predict the material properties based on the nonlinear mechanics, which is to be briefly reviewed in the next section.

## 2.4 Linear and Nonlinear elastic material behaviours

The behaviour of materials subject to tensile/compression forces can be described by a stress-strain graph. Figure 2.7 shows schematically the three main type of stress strain relationships in soft materials (such as rubber, foams and biological tissues), namely linear elastic (a), elastically non-linear (b) and Viscoelastic (c). For an elastic material, the stress is proportional to strain, the strain is recoverable if the stress is removed, i.e. the specimen returns to its original dimensions. This occurs in the initial linear region of the stress-strain curve of flexible foams and some rigid foams. A linear elastic relationship between compressive or tensile stress and strain can be described by:

$$\sigma_x = E\varepsilon_x \tag{2.4.1}$$

where the constant E is the Young's modulus.

The absolute value of the ratio of the lateral strain to the longitudinal strain is the Poisson's ratio:

$$\nu = -\frac{\varepsilon_y}{\varepsilon_x} \tag{2.4.2}$$

At small strain for both compression and tension, the average experimentally observed Poisson's ratio, $\nu$, of foams is about 0.33. At larger strains it is commonly observed that Poisson's ratio is effectively zero during compression — the buckling of the cell walls does not result in any significant lateral deformation. However, during tension, the Poisson's ratio is nonzero, which is a result of the alignment and stretching of the cell walls. For an isotropic material, the shear modulus G can be calculated using:

$$G = \frac{E}{2(1+\nu)} \tag{2.4.3}$$

As shown in Figure 2.7 (b), non-linear relationships between stress and strain are usually convex upwards in compression (compressive stresses and strains are taken to be positive). For foam or biological tissues, the non-linearity occurs due to changes in its geometry at high strains. At small strains the material deforms in a linear, elastic manner as a result of cell wall bending. At large strain, the cell walls rotate and align, resulting in an increased stiffness. The walls are substantially aligned at a tensile strain of about 0.33. When the material is under cyclic loading, it will exhibit a typical viscoelastic material behaviour illustrated in Figure 2.7 (c). This is a type of

deformation exhibiting the mechanical characteristics of viscous flow and elastic deformation. Most foam materials and biological material exhibited highly nonlinear and viscoelastic behaviors *(Mills et al, 2003)*. Nonlinear materials behaviour is significantly different from linear deformation and it has to be understood based on the nonlinear mechanics.

## 2.5 The basics of non-linear continuum mechanics for finite element analysis

### 2.5.1 Deformation gradient

In continuum mechanics, an initial configuration $k^0$, and a deformed configuration $k^t$ of the considered continuum has to be considered as shown in Figure 2.8.

$x \in k^t$ , is the corresponding configuration mapping of the initial configuration $X \in k^0$ transformed through a displacement vector *u(X)*.

$$x = u(X) + X \tag{2.5.1}$$

$$x = \varphi(X,t) \tag{2.5.2}$$

The components of the total differential *dx* is given in terms of the components of $dX$ and the partial derivatives of $\varphi$ by Atkin and Fox *(1980)*.

$$dx_i = \frac{\partial \varphi_i(X,t)}{\partial X_A} dX_A = \varphi_{i,A} dX_A \tag{2.5.3}$$

The quantities $\varphi_{i,A}$ are known as the deformation gradients. They are the components of a second-order tensor known as the deformation gradient tensor denoted by $F$.

$$F_{iA} = \varphi_{i,A} = \frac{\partial x_i}{\partial X_A} \quad \text{(i, A=1,2,3)} \quad \text{or} \quad F = \frac{\partial \varphi}{\partial X} = \frac{\partial x}{\partial X} \tag{2.5.4}$$

where F is the deformation gradient tensor with component $F_{iA}$. By the rules of index notation that F is a second order tensor, since it has two independent indices. It is also important to note that F is not symmetric. The deformation gradient tensor can also be written in matrix format as:

$$F = \begin{pmatrix} F_{11} & F_{12} & F_{13} \\ F_{21} & F_{22} & F_{23} \\ F_{31} & F_{32} & F_{33} \end{pmatrix} = \begin{pmatrix} \frac{\partial \varphi_1}{\partial X_1} & \frac{\partial \varphi_1}{\partial X_2} & \frac{\partial \varphi_1}{\partial X_3} \\ \frac{\partial \varphi_2}{\partial X_1} & \frac{\partial \varphi_2}{\partial X_2} & \frac{\partial \varphi_2}{\partial X_3} \\ \frac{\partial \varphi_3}{\partial X_1} & \frac{\partial \varphi_3}{\partial X_2} & \frac{\partial \varphi_3}{\partial X_3} \end{pmatrix} \tag{2.5.5}$$

The deformation gradient is the most basic object used to quantify the local deformation at a point in a solid.

Assuming the Jacobian exists at each point of deformed configuration, which physically can be interpreted as the ratio of the undeformed volume over the deformed volume for a homogeneous deformation at a material point.

$$J = \det(F) > 0 \tag{2.5.6}$$

then the material of the body cannot penetrate itself, and that material occupying a finite non-zero volume in initial configuration cannot be compressed to a point or expanded to infinite volume during the motion *(Atkin and Fox, 1980)*. Assuming that a volume element $dV_0$ in initial configuration deforms into a volume element $dV$ in deformed configuration where

$$dV = JdV_0 \tag{2.5.7}$$

Let $\rho$ denote the density of the body in the deformed configuration and $\rho_0$ the density in initial configuration. Then the next equation should exist

$$\int_V \rho dV = \int_{V_0} \rho_0 dV_0 \tag{2.5.8}$$

So

$$J = \frac{\rho_0}{\rho} \tag{2.5.9}$$

where $\rho_0$ and $\rho$ are the initial and deformed material densities, respectively.

For an incompressible material, $J = 1$ for all admissible deformations *(Weiss and Gardiner, 2001)*.

### 2.5.2 Strain tensor and principle strain invariants

Related to the deformation gradient tensor $F$, two more convenient measures of the stretching part of the deformation can be defined.

$$C = F^T F \tag{2.5.10}$$

$$B = FF^T \tag{2.5.11}$$

$C$ and $B$ are right and left Cauchy-Green strain tensors, respectively, which are symmetric second-order tensors. These tensors provide measures of material stretching that are independent of rigid body rotation and form the basis of constitutive model development for soft materials.

Since the right Cauchy strain tensor is symmetric and positive definite, it will have three real eigenvalues. The square roots of these eigenvalues are denoted as the principal stretch of the material

If the three principal stretches are defined as $\lambda_1$, $\lambda_2$, $\lambda_3$, then, the deformation can be represented by $x_{1\text{-}3}$ in the three directions:

$$x_1 = \lambda_1 X_1, \qquad x_2 = \lambda_2 X_2, \qquad x_3 = \lambda_3 X_3$$

$$F = \begin{pmatrix} \lambda_1 & 0 & 0 \\ 0 & \lambda_2 & 0 \\ 0 & 0 & \lambda_3 \end{pmatrix} = F^T$$

$$C = F^T F = \begin{pmatrix} \lambda_1 & 0 & 0 \\ 0 & \lambda_2 & 0 \\ 0 & 0 & \lambda_3 \end{pmatrix} * \begin{pmatrix} \lambda_1 & 0 & 0 \\ 0 & \lambda_2 & 0 \\ 0 & 0 & \lambda_3 \end{pmatrix} = \begin{pmatrix} \lambda_1^2 & 0 & 0 \\ 0 & \lambda_2^2 & 0 \\ 0 & 0 & \lambda_3^2 \end{pmatrix} \tag{2.5.12}$$

The principle strain invariants are:

$$I_1 = trC = \lambda_1^2 + \lambda_2^2 + \lambda_3^2$$

$$I_2 = \frac{1}{2}(trC)^2 - \tfrac{1}{2} trC^2 = \lambda_1^2\lambda_2^2 + \lambda_2^2\lambda_3^2 + \lambda_3^2\lambda_1^2 \tag{2.5.13}$$

$$I_3 = \det C = \lambda_1^2\lambda_2^2\lambda_3^2$$

Where "tr" denotes the trace of the tensor. These parameters ($I_1$, $I_2$, $I_3$), the principle strain invariants of the right Cauchy strain tensor, are commonly used to define the strain energy functions together with the corresponding stress tensors *(Atkin and Fox, 1980)*.

In finite deformation theory, different measures of stress and strain are employed depending on whether the quantity is to be referred to the reference configuration or the deformed configuration. The Green-Lagrange strain tensor is used when strain is referred to the reference configuration *(Weiss and Gardiner, 2001)*:

$$E = \frac{1}{2}(F^T F - I) \tag{2.5.14}$$

where $I$ represents the identity tensor.

Re-writing equation (2.5.14) into a different form as:

$$E = \frac{1}{2}(C - I) \tag{2.5.15}$$

C is the right Cauchy deformation tensor defined in equation (2.5.10). As with all strain tensors that correctly describe large deformation, $E = 0$ for rigid body motion *(Weiss and Gardiner, 2001).*

The Green-Lagrange strain tensor can be written in terms of the deformation gradient tensor as follow:

$$E_{ij} = \frac{1}{2}(F_{ki}F_{kj} - \delta_{ij}) \tag{2.5.16}$$

Where $\delta_{ij}$ is the kroneckor delta, which follows:

$$\delta_{ij} = \begin{cases} 1, & i = j \\ 0, & i \neq j \end{cases} \qquad i, j=1,2,3 \tag{2.5.17}$$

Using the definition of the deformation gradient, the Green-Lagrange strain tensor can be written in terms of the displacements as:

$$E_{ij} = \frac{1}{2}(\frac{\partial u_k}{\partial X_i} * \frac{\partial u_k}{\partial X_j} + \frac{\partial u_j}{\partial X_i} + \frac{\partial u_i}{\partial X_j}) \tag{2.5.18}$$

This relationship shows that the large deformation strain tensor contains a quadratic term. This means that all large deformation analyses are non-linear. Ignoring the quadratic term, the small deformation strain tensor can be defined as

$$\varepsilon_{ij} = \frac{1}{2}(\frac{\partial u_j}{\partial X_i} + \frac{\partial u_i}{\partial X_j}) \tag{2.5.19}$$

where $\varepsilon_{ij}$ is an approximate measure of strain that is only accurate for infinitesimal strains which is less than 1%.

### 2.5.3 Stress tensor

The Cauchy stress, $T$, is defined as the force acting on the deformed configuration, i.e. force/(unit deformed area). The problem with using the Cauchy stress tensor for

analysing materials undergoing large deformation is that the area in the deformed configuration generally is not known. For this reason, it is often advantageous to use a stress tensor that is defined in terms of the reference or initial configuration.

Two commonly used measures are the first and second Piola-Kirchoff stress tensors. They are defined respectively as

$$P = JF^{-1}T \tag{2.5.20}$$

$$S = JF^{-1}TF^{-T} = PF^{-T} \tag{2.5.21}$$

The first Piola-Kirchoff stress $P$, sometimes referred to as engineering stress, is the component of force in the current configuration on a surface that is normal to the axes in the reference configuration, measured per unit surface area *(Spencer, 1980)*. The components of $P$ can be directly measured experimentally, which is not symmetric.

The stress tensor $S$, second Piola-Kirchoff, is symmetric, but it does not have a direct physical interpretation. $S$ is used more commonly than $P$ because it is energetically conjugate to the Green-Lagrange strain tensor $E$. The tensors S and $E$ often appear together in constitutive models for large deformation elasticity. In the case of finite deformations, the Piola-Kirchhoff stress tensors are used to express the stress relative to the reference configuration. This is in contrast to the Cauchy stress tensor which expresses the stress relative to the present configuration. For infinitesimal deformations or rotations, the Cauchy and Piola-Kirchoff tensors are identical.

### 2.5.4 Strain energy functions

Strain energy refers to the Potential energy stored in a body by virtue of deformation. If the material is perfectly elastic the strain energy is equal to the work that must be done to produce both normal and shear strains. Once the stress causing the strain is removed, the strain energy is recovered. The recovery is total for perfectly elastic material and partial for plastic material due to energy dissipation. The strain energy function, $W$, is a function which relates the strain of a material to the energy developed by this deformation. Such a function is only properly defined for elastic material. Strain energy density ($U$): Strain Energy Density (SED) is strain energy

measured per unit volume of the body. SED represents a better indication of the material since it is normalized to the size of the body. The strain energy function can be viewed as a generalization of Hooke's law that allows us to describe complex elastic components (linear and nonlinear as shown in Figure 2.7) in a systematic way.

Nonlinear elastic materials (such as rubber, foams and biological tissues) undergo large deformations. Figure 2.9 shows typical stress strain curves for rubber under tension. The material can undergo a very large deformation generally known as hyperelastic behaviour. Typical examples include foams, rubber and many biological tissues. For an elastic material, the stress at any point can be defined solely as a function of the deformation gradient F at that point. A change in stress arises only in response to a change in configuration, and the material is indifferent to the manner in which the change in configuration arises in space and time. For a hyperelastic material, the above definition applies, and there is an additional scalar function from which the stress can be derived at each point. The scalar function is the stored energy or strain energy function, *W*, which can also be defined solely in terms of the deformation gradient as presented in Section 2.5.1*(Weiss and Gardiner, 2001)*.

$$W = \tilde{W}(F) \tag{2.5.22}$$

The strain energy, *W*, must obey the Principle of Material Frame Indifference. This principle ensures that rigid body motions will not change the value of the strain energy function. Consequently, *W* may be expressed in the form

$$W = \tilde{W}(C) \tag{2.5.23}$$

where $C$ is the right Cauchy-Green strain tensor. Then, the second Piola-Kirchhoff stress is derived directly from the strain energy as

$$S = 2\frac{\partial W}{\partial C} \tag{2.5.24}$$

Hyperelasticity provides a convenient framework for the formulation of constitutive equations for materials such as foams or biological soft tissues because it allows for large deformations and anisotropy *(Weiss and Gardiner, 2001)*.

Any hyperelastic material maybe represented by a strain energy function. For Hookean (linear) elastic materials, this takes the following form:

$$W = W(I_1, I_2, I_3) \tag{2.5.25}$$

Where

$$I_1 = trC; \qquad I_2 = \frac{1}{2}[(trC)^2 - trC^2]; \qquad I_3 = \det C$$

The isotropic hyperelastic material reduces to linearised elasticity when appropriate assumptions regarding the magnitude of strains and rotations are made *(Weiss and Gardiner, 2001).*

For nonlinear Finite Element analysis, the solution process often proceeds by searching for a configuration that is close to a known equilibrium state that provides a balance between incrementally applied loads and the current stress field in the material. In this case, the elasticity tensor plays an important role in the iterative solution process *(Weiss and Gardiner, 2001).*

## 2.6 Strain energy functions for rubber, foams and biological materials

Many strain energy function models have been developed to characterise different material systems which undergo large deformation, typically Mooney-Rivlin model, neo-Hookean form, Ogden model and hyperfoam model *(Ogden, 1972a; Petre et al, 2007).* The hyper foam model is for highly compressible material (such as polymer foams) whiles the other three are for incompressible materials (such as rubber and water filled structures). These material models have been employed in several computational software including ABAQUS, which are briefly described below.

### 2.6.1 Models for incompressible material

**Mooney-Rivlin model**

Mooney derived an expression for the strain energy function for rubber starting from several assumptions: (1) The material is homogeneous and free from hysteresis; (2) The material is isotropic initially and throughout the deformation; (3) The deformations occur without change in volume; (4) The traction in simple shear in any isotropic plane is proportional to the shear *(Mooney, 1940).*

The linear form of strain energy function Mooney initially proposed is:

$$W = C_1(I_1 - 3) + C_2(I_2 - 3) \qquad (2.6.1)$$

where $C_1$ and $C_2$ are constants. It is the most general form admitting a linear relationship between stress and strain in simple shear, and has since been referred to as the Mooney-Rivlin model. With suitable choices of $C_1$ and $C_2$, this equation gives a marginally better fit to some of the experimental data of rubber than pure elastic models *(Atkin and Fox, 1980).*

The strain energy W (Equation 2.6.1) can be split into to two parts, the deviatoric and volumetric terms. Then the form of the Mooney-Rivlin strain energy density becomes (*ABAQUS*).

$$U = C_{10}(\bar{I}_1 - 3) + C_{01}(\bar{I}_2 - 3) + \frac{1}{D_1}(J^{el} - 1)^2 \qquad (2.6.2)$$

where $U$ is the strain energy per unit of reference volume; $C_{10}$, $C_{01}$, and $D_1$ are temperature-dependent material parameters, $\bar{I}_1$, $\bar{I}_2$ are the first and second deviatoric strain invariants defined as

$$\bar{I}_1 = \bar{\lambda}_1^2 + \bar{\lambda}_2^2 + \bar{\lambda}_3^2 \qquad and \qquad \bar{I}_2 = \bar{\lambda}_1^{(-2)} + \bar{\lambda}_2^{(-2)} + \bar{\lambda}_3^{(-2)} \qquad (2.6.3)$$

where the deviatoric stretches $\bar{\lambda}_i = \bar{J}^{\frac{1}{3}}\lambda_i$; $J$ is total volume ratio; $J^{el}$ is the elastic volume ratio. $\lambda_i$ are the principal stretches. The initial shear modulus ($\mu_0$) and bulk modulus ($K_0$) are given by

$$\mu_0 = 2(C_{10} + C_{01}) \qquad (2.6.4)$$

$$K_0 = \frac{2}{D_1} \qquad (2.6.5)$$

Only isotropic thermal expansion is permitted with the hyperelastic material model. The elastic volume ratio, $J^{el}$, relates the total volume ratio ($J$) and the thermal volume ratio ($J^{th}$) following this equation:

$$J^{el} = \frac{J}{J^{th}} \qquad (2.6.6)$$

$J^{th}$ is given by

$$J^{th} = (1 + \varepsilon^{th})^3 \qquad (2.6.7)$$

where $\varepsilon^{th}$ is the linear thermal expansion strain that is obtained from the temperature and the isotropic thermal expansion coefficient.

**Neo-Hookean form mode**

The form of the neo-Hookean strain energy potential is given by

$$U = C_{10}(\bar{I}_1 - 3) + \frac{1}{D_1}(J^{el} - 1)^2 \qquad (2.6.8)$$

where $C_{10}$, and $D_1$ are temperature-dependent material parameters, $\bar{I}_1$ is the first deviatoric strain invariants; $J^{el}$ is the elastic volume ratio.

## Ogden form models

Another commonly used model is the Ogden model *(Ogden, 1972a)*. Instead of taking $U$ as a function of $I_1$ and $I_2$, the model is based on an assumption that $U$ is a function of the principle values $b_1$, $b_2$, $b_3$ of $B$.

$$U = \sum_n (\mu_n / \alpha_n)(b_1^{\alpha_n} + b_2^{\alpha_n} + b_3^{\alpha_n} - 3) \tag{2.6.9}$$

where $\mu_n$ are constants, and the $\alpha_n$ are not necessarily integers and may be positive or negative. $B$ is left Cauchy-Green strain tensor and defined in equation (2.5.11). $b_1$, $b_2$, $b_3$ are principle values of $B$. $B$ is left Cauchy-Green strain tensor and defined in equation 2.5.11. The general form of the Ogden strain energy potential is

$$U = \sum_{i=1}^{N} \frac{2\mu_i}{\alpha_i^2}(\bar{\lambda}_1^{\alpha_i} + \bar{\lambda}_2^{\alpha_i} + \bar{\lambda}_3^{\alpha_i} - 3) + \sum_{i=1}^{N} \frac{1}{D_i}(J^{el} - 1)^{2i} \tag{2.6.10}$$

where $\bar{\lambda}_i$ are the deviatoric principle stretches; $\lambda_i$ are the principle stretches; $N$ is a material parameter; $\mu_i$, $\alpha_i$, and $D_i$ are temperature-dependent material parameters *(ABAQUS)*.

The initial shear modulus and bulk modulus for the Ogden form are given by

$$\mu_0 = \sum_{i=1}^{N} \mu_i, \qquad K_0 = \frac{2}{D_1} \tag{2.6.11}$$

Following this form, the Mooney-Rivlin form can also be obtained from the general Ogden strain energy potential for special choices of $\mu_i$ and $\alpha_i$.

### 2.6.2 Models for compressible material

In reality, all rubbers are compressible to certain extent, however when subjected to very high hydrostatic pressures, vulcanized rubber undergoes only very small volume changes, so that for practical purposes it can be regarded as incompressible. For foams this is no longer the case and, motivated by the above considerations, studies have

been made on the appropriate forms of W for compressible rubberlike materials *(Blatz and Ko, 1962; Ogden, 1972b)*.

Using a combination of theoretical arguments and experimental results, Blatz and Ko *(1962)* suggested a strain energy function density of the following form

$$U=\frac{1}{2}\mu f\left\{J_1-1-\frac{1}{\nu}+\frac{1-2\nu}{\nu}J_3^{-2\nu/(1-2\nu)}\right\}+\frac{1}{2}\mu(1-f)\left\{J_2-1-\frac{1}{\nu}+\frac{1-2\nu}{\nu}J_3^{2\nu/(1-2\nu)}\right\} \tag{2.6.12}$$

where $\mu, f, \nu$ are constants, and

$$J_1=I_1, \qquad J_2=I_2/I_3, \qquad J_3=I_3^{1/2} \tag{2.6.13}$$

When $\nu$=0.5 and the material is incompressible so that $I_3=1$, the strain energy function reduces to the Mooney-Rivlin form

$$U=\frac{1}{2}\mu f\{I_1-3\}+\frac{1}{2}\mu(1-f)\{I_2-3\}$$

$$U=C_1(I_1-3)+C_2(I_2-3) \tag{2.6.14}$$

In the case of 47% foamed polyurethane rubber, the results of Blatz and Ko indicate that $f=0, \qquad \mu=\frac{1}{4}$, in which case

$$U=\frac{1}{2}\mu\{J_2+2J_3-5\} \tag{2.6.15}$$

and clearly $U$ is independent of $I_1$.

By generalising the Ogden model for incompressible materials, a new form of compressible materials was proposed *(Ogden, 1972b)*.

$$U=\sum_n(\mu_n/\alpha_n)(b_1^{\alpha_n}+b_2^{\alpha_n}+b_3^{\alpha_n}-3)+F((b_1b_2b_3) \tag{2.6.16}$$

in which the compressibility is accounted for by the additive function F of $b_1b_2b_3$. In finite element modelling, an improved equation is suggested known as the elastomeric foam material model *(ABAQUS)*.

$$U=\sum_{i=1}^{N}\frac{2\mu_i}{\alpha_i^2}\left[\hat{\lambda}_1^{\alpha_i}+\hat{\lambda}_2^{\alpha_i}+\hat{\lambda}_3^{\alpha_i}-3+\frac{1}{\beta_i}((J^{el})^{-\alpha_i\beta_i}-1)\right] \tag{2.6.17}$$

where $N$ is a material parameter; $\mu_i$, $\alpha_i$ , and $\beta_i$ are temperature-dependent material parameters;

$$\hat{\lambda}_i = (J^{th})^{-\frac{1}{3}} \lambda_i \tag{2.6.18}$$

so,

$$\hat{\lambda}_1 \hat{\lambda}_2 \hat{\lambda}_3 = J^{th} \lambda_1 \lambda_2 \lambda_3 = J^{th} J = J^{el} \tag{2.6.19}$$

and $\lambda_i$ are the principal stretches. The elastic and thermal volume ratios are: $J^{el}$ and $J^{th}$ respectively.

The coefficients $\mu_i$ are related to the initial shear modulus, $\mu_0$, by

$$\mu_0 = \sum_{i=1}^{N} \mu_i \tag{2.6.20}$$

while the initial bulk modulus, $K_0$, follows the form

$$K_0 = \sum_{i=1}^{N} 2\mu_i (\frac{1}{3} + \beta_i) \tag{2.6.21}$$

For each term in the energy function, the coefficient $\beta_i$ determines the degree of compressibility, which is related to the Poisson's ratio, $\nu_i$ , by the expressions

$$\beta_i = \frac{\nu_i}{1-2\nu_i}, \qquad \nu_i = \frac{\beta_i}{1+2\beta_i} \tag{2.6.22}$$

Thus, if $\beta_i$ is the same for all terms, a single effective Poisson's ratio, $\nu_i$ can be derived. This effective Poisson's ratio is valid for finite values of the logarithmic principal strains ($\varepsilon_1$, $\varepsilon_2$, $\varepsilon_3$) in uniaxial tension ($\varepsilon_2 = \varepsilon_3 = -\nu\varepsilon_1$). Then the stress-strain relations are defined in terms of the nominal stress (the force divided by the original undeformed area) and the nominal, or engineering, strains, $\varepsilon_i$. The principal stretches, $\lambda_i$, are related to the principal nominal strains, $\varepsilon_i$, by

$$\lambda_i = 1 + \varepsilon_i \tag{2.6.23}$$

## 2.7 Materials testing and parameters identification

As shown in the last section, most of these nonlinear strain energy functions include more than one material parameter. It is a challenging task to accurately derive these functions. Conventionally, the determination of material parameters is based on the use of test samples with a standardised geometry and strain state (as shown in Figure 2.10). Such that particular conditions on the stress and strain field are satisfied in the sample/or part of the sample. Then the unknown model parameters are obtained *via* curve fitting from experimental data.

Current standard approaches normally require large numbers of tests and samples with well-defined geometries *(Mills and Zhu, 1999; Mills et al, 2003; Moreu amd Mills, 2004; Petre et al, 2007)*. For example, for foam materials, a wide range of tests have to be used (e.g. compression test, shear test, volumetric test, etc.) in order to predict these parameters. In a shear test, the assembly has to use adhesives to bond the sample and loading platen which limits the strain level can be reached by the maximum strength of the adhesive bond *(Payne, 1991; Petre et al, 2006)*. In addition, the method is inconvenient or even impossible where standard specimens are not readily available, or for *in situ* monitoring the mechanical strength of the materials.

Recently, some effort has been made to use non-standard tests under more complex conditions to determine the material parameters. The uses of a range of tests have been explored including suction, intension, torsion, bending test or indentation *(Vannah and Childress, 1996; Diridollou et al, 2000; Knight et al, 2001; Elsner, 2002; Vescovo et al, 2002; Mattei and Zahouani, 2004)*. Generally, these tests involve applying a predefined stress/deformation on the sample surface and the monitoring of the load/displacement. In the case of the indentation test, an indenter is pressed onto the sample surface and the force-indentation depth data is used to represent the resistance of the material. This method is convenient to use and requires smaller testing areas than other testing methods. In addition, the loading mode is directly relevant to the human perception of materials softness. These made it attractive method for application in biomedical or sport engineering *(Bader and Boeker, 1983; Erdermir et al, 2006)*. Recent development of continuous indentation method has

greatly improved the information can be determined from indentation tests for different type of materials *(Giannakopoulos, 2006; Vandamme and Ulm, 2006)*. In an indentation test, the stress and strain is not well defined, so it could not be used to directly determine the material parameters. Recent development of inverse modelling techniques opened up the possibility to combine indentation test and FE modelling (simulating the test itself) to derive the material parameters through inverse FE modelling *(Delallea et al, 2006; Erdemir et al, 2006)*. In this process, the material properties are determined by using FE modelling to find out an optimum material sets which match the experimental test data. The searching and optimisation process is associated with setup of the experimental works and the inverse program.

## 2.8 Inverse problems and its application in material properties prediction

Inverse modelling has been applied to many problems in engineering fields. General areas in inverse problems in engineering mechanics were the subjects of mathematical and computational aspects of inverse problems, parameter or system identification, shape determination, sensitivity analysis, optimization, material property characterization, ultrasonic non-destructive testing, elastodynamic inverse problems, thermal inverse problems, and other engineering applications *(Tanaka and Dulikravick, 2000)*. Parameter estimation can be treated as one form of inverse problem of optimisation that deals with the determination of the mechanical system with unknown material properties, geometry sources or boundary conditions, from the knowledge of response to given excitations on its boundary *(Neaupane and Sugimoto, 2003)*. A successful program for predicting material parameter has to be accurate, efficient and robust and this depends on testing method used, inverse program, optimisation method etc.

### 2.8.1 Inverse parameter estimation

An inverse problem is the task that often occurs in many branches of science and mathematics where the values of some model parameter(s) must be obtained from the observed data (Data → Model parameters). A quotation attributed to Prof. Oleg Mikailivitch Alifanov, a great Russian proponent of Inverse Methods, says: "Solution of an inverse problem entails determining unknown *causes* based on observation of their *effects*". On the contrary, the corresponding direct problem involves finding effects based on a *complete* and *precise* description of their causes. Figure 2.11 displays a graphical representation of the concepts mentioned above. The solution for an inverse problem can be searched formulating it as an optimisation problem. A technique for property reconstruction from measurements can be described as a generalised least squares approximation. The standard least squares solution can guarantee the existence of a solution, but it can be unstable in the presence of noise, a permanent feature in experimental data *(De Campos et al, 2007)*.

Inverse problems belong to the class of ill-posed problems, in the sense that the existence, uniqueness and stability of the solutions cannot be assured. In order to have a well-posed inverse problem, assuring a final solution that is stable and physically acceptable, some *priori* information must be added to the quadratic difference term. In general, this additional information associated with the inverse solution means smoothness *(De Campos et al, 2007).*

Denoting $x = (x_1, x_2, .....x_n)^T$, the unknown vector to be determined by the inverse analysis, the inverse problem can be formulated as a nonlinear constrained minimization problem,

$$\min\ O(x), \qquad l_q \le x_q \le u_q \qquad (q=1,2,\ldots\ldots n) \tag{2.8.1}$$

where 'n' denotes the number of unknown parameters, the lower and upper bounds $l_q$ and $u_q$ are chosen in order to allow the inversion to lie within some known physical limits, and the objective function is given by

$$O(x) = \sum_{i=1}^{Nm} \left[ \Phi_i^{Exp} - \Phi_i^{Mod}(x) \right]^2 + \Omega(x) \tag{2.8.2}$$

where $N_m$ denotes the number of measurement points (or points for comparison), $\Omega$ the regularisation operator, and $\Phi$ a variable that can be measured and modelled (simulated) in a mathematical formulation *(De Campos et al, 2007).* There are two formulations for solving inverse problems *(Beck et al, 1985).* The unknown function can be solved in a parameter estimation approach, or a function estimation approach, where the functional form is not available.

### 2.8.2 Optimisation Methods

There are many methods available to solve the parameter estimation problems. The computational cost of the inverse analysis depends mainly on the applied optimisation algorithms *(Szeligo et al, 2004)*, the method of minimisation of an objective function or residuals of an equation set. In general, optimization methods can be classified as stochastic/deterministic.

## Stochastic optimisation methods

Stochastic optimisation methods, in general, search for the position of the minimum in the parameter space with a couple of parameter vectors $\{x_i\}_{i=1,2,...} \in X$. The quality of parameter vectors such composed is checked with the least square- functional $f^2(x)$. The best parameter vector is then chosen as the optimal solution. The advantage of these methods is that they can overcome local minimum and are therefore well suited to find the global minimum. Unfortunately, the frequent calculation of the least-square-functional may result in high numerical cost. Several stochastic methods have been proposed, such as the evolution strategy and simulated annealing *(Schwefel, 1981)*.

The simulated annealing (SA) method is inspired by a physical process of slow cooling of initially melted material. This process looks for obtaining perfect crystals which, at the end of cooling, have the smallest possible internal energy. In the process of cooling, the molecules move into the interior of the mixture randomly, positioning them in a crystal network when the temperature is reduced. The method uses the Metropolis' algorithm *(Metropolis et al, 1953; Press et al, 1996; De Campos et al, 2007)* and the search is initiated at some point of the search space. The main steps for SA implementation *(Press et al, 1996; De Campos et al, 2007)* are as outlined follows:

1. Define initial candidates, and compute the objective function value for each candidate. Define an initial temperature for the problem.
2. Chose new candidates randomly (if they have the same value for the mathematical model, choose others). Re-compute for each one the objective function.
3. If the value of the objective function decreases between two consecutive iterations, the changing is then accepted and the process continues. If the value is greater, the changing is accepted with probability of $p = e^{-(\Delta O(x)/T)}$, where

$\Delta O(x)$ is the difference in the value of the objective function between two iterations.

4. Decrease the temperature to $r*T$ (annealing schedule) after a certain number of iterations of step (2). Here, T is the temperature in the step (3), and $r$ is a reduction factor.
5. Repeat steps 2-3-4 up to the convergence.

The SA algorithm employs a random search mechanism which accepts not only changes that decrease objective function $O(x)$, but also some changes that increase it.

## Gradient-based deterministic optimisation methods

In gradient-based deterministic optimization methods, in every iteration step, the program calculates the gradient of the least-square-functional $f^2(x)$ with respect to the parameters $x$, namely

$$\nabla f^2(x) = \frac{\partial f^2(x)}{\partial x} \tag{2.8.3}$$

The differentiability of the least-square-functional with respect to the parameters has to be guaranteed. Additionally, the iterative solution requires an appropriate choice of initial values for the parameters. The disadvantage of these methods is that they are only suited to find local minima. Two examples of gradient-based deterministic method include the simple gradient method *(Seifert, 2003)* and the Levenberg-Marquardt-method *(Press et al, 1996)*. Due to its robustness, the latter proved to be a well suited method when dealing with parameter identification *(Seifert, 2003)*.

In the simple gradient method, starting from the current parameter vector $\{x_i\}$, in the negative direction of the gradient $\nabla f^2|_{x_i}$, i.e. in the direction of the steepest descent:

$$x_{i+1} = x_i - \alpha \nabla f^2|_{x_i} \tag{2.8.4}$$

The constant α defines the length of the gradient step and is an additional unknown. It has to be identified in a sub-optimisation-procedure to find the next local minimum (if

convergence is given). As mentioned above, an initial parameter vector $x_0$ is needed to start the calculation. The update is performed until a stop criteria is fulfilled, as e.g.

$$| f^2(x_{i+1}) - f^2(x_i) | \leq \delta. \tag{2.8.5}$$

where $\delta$ is a defined tolerance.

The Levenberg-Marquardt method is based on a gradient-strategy for a least-square-functional $f^2(x)$ which depends non-linearly on the unknown parameter vector $x$. A Taylor expansion of $f^2(x)$ around the current parameter vector $x_i$ truncated after the quadratic term yields

$$f^2(x) \approx f^2(x_i) + (x - x_i) \cdot \nabla f^2 |_{x_i} + \frac{1}{2}(x - x_i)^2 \cdot \nabla\nabla f^2 |_{x_i} \tag{2.8.6}$$

The following definitions for the gradient $\nabla f^2 |_{x_i}$ and the Hessian matrix $\nabla\nabla f^2 |_{x_i}$:

Set

$$b = -\nabla f^2 |_{x_i} \tag{2.8.7}$$

$$A = \nabla\nabla f^2 |_{x_i} \tag{2.8.8}$$

near the minimum the following equation can be employed:

$$x_{i+1} = x_i + A^{-1} \cdot b \tag{2.8.9}$$

In the case that $f^2(x)$ is independent (or almost independent) of one component of $p_i$, then the matrix A would be singular, i.e. the inverse $A^{-1}$ would not exist. Such a case is present if the experimental data is not sensitive on one of the components of $x_i$. A singularity of A can be treated numerically with the singular value decomposition, described in some published works *(Press et al, 1996; Stoer and Burlisch, 1980).*

Equation (2.8.9) can be considered as a linear set of equations

$$A \cdot \Delta x = b \tag{2.8.10}$$

where the parameter increment $\Delta x$ is given by

$$\Delta x = x_{i+1} - x_i \tag{2.8.11}$$

Further from the minimum a gradient step is used according to equation (2.8.4), which can be recast into

$$\Delta x = \alpha b \tag{2.8.12}$$

The Levenberg-Marquardt method interpolates between equations (2.8.10) and (2.8.12) by making additional assumptions: The constant $\alpha$ in equation (2.8.12) is replaced by the inverse of the product of a scaling parameter $\lambda$ and the corresponding element of the diagonal of A. Equation (2.8.12) now reads:

$$\lambda A_{jj} \Delta x_j = b_j \text{ (no summation over j)} \tag{2.8.13}$$

Merging equations 2.8.10 and 2.8.13 yields

$$\overline{A}_{jk} = \begin{cases} A_{jk}(1+\lambda) & j = k \\ A_{jk} & j \neq k \end{cases} \text{ j,k =1, 2, ... n} \tag{2.8.14}$$

and the linear set of equations

$$\overline{A} \cdot \Delta x = b \tag{2.8.15}$$

can be used to compute the increment $\Delta x$. With $\Delta x$, the equation can be used to evaluate the least-square-functional $f^2(x)$ with the update of the parameter

$$x_{i+1} = x_i + \Delta x \tag{2.8.16}$$

If

$$f^2(x_{i+1}) \geq f^2(x_i) \tag{2.8.17}$$

then

$$\lambda = 10 * \lambda \tag{2.8.18}$$

else

$$\lambda = \lambda / 10 \tag{2.8.19}$$

yields an update of $\lambda$ for the next iteration step. In this iterative solution an initial value for $\lambda$ has to be specified, e.g. $\lambda_0 = 10^{-3}$. Again, equation (2.8.5) can be used as a stop criteria. Mohrmann modified the update of $\lambda$ by a sub-optimization procedure

of $f^2$ in direction of $\lambda$. This modification results in a better convergence rate *(Seifert, 2003)*.

A successfully inverse FE modelling program requires the combination of FE modelling and data analysis. Commonly used methods in material parameters estimation include three main approaches (i) general minimization procedure with interactive data processing method; (ii) Artificial Neural Network (ANN) algorithm and (iii) Kalman filtering techniques. Details of each approach and their application are described in section 2.8.3 -2.8.5.

### 2.8.3 An optimisation method with interactive data processing

Figure 2.12 shows a typical inverse modelling approach used an interactive method *(Meuwissen et al, 1998)*. This process involves interactively changing the material parameters in the FE models until the predicted results or results match the experimental results. In this approach, an optimisation algorithm is coupled with the finite element method in order to find the optimal values for a set of target material parameters to be determined. A user defined objective function serves to measure the optimality of the parameters. Finally, an optimal fit of the simulated data to the experimental is reached. This approach has been used for different materials including metals, polymeric foam and bio-*materials (Kauer 2001; Bolzon et al, 2004; Gerard et al, 2005; Hendriks et al, 2006; Ren et al, 2006)*. As shown in Figure 2.12 the FE modelling is repeated with changing material parameters until an optimum combination of material properties is found. This approach required re-running the FE models during the optimisation process, which may take a large amount of time to reach the optimal solution with increased the computational cost.

Kauer *(2001)* applied this method with suction tests to determine the linear material parameter of the human skin. In this work, the experimental data is the pressure displacement data. The parameters in FE models of the suction test were varied until a close match between the experimental results and numerical was reached. Gerard *et al (2005)* employed similar iterative optimal method with indentation experiments

characterizing the mechanical behavior of the human tongue. To determine the constitutive law from this indentation experiment, i.e. the global relationship that can be assumed between strain and stress inside the body, an optimization algorithm based on an "*analysis by synthesis*" strategy was elaborated. It consists of (1) assuming a given constitutive law, (2) building a finite element analysis (FEA) of the indentation experiment, (3) comparing the simulations provided by this FEA with the indentation measurements, (4) using this comparison to propose a change of the constitutive law that should bring the FEA simulations and the measurements closer, and (5) starting again with (2) up to the point where the comparison carried out in (3) gives satisfactory results *(Gerard et al, 2005)*. Recently, Ren *et al (2006)* developed parametric approach to determine the results from *in vivo* surface testing. The approach is shown in Figure 2.13. This approach involves a two-staged approach using a rough range data first and then refines the material. This method could effectively reduce the amount of computational works required but the approach has to be based on a good pre-knowledge of the materials.

### 2.8.4 Artificial Neural Network (ANN)

Artificial neural networks consist of simple processing units called neurons arranged in layers connecting inputs to the outputs. A typical example of a single layer neural network structure is shown in Figure 2.14. The most popular of these is the feed-forward network where the output of one neuron is the input to neurons of the next layer only. The hidden layers provide the necessary complexity for non-linear problems. A typical neuron receives input signals $x[k]$, sums them according to their weights $w[k]$, passes it through a function (F) and produces an output $y[k]$. This output is then a weighted input for other neurons in the next layer, which perform similar functions. The final calculated outputs are then compared with the experimentally obtained outputs $T[k]$, and the error $e[k]$ is calculated. This error is then propagated backwards and used for adjusting the weights of each of the neurons. The process of using the experimental outputs to minimise the error iteratively is

called as training the network. The weights of the trained network are stored, and can be used later for predicting outputs given a different set of inputs *(Wasserman, 1989).*

Recently, Artificial Neural Network (ANN) algorithm has been used to model complex non-linear relationship based on indentation results. Huber *et al (2000; 2002*) presented artificial neural network models to determine the constitutive properties of thin films on a substrate based on the force-depth curves of spherical indentation. Their models enabled the material properties of both the thin film and the substrate to be identified from a single indentation load–displacement curve. Tho *et al (2004)* proposed artificial neural network model to characterise elasto-plastic material properties of metals following the work hardening rules. Kapoor *et al (2005) and* Araujo *et al (2006)* employed ANN technique to predict mechanical properties of a kind of alloy with a laminated structure based on a two layered system as shown in Figure 2.15. In addition, Tyulyukovskiy and Huber *(2007)* used neural networks combined with FE model and experiments to analyse bulk material and thin films for their creep behaviour.

There are some main advantages of ANN method. Firstly, A major advantage of the use of neural networks for data modelling is that they are able to fit complex nonlinear models and these models do not have to be specified in advance. Secondly, It is possible to train a neural network to perform a particular function by adjusting the values of connections (weights) between elements. Thirdly, Neural networks are composed of elements operating in parallel, which allows increased speed of calculation compared to slower sequential processing. Fourthly, Neural networks have the ability to detect all possible interactions between predictor variables: The hidden layer of a neural network gives it the power to detect interactions or interrelationships between all of the input variables.There are also some disadvantages of ANN method limiting its applications. ANN operates as black boxes. The rules of operation in neural networks are completely unknown. All dependencies (between parameters and responses) are hidden within neural network structure. Neural network model development is a computationally intensive procedure that requires much greater computational time.. In addition, it can be difficult to determine what patterns the system has found and to figure out how it arrived at its conclusions. Furthermore, the

weight matrix of ANN is complex. To reduce the training time and get the optimal solution, an expert system, which produce reasonable weight matrix, is needed *(Cllinan, 2003; Szeliga, 2004).*

### 2.8.5 An optimisation method with post data processing –the Kalman filter method

The Kalman filter was developed as an optimal, recursive, signal-processing algorithm *(Kalman, 1960).* Since then, the Kalman filter has been the subject of extensive research and application. The inverse procedure has been applied in signal processing, inertial navigation, radar tracking, sensor calibration, manufacturing and other aspects *(Grewal and Andrews, 2001).* It provides an efficient computational solution based on the least- squares theory. The method is effective in estimating unknown state variables using measurements that may contain substantial *error* or *noise.* Essentially, the algorithm updates the previous estimates through indirect measurements of the state variables and the covariance information of both the state and measurement variables.

Figure 2.16 shows kalman filter supplies an efficient computational method to compare the experiments and the modeling/simulation data recursively. In the figure, $u$ denotes the observation of experiments, $h$ the output of the numerical/finite-element modeling. One significant different between this approach and the interactive method (shown in Figure 2.12) lies in that this approach does not need to run FE model interactively. This will cut down the computational cost and help to reduce the dependence on using FE modelling packages. Since Kalman filter method was initially developed for the optimisation of electronic/control systems (signal-processing algorithm) *(Grewal and Andrews, 2001).* The method is effective in estimating unknown state variables using measurements that may contain substantial *error* or *noise* and provides an efficient computational solution based on the least-squares theory. In addition, the capacity of the program in dealing with noises made it suitable for characterising *in vivo* skin tests, which is often difficult to control due to the nature of the testing on human subjects.

The Kalman filter has been used in seeking unknown parameters of homogeneous material models *(Hoshiya, and Saito, 1984; Aoki et al, 1997; Delalleau et al, 2006; Gu et al, 2003; Nakamura et al, 2000).* Neaupane and Sugimoto *(2003)* used extended Kalman filter coupled with the finite element method to formulate an inverse problem and estimate the thermal boundary known as heat transfer coefficient (HTC). In their research a simple non-linear formulation based on steady-state heat conduction has been incorporated in the Kalman filter loop. From the laboratory experiment, steady state temperatures were measured at predefined locations. The heat transfer coefficient (HTC) was estimated inversely from these measurements *(Neaupane and Sugimoto, 2003).* Nakamura *et al (2000)* used Kalman filter technique in their research to estimate material properties of graded material and suggested the procedure is also applicable in estimating other physical and mechanical properties of any coating/layered materials *(Nakamura et al, 2000).* Gu *et al (2003)* built an inverse analysis model based on Kalman filter technique to characterise elastic-plastic properties of graded materials. The results showed excellent agreement between the indented load-displacement relations from finite element analysis with the estimated properties and that of measured record, which assures a high degree of accuracy in the current measurement procedure.

## 2.9 Main challenges for material parameter identification based on t he indentation tests

According to Tikhonov and Arsenin *(Tikhonov and Arsenin, 1977),* ill-posed problems can yield stable solutions if sufficient a priori information about the true solution is available. Such information is added to the least squares approximation by means of a regularization term, in order to complete the solution for the inverse problem. As discussed in section 2.8, robust inverse modelling techniques are not effective unless they satisfy convergence and consistency conditions. This requires an accurate FE model of the system, an effective estimation mechanism and proper experimental setup. As detailed in section 2.6, a range of strain energy functions have to be used for different material behaviour and the potential effect on the inverse modelling process has to be systematically established.

As in many inverse analyses, the model is initially "ill-posed" or "ill-conditioned" (i.e., not able to achieve good convergence characteristics) with single indenter measurements. One potential approach is to use of an additional indenter with different radius. In a previous work, additional indenter approach has showed significant improvement on the inverse process of elastic plastic materials. It is important to extend this into nonlinear materials models and use these methods to characterise some key nonlinear materials including polymer foam and biological tissues *in vivo.*

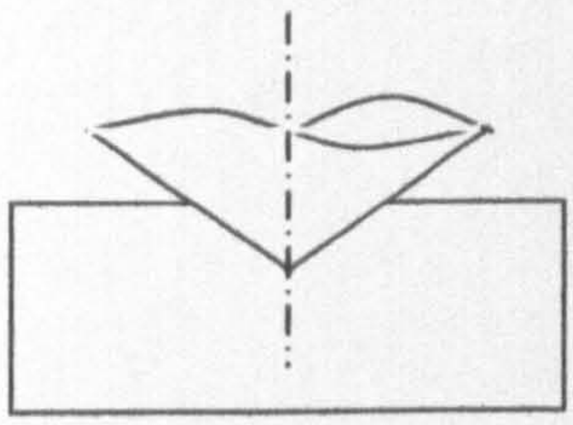

(a) Conical indenter

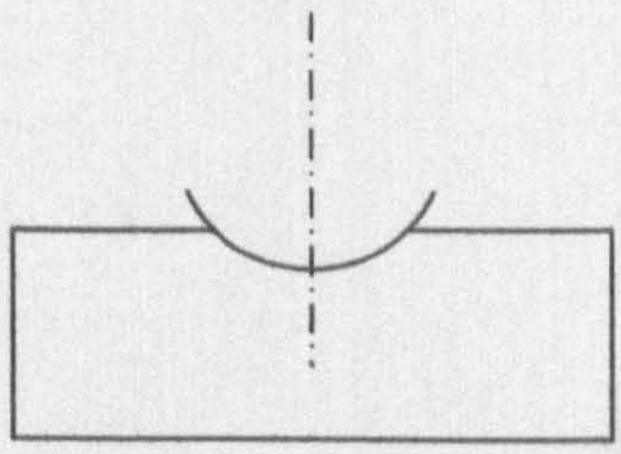

(b) Spherical indenter

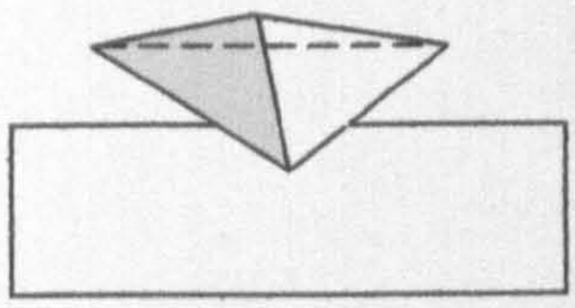

(c) pyramidal tip (trilateral) indenter

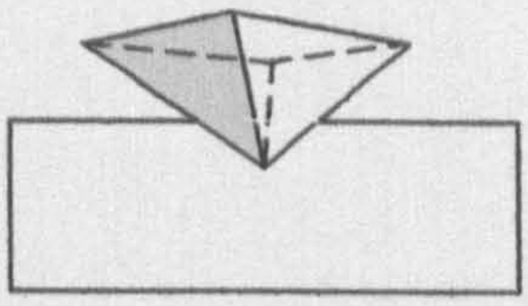

(d) pyramidal tip (quadrilateral) indenter

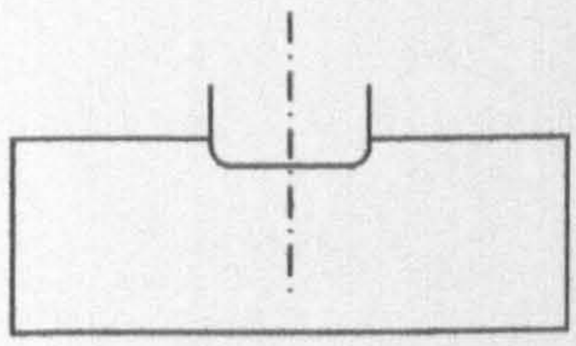

(e) Flat indenter

**Figure 2.1** Schematic showing different types of indenters.

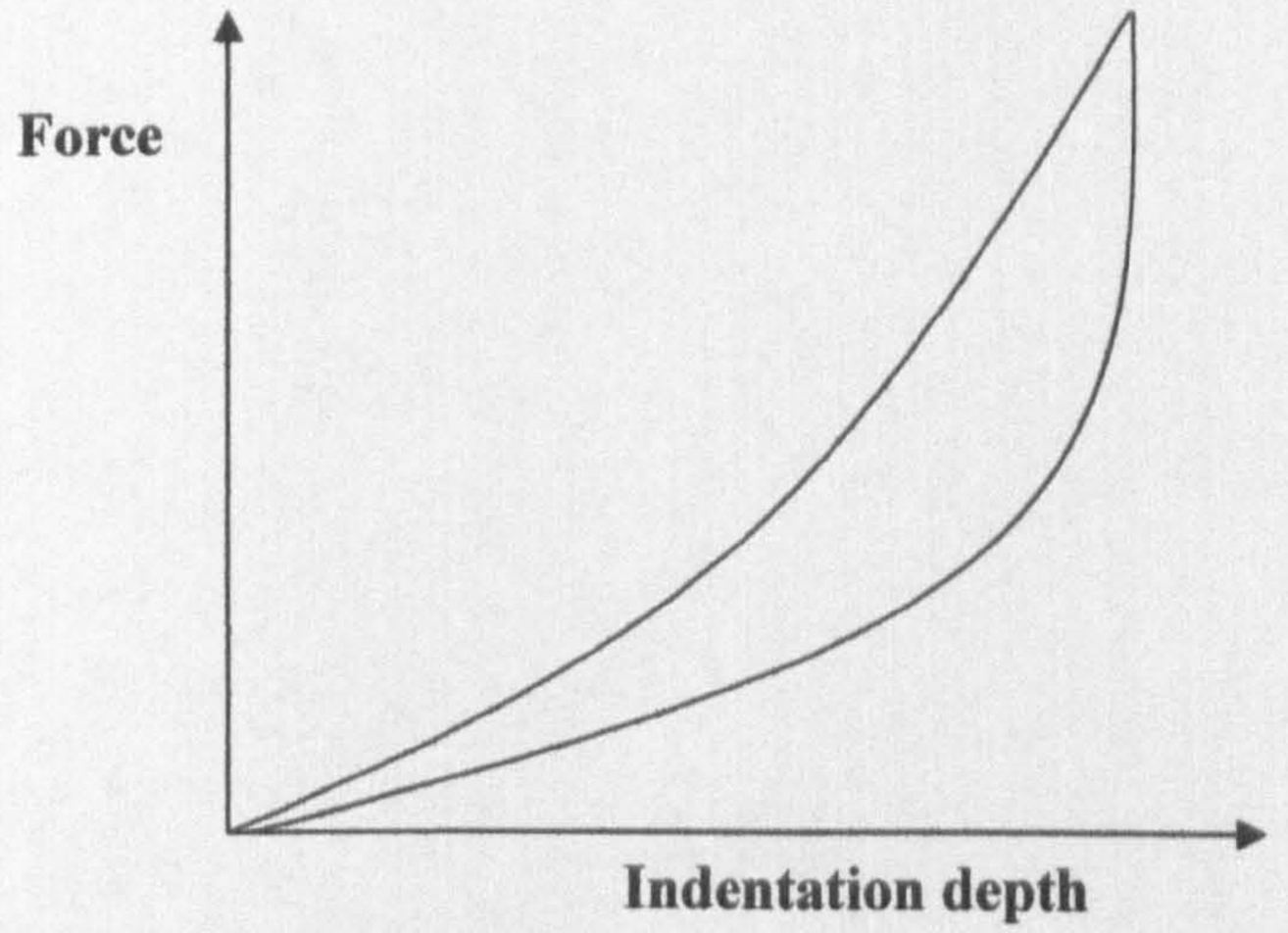


**Figure 2.2** Schematic showing a typical continuous indentation curve of foam/rubber materials.

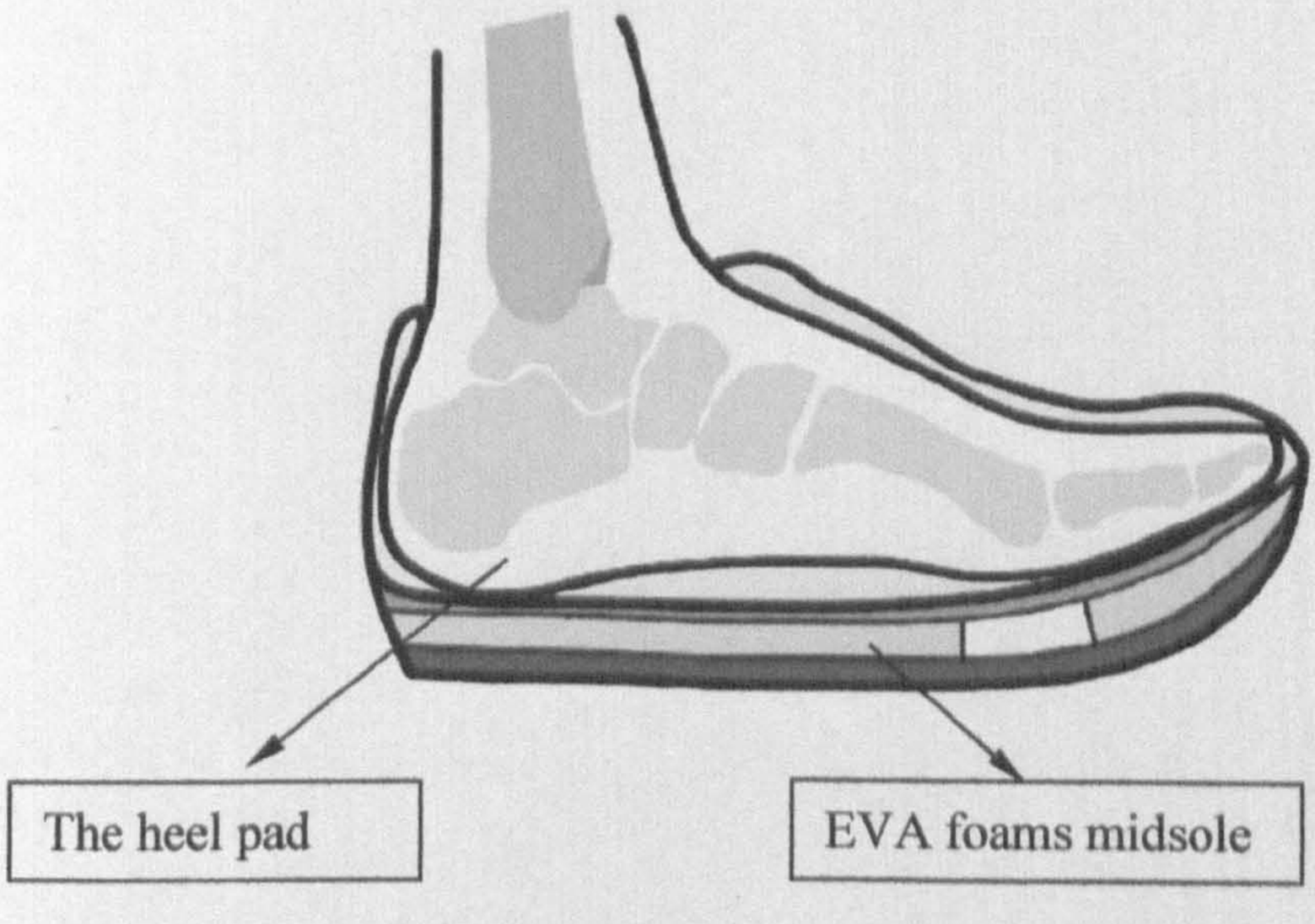


**Figure 2.3** Schematic showing the structure of the human foot and heel pad in an assembly with a running shoe of EVA midsole.

# PAGE/PAGES EXCLUDED UNDER INSTRUCTION FROM UNIVERSITY

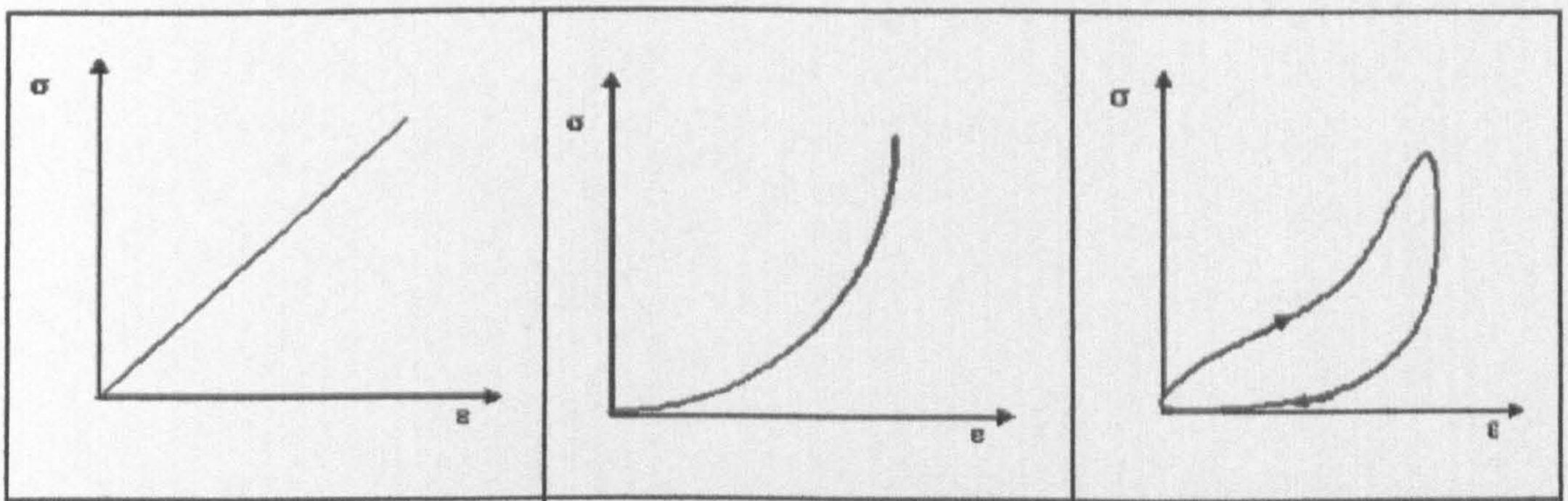


| (a) Linearly elastic and isotropic | (b) Elastically non-linear | (c) Viscoelastic |
|---|---|---|

**Figure 2.7** Schematics showing the linear elastic and nonlinear elastic material behaviors.

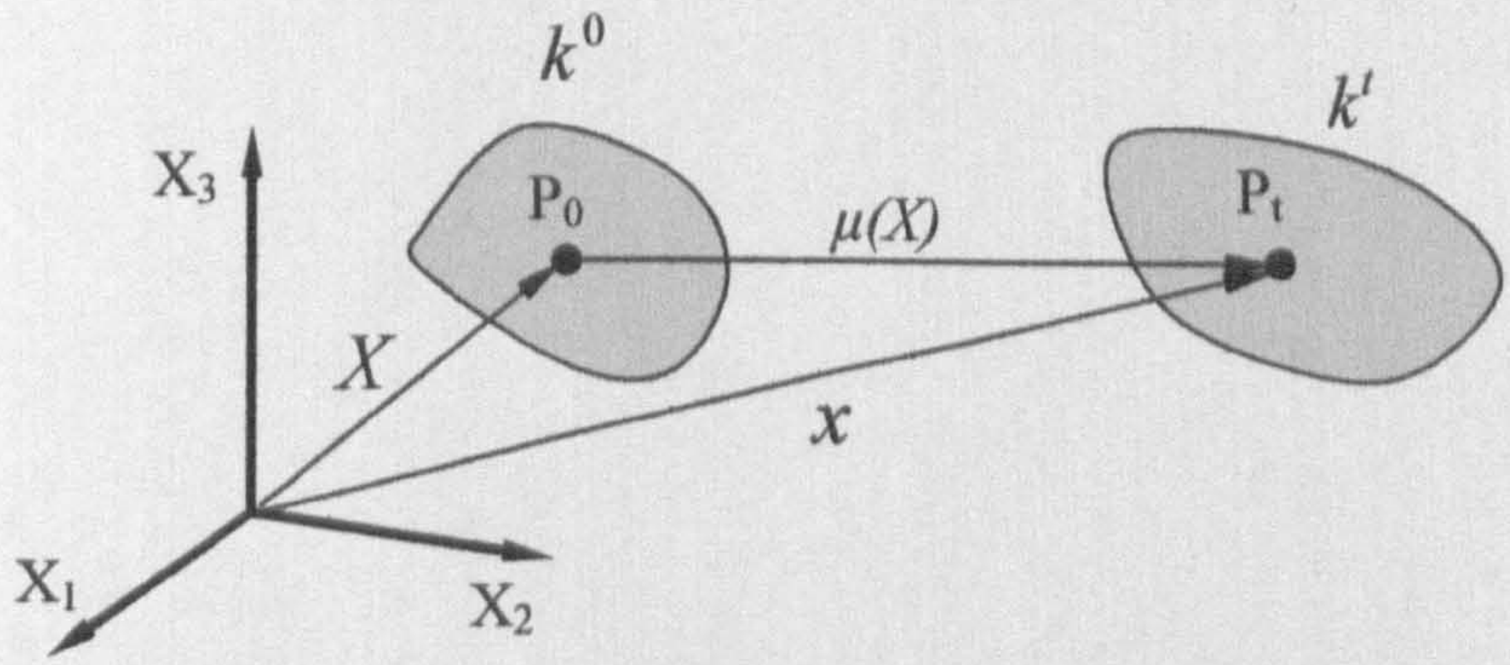


**Figure 2.8** Initial configuration $k^0$ and deformed configuration $k'$ representing the deformation field.

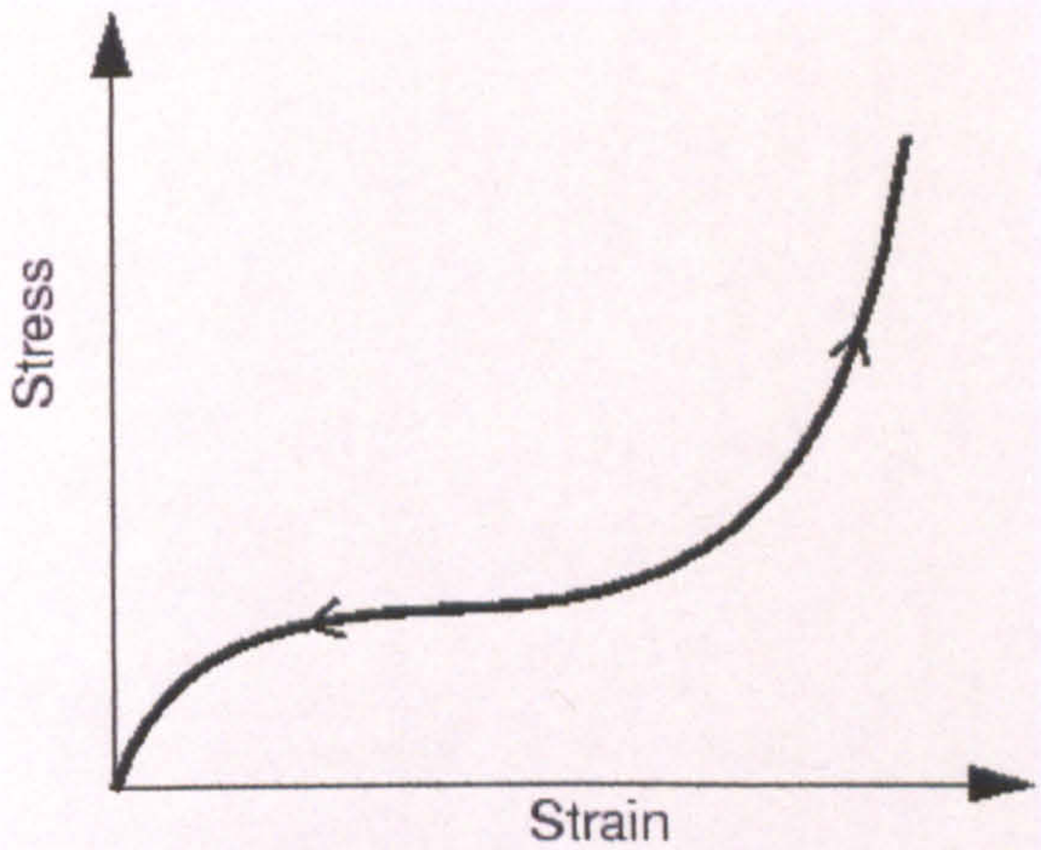


**Figure 2.9** Typical stress strain curve for rubber showing a typical hyperelastic material behaviour.

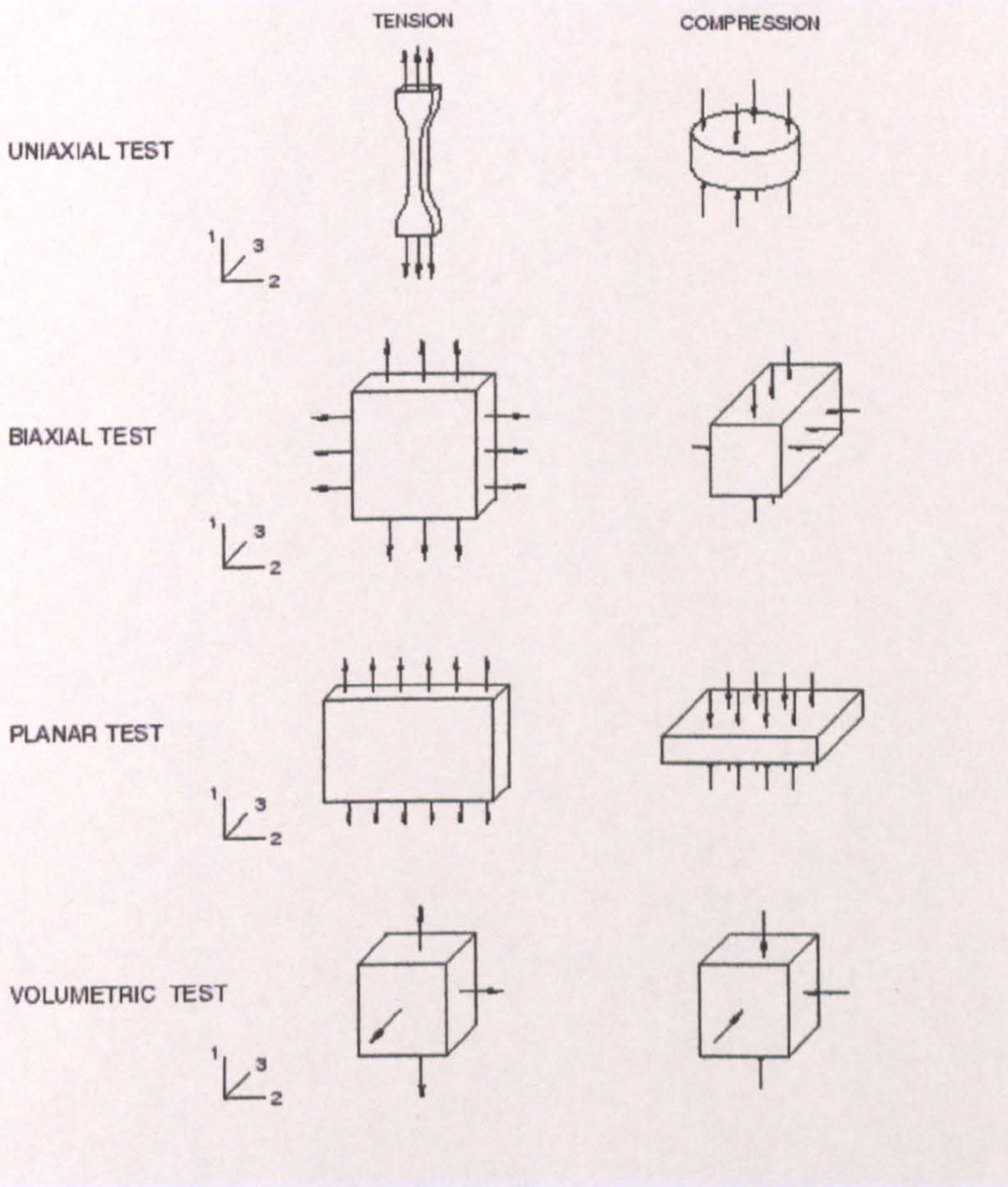


**Figure 2.10** Deformation modes of various experimental tests for defining hyperelastic material parameters (*ABAQUS*).

# PAGE/PAGES EXCLUDED UNDER INSTRUCTION FROM UNIVERSITY

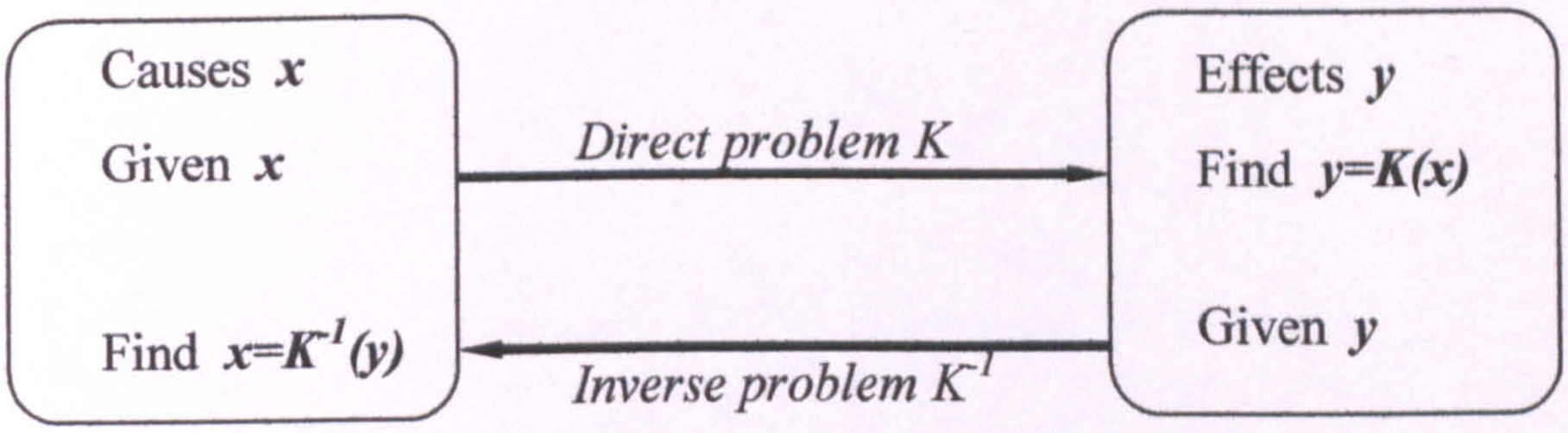


**Figure 2.11** Representation of the direct/forward and of inverse problems.

**Figure 2.12** Block diagram of the mixed numerical–experimental method ($u$ denotes the observation of experiments, $h$ the output of the numerical/finite-element modeling) *(Meuwissen et al, 1998).*

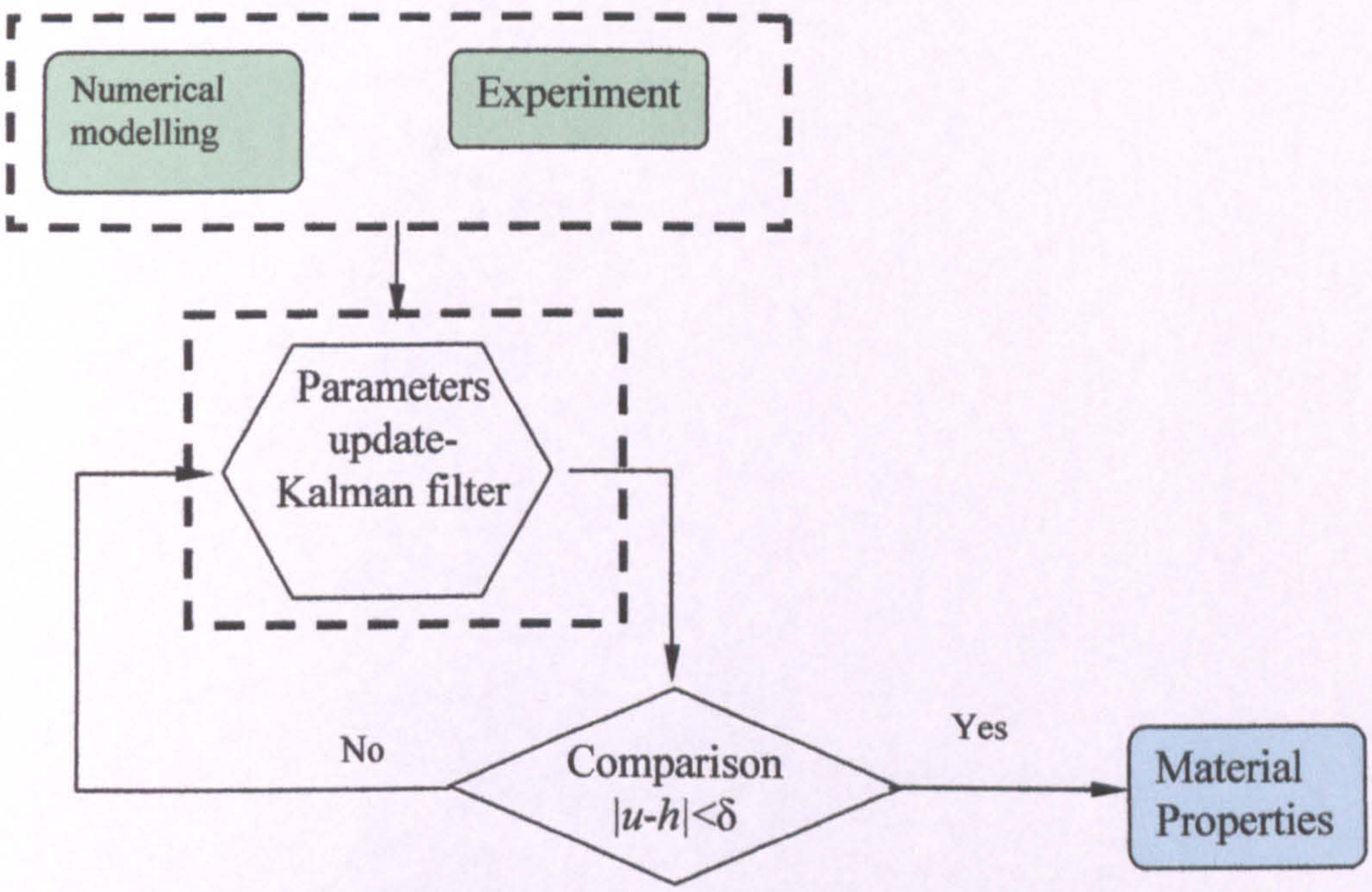


**Figure 2.16** Flow chart showing a post-modelling approach based on the Kalman Filter method.

# CHAPTER THREE

# INVERSE FINITE ELEMENT (FE) MODELLING METHOD TO DETERMINE THE MATERIAL PARAMETERS BASED ON INDENTATION TESTS

## 3. 1 Introduction

In this chapter, an inverse FE modelling program based on the Kalman filter technique to extract material parameters from indentation tests is developed and applied to three material models (linear elastic, hyperelastic and hyperfoam). The Kalman filter method was initially developed for optimization of electronic/control systems (signal-processing algorithm) *(Grewa and Andrew, 2001)*. Essentially the algorithm updates the previous estimates through indirect measurements of unknown state variables and covariance information of both the state and measurement variables based on the least-squares theory. Its capacity for noise filtering makes it potentially an important tool in dealing with materials testing data, which normally associate with significant noise.

The framework of the inverse program with Kalman filter technique has been developed for material parameters identification based on testing data from a single indenter or two indenters of different sizes. These two approaches are designated 'single indenter' and 'dual indenter method'. Two error treatment processes for processing indentation tests data and parameters are proposed and incorporated in the program in MATLAB. The program is evaluated using blind tests with numerical experimental data to investigate their validity, efficiency and robustness in analysing different material models.

For each material system, finite element (FE) models of continuous indentation with spherical indenters of different radius are developed. The effects of some key modelling parameters (such as mesh density, frictional conditions, etc.) on the indentation curves are investigated using parametric studies in ABAQUS and the optimum modelling conditions are established. The elastic model is also validated against published analytical solutions. These FE models are then used to map the effects of material properties on the loading curves using parametric studies in ABAQUS. Based on the parametric studies, simulation spaces covering a wide range of potential material properties are constructed, which provide the program with a

database for material parameters identification. The inverse program is evaluated with numerical data with known material properties. The validity and accuracy of each approach with a single indenter or dual indenter are assessed and robust approaches for different materials models are established. The sensitivity of the estimated mechanical properties to variations of the input parameters (e.g. potential perturbation of the load) is also investigated.

## 3.2 Parameter estimation model based on the extended Kalman filter technique

Figure 3.1 shows a typical inverse FE modelling approach commonly for materials parameter estimations. The database normally includes experimental data and FE simulation data arranged into a simulation space. The inverse program explores the simulation space starting from a given initial guessed value to work out optimum material properties, which produce numerical results closely matching the testing results. The simulation space is normally constructed by using finite element models mimicking the testing and true boundary conditions. In this work, the inverse program is developed based on the Kalman filter method due to its noise filtering capacity *(Nakamura et al, 2000).* The main theory and searching mechanism is described in the next section within the context of parameter identification based on experimental data.

A Kalman filter is essentially a set of mathematical equations that implements a predictor-corrector type estimator to minimize the estimated error covariance – when some presumed conditions are met *(Leustean and Rosu, 2003).* The parameter estimation problems can be described by the following equations.

$$x_{k+1} = x_k + w_k \tag{3.2.1}$$

$$z_k = h(x_k) + v_k \tag{3.2.2}$$

Equation (3.2.1) is the process model describing the parameter of the state over time — the value of the parameter '$x$' at time '$k$+1' is the same as its value at the previous time '$k$' with a process noise vector '$w_k$'. Equation (3.2.2) is the measurement model presenting the relationship between the measurement parameter $z_k$ and its prediction $h(x_k)$ retrieved from parameter '$x$' at time '$k$' and '$v_k$' is the measurement noise. The function '$h$' cannot be measured directly. The process noise '$w_k$' and measurement noise '$v_k$' is assumed to be independent of each other and follow a normal probability distribution (Equation 3.2.3-3.2.4).

$$p(w_k) \sim N(0, Q_k) \tag{3.2.3}$$

$$p(v_k) \sim N(0, R_k) \tag{3.2.4}$$

The prior estimate of the parameter '$\hat{x}$' and measurement prediction vectors '$z$' are defined as follows:

$$\hat{x}_{k+1}^{-} = \hat{x}_k \tag{3.2.5}$$

$$z_k^{-} = h(\hat{x}_k^{-}) \tag{3.2.6}$$

Where, in Equation (3.2.5), ' $\hat{x}_k$ ' is the best posterior estimation at time $k$, ' $\hat{x}_{k+1}^{-}$ 'is the prior estimation at time $k$+1. The function '$h$' in Equation 3.2.6 represents the potential relationship between measurement vector '$z$' and retrieved parameter vector '$x$'.

The goal of the Kalman filter is defined as:

$$\hat{x}_k = \hat{x}_k^{-} + K_k(z_k - h(\hat{x}_k^{-})) \tag{3.2.7}$$

This equation computes a posterior estimation ' $\hat{x}_k$ ' as a linear combination of a priori estimate ' $\hat{x}_k^{-}$ ' and a weighted difference between the actual measurement ' $z_k$ ' and the measurement prediction $z_k^{-}$ or $h(\hat{x}_k^{-})$ . The difference $(z_k - h(\hat{x}_k^{-}))$ is called the measurement innovation (or the residual) that reflects the discrepancy between the predicted measurement $z_k^{-}$ or $h(\hat{x}_k^{-})$ and the actual measurement ' $z_k$ '. A residual of zero means that the two are in complete agreement.

The non-linear function $h$ (Equation 3.2.2) can be approximated with Taylor series expansion retaining the first order term:

$$h(x_k) = h(\hat{x}_k^{-}) + H_k(x_k - \hat{x}_k^{-}) \tag{3.2.8}$$

Where ' $H_k$ ' is the Jacobian matrice of partial derivatives of ' $h(x_k)$ ' with respect to '$x$':

$$H_k = (\frac{\delta h_i}{\delta x_j}(\hat{x}_k^{-}))_{i,j} \tag{3.2.9}$$

Equation (3.2.2) can then be re-written in the following form:

$$z_k = z_k^{-} + H_k(x_k - \hat{x}_k^{-}) + v_k \tag{3.2.10}$$

The matrix $K_k$ in Equation 3.2.7 is called Kalman gain that minimises the posterior estimate error covariance ' $P_k$ ', which can be expressed as:

$$P_k = E[(x_k - \hat{x}_k)(x_k - \hat{x}_k)^T]$$

$$= E[(x_k - \hat{x}_k^{-} - K_k(z_k - h(\hat{x}_k^{-})))(x_k - \hat{x}_k^{-} - K_k(z_k - h(\hat{x}_k^{-})))^T]$$

$$= E\left[(x_k - \hat{x}_k^- - K_k(H_k(x_k - \hat{x}_k^-) + v_k))(x_k - \hat{x}_k^- - K_k(H_k(x_k - \hat{x}_k^-) + v_k))^T\right]$$

$$= E\left[((I_n - K_k H_k)(x_k - \hat{x}_k^-) - K_k v_k))((I_n - K_k H_k)(x_k - \hat{x}_k^-) - K_k v_k))^T\right]$$

$$= E\left[((I_n - K_k H_k)(x_k - \hat{x}_k^-)(x_k - \hat{x}_k^-)^T (I_n - K_k H_k)^T - K_k v_k (x_k - \hat{x}_k^-)^T (I_n - K_k H_k)^T \right.$$
$$\left. -(I_n - K_k H_k)(x_k - \hat{x}_k^-) v_k{}^T K_k{}^T + K_k v_k v_k{}^T K_k{}^T \right]$$

$$= (I_n - K_k H_k) P_k^- (I_n - K_k H_k)^T - K_k E\left[v_k (x_k - \hat{x}_k^-)^T\right](I_n - K_k H_k)^T$$
$$-(I_n - K_k H_k) E\left[(x_k - \hat{x}_k^-) v_k{}^T\right] K_k{}^T + K_k R_k K_k{}^T \quad ] \qquad (3.2.11)$$

Here, $(x_k - \hat{x}_k^-)$ is uncorrelated with the measurement noise $v_k$, and

$$E[v_k v_i^T] = \begin{cases} R_k, & \text{if } i = k \\ 0, & \text{if } i \neq k \end{cases} \qquad (3.2.12)$$

Then

$$P_k = (I_n - K_k H_k) P_k^- (I_n - K_k H_k)^T + K_k R_k K_k{}^T$$

$$= (I_n - K_k H_k) P_k^- (I_n^T - H_k{}^T K_k{}^T) + K_k R_k K_k{}^T$$

$$= (P_k^- - K_k H_k P_k^-)(I_n^T - H_k{}^T K_k{}^T) + K_k R_k K_k{}^T$$

$$= P_k^- - P_k^- H_k{}^T K_k{}^T - K_k H_k P_k^- + K_k H_k P_k^- H_k{}^T K_k{}^T + K_k R_k K_k{}^T$$

$$= P_k^- - P_k^- H_k{}^T K_k{}^T - K_k H_k P_k^- + K_k (H_k P_k^- H_k{}^T + R_k) K_k{}^T$$

The trace of $P_k$ is minimised when the matrix derivative is zero:

$$\frac{d(trace(P_k(K_k)))}{d(K_k)} = 0 \qquad (3.2.13)$$

Differentiation of the trace of '$P_k$' with respect to '$K_k$' needs to follow these three matrix differentiation formulas:

$$\frac{d(trace(xA))}{d(x)} = \frac{d(trace(xA)^T)}{d(x)} = A^T, \qquad \text{where } xA \text{ is a square matrix}$$

$$\frac{d(trace(xAx^T))}{d(x)} = 2xA, \qquad \text{where A should be a symmetric matrix}$$

Since the matrices $P_k^-$ and $H_k P_k^- H_k{}^T + R_k$ are symmetric and matrix $H_k P_k^-$ is a square matrix, so

$$\frac{d(trace(P_k(K_k)))}{d(K_k)} = \frac{d(trace(P_k^- - P_k^- H_k{}^T K_k{}^T - K_k H_k P_k^- + K_k (H_k P_k^- H_k{}^T + R_k) K_k{}^T))}{d(K_k)}$$

$$= -(H_k P_k^-)^T - (H_k P_k^-)^T + 2K_k(H_k P_k^- H_k^T + R_k) = 0$$

Then

$$-(H_k P_k^-)^T - (H_k P_k^-)^T + 2K_k(H_k P_k^- H_k^T + R_k) = 0$$

$$2(H_k P_k^-)^T = 2K_k(H_k P_k^- H_k^T + R_k)$$

$$K_k = P_k^- H_k^T (H_k P_k^- H_k^T + R_k)^{-1} \tag{3.2.14}$$

The posterior estimate error covariance matrix can be worked out as:

$$P_k = P_k^- - P_k^- H_k^T K_k^T - K_k H_k P_k^- + K_k(H_k P_k^- H_k^T + R_k)K_k^T$$

$$= P_k^- - P_k^- H_k^T K_k^T - K_k H_k P_k^- + P_k^- H_k^T K_k^T$$

$$= P_k^- - K_k H_k P_k^-$$

$$= (I_n - K_k H_k) P_k^- \tag{3.2.15}$$

Finally, the prior covariance matrix $P_{k+1}^-$ at time $k$+1 can be determined:

$$P_{k+1}^- = E\left[(x_{k+1} - \hat{x}_{k+1}^-)(x_{k+1} - \hat{x}_{k+1}^-)^T\right] \tag{3.2.16}$$

According to equation 3.2.1 and 3.2.5,

$$x_{k+1} - \hat{x}_{k+1}^- = x_k - \hat{x}_k + w_k$$

So

$$P_{k+1}^- = E\left[((x_k - \hat{x}_k) + w_k)((x_k - \hat{x}_k) + w_k)^T\right]$$

$$P_{k+1}^- = E\left[(x_k - \hat{x}_k)(x_k - \hat{x}_k)^T + w_k(x_k - \hat{x}_k)^T + (x_k - \hat{x}_k)w_k^T + w_k w_k^T)\right]$$

$$= P_k + Q_k \tag{3.2.17}$$

$$E[w_k w_i^T] = \begin{cases} Q_k, & if\ i = k \\ 0, & if\ i \neq k \end{cases} \tag{3.2.18}$$

Here, $(x_k - \hat{x}_k^-)$ is uncorrelated with the process noise $w_k$. Equation 3.2.17 indicates the relationship between prior covariance matrix $P_{k+1}^-$ and posterior covariance matrix $P_k$ (*Grewal and Andrews, 2001*).

Figure 3.2 shows the calculation loop of the parameter estimation used in this work based on the extended Kalman filter theory described above. In the figure, $\hat{x}_k$ is the vector of retrieved parameters , $\hat{x}_0^-$ is the first-guess value of the vector , $P_0$ is the

initial covariance matrix, $z_k$ is the vector of measurement , $h(\hat{x}_k^-)$ is the corresponding prior information vector. $\hat{x}_k$ is the output. Furthermore, $H_k$ is the Jacobian matrice and the matrix $K_k$ is the Kalman gain. In the extended Kalman filter calculation loop, the parameters $Q_k$ and $R_k$ are related to the process noise' $w_k$ ' and measurement noise' $v_k$ '.

## 3.3 Inverse FE indentation modelling based on the Kalman filter method

The indentation process involves pressing an indenter into the surface of the material. The resistance of the material is typically represented by the force ($P$) and displacement ($h$) data. The $P$-$h$ relationship is a function of the indenter size, interfacial condition and the material properties (*Zahouani et al, 2002*). The material properties are not readily available from the $P$-$h$ curves, and have to be estimated through inverse fitting process. Figure 3.3 shows the flow chart for material parameter identification from indentation curves using the Kalman filter method. In this model, FE modelling data was used to form the database for seeking the solution which produces an indentation curve closely matching the experimental data. The inverse model employs extended Kalman filter calculation loop as detailed in section 3.2. The programming of this algorithm has been conducted with MATLAB. The three main parts of the programme, key processes and factors influencing the results are described below.

### 3.3.1 Treatment of the experimental and FE modelling data

The experimental data used is in the form of force-indentation depth curves. The data was acquired from indentation test or from numerical models with known material parameters for evaluating the program. In the FE modelling part, numerical models mimicking the geometry and boundary conditions of the indentation tests were developed using the software 'ABAQUS'. Details of the FE model for different material models will be presented in sections 3.4-3.6.

One crucial aspect of inverse FE modelling is that the experimental data used must be sufficient to reflect the effect of material parameters on the experimental data to be able to predict the parameter values. In this work, two approaches have been investigated. One is to use experimental data from a single indenter; the other is to use data from two indenters of different sizes. The hypothesis for using more than one indenter is to increase the redundancy of the experimental data to improve the robustness of the program and improve its sensitivity to potential perturbation in the

experimental data. These are essential for material testing, in which the robustness and accuracy is the main priority rather than computational time and efficiency.

### 3.3.2 Development of the simulation space

Parametric studies were performed to generate a series of models with material properties over a potential range to form the simulation space. The parametric studies is a function in ABAQUS, which allow the user to generate, execute, and gather the results of multiple analyses that differ only in the values of some of the input parameters, such as material parameters or dimensional parameters *(Ren et al, 2006)*. The numerical force-indentation depth curves were processed into discrete data with evenly spaced points against the indentation depth (termed indentation points). The numerical data were then processed to form simulation surfaces at each indentation depth, which represents the variation of the strength for different combination of material properties at certain indentation depth. If the whole indentation depth is divided into 'n' divisions, then there are 'n+1' simulation surfaces and these simulation surfaces form a simulation space. In the parameter searching process, the experimental data (input data) were processed into discrete data with equal number of the indentation points corresponding to formations of the simulation space. The inverse program explores the simulation space starting from a given initial guessed value to work out optimum material properties which produce numerical results closely matching the input data.

### 3.3.3 Error treatment methods for covariance matrix $Q_k$ and $R_k$

As detailed in section 3.2, error treatment is a very important aspect of the inverse modelling process for material parameter identification. The noise characteristics may vary with the experimental or material conditions. There are two main errors which have to be considered for inverse indentation tests. One is the Measurement noise ($w_k$) while the other is the Process noise ($v_k$) (Equation 3.2.1-3.2.2). The measurement error is represented by the difference between the measured force and the predicted

values. The process noise represents the tolerance of the predicted parameters within the targeted accuracy of the material behaviour.

Two different error treatment approaches are to be developed in the program and comparatively studied in this work to deal with the error distribution. One method is to assume constant distribution, i.e. to set $R_k$ as a time independent matrix. The components can be estimated based as a percentage of the maximum measurement error based on the machine resolution. A constant percentage (1%-10%) error of the potential material parameters is also assigned to the matrix $Q_k$. This represents the required accuracy (tolerance) on the final parameters. This method was conventionally used in the other works *(Gu et al, 2003)*, however, the suitability (accuracy, robustness) of this approach for the characterisation of different material systems and testing method needs to be investigated. A new approach proposed in this work for this particular field is to use normal distribution (Figure 3.4), i.e. both $R_k$ and $Q_k$ are treated as time dependent and varies from the true values following a normal distribution. With this method, the materials properties is not required to be pre-known, which could be an major advantage for material characterisation in particular when dealing with nonlinear material models. In this method, the measurement noise and the process noise was assumed to follow a normal distribution.

The normal distribution is also called Gaussian distribution (Figure 3.4), which is a bell-shaped curve centred on, and symmetric about, $x = \mu$. The width is controlled by the parameter $\sigma$, which is also the standard deviation of the distribution.

The probability distribution function for a Gaussian distribution is:

$$p(x,\mu,\sigma) = \frac{1}{\sigma\sqrt{2\pi}} e^{-(x-\mu)^2/2\sigma^2} \tag{3.3.1}$$

In this equation, $\mu$ is the mean of the distribution. If $\mu = 0$, the mean of the random variable is 0, the equation then becomes:

$$p(x,\mu,\sigma) = \frac{1}{\sigma\sqrt{2\pi}} e^{-x^2/2\sigma^2} \tag{3.3.2}$$

This format is often called the *unit Gaussion* or *unit normal* distribution. The area between the curve and the horizontal axis (Figure 3.4) is:

$$\int_{-\infty}^{\infty} \frac{1}{\sigma\sqrt{2\pi}} e^{-x^2/2\omega^2}\, dx = 1 \qquad (3.3.3)$$

It is well documented that the area lying within $x = \pm\sigma$ and the curve is 68.27%, 95.45% of the area lies within $x = \pm 2\sigma$, and 99.73% of the area lies within $x = \pm 3\sigma$. When values are quoted with a random error, having Gaussian standard $\sigma$, then this error will be presented $l \pm 3\sigma$, which guarantee 99.73% of the measurement lies between $l - 3\sigma$ and $l + 3\sigma$ *(Barlow, 1989).*

Re-writing Equations 3.2.1 and 3.2.2 in a different format:

$$w_k = x_{k+1} - x_k \qquad (3.3.3)$$

$$v_k = z_k - h(x_k) \qquad (3.3.4)$$

In the process model, the difference of the parameter between the prior state and current state reflects the process noise (Equation 3.3.3). In the measurement model, the difference between the measurement and prediction reflects the measurement error (Equation 3.3.4). Based on Gaussian distribution of the errors, the following equations can be employed to calculate the covariance matrix $Q_k$ and $R_k$, which offers a different approach to the constant error method.

$$Q_k = \left(\frac{x_{k+1} - x_k}{3}\right)^2 \qquad (3.3.5)$$

$$R_k = \left(\frac{h(x_k) - Z_k}{3}\right)^2 \qquad (3.3.6)$$

During the searching process, $x_k$ and $Z_k$ are assumed as the mean values of the unknown parameter and measurement at time *k*, respectively.

### 3.3.4 The material parameter searching procedure for single indenter and dual indenter methods

Figure 3.5 outlines the main procedures to evaluate the inverse FE program for different material models (i.e. linear elastic, hyperelastic and hyperfoam model). The program was assessed by blind tests before being applied to real experimental tests.

Details of the material models are to be detailed in the section 3.4. The most important process in the inverse program is the calculation of the Kalamn gain based on an initial guessed value. The subsequent calculation of the Kalman gain will be based on each updated values. The main calculation steps when using single indenter or dual indenters is detailed below.

**Single indenter method**

Assume the unknown material parameter set is vector X, which includes two elements A and B. With initial guessed values of material properties $(A_0, B_0)$:

$$X_1^T = (A_0, B_0) \tag{3.3.7}$$

and assume an unit matrix for

$$P_1^- = \begin{pmatrix} 1^2 & 0 \\ 0 & 1^2 \end{pmatrix} \tag{3.3.8}$$

The Kalman gain can be calculated based on the Equation 3.2.14, the nonlinear function $h$ represents the relationship between the unknown parameters and measurements as explained earlier.

$$K_1 = \begin{pmatrix} 1^2 & 0 \\ 0 & 1^2 \end{pmatrix} * \begin{pmatrix} \frac{\partial h_1}{\partial A} \\ \frac{\partial h_1}{\partial B} \end{pmatrix} * \left[ \begin{pmatrix} \frac{\partial h_1}{\partial A} & \frac{\partial h_1}{\partial B} \end{pmatrix} * \begin{pmatrix} 1^2 & 0 \\ 0 & 1^2 \end{pmatrix} * \begin{pmatrix} \frac{\partial h_1}{\partial A} \\ \frac{\partial h_1}{\partial B} \end{pmatrix} + R_1 \right]^{-1} \tag{3.3.9}$$

For inconstant random error normal distribution treatment,

$$R_1 = \left( \frac{h_1^{measured} - h_1}{3} \right)^2 \tag{3.3.10}$$

For constant random error normal distribution treatment

$$R_1 = \sigma_{\Delta h}^2 \tag{3.3.11}$$

Where $h_1{}^{\text{measured}}$ represents experiment of indentation using indenter radius r. $h_1$ represents data calculated from FE model with $A_0$ and $B_0$ at the first indentation point. $\sigma_{\Delta h}^2$ represents the measurement error.

So, $A_0$ and $B_0$ are updated following:

$$\begin{pmatrix} A_1 \\ B_1 \end{pmatrix} = \begin{pmatrix} A_0 \\ B_0 \end{pmatrix} + K_1 * (h_1^{measured} - h_1) \tag{3.3.12}$$

$$X_2^T = (A_1, \quad B_1) \tag{3.3.13}$$

$X_2^T$ is then ready for next calculation loop. $P_1$ and $P_2^-$ are updated (calculated) using the following equations.

$$P_1 = \left[ \begin{pmatrix} 1 & 0 \\ 0 & 1 \end{pmatrix} - K_1 * \begin{pmatrix} \frac{\partial h_2}{\partial A} & \frac{\partial h_2}{\partial B} \end{pmatrix} \right] * \begin{pmatrix} 1^2 & 0 \\ 0 & 1^2 \end{pmatrix} \tag{3.3.14}$$

$$P_2^- = P_1 + Q_1 \tag{3.3.15}$$

For inconstant random error normal distribution treatment,

$$Q_1 = \begin{pmatrix} \left( \frac{A_1 - A_0}{3} \right)^2 & 0 \\ 0 & \left( \frac{B_1 - B_0}{3} \right)^2 \end{pmatrix} \tag{3.3.16}$$

For constant random error normal distribution treatment

$$Q_1 = \begin{pmatrix} \sigma_{\Delta A}^2 & 0 \\ 0 & \sigma_{\Delta B}^2 \end{pmatrix} \tag{3.3.17}$$

Where $F_2$ represents updated data calculated from FE model of r with material parameters $A_1$, $B_1$ at the second measurement point. This loop is repeated until the last point. $\sigma_{\Delta A}^2$ and $\sigma_{\Delta B}^2$ are determined by the accuracy of the estimations.

**Dual indenter method**

Assuming the initial material parameters is '$A_0$' and '$B_0$'. The measurements $h^1$, $h^2$ are obtained by using indenters $r_1$ and $r_2$, respectively.

$$X_1^T = (A_0, B_0), \; P_1^- = \begin{pmatrix} 1^2 & 0 \\ 0 & 1^2 \end{pmatrix}$$

Then, the Kalman gain (K), can be calculated following:

$$K_1 = \begin{pmatrix} 1^2 & 0 \\ 0 & 1^2 \end{pmatrix} * \begin{pmatrix} \frac{\partial h_1^1}{\partial A} & \frac{\partial h_1^2}{\partial A} \\ \frac{\partial h_1^1}{\partial B} & \frac{\partial h_1^2}{\partial B} \end{pmatrix} * \left[ \begin{pmatrix} \frac{\partial h_1^1}{\partial A} & \frac{\partial h_1^1}{\partial B} \\ \frac{\partial h_1^2}{\partial A} & \frac{\partial h_1^2}{\partial B} \end{pmatrix} * \begin{pmatrix} 1^2 & 0 \\ 0 & 1^2 \end{pmatrix} * \begin{pmatrix} \frac{\partial h_1^1}{\partial A} & \frac{\partial h_1^2}{\partial A} \\ \frac{\partial h_1^1}{\partial B} & \frac{\partial h_1^2}{\partial B} \end{pmatrix} + R_1 \right]^{-1} \quad (3.3.18)$$

For inconstant normal distribution

$$R_1 = \begin{pmatrix} \left( \frac{h_1^{measured1} - h_1^1}{3} \right)^2 & 0 \\ 0 & \left( \frac{h_1^{measured2} - h_1^2}{3} \right)^2 \end{pmatrix} \quad (3.3.19)$$

For constant normal distribution

$$R_1 = \begin{pmatrix} \sigma_{\Delta h^1}^2 & 0 \\ 0 & \sigma_{\Delta h^2}^2 \end{pmatrix} \quad (3.3.20)$$

Where $h_1^{measured1}$ and $h_1^{measured2}$ represent indentation force at an indentation point (depth) with an indenter sizes of $r_1$ and $r_2$, respectively. $h_1^1$ and $h_1^2$ represent data from FE models with different indenter sizes ($r_1$ , $r_2$ ).

Then the updated material parameters can be worked out as:

$$\begin{pmatrix} A_1 \\ B_1 \end{pmatrix} = \begin{pmatrix} A_0 \\ B_0 \end{pmatrix} + K_1 \left[ (h_1^{measured1} - h_1^1) \quad (h_1^{measured2} - h_1^2) \right] \quad (3.3.21)$$

$$X_2^T = (A_1, \quad B_1) \quad (3.3.22)$$

The posterior estimate error covariance $P_1$ can be calculated:

$$P_1 = \left[ \begin{pmatrix} 1 & 0 \\ 0 & 1 \end{pmatrix} - K_1 * \begin{pmatrix} \frac{\partial h_2^1}{\partial A} & \frac{\partial h_2^1}{\partial B} \\ \frac{\partial h_2^2}{\partial A} & \frac{\partial h_2^2}{\partial B} \end{pmatrix} \right] * \begin{pmatrix} 1^2 & 0 \\ 0 & 1^2 \end{pmatrix} \quad (3.3.23)$$

The prior covariance matrix $P_2^-$ at second point is updated as following

$$P_2^- = P_1 + Q_1 \quad (3.3.24)$$

For inconstant normal distribution

$$Q_1 = \begin{pmatrix} \left(\frac{A_1 - A_0}{3}\right)^2 & 0 \\ 0 & \left(\frac{B_1 - B_0}{3}\right)^2 \end{pmatrix} \tag{3.3.25}$$

For constant normal distribution

$$Q_1 = \begin{pmatrix} \sigma_{\Delta A}^2 & 0 \\ 0 & \sigma_{\Delta B}^{2\ 2} \end{pmatrix} \tag{3.3.26}$$

The new data will then be used as the input to update the calculation at the next point.

## 3.4 Application of the inverse FE modelling approach to different material systems

In this section, the feasibility of the inverse FE program to analyzed three commonly used material models (i.e. linear elastic, hyperelastic and hyperfoam) has been systematically studied. The main governing constitutive equations and parameters of the material models are listed in Table 3.1. These materials are commonly used in a wide range of applications in particularly in sport and protection facilities.

**Table 3.1 List of material models.**

| Materials Models | Governing Equations | Main material parameters | Typical materials |
|---|---|---|---|
| Linear elastic model | $\sigma = E\varepsilon$ | E, Young's modulus<br>ν, Poisson's ratio | Rubbers at small strains. |
| Hyperelastic model | $U = \sum_{i=1}^{N} \frac{2\mu_i}{\alpha_i^2}\left(\bar{\lambda}_1^{\alpha_i} + \bar{\lambda}_2^{\alpha_i} + \bar{\lambda}_3^{\alpha_i} - 3\right) + \sum_{i=1}^{N} \frac{1}{D_i}(J^{el} - 1)^{2i}$ | $\mu_i$, $\alpha_i$, $D_i$<br>$\bar{\lambda}_i = J^{-\frac{1}{3}}\lambda_i$ | Human heel pad, muscle, skin etc. |
| Hyperfoam model | $U = \sum_{i=1}^{N} \frac{2\mu_i}{\alpha_i^2}\left[\hat{\lambda}_1^{\alpha} + \hat{\lambda}_2^{\alpha} + \hat{\lambda}_3^{\alpha} - 3 + \frac{1}{\beta_i}\left(J^{el}\right)^{-\alpha_i\beta_i} - 1\right]$<br>$\bar{\lambda}_i = \left(J^{th}\right)^{-\frac{1}{3}}\lambda_i$ | $\mu_i$, $\alpha_i$, $\beta_i$ | EVA foams in Running shoes. |

FE model for each material/system was developed using a commercial simulation software ABAQUS. In each case, an optimum modelling approach has been developed based on detailed investigation of the influence of boundary conditions, mesh sensitivity and the effect of materials properties over different strain spectrums. The numerical results of the elastic model were compared to an available analytical model to validate the FE program. The establish FE model was then used to develop the simulation space by running models with a wide range of materials properties. The parametric study feature is a function in ABAQUS, which allow the user to generate,

execute, and gather the results of multiple analyses that differ only in the values of some of the input parameters, such as material parameters or dimensional parameters *(Ren et al, 2006)*. The inverse program was evaluated using blind tests with numerical experimental data (numerical results with known material properties). This is commonly used approach in developing inverse programs *(Delalleau et al, 2006)*. It allows the uniqueness, accuracy and sensitivity of these inverse FE methods to be systemically investigated. The results for linear elastic, hyperelastic, hyperfoam systems have been presented in the section 3.5-3.8.

Two main approaches have been studied to predict the material parameters from indentation tests. The first one is to use one indentation test only (designated single indenter method). This approach has been used by many researchers but the accuracy and validity were not well established. In many cases, it heavily depends on the pre-knowledge about the material or the initial guessed value, in other words, the data could be ill conditioned. The new approach to be explored is to use experimental data from two indenters of different sizes (designated dual indenters method). One hypothesis for using more than one indenter is that, by using indenters of different dimensions and sizes, material behaviour at different strain-stress conditions could be produced and this would potentially help to predict multiple material parameters.

## 3.5 FE modelling of indentation of linear elastic materials and inverse parameters identification

### 3.5.1 Elastic FE indentation model

As shown in Figure 3.6(a), a 2-D axial symmetric model was used due to the symmetry of the spherical indenter. The indenter was assumed to be analytically rigid body as it is much harder than the indented material. The element type of the material used is CAX4R (an axisymmetric element) and finer meshes have been applied around the indenter to improve the accuracy. The thickness and width of the model is 36 mm and 36mm, respectively; both are six times larger than the indenter radius to avoid potential sample size and boundary effects *(Johnson, 1985)*. The bottom face of the material was fixed in all degrees of freedom (DOF). Contact has been defined between the indenter surface and sample surface. The material of interest is allowed to move and the contact between the indenter surface and the material surface was maintained at all the times.

In FE modelling, the accuracy of the results is influenced by many factors such as the mesh density, frictional condition and validation of the boundary conditions. The most relevant factors for the simulation of indentation process are the mesh density and frictional conditions *(Taljat and Zacharia, 1998)*. The friction coefficient used is 0.5, which is commonly used in indentation testing of soft materials. The meshes in the model were generated with pertinent symmetry consideration to reduce the domain size with different mesh density for different regions. The potential influence of all these factors on the accuracy of the modelling process needs to be investigated. This was assessed by varying the meshing scheme (i.e. mesh density) in the FE models, and then comparing the P-h curves. Figure 3.6 (c) shows the P-h curves with different meshing approaches (Figure 3.6 (b)). It is clearly shown that models with coarser meshes (larger element size) near the indenter have resulted in lower indentation forces. The indentation curve became very close for models with mesh 2 and mesh 3, eventually the results became insensitive to the mesh density, therefore Mesh 3 was set as the suitable mesh density. Tests on other material properties showed similar results.

### 3.5.2 Validation of the FE model with analytical solutions

Figure 3.7 compares the numerical force displacement data and corresponding result using the following analytical solution *(Johnson, 1985).*

$$F_Z = (\frac{16R}{9})^{\frac{1}{2}} * \frac{E}{1-\nu^2} * \delta^{\frac{3}{2}} \qquad (3.5.1)$$

In the equation, '$F_Z$' is the reaction force, '$R$' is the indenter radius; '$E$' and '$\nu$' are the Young's modulus and Poisson's ratio of the material. 'δ' is the indentation depth. As shown in figure 3.7, the two sets of data showed good agreement. The correlation coefficients between these two curves using a least square regression method is within 99.9%. Similar agreement between numerical results and analytical results were observed with other indenter sizes, which suggests that the FE model is congruous with the analytical model. Please note the analytical solution is only valid at smaller strain level, it becomes invalid as the model goes into large strain.

### 3.5.3 Effect of indenter seize and material parameters on the indentation curves and simulation spaces

Figure 3.8 compares the force-indentation depth curves and stress distribution for different sized indenters. As shown in Figure 3.8(a), the force-indentation curve is stiffer when larger indenter is used. The stress around the indenter showed similar distribution patterns, however, the peak stress value and the volume of the deformed material are different. When a larger indenter is used, the effectively deformed material volume is significantly larger. These differences may reflect the different contribution of the two material parameters (i.e. E and ν) to the indentation force, which could potentially provide a mechanism to be used in the inverse modelling process to extract these material parameters.

Figure 3.9 shows the effects of the Young's Modulus (E) and the Poisson's ratio (ν) on the force-indentation depth data. The Poisson's ratio was fixed at 0.28 in (a); while the Young's modulus was fixed at 0.25 (MPa) in (b). As shown in the figures, the slopes of the force-indentation depth curves increased when the Young's modulus and

Poisson's ratio was increased, but the Young's modulus exhibited much more profound effect than the Poisson's ratio. It is also evident that the force-indentation depth data becomes less sensitive to the Poisson's ratio when '$\nu$' approaches to zero. These sensitivity test results will provide guidelines in designing the inverse modelling strategy.

In the parametric studies, the Young's modulus was varied from 0.05 (MPa) to 0.45 (MPa) with values 0.05, 0.15, 0.25, 0.35, 0.45. The Poisson's ratio used was ranged from 0.12 to 0.44 with values 0.12, 0.20, 0.28, 0.36, 0.44. The numerical results were then recorded and stored into a database to form a simulation space. As described in section 3.4, the simulated force-indentation depth data has to be transformed into a discrete form for the data searching process. To avoid potential uncertainty of the data at very small indentation depth, the study domain selected corresponded to the indentation depth of 0.025-0.5mm and each curve was divided into 190 equally spaced divisions. Figure 3.10(b) shows typical simulation surfaces at the $71^{th}$ indentation point (corresponding to a depth of 0.2mm) and $151^{th}$ (corresponding to a depth of 0.4mm) indentation point. Each surface represents the reaction force at the certain indentation depth within the range of Young's modulus 'E' and Poisson's ratio ν. In the parameter fitting process, the program searches through this space and determine a set of material properties that produce force displacement result matching the input experimental data.

### 3.5.4 Searching process of elastic properties based on the single indenter method

Figure 3.11 illustrates the parameters searching process based on the single indenter method using an indentation curve for R=4mm (Figure 3.8 (a)) as the input data. The initial values used were $E_0$=0.30 MPa and $\nu_0$=0.40, while the target values are E=0.14 (MPa), $\nu$=0.43. Figures (a) and (b) show the material properties searching process with constant error treatment and random error treatment. At each indentation point, the program searches for a combination of material properties (E and $\nu$), which gives the best fit to the target point on the experimental curve. As shown in the figures, the fitting process of material parameters involved significant scatter in the earlier stage

starting from the initial value. In the later stage, the predicted results came closer to the real values, and then converged into a stable set of properties. It is clearly shown that the process with random error is much more stable and quick to converge than the method with a constant error of 5%. Inverse programme with different level of constant error (1%, 5%, 10%) have been assessed and the searching process exhibits very similar trend (results not shown to preserve clarity). The program failed to converge when the percentage error used is smaller than 1%. As shown in the figures, the predicted properties from both approach are close to the true material properties (E=0.14 MPa), $\nu$=0.43) in this case.

To assess the robustness of the program and avoid ill conditioning, the effect of the initial guessed values on the converged results have been studied. As shown in Figure 3.12, each grid point was used as an initial guessed value then the predicted material properties is summarised to study potential effect of initial value on the predicted results. Figure 3.13 shows the distribution of the converged results. As shown in the figure, the results with constant error approach (Figure (a)) is randomly scattered over a wide range. The converged results for random error approach are focused at three main points but the overall range is similar to that for the constant error approach (Figure (b)).

Multiple FE models have been developed with material properties selected from the converged material properties (circled in Figure 3.13(b)) and the P-h curves were compared with the input numerical experimental data. As shown in Figure 3.13(c), these P-h curves agree very well with the numerical experimental data. This suggests that these significantly different parameters have identical P-h curves, in other words, the material property could not be determined uniquely using one indenter only.

### 3.5.5 Searching process based on dual indenters

Figure 3.14 illustrates the parameter searching process using experimental data from two indenters (R=4 and R=6 mm) simultaneously. The initial values used were $E_0$=0.30 MPa and $\nu_0$=0.40, while the target values are $E_T$=0.14 (MPa), $\nu_T$=0.43. At

each indentation point, the program searches for a set of material properties (E and $\nu$) which gives the best fit to the experimental curves from both R4 and R6. Figures (a) and (b) show the material properties searching process with constant error treatment and random error treatment. As shown in the figures, the fitting process started from random picked initial values, and then it came closer to a stable value (figure 3.14(b)). The results shows clearly that the process with random error is much more quick to converge (reach a plateau) than the constant error method. In this run, the results obtained are close to the true material properties as highlighted on the figure with the straight line. The results predicted were 0.141 for E and 0.4228 for v, with the error percentage is 0.79% and 2.14%, respectively.

Similar to the single indenter approach, a range of initial values have been used to assess the robustness of the program. The result is plotted in Figure 3.15. The results for the constant error treatment (1%, 5% and 10%) (Figure 3.15(a)) are similar to the results of the single indenter approach (Figure 3.13(a)). The results from the random error approach are much more focused with all the converged results close to the true material materials. Multiple FE models have been developed with material properties selected from the converged material properties (circled in Figure 3.15(b)) and the P-h curves were compared to the input numerical experiment data. As shown in Figure 3.15(c), these P-h curves agree very well with the numerical experimental data. This suggests that the dual spherical indenters with random error treatment could be used to predict the two elastic parameters (E and v) of materials.

Several sets of material properties (E and $\nu$) have been used as the true material properties in the blind tests to assess the robustness and accuracy of the program. Typical comparison of the predicted results and the true parameters were listed in Table 3.2 and selected data was shown in Figure 3.16. In each case, there are a few material data sets over a small region matching the input data. The results suggest that the dual indenters could produce unique results.

**Table 3.2** Typical predicted results by inverse FE modelling based on the dual indenters method on elastic materials.

| Target value | | Predicted value | | Up limit | | Low limit | |
|---|---|---|---|---|---|---|---|
| $E_T$ | $\nu_T$ | E | $\nu$ | E | $\nu$ | E | $\nu$ |
| 0.1 | 0.15 | 0.0999 | 0.1582 | 0.1000 | 0.1489 | 0.0997 | 0.1696 |
| 0.2 | 0.15 | 0.1996 | 0.1576 | 0.2002 | 0.1458 | 0.1987 | 0.1701 |
| 0.3 | 0.15 | 0.2986 | 0.1634 | 0.3001 | 0.1498 | 0.2969 | 0.1744 |
| 0.4 | 0.15 | 0.3995 | 0.1575 | 0.4005 | 0.1431 | 0.3986 | 0.1693 |
| 0.1 | 0.2 | 0.0999 | 0.2069 | 0.1001 | 0.1964 | 0.0996 | 0.2184 |
| 0.2 | 0.2 | 0.2000 | 0.1993 | 0.2008 | 0.1915 | 0.1989 | 0.2073 |
| 0.3 | 0.2 | 0.2988 | 0.2111 | 0.3006 | 0.1937 | 0.2967 | 0.2257 |
| 0.4 | 0.2 | 0.3979 | 0.2138 | *0.3998* | *0.2012* | 0.3956 | 0.2286 |
| 0.1 | 0.25 | 0.0999 | 0.2536 | 0.1000 | 0.2460 | 0.0997 | 0.2609 |
| 0.2 | 0.25 | 0.1998 | 0.2535 | 0.2006 | 0.2414 | 0.1989 | 0.2660 |
| 0.3 | 0.25 | 0.2992 | 0.2581 | 0.3010 | 0.2419 | 0.2977 | 0.2708 |
| 0.4 | 0.25 | 0.3988 | 0.2570 | 0.401 | 0.243 | 0.3977 | 0.2664 |
| 0.1 | 0.3 | 0.1002 | 0.2977 | 0.1005 | 0.2906 | 0.0999 | 0.3017 |
| 0.2 | 0.3 | 0.1999 | 0.3007 | 0.2008 | 0.2922 | 0.1990 | 0.3089 |
| 0.3 | 0.3 | 0.2988 | 0.3077 | 0.3011 | 0.2925 | 0.2962 | 0.3245 |
| 0.4 | 0.3 | 0.4004 | 0.2980 | 0.4040 | 0.2825 | 0.3970 | 0.3145 |
| 0.1 | 0.35 | 0.1003 | 0.3464 | 0.1012 | 0.3338 | 0.0996 | 0.3566 |
| 0.2 | 0.35 | 0.1998 | 0.3520 | 0.2007 | 0.3254 | 0.1987 | 0.3697 |
| 0.3 | 0.35 | 0.3001 | 0.3499 | 0.3012 | 0.3441 | 0.2986 | 0.3568 |
| 0.4 | 0.35 | 0.4004 | 0.3477 | 0.4027 | 0.3364 | 0.3981 | 0.3579 |
| 0.1 | 0.4 | 0.1003 | 0.3959 | 0.1019 | 0.3754 | 0.0991 | 0.4093 |
| 0.2 | 0.4 | 0.2015 | 0.3912 | 0.2065 | 0.3600 | 0.1971 | 0.4156 |
| 0.3 | 0.4 | 0.3021 | 0.3919 | 0.3118 | 0.3584 | 0.2984 | 0.4053 |
| 0.4 | 0.4 | 0.4030 | 0.3911 | 0.4065 | 0.3706 | 0.4012 | 0.3965 |

## 3.6 FE modelling of indentation of hyperelastic materials and inverse parameters identification

### 3.6.1 FE models

Hyper-elastic models are widely used to describe the non-linear material behaviour of biological tissue such as skin, heel pad *(Serup and Jemec, 1999)*. One of the mostly used models in ABAQUS is the Ogden material model. This model is able to capture the stiffening behaviour at large strains.

The first order form of the Ogden strain energy potential ($U$) is in the following form (*Twizell and Ogden, 1986*)

$$U = \frac{2\mu}{\alpha^2}(\lambda_1^\alpha + \lambda_2^\alpha + \lambda_3^\alpha - 3) \tag{3.6.1}$$

Where $\lambda_1$ , $\lambda_2$ , $\lambda_3$ are the deviatoric principal stretches and 'μ' and 'α' are the material parameters representing the hyper-elastic behaviour under uniaxial compression.

$$\lambda_1 = \lambda;\ \lambda_2 = \lambda_3 = \lambda^{-1/2};\ \lambda = 1+\varepsilon \tag{3.6.2}$$

Where ε is the compressive strain. The compressive stress (σ) is calculated from strain energy function $U$.

$$\sigma = \frac{2\mu}{\alpha}(\lambda^{\alpha-1} - \lambda^{\frac{\alpha}{2}-1}) \tag{3.6.3}$$

Figure 3.17 shows a 2-D axial symmetric model with a spherical indenter. Similar to the previous indentation FE model, the indenter was modelled as an analytically rigid body. The axisymmetric element CAX4R is used and finer meshes have been applied around the indenter to improve the accuracy. The thickness and the width of the model are 14 mm and 26mm, respectively. The bottom face of the material volume was fixed in all degrees of freedom (DOF). Contact has been defined between the indenter surface and material surface with friction coefficient of 0.5. The mesh in the regions directly under the indenter tip was refined with high mesh density in order to obtain accurate results.

Figure 3.17(b) shows a typical numerical force indentation depth curve of a spherical indenter (R= 4 mm). Mesh size effects have been assessed by varying the mesh

density and the results are shown in Figure 3.17(c&d). At lower mesh density level, the peak forces is considerably higher, then eventually the result become less sensitive to the mesh size. When the mesh density near the indenter reaches certain level, the P-h curves became identical. This mesh scheme was selected as the suitable mesh for all the tests. Tests on other material properties showed similar trend.

### 3.6.2 Effect of the indenter size and material parameters on the indentation curves and simulation spaces

Figure 3.18(a) represents the force-indentation depth curves using different indenters. The stress distributions underneath the indenters were shown in Figure 3.18(b). The differences could potentially provide a mechanism to be used in the inverse modelling process to extract the material properties. Figure 3.19 shows the effects of the hyper-elastic material coefficient 'μ' and 'α' on the force-indentation depth data. A fixed coefficient 'α' of 8.0 was used in (a) and 'μ' was 0.05 (MPa) in (b). As shown in the Figure (a), the slopes of the force-indentation depth data increased as the coefficient 'μ' increased. The effect of the 'μ' is profound starting right from the low indentation depth while, the effect of 'α' is not significant at low indentation depth (up to 2mm in this case). At large indentation depth, it is clearly shown that the slopes of the force-indentation data increased when 'α' was increased. This suggests that 'μ' has much more significant effect than the 'α'. These sensitivity test results will provide guidelines in designing the inverse modelling strategy.

To build up the simulation space, a range of material sets μ=0.008, 0.03, 0.05, 0.08, 0.12 (MPa) and α=4.0, 6.0, 8.0, 10.0, 12.0) have been used in the parametric studies. Figure 3.20 shows the relationship between the simulated force-indentation depth data and the corresponding simulation surfaces. The curves were divided into 190 equally spaced divisions and the simulation surface shown in the figure is for the $116^{th}$ indentation points (indentation depth of 2.5mm) and the $166^{th}$ indentation points (indentation depth of 3.5mm), respectively. Each surface represents the reaction force at a certain indentation depth within the material property range. In the parameter fitting process, the program searches through this space and determine a set of

material properties that produce force displacement result matching the input experimental data.

### 3.6.3 Inverse parameters identification based on the single indenter method

Figure 3.21 illustrates the searching process of hyperelastic parameters using the curve for R=4mm. The initial guessed value was $\mu_0$=0.045 and $\alpha_0$ =8.0 while the target values (or true material parameters) were $\mu_T$=0.07 and $\alpha_T$ =6.2. Figure 3.21 (a) and (b) shows the material parameters searching process with the constant error treatment and random error treatment method, respectively. At each indentation point, the inverse program searches for a combination of material properties ($\mu$ and $\alpha$) which gives the best fit to the input experimental curve. As shown in Figure 3.21(a), the searching process of parameter '$\mu$' involved significant scatter in the initial stage, then the predicted result became stable and came closer to the target value. The results also show clearly that the searching process for '$\mu$' is much smoother than the searching process for '$\alpha$'. This is probably due to the lower sensitivity of $\alpha$ on the indentation curves as shown in Figure 3.19(b). The converged data for the searching process with the random error method is much closer to the target value than the results for the constant error method as highlighted by the solid line.

To assess the robustness of the inverse program to avoid ill conditioning, a range of initial guessed values has been used (Figure 3.22) and the distribution of the converged results are shown in Figure 3.23. The results from the constant error approach is much more scattered and the results with different constant error levels (1%, 5%, 10%) are comparable. Multiple FE models have been developed with some selected material parameters in Figure 3.23(a) and the P-h curves are compared with the input numerical experiment data. As shown in Figure 3.22(b), these P-h curves are different but the constant method failed to distinguish them. As shown in Figure 3.23 (c), the predicted values with random error treatment are much more focused and the value is in good agreement with the true material value.

### 3.6.4 Inverse hyperelastic parameters identification based on the dual indenters method

Figure 3.24 illustrates the parameters searching process using data for R=4 and R=6 mm. The initial guessed value was $\mu_0$=0.04 and $\alpha_0$ =8.0 while the target values are $\mu_T$=0.07 and $\alpha_T$ =6.2. The searching process with constant error treatment and random error treatment was shown in Figures (a) and (b) respectively. At each indentation point, the program searches for a combination of material properties which gives the best fit to the experimental curves. Similar to the single indenter approach, the searching process for '$\mu$' is much smoother than the process for '$\alpha$'. In the later stage, the predicted results came closer to the real values. In this run, the results obtained from these two approaches are comparable and close to the true materials properties.

Similar to the single indenter approach, a range of initial guessed values have been used and the converged result was plotted in Figure 3.25. Several constant error levels (1%, 5% and 10%) have been assessed and the results were presented in Figure (a). The program has failed to converge when the error level was set within 1% or greater than 10%. The distribution of the converged results for the constant error and random error method is very similar and confined to a small region. The ranges of both parameters ('$\mu$' and '$\alpha$') obtained are much narrower than the results for the single indenters indentation. Multiple FE models have been developed with these material properties and the P-h curves agreed very well with the numerical experimental data. This suggests that the material property could be determined uniquely using two indentations using either constant error treatment or the random error approach. But the random error approach was much more stable. In both cases, the data range is much more focused than the converged data for the single indenter method (Figure 3.23).

Several materials sets (i.e. true material properties) with different parameters have been used as input data. Comparison of the predicted results and the true parameters were listed in Table 3.3 and selected data was shown in Figure 3.26. In each case, the predicted material data match the true material properties very well. This suggests the dual indenters could produce unique results.

**Table 3.3** Typical predicted results for hyperelastic materials by inverse FE modelling based on the dual indenters method

| Target value | | Predicted value | | Up limit | | Low limit | |
|---|---|---|---|---|---|---|---|
| $\mu_T$ | $\alpha_T$ | $\mu$ | $\alpha$ | $\mu$ | $\alpha$ | $\mu$ | $\alpha$ |
| 0.018 | 5 | 0.0180 | 4.9759 | 0.0180 | 4.9828 | 0.0180 | 4.9437 |
| 0.040 | 5 | 0.0400 | 4.9640 | 0.0401 | 5.0358 | 0.0400 | 4.9266 |
| 0.062 | 5 | 0.0620 | 5.0060 | 0.0620 | 5.0780 | 0.0620 | 4.9721 |
| 0.084 | 5 | 0.0840 | 5.0529 | 0.0841 | 5.1140 | 0.0840 | 5.0040 |
| 0.106 | 5 | 0.1060 | 4.9744 | 0.1061 | 5.0638 | 0.1059 | 4.7045 |
| 0.018 | 7 | 0.0180 | 6.9906 | 0.0180 | 7.0032 | 0.0180 | 6.9807 |
| 0.040 | 7 | 0.0400 | 7.0501 | 0.0400 | 7.0691 | 0.0400 | 7.0383 |
| 0.062 | 7 | 0.0621 | 6.9453 | 0.0621 | 6.8696 | 0.0620 | 7.0114 |
| 0.084 | 7 | 0.0840 | 6.9958 | 0.0840 | 6.9851 | 0.084 | 7.0098 |
| 0.106 | 7 | 0.1060 | 6.9899 | 0.1061 | 6.9890 | 0.1059 | 7.0039 |
| 0.018 | 9 | 0.0180 | 8.9579 | 0.0180 | 8.9870 | 0.0180 | 8.9442 |
| 0.040 | 9 | 0.0400 | 8.9487 | 0.0400 | 9.0033 | 0.0400 | 8.8930 |
| 0.062 | 9 | 0.0620 | 8.9993 | 0.0620 | 9.0180 | 0.0620 | 8.9277 |
| 0.084 | 9 | 0.0839 | 9.0008 | 0.0840 | 9.0120 | 0.0839 | 8.9721 |
| 0.106 | 9 | 0.1059 | 9.0567 | 0.1059 | 9.0424 | 0.1058 | 9.0660 |
| 0.018 | 11 | 0.0180 | 10.9854 | 0.0180 | 11.0353 | 0.0180 | 10.9353 |
| 0.040 | 11 | 0.0400 | 10.9579 | 0.0400 | 10.9727 | 0.0400 | 10.9511 |
| 0.062 | 11 | 0.0620 | 10.9911 | 0.0620 | 10.9702 | 0.0619 | 11.0730 |
| 0.084 | 11 | 0.0839 | 11.0374 | 0.0840 | 10.9977 | 0.0838 | 11.0814 |
| 0.106 | 11 | 0.1062 | 10.9487 | 0.1087 | 10.1355 | 0.1059 | 11.0767 |

## 3.7 FE modelling of indentation of hyperfoam materials and inverse parameters identification

### 3.7.1 FE models

Hyperfoam model is widely used to describe the behavior of foam materials for sport and protect equipments (e.g. EVA foams). This model is able to capture the nonlinear stiffening behaviour of materials at large strains. The strain energy density function (U) is represented by next two equations *(ABAQUS)*:

$$U=\sum_{i=1}^{N}\frac{2\mu_i}{\alpha_i^2}\left[\hat{\lambda}_1^{\alpha_i}+\hat{\lambda}_2^{\alpha_i}+\hat{\lambda}_3^{\alpha_i}-3+\frac{1}{\beta_i}((J^{el})^{-\alpha_i\beta_i}-1)\right] \quad (3.7.1)$$

$$\hat{\lambda}_i=(J^{th})^{-\frac{1}{3}}\lambda_i;\ \hat{\lambda}_1\hat{\lambda}_2\hat{\lambda}_3=(J^{th})^{-1}\lambda_1\lambda_2\lambda_3=(J^{th})^{-1}J=J^{el} \quad (3.7.2)$$

where $\lambda_1$, $\lambda_2$, $\lambda_3$ are the principal stretches; $J^{el}$, $J^{th}$ and $J$ are the elastic volume ratio, the thermal volume ratio and the total volume ratio, respectively.

Taking the first term of the hyperfoam strain energy density function without considering the thermal effect, there is

$$U=\frac{2\mu}{\alpha^2}\left[\lambda_1^{\alpha}+\lambda_2^{\alpha}+\lambda_3^{\alpha}-3+\frac{1}{\beta}((J^{el})^{-\alpha\beta}-1)\right] \quad (3.7.3)$$

where μ, α and β are the material properties representing the compressible foam behavior. β is related to the the effective Poisson's ratio (ν) following

$$\beta=\frac{\nu}{1-2\nu} \quad (3.7.4)$$

If the Poisson's ratio is known, then the material behavior is mainly governed by the two parameters 'μ' and 'α', which could be identified through inverse modelling of indentation tests.

A 2-D axial symmetric indentation FE model (Figure 3.27) was built to simulate the hyperfoam indentation process. The indenter itself was assumed to be analytical rigid body. The axisymmetric element CAX4R was used. Similar to the elastic and hyperelastic models, finer mesh has been applied around the indenter to improve the accuracy. The thickness and width of the model is 20 mm and 30mm, respectively.

The bottom face of the foam was fixed in all degrees of freedom (DOF). Contact was defined between the indenter surface and the top surface of the foam with a frictional coefficient of 0.5. The material of interest is allowed to move and the contact between the indenter surface and the material was maintained at all the times.

Figure 3.27(b) shows a typical numerical force indentation depth curve simulated by this model with a spherical indenter of R= 4 mm. Mesh size effects was assessed by varying the mesh density (Figure 4.27 (c)) and the results were shown in Figure 3.27(d). With reduced mesh size (e.g. Mesh 2) underneath the indenter, the force indentation depth curves become less sensitive to the mesh density and the P-h curves become identical. This helps to establish the suitable mesh density and optimise the requirement on the computational resources.

### 3.7.2 Effect of indenter sizes and material parameters on the indentation curves and simulation spaces

The force-indentation depth data curves and stress distributions underneath the indenter were presented in Figure 3.28. The stress around the indenter showed similar distribution patterns, however, the peak stress value and the volume of the deformed material are different with different indenter sizes. When a larger indenter is used, the effectively deformed material volume is significantly larger. These differences may reflect the different contribution of the two material parameters (i.e. E and $\nu$) to the indentation force, which could potentially provide a mechanism to be used in the inverse modelling process to extract these material parameters.

Figure 3.29 shows the effects of the coefficient '$\mu$' and '$\alpha$' on the force-indentation depth curve. The coefficient '$\mu$' used in (a) was 0.2 and '$\alpha$' of 4.0 was used in (b). As shown in the Figure (a), the slopes of the force-indentation depth data increased with increasing coefficient '$\mu$', while, the slopes of the force-indentation data increased when '$\alpha$' is decreased. This is significantly different from the hyper elastic model. These sensitivity test results will provide guidelines in designing the inverse modelling strategy.

The simulation surfaces (Figure 3.30) were constructed from numerical results with 'μ' ranged from (0.008, 0.06, 0.2, 0.5, 0.8) (MPa) and 'α' from (0.08, 2.0, 4.0, 8.0, 12.0). The numerical results were then recorded and stored into a database to form the simulation space. As described in section 3.4, the simulated force-indentation depth data has to be transformed into a discrete form. In this case, the curves, (which indentation depth from 0.02mm to 3.72mm) were divided into 176 equally spaced divisions. Typical simulation surfaces at the $90^{th}$ and $140^{th}$ indentation point were shown in the figure representing the variation of indentation forces within property range studied at the depth of 2mm and 3mm respectively. In the parameter fitting process, the program searches through this space and determine a set of material properties that produce force displacement result matching the input experimental data.

### 3.7.3 Inverse parameters identification based on the single indenter method

Figure 3.31 illustrates the property searching process based the single indenter method using the data for R=4mm in Figure 3.30 as the input data. The initial guessed value was '$\mu_0$=0.16' and '$\alpha_0$ =2.0' while the target values were '$\mu_T$=0.6' and '$\alpha_T$ =8.0'. Figures (a) &(b) shows the material properties searching process with a constant error treatment and random error distribution, respectively. At each indentation point, the program searches for a combination of material properties (μ and α) which gives the best fit to the target point on the experimental curve. As shown in Figure (a), the fitting process involved significant scatter when the search started from the initial value in the early stage, then converged into a stable value.

To assess the robustness of the program, a range of initial guessed values has been used over a wide potential parameter range (Figure 3.32) and converged results are shown in Figure 3.33. The predicted results from constant error with different error levels (1%, 5%, 10%) scattered over a wide range. The program failed to converge when the noise level was set within 1%. The converged results for random error approach is much more focused but it still scattered over a wide range.

### 3.7.4 Inverse parameters identification based on the dual indenters method

Figure 3.34 illustrates the property searching process based on the dual indenters method using data for R=4 and R=6 mm. The initial guessed value was $\mu_0$=0.16 and $\alpha_0$ =2.0 while the true material parameters values were $\mu_T$=0.6 and $\alpha_T$ =8. At each indentation point, the program searches for a combination of material properties (E and $\nu$) which give the best fit to the target point on both the experimental curve. Figure (a) & (b) shows the material properties searching process with the constant error and random error method, respectively. In both cases, the search process is much smoother than the case for hyperelastic model and the results obtained are in good agreement with the true materials properties.

Similar to the single indenter approach, the effect of the initial values has been assessed and the result was plotted in Figure 3.35. Different constant error levels (1%, 5%, 10%) have been used and the distribution of the converged results showed similar pattern. The program failed to converge when the error level was set within 1%. Comparing Figures 3.35(a) and (b). It is evident that converged results based on the random error approach are much more focused. This suggests that the random error method is much more robust than the constant error approach with all the predicted values close to true material properties.

Several different material properties have been used as input data to assess the capacity of the program in dealing with different materials. Typical results were listed in Table 3.4 and selected results were shown in Figure 3.36. The results clearly showed that the dual indenters could produce accurate results.

**Table 3.4** Typical predicted results by inverse FE modelling based on the dual indenters method on hyperfoam material.

| Target value | | Predicted value | | Up limit | | Low limit | |
|---|---|---|---|---|---|---|---|
| $\mu_T$ | $\alpha_T$ | $\mu$ | $\alpha$ | $\mu$ | $\alpha$ | $\mu$ | $\alpha$ |
| 0.1 | 1.6 | 0.1000 | 1.6018 | 0.1001 | 1.6237 | 0.1000 | 1.5905 |
| 0.3 | 1.6 | 0.2999 | 1.5919 | 0.3000 | 1.5996 | 0.2997 | 1.5869 |
| 0.5 | 1.6 | 0.4998 | 1.6302 | 0.5000 | 1.6982 | 0.4996 | 1.5923 |
| 0.7 | 1.6 | 0.6991 | 1.5795 | 0.7000 | 1.6029 | 0.6962 | 1.5356 |
| 0.1 | 3.7 | 0.0999 | 3.6728 | 0.1001 | 3.7134 | 0.0998 | 3.6627 |
| 0.3 | 3.7 | 0.2999 | 3.6888 | 0.3000 | 3.6987 | 0.2997 | 3.6589 |
| 0.5 | 3.7 | 0.4995 | 3.6857 | 0.5001 | 3.7005 | 0.4976 | 3.6302 |
| 0.7 | 3.7 | 0.7001 | 3.7021 | 0.7013 | 3.7324 | 0.6990 | 3.6753 |
| 0.1 | 5.8 | 0.1000 | 5.7993 | 0.1004 | 5.8686 | 0.0994 | 5.7168 |
| 0.3 | 5.8 | 0.3001 | 5.8039 | 0.3004 | 5.8188 | 0.2985 | 5.7375 |
| 0.5 | 5.8 | 0.4993 | 5.7760 | 0.5003 | 5.8078 | 0.4973 | 5.6935 |
| 0.7 | 5.8 | 0.7016 | 5.8382 | 0.7031 | 5.8866 | 0.6971 | 5.7367 |
| 0.1 | 7.9 | 0.0999 | 7.8789 | 0.1003 | 7.9523 | 0.0994 | 7.7994 |
| 0.3 | 7.9 | 0.2997 | 7.8619 | 0.3009 | 7.9476 | 0.2976 | 7.7759 |
| 0.5 | 7.9 | 0.4994 | 7.8816 | 0.5008 | 7.9268 | 0.4912 | 7.6280 |
| 0.7 | 7.9 | 0.6995 | 7.8890 | 0.7019 | 7.9426 | 0.6978 | 7.8499 |
| 0.1 | 10 | 0.0999 | 9.9776 | 0.1004 | 10.0614 | 0.0989 | 9.8085 |
| 0.3 | 10 | 0.2994 | 9.9617 | 0.2998 | 9.9884 | 0.2976 | 9.8579 |
| 0.5 | 10 | 0.4940 | 9.7871 | 0.4997 | 9.9922 | 0.4387 | 7.8200 |
| 0.7 | 10 | 0.7001 | 10.0041 | 0.7037 | 10.0997 | 0.6979 | 9.9413 |

### 3.8 Sensitivity analysis and results

Sensitivity of the predicted material properties due to variations of the input parameters is essentially an intrinsic characteristic of inverse problems, which has been a major difficulty in using inverse or reverse method (*Venkatesh et al, 2000; Dao et al, 2001)*. In this work the input data were taken from numerical models, however, in a real testing situation, there can be potentially both system and random errors. Factors such as error in the indenter angle, roundness of the tip, alignment and accuracy of the recorded indentation force or depth all influence the measurement results *(Dao et al, 2001)*. From the results shown in Section 3.5, 3.6 and 3.7, the dual indentation method with random error approach is a more robust approach for all the models; therefore, the sensitivity of the estimated properties to variations in the input parameters was investigated in these three cases. This was conducted by adding a systematic percentage error to the input data, then systematically comparing the change in the converged material parameters.

Figure 3.37 shows the sensitivity of estimated linear elastic properties to perturbations in the indentation force for the dual indentation approaches with an original property of E=0.14 and v=0.43. The result showed that the Young's modulus of the material can be predicted within ±0.01 MPa variation if the *P-h* response can be measured within 5% error. The Poisson's ratio of these materials can be determined using the existing inverse FE modelling within ±0.03 if the *P-h* response can be measured with 5% error. Several materials sets have been used to investigate the accuracy and sensitivity with respect to the material parameters. The predicted results and sensitivity respecting to 5% perturbation in the indentation force were listed in Table 3.5. The smaller scatter in the predicted properties reflects the higher accuracy and the greater scatter in the sensitivity results reflects the stronger sensitivity with respect to the properties. The percentage of scatters for E ($\Delta E/E$ ) and $\nu$ ($(\Delta \nu/\nu$ ) of all the materials with respect to the ±5% perturbation of *P* (indentation force) are within ±6% to ±8%, respectively. This level of variation is reasonable of engineering application.

**Table 3.5** Sensitivity study results of inverse FE modelling based on dual spherical indenters for linear elastic materials.

| Input | | Accuracy study | | | | Sensitivity study (with ±5% error of *P*) | | | |
|---|---|---|---|---|---|---|---|---|---|
| | | Predicted values | | Accuracy (error%) | | Sensitivity (error+5%) | | Sensitivity (error-5%) | |
| $E_T$ | $\nu_T$ | E | $\nu$ | ΔE/E | $\Delta\nu/\nu$ | ΔE / $\Delta\nu$ | ΔE/E / $\Delta\nu/\nu$ | ΔE / $\Delta\nu$ | ΔE/E / $\Delta\nu/\nu$ |
| 0.1 | 0.2 | 0.0999 | 0.2069 | -0.10% | 3.45% | 0 0058 / -0.0082 | 5.77% / -4 12% | -0.0056 / 0.0057 | -5.60% / 2 85% |
| 0.3 | 0.2 | 0.2988 | 0.2111 | -0.40% | 5.55% | 0.0146 / 0.0147 | 4.86% / 7.37% | -0.0155 / -0 0145 | -5.17% / -7.27% |
| 0.1 | 0.25 | 0.0999 | 0.2536 | -0.10% | 1.44% | 0.0046 / 0.0181 | 4.63% / 5.18% | -0.0052 / -0 0076 | -5.23% / -2.17% |
| 0.2 | 0.35 | 0.1998 | 0.3520 | -0.10% | 0.57% | 0.0051 / 0.0243 | 2.57% / 6.95% | -0.0032 / -0.0122 | -1.62% / -3.50% |
| 0.4 | 0.4 | 0.4030 | 0.3911 | 0.75% | -2.23% | 0.0164 / 0.0114 | 4.10% / 2 85% | -0.0139 / -0 0212 | -3.48% / -5 3% |

*The sensitivity study is using ±5% perturbation of the *P* in the *P-h* curves

Figure 3.38 shows typical sensitivity study result of estimated hyperelastic properties to the perturbation in the indentation force for the dual indentation approaches with an original property of $\mu_0$=0.07MPa, $\alpha_0$=6.2. The result showed that the parameter '$\mu$' can be predicted within ±0.004MPa if the *P-h* response can be measured with 5% error. The parameter '$\alpha$' of these materials can be determined using the existing inverse FE modelling program within ±0.25 if the *P-h* response can be measured with 5% error. Several material sets have been used to investigate the accuracy and sensitivity of the program and the results were listed in Table 3.6. The percentage scatter of $\mu(\Delta\mu/\mu)$ and $\alpha$ $(\Delta\alpha/\alpha)$ of all the materials with respect to the ±6% and ±3%, respectively, perturbation of the indentation force are from -5% to +5%. This suggests that the program is robust and not affected by the perturbation in the testing data, which is important for dealing with material tests.

**Table 3.6** Sensitivity study results of inverse FE modelling based on dual spherical indenters for hyperelastic materials.

| Input | | Accuracy study | | | | Sensitivity study (with ±5% error of *P*) | | | |
|---|---|---|---|---|---|---|---|---|---|
| | | Predicted values | | Accuracy (error%) | | Sensitivity (error+5%) | | Sensitivity (error-5%) | |
| $\mu_T$ | $\alpha_T$ | $\mu$ | $\alpha$ | $\Delta\mu/\mu$ | $\Delta\alpha/\alpha$ | $\Delta\mu$ / $\Delta\alpha$ | $\Delta\mu/\mu$ / $\Delta\alpha/\alpha$ | $\Delta\mu$ / $\Delta\alpha$ | $\Delta\mu/\mu$ / $\Delta\alpha/\alpha$ |
| 0.04 | 5.0 | 0.0400 | 4.9640 | 0.03% | -0.72% | 0.0021 / 0 0257 | 5.13% / 0 51% | -0.0019 / 0.1078 | -4.83% / 2 16% |
| 0.062 | 11 | 0.0620 | 10.9911 | -0.01% | -0.08% | 0.0031 / 0 0249 | 5.00% / 0.23% | -0.0032 / 0.0165 | -5.11% / 0.15% |

| | | | | | | | | | |
|---|---|---|---|---|---|---|---|---|---|
| 0.062 | 7.0 | 0.0621 | 6.9453 | 0.15% | -0.78% | 0.0031 / -0.007 | 4.95% / -0.06% | -0.0032 / 0 0479 | -5.16% / 0.44% |
| 0.084 | 7.0 | 0 0840 | 6.9958 | 0.00% | -0.06% | 0.0042 / 0.0007 | 5.04% / 0.01% | -0.0043 / 0.0315 | -5.08% / 0.45% |
| 0.106 | 10 | 0.1061 | 10.0324 | 0.05% | 0.32% | 0.0053 / 0.0103 | 4.97% / 0.1% | -0.0052 / -0.0444 | -4.91% / -0.44% |

*The sensitivity study is using ±5% perturbation of the $P$ in the $P$-$h$ curves

Figure 3.39 shows the sensitivity study results of the hyperfoam properties to the perturbation in the indentation force for the dual indentation approaches with an original property of $\mu_0$=0.0164, $\alpha_0$=6.82. The result showed that the parameter '$\mu$' can be predicted within ±0.001MPa variation if the $P$-$h$ response can be measured with 5% error. The parameter '$\alpha$' of these materials can be determined using the existing inverse FE modelling within ±0.2 if the $P$-$h$ response can be measured within 5% error. Several materials sets have been used to investigate the sensitivity with respect to the material parameters and the results were listed in Table 3.7. A greater scatter in the sensitivity results represents stronger sensitivity with respect to the properties. As listed in the table, The percentage scatter of $\mu(\Delta\mu/\mu)$ and $\alpha$ $(\Delta\alpha/\alpha)$ of all the materials with respect to ±6% and ±1% respectively, perturbation of the indentation force are from –5% to +5%. This suggests that the program is robust and not affected by the perturbation in the testing data, which is important for dealing with material tests.

**Table 3.7** Accuracy and sensitivity study results of inverse FE modelling based on dual spherical indenters for hyperfoam materials.

| | | Accuracy study | | | | Sensitivity study (with ±5% error of $P$) | | | |
|---|---|---|---|---|---|---|---|---|---|
| Input | | Predicted values | | Accuracy (error%) | | Sensitivity (error+5%) | | Sensitivity (error-5%) | |
| $\mu_T$ | $\alpha_T$ | $\mu$ | $\alpha$ | $\Delta\mu/\mu$ | $\Delta\alpha/\alpha$ | $\Delta\mu$ / $\Delta\alpha$ | $\Delta\mu/\mu$ / $\Delta\alpha/\alpha$ | $\Delta\mu$ / $\Delta\alpha$ | $\Delta\mu/\mu$ / $\Delta\alpha/\alpha$ |
| 0.1 | 1.6 | 0.1000 | 1.6018 | 0.03% | 0.11% | 0.0052 / 0.0122 | 5.20% / 0.76% | -0.0052 / -0 0136 | -5.15% / -0 85% |
| 0.5 | 3.7 | 0.4996 | 3.6892 | -0.72% | -0.29% | 0.0261 / 0.0214 | 5.22% / 0 58% | -0.0262 / -0 0252 | -5.24% / -0 68% |
| 0.3 | *5.8* | 0.3001 | *5.8037* | 0.04% | 0.05% | 0.0157 / 0.0277 | 5.22% / 0.48% | -0.0153 / -0.0132 | -5.10% / -0.23% |
| 0.5 | *7.9* | 0.4994 | *7.8816* | -0.13% | -0.23% | 0.0254 / 0.0019 | 5.07% / 0.03% | -0.0268 / -0.0452 | -5.35% / -0.57% |
| 0.7 | *7.9* | 0.6995 | *7.8890* | -0.07% | -0.14% | 0.0333 / -0.0320 | 4.75% / -0.41% | -0.0354 / -0 0139 | -5.06% / -0.18% |
| 0.1 | *10* | 0.0999 | *9.9776* | -0.12% | -0.23% | 0 0050 / -0.0105 | 0.71% / -0.11% | -0 0050 / 0.0043 | -0.71% / 0.04% |

*The sensitivity study is using 5% perturbation of the $P$ in the $P$-$h$ curves

## 3.9 Summary

In this chapter, an inverse FE modelling program based on the Kalman filter technique has been developed and applied to study three material models (linear elastic hyperelastic and hyper foam). Two error distribution treatment methods have been implemented in the program and their feasibilities for different material systems has been established. FE models simulating the indentation of three typical material behaviours have been developed and factors such as mesh sensitivity, material properties were systematically studied to validate the FE models. Simulation spaces over a wide range of material properties have been developed for each material model, which successfully provided the data for the material properties prediction. The use of single indenter and dual indenters has been comparatively studied in terms of accuracy, convergence and robustness, which are important for materials characterisation.

The program was evaluated using blind tests with numerical experimental data including their validity, efficiency and robustness of the program with different material models. The results showed that single indenter method were initial dependent for elastic, hyperfoam and hyperelastic materials. The results also showed that the new uncertainty random error distribution treatment method is applicable to all the three material models while the program with the constant error distribution treatment was initial value dependent. The results demonstrate that Kalman filter is a feasible method and the random error treatment is more practical approach for characterisation material which is not initial value dependent and can be universally applied to different material models. The application of this method in charactering the properties of EVA foams and the human heel pad tissue *in vivo* is to be presented in the next chapter.

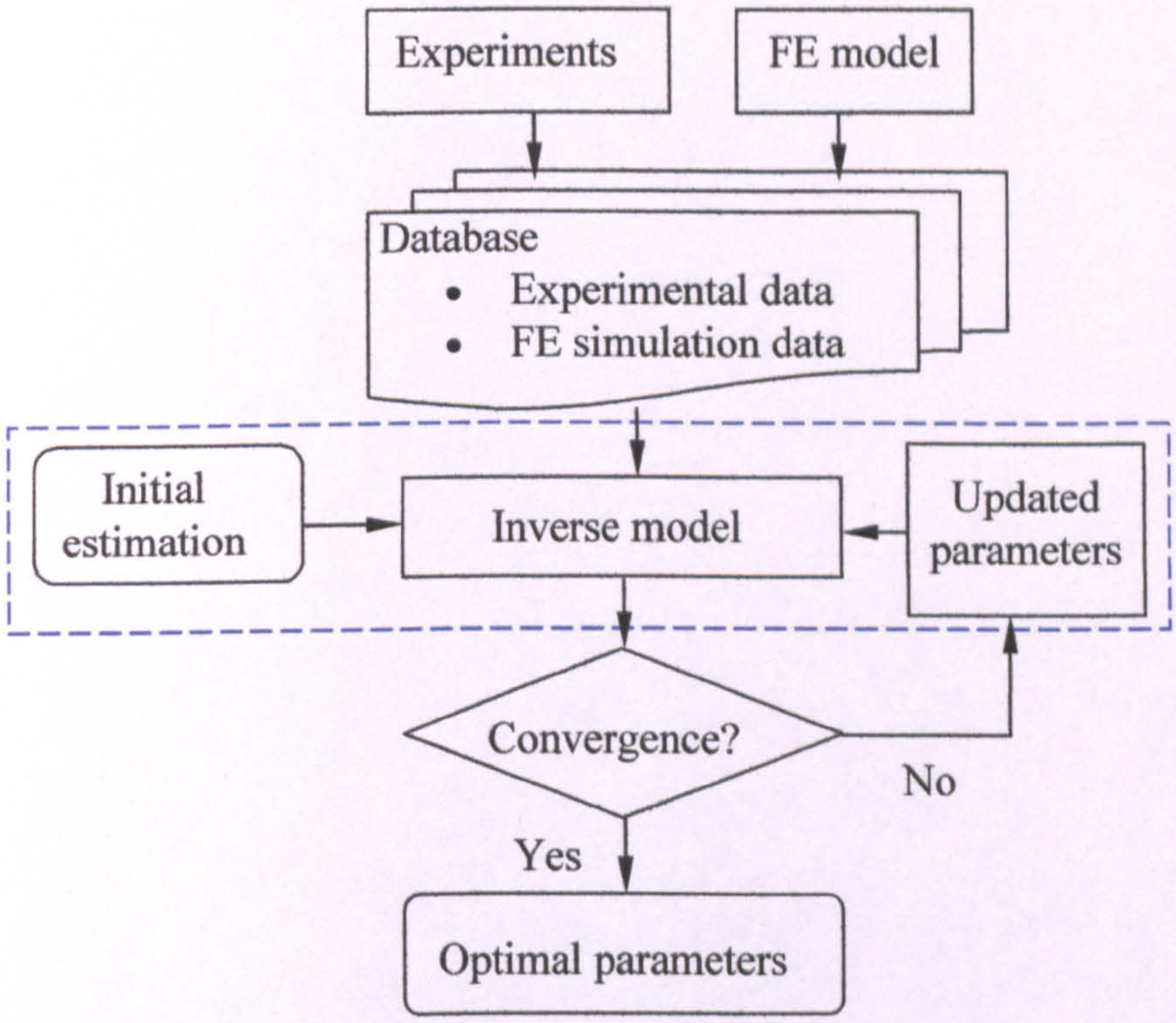


**Figure 3.1** Flow chart showing the main procedures in an inverse FE modelling scheme for parameters estimation.

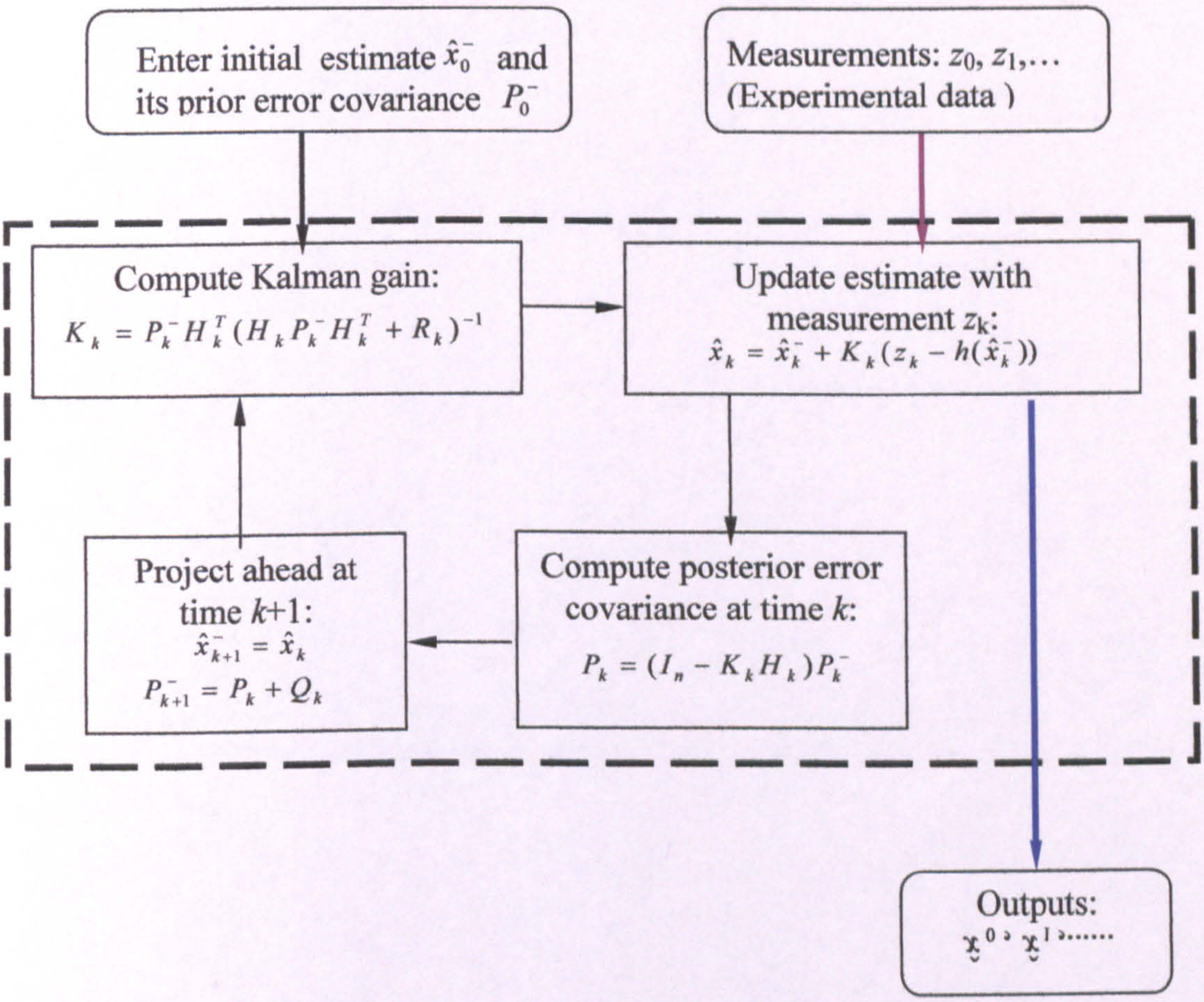


**Figure 3.2** Extended Kalman filter calculation loop for parameter estimation.

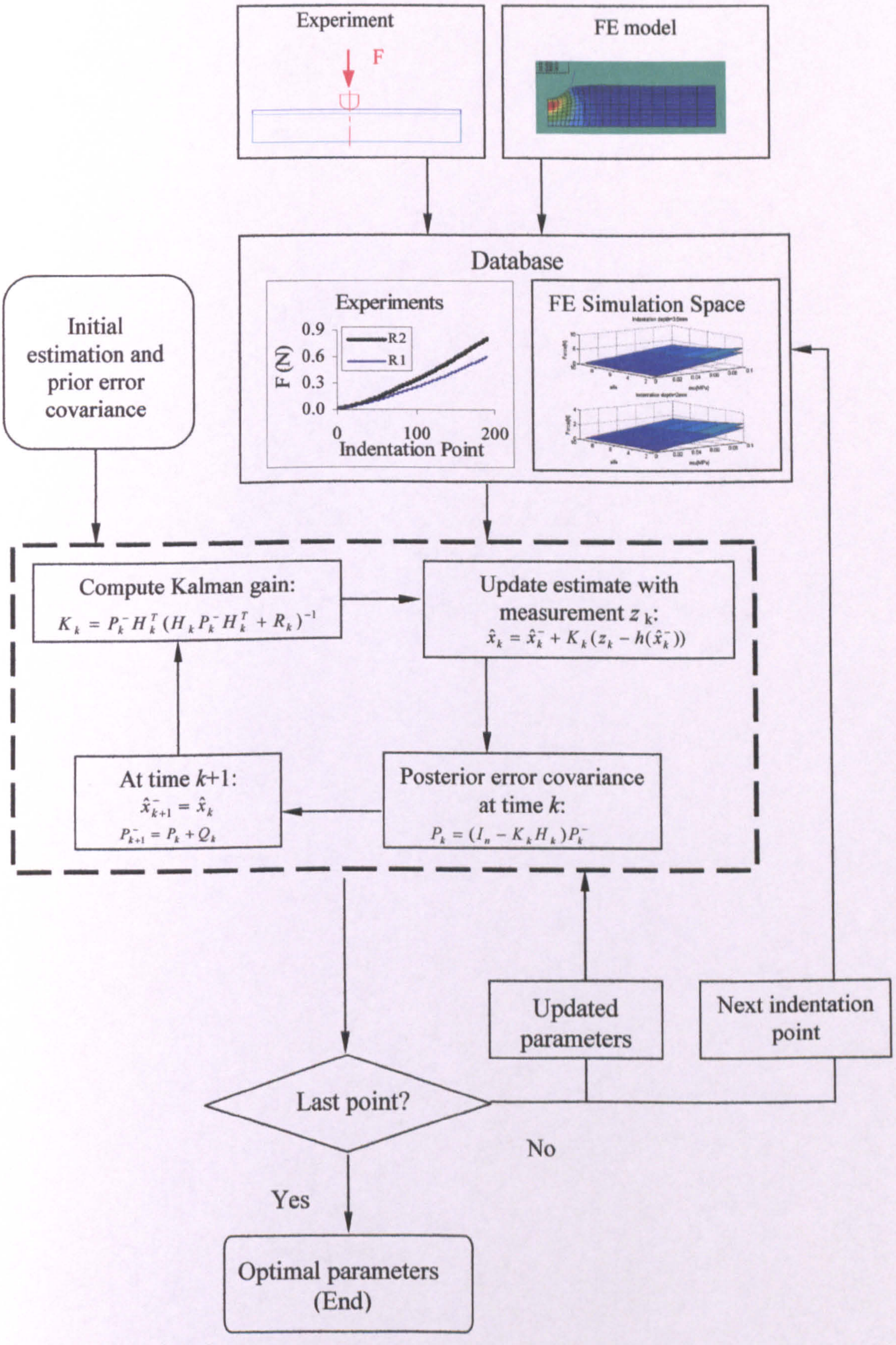


**Figure 3.3** Flow chart showing the inverse FE indentation method for material properties estimation based on the Kalman filter technique.

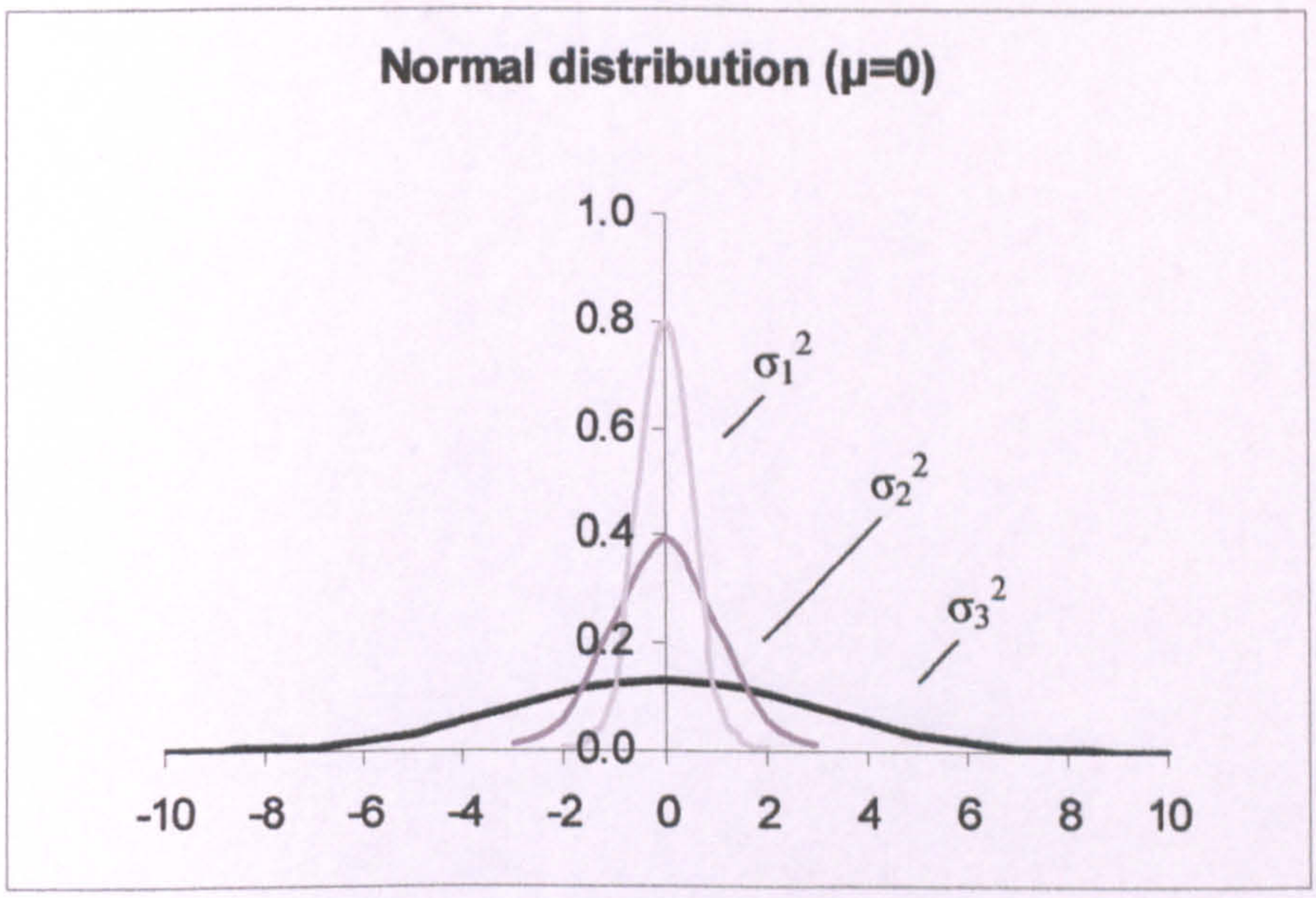


**Figure 3.4** Random error treatments for the experimental and estimation errors.

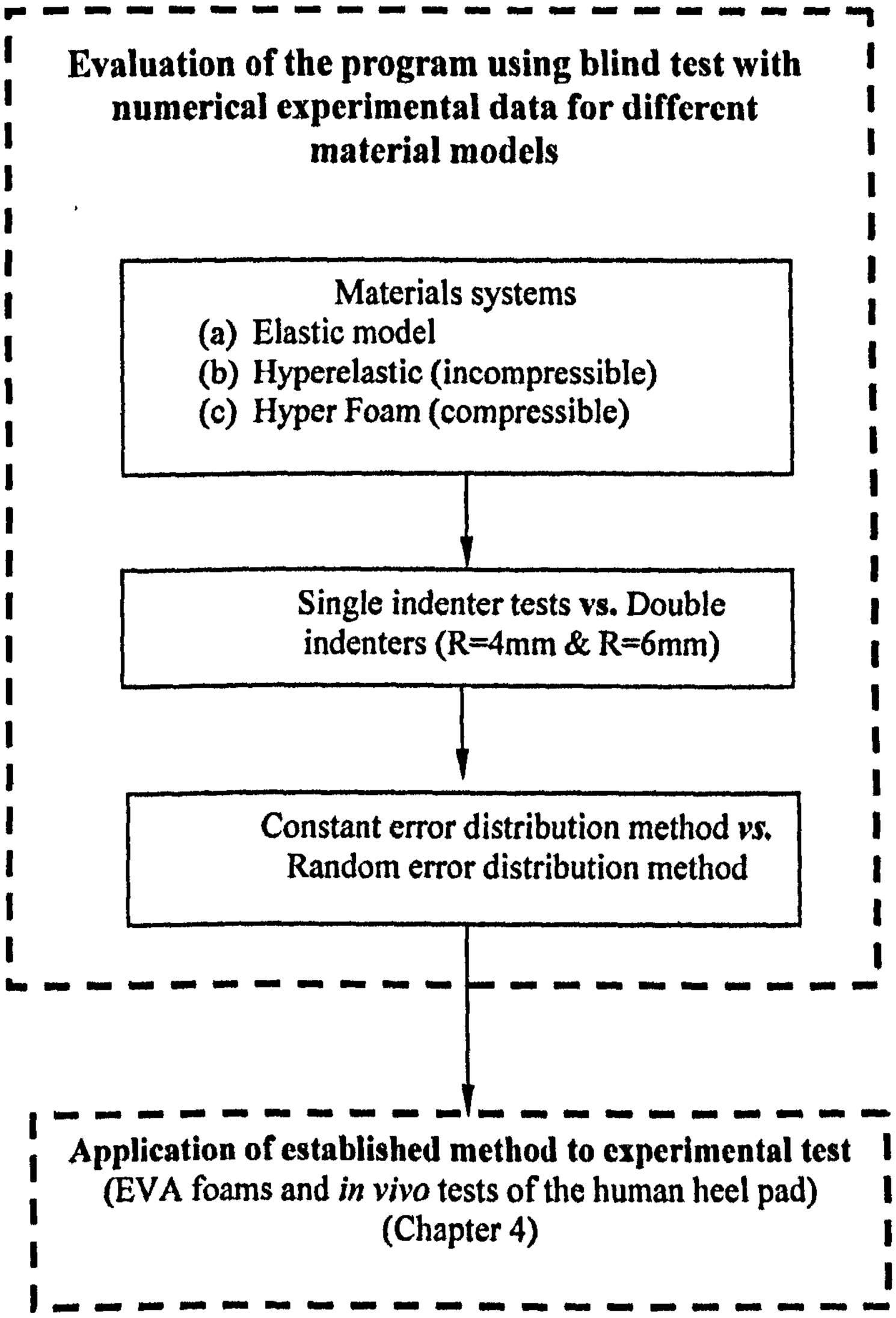


**Figure 3.5** Main procedures to evaluate the inverse FE program for different material models.

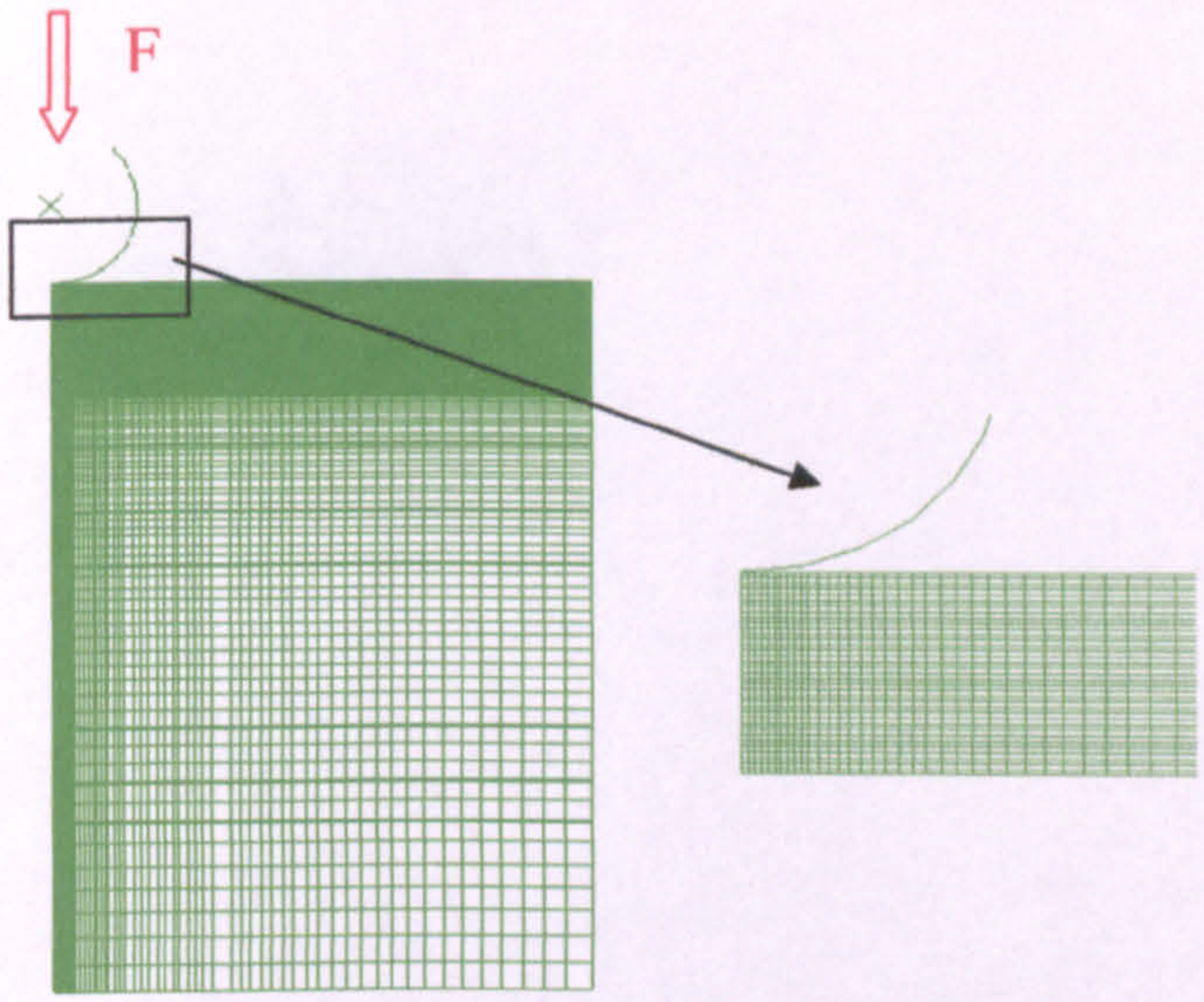


(a) FE model of indentation process with a spherical indenter.

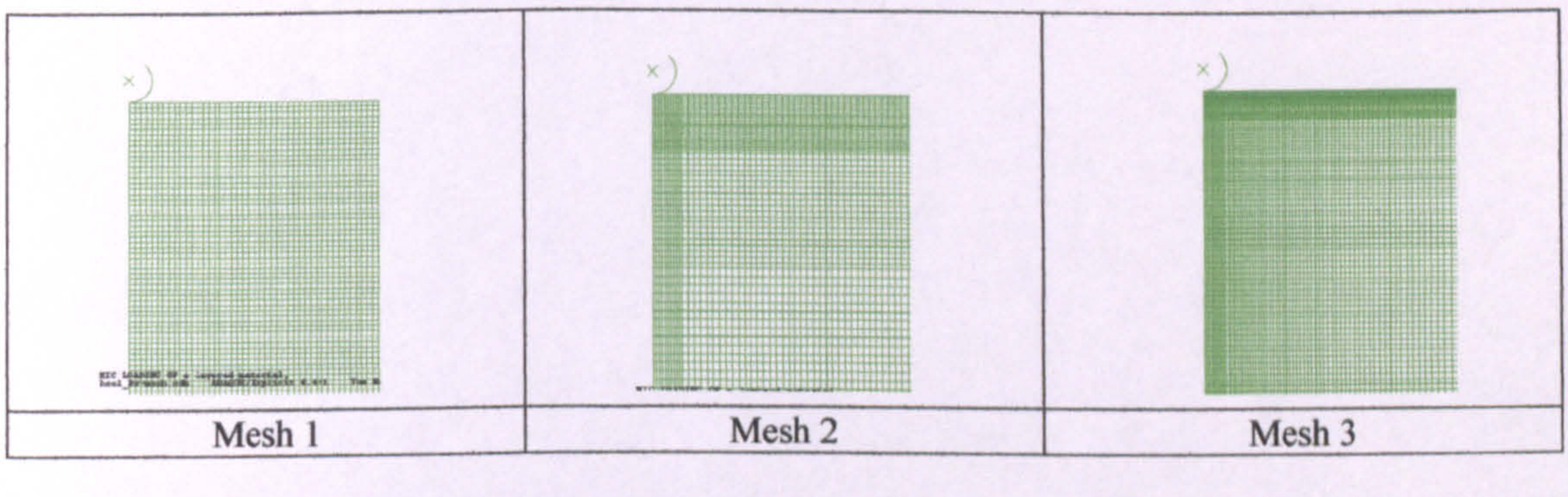


(b) FE models with different mesh densities.

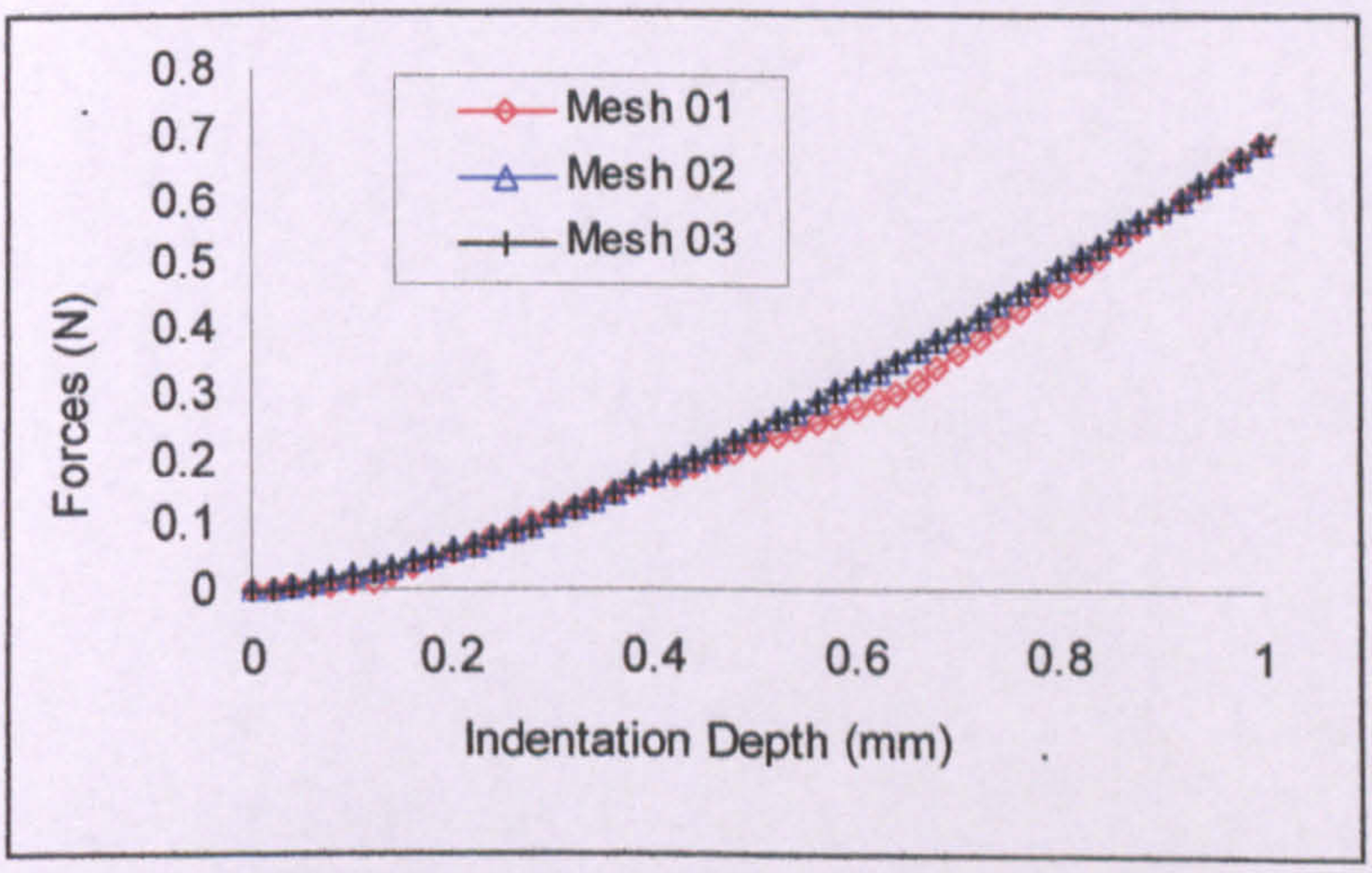


(c) Force indentation depth curves from FE models of different meshing schemes.

**Figure 3.6** FE modeling of the indentation process of a linear elastic material, typical force-indentation depth (*p-h*) curve and effect of meshing schemes.

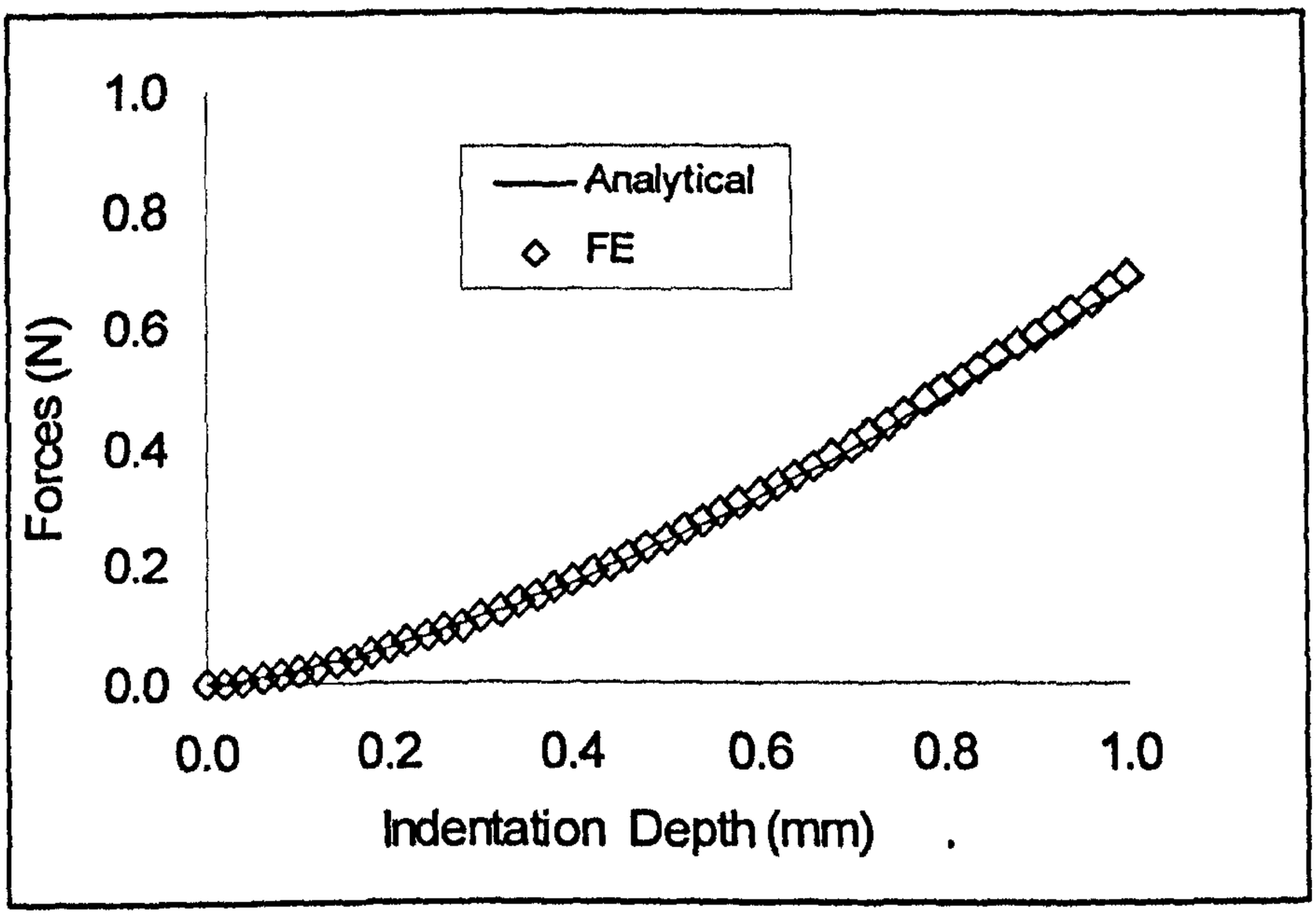


**Figure 3.7** Validation of the FE results against a known analytical solution.

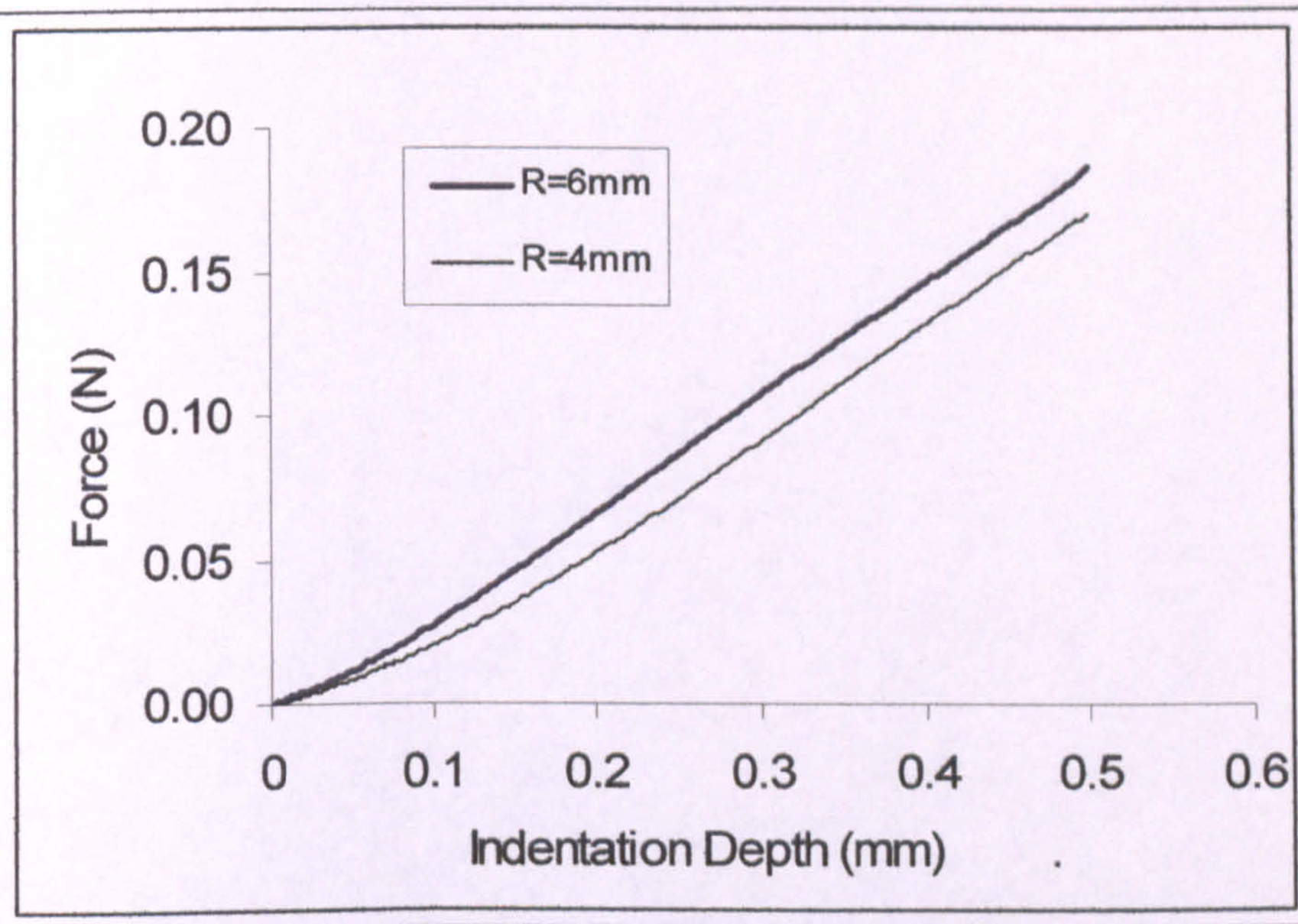


(a) P-h curves for different indenter sizes (R=4mm and R=6mm).

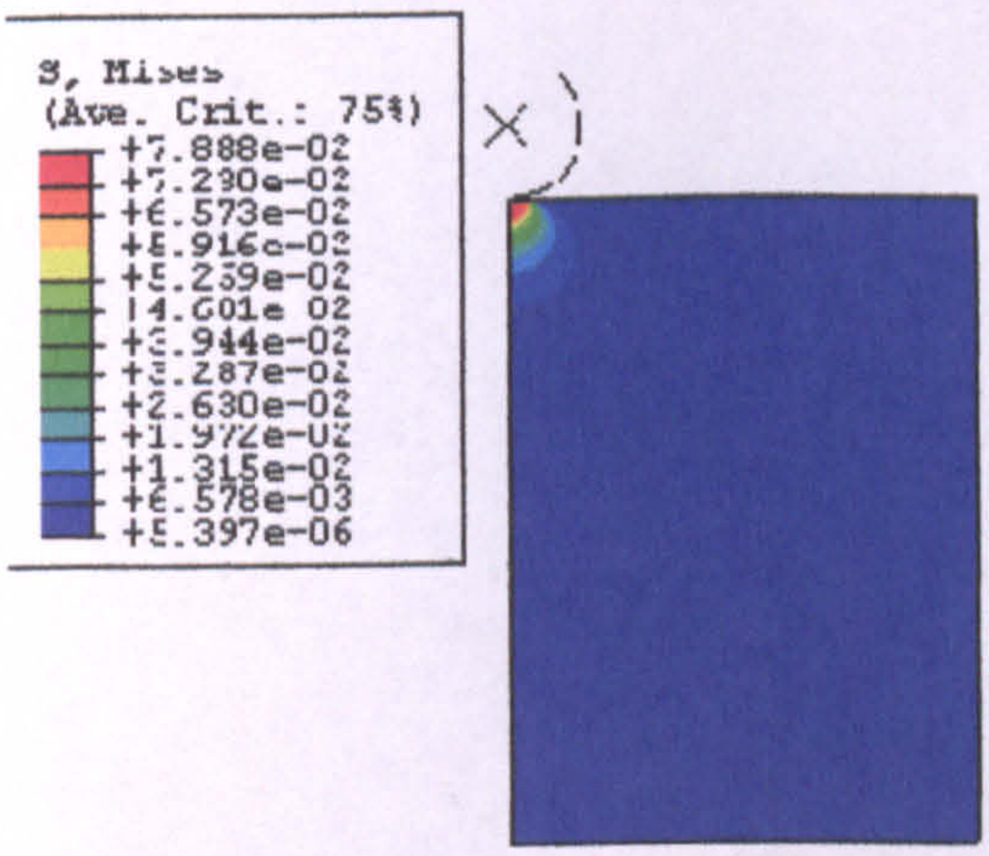


(b) Stress distribution under indentation (R=4mm)

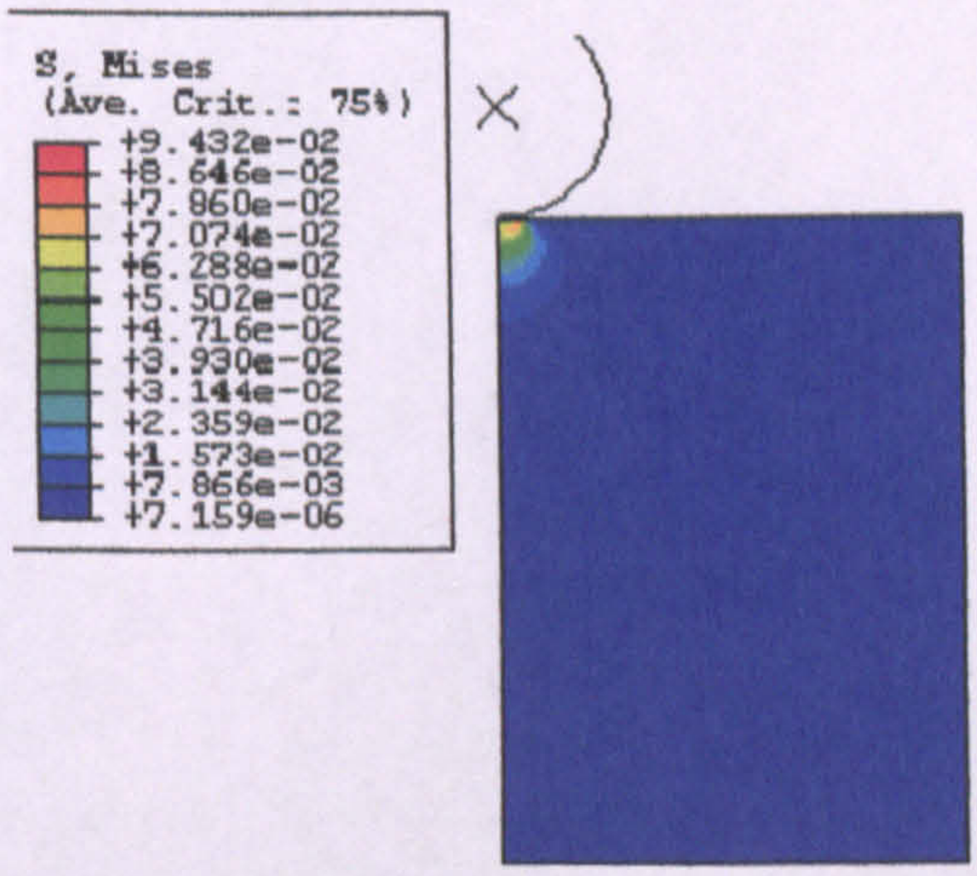


(c) Stress distribution under indentation (R=6mm)

**Figure 3.8** Effect of the indenter radius on the indentation curve and stress distributions.

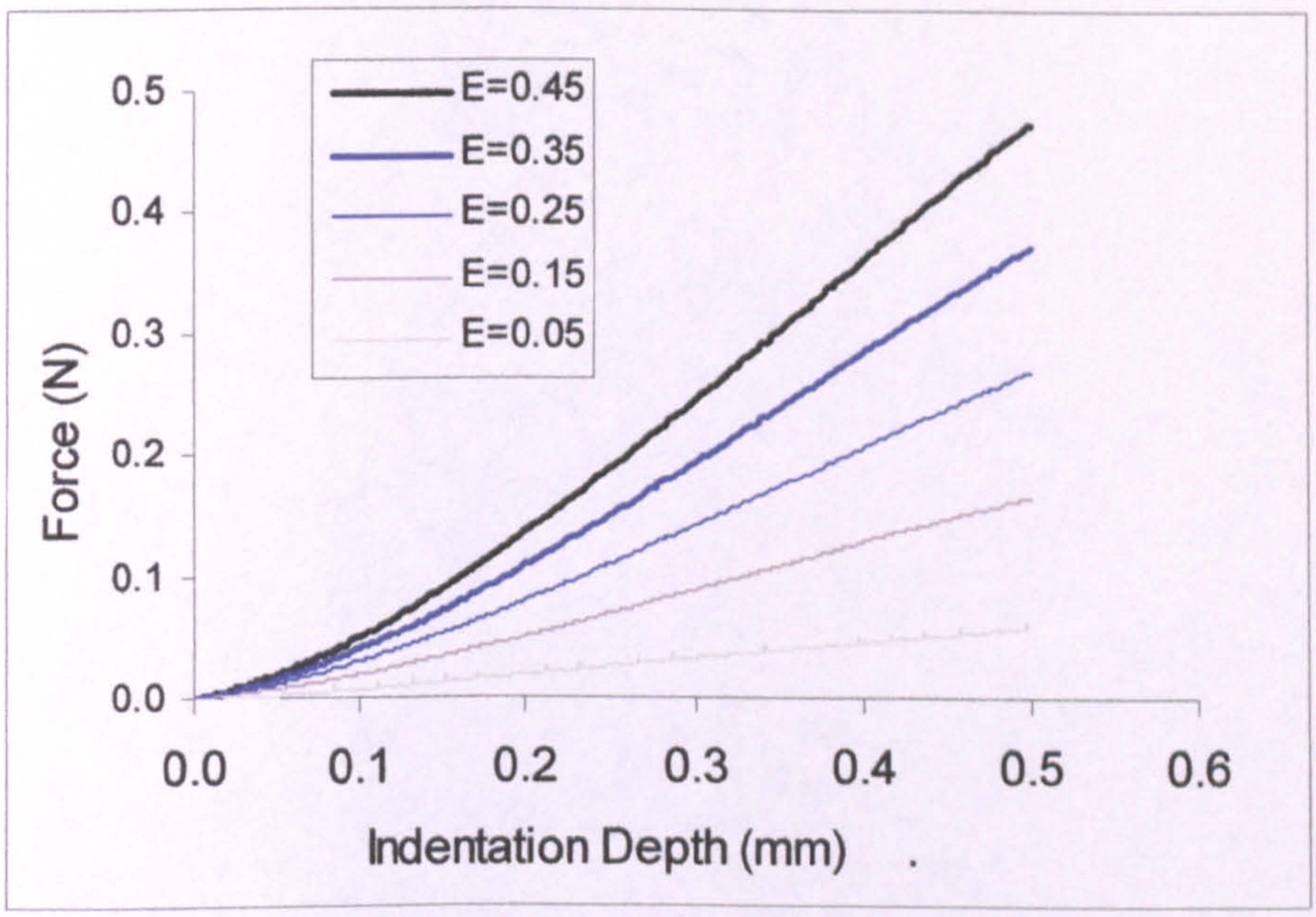


(a) Effect of the Young's modulus ($\nu$=0.28).

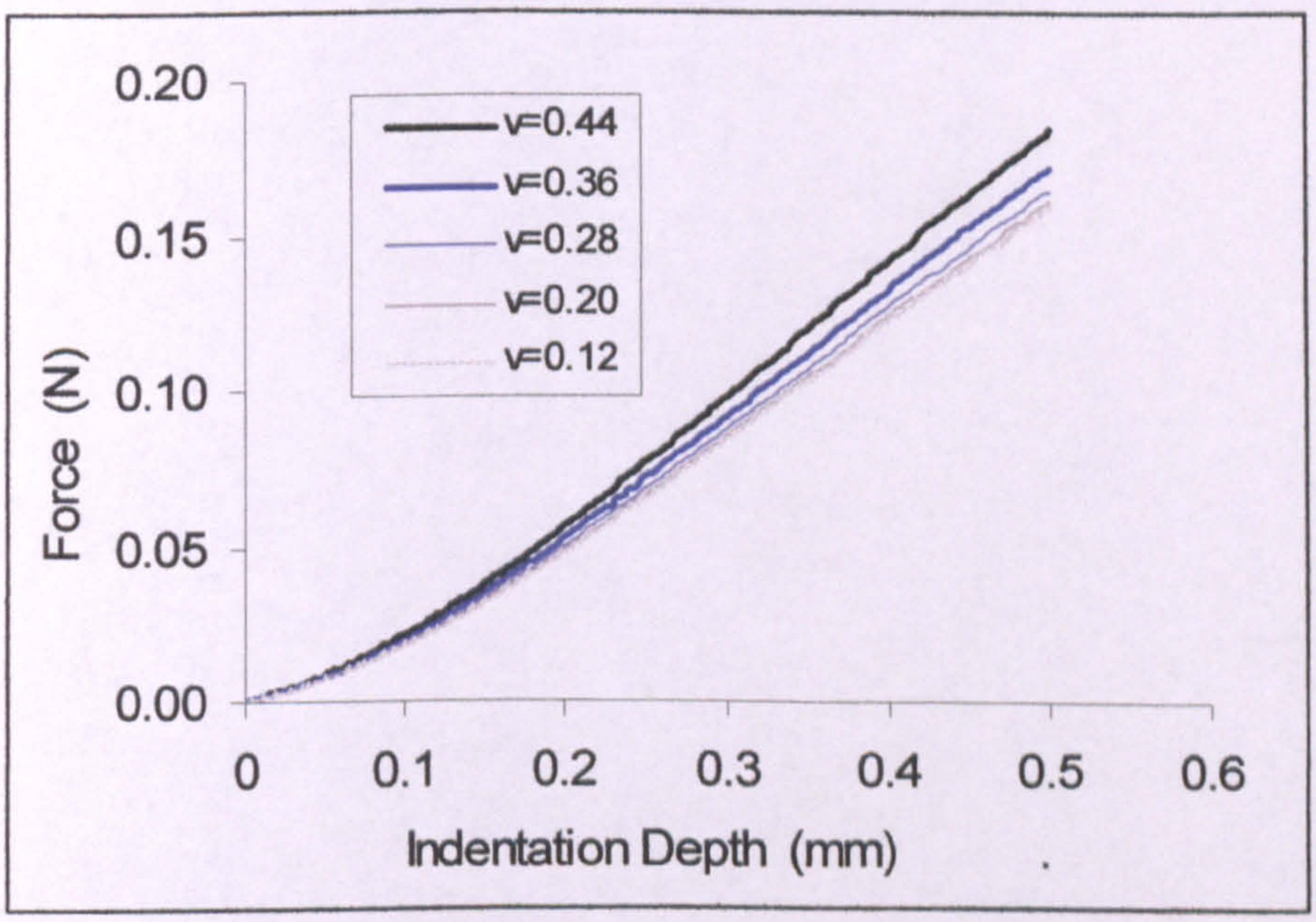


(b) Effect of the Poisson's ratio (E=0.25 MPa).

**Figure 3.9** Effects of elastic material properties (E and $\nu$) on the force-indentation depth relationship (R=4mm).

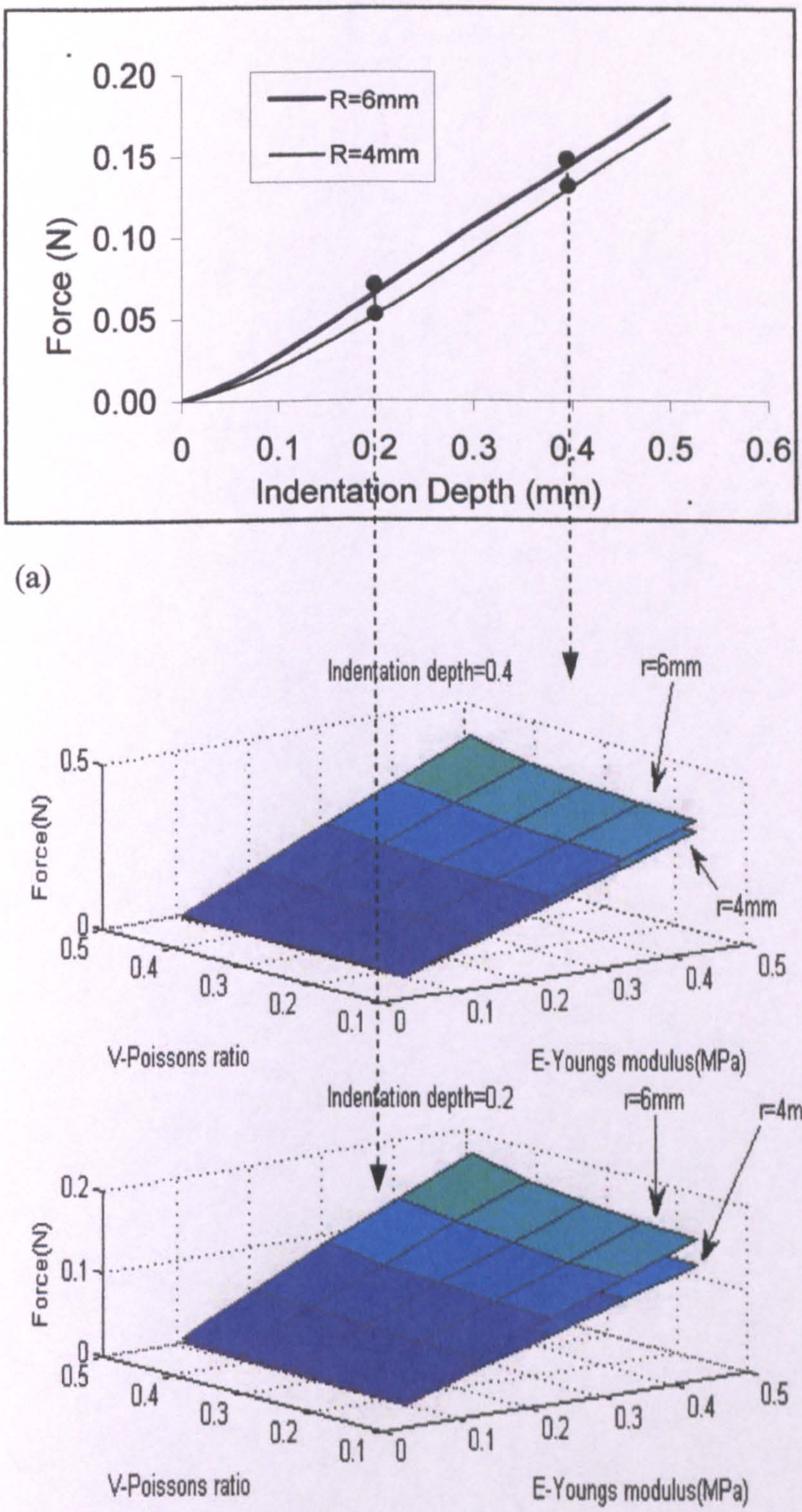


**Figure 3.10** Typical numerical experimental data with different indenter sizes (a) and simulation surfaces at indentation depth of 0.2mm and 0.4 mm.

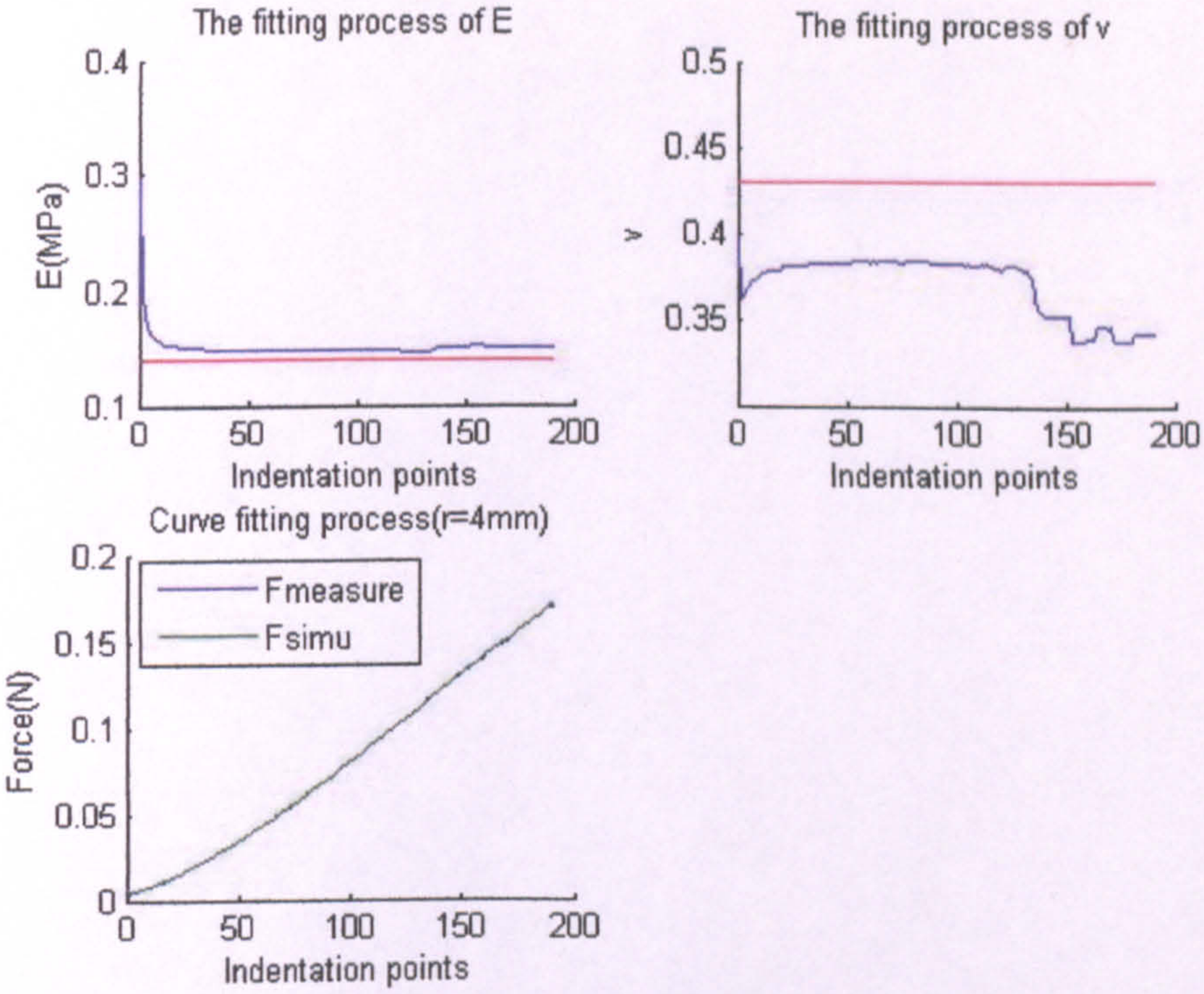


(a) Parameter searching process with a constant error (R=4mm).

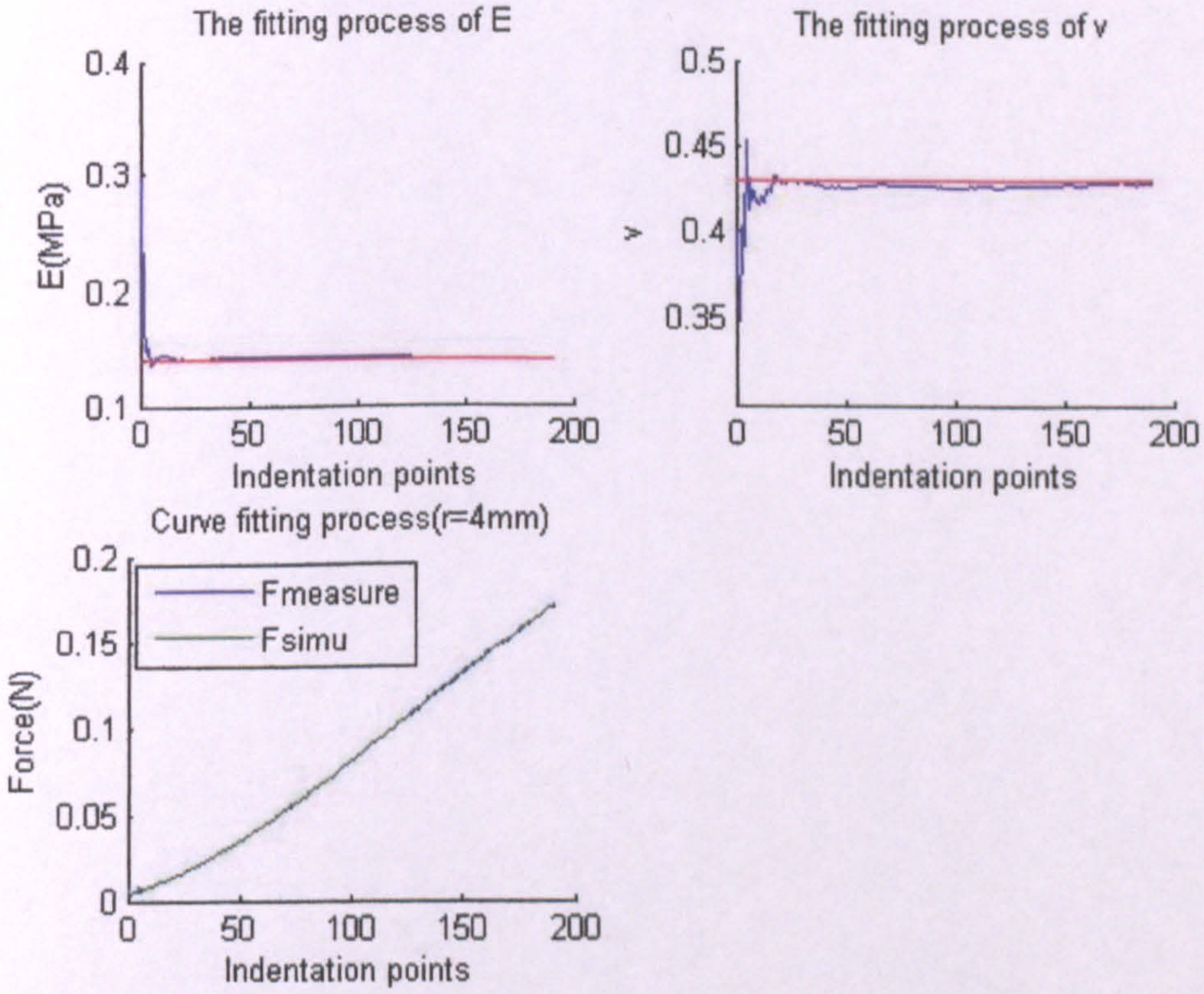


(b) Parameters searching process with Random error (R=4mm).

**Figure 3.11** Typical material parameter fitting curves for single indenter test (R=4mm) with the constant and Random error method. (The true material properties are $E_T$=0.14, $v_T$=0.43; the initial guessed value used are $E_0$=0.30 MPa and $v_0$=0.40).

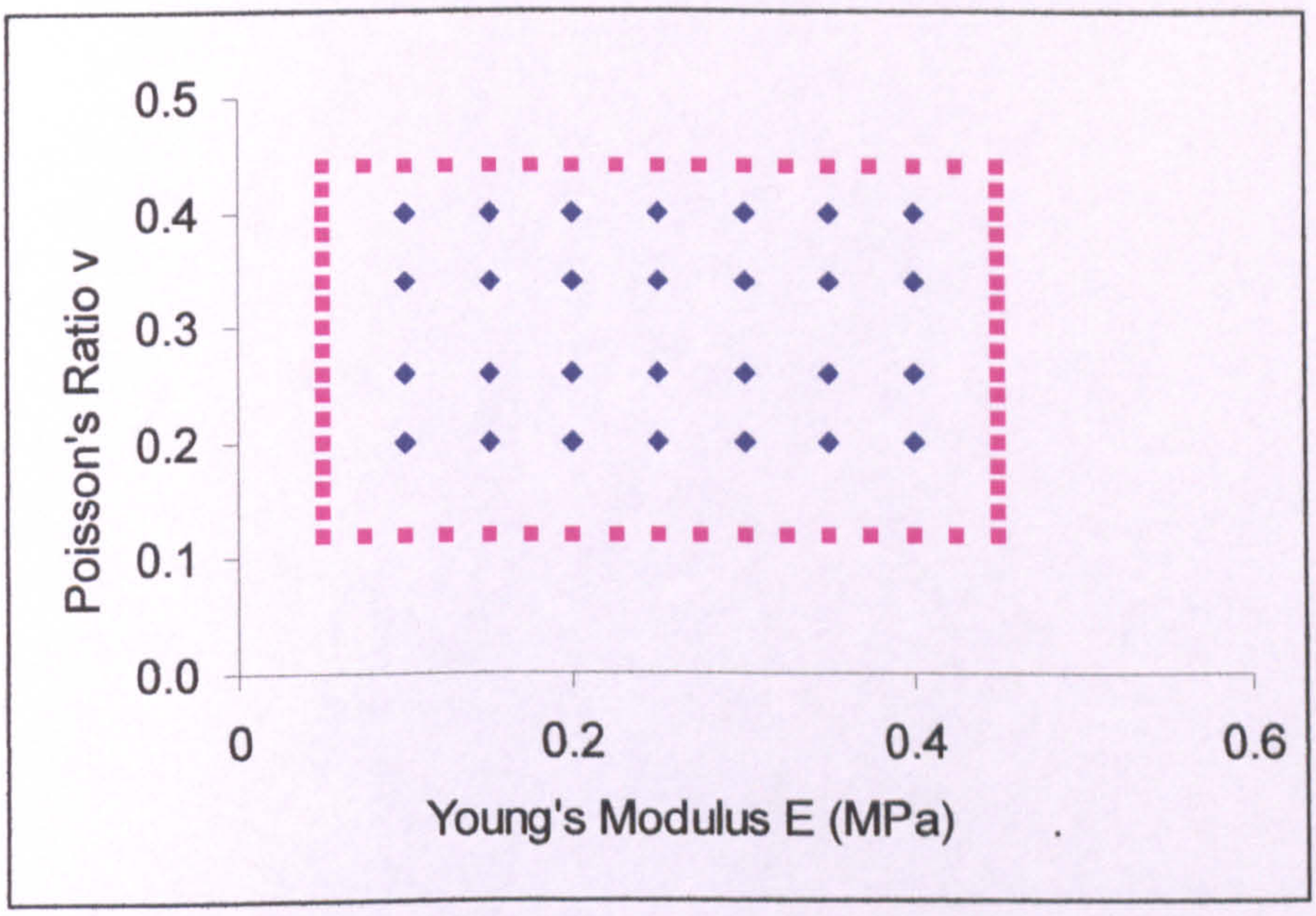


**Figure 3.12** Matrix of initial guessed values used to study the effect of initial values on the convergence of the program.

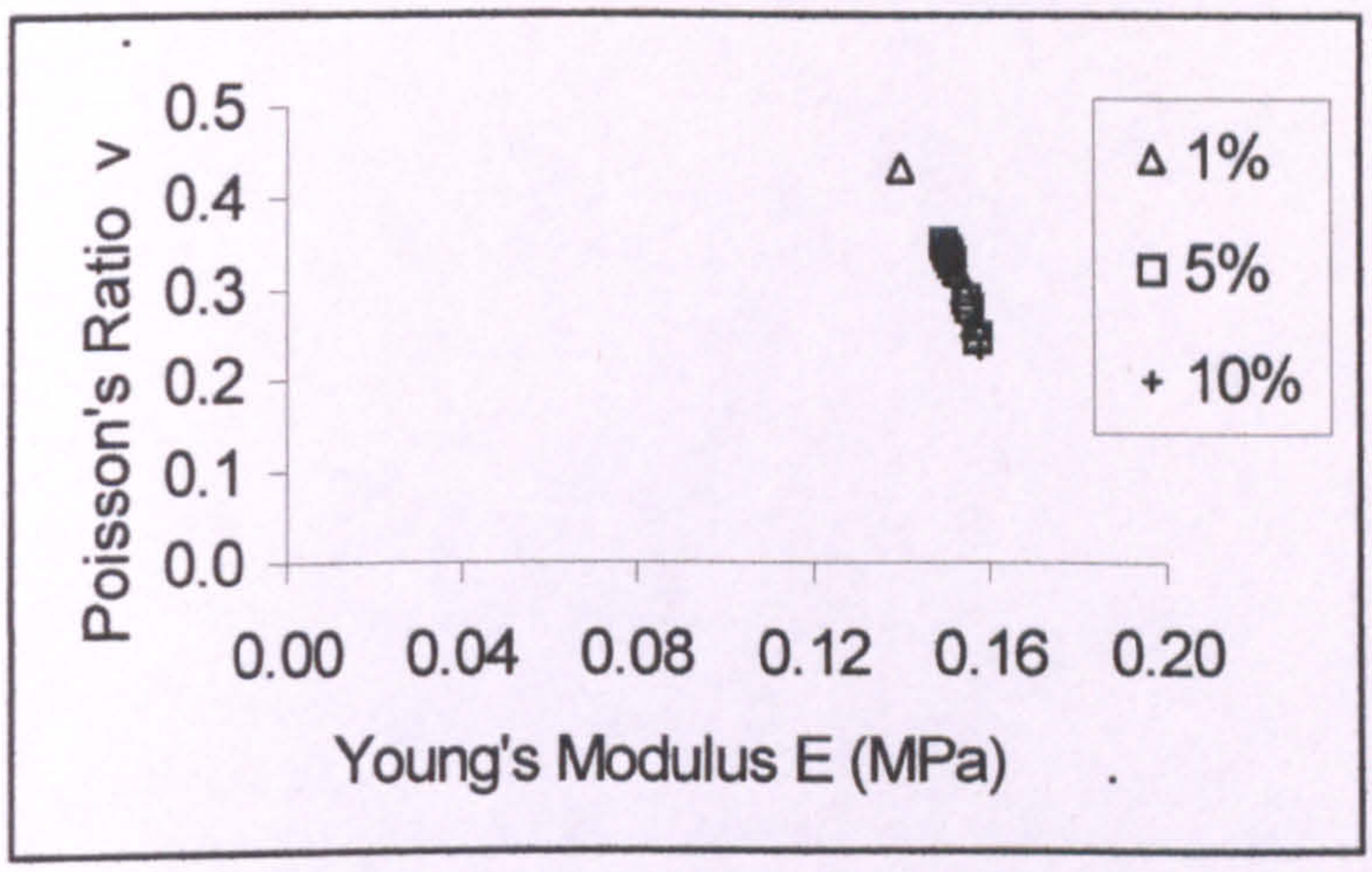


(a) Converged results based on the constant error method.

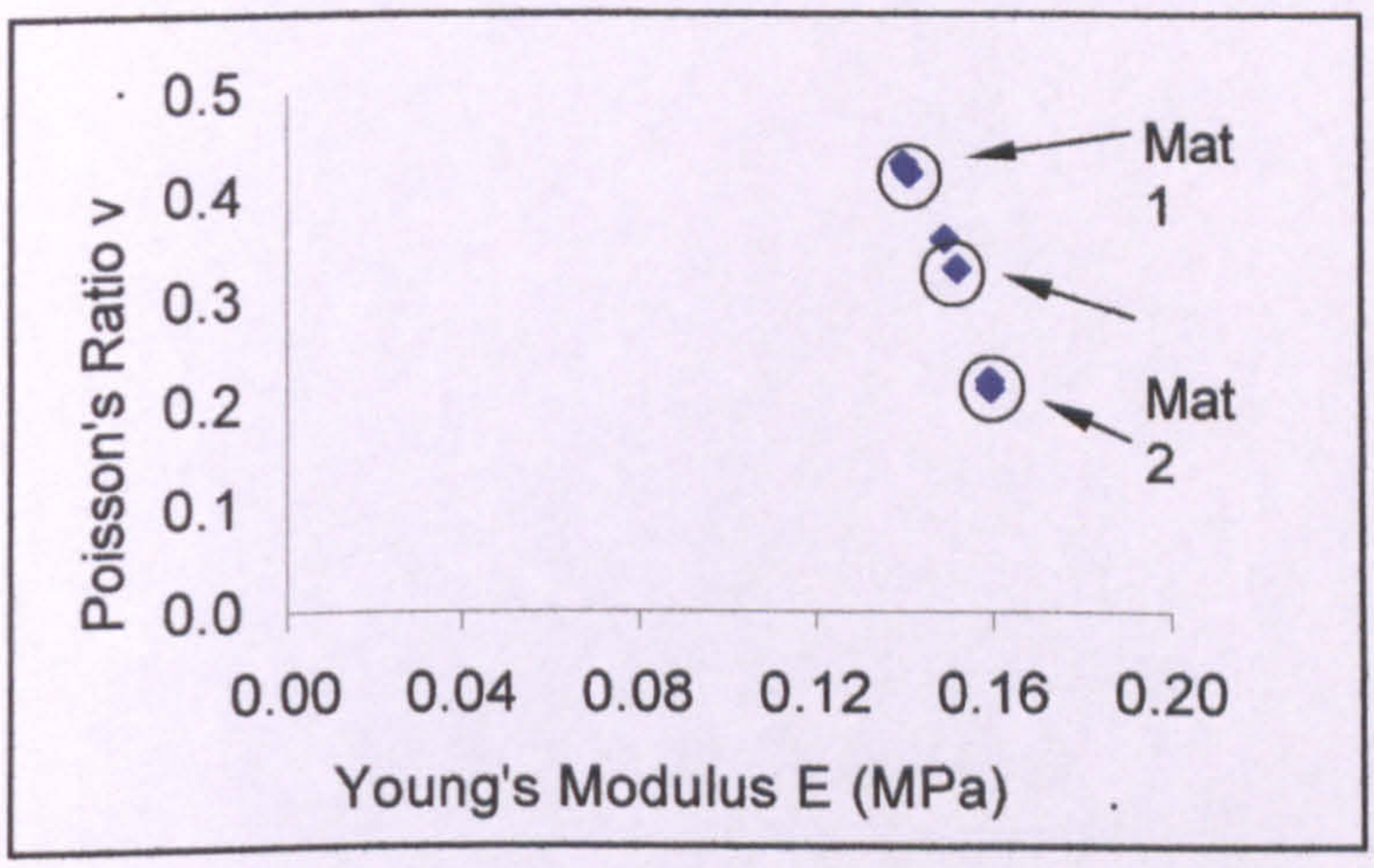


(b) Converged results based the random error method.

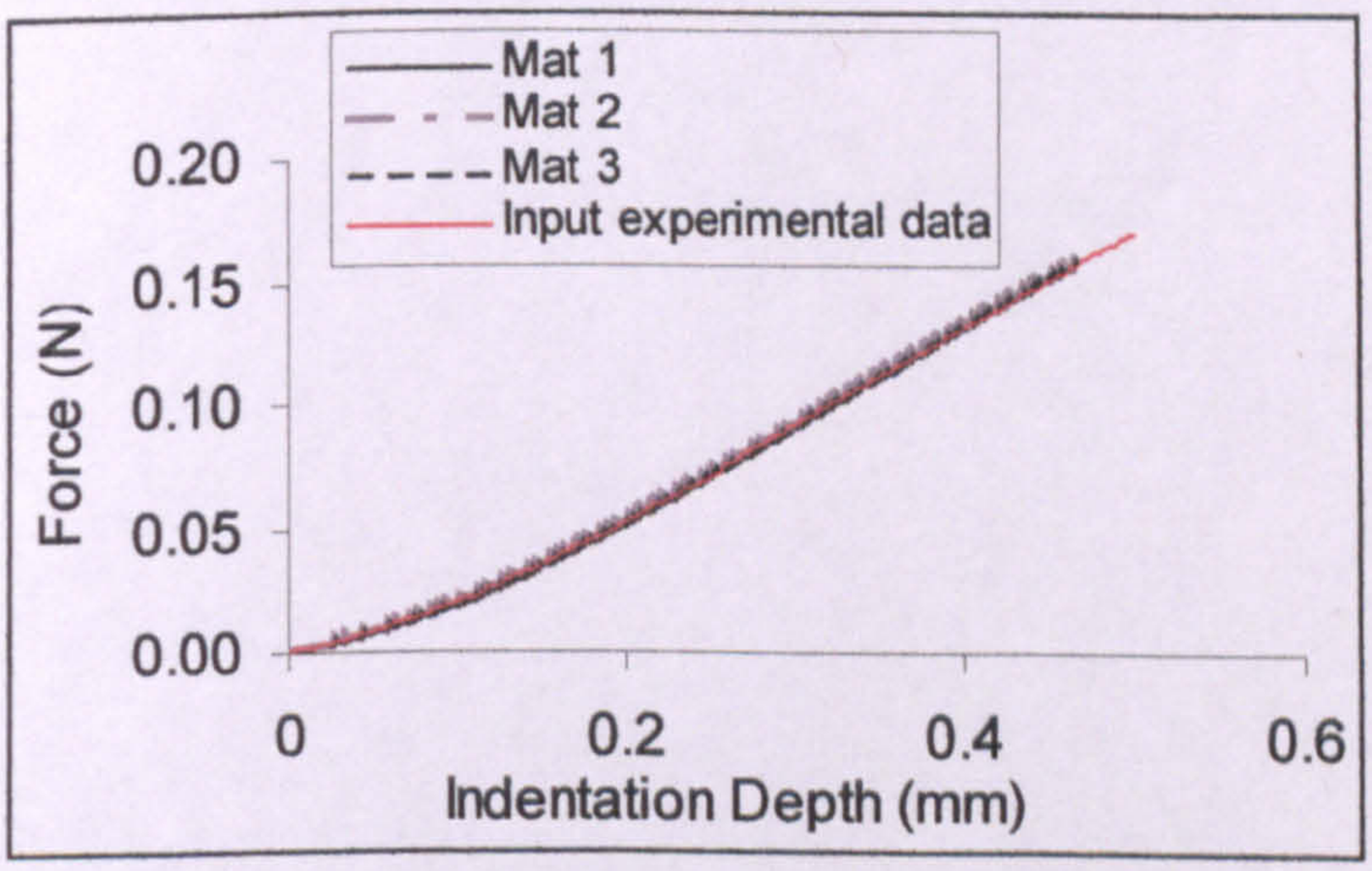


(c) Comparison between predicted indentations curves using the converged parameters (Mat 1-3 in (b)) and the original input experimental data.

**Figure 3.13** Converged results with different initial values based on the single indenter method.

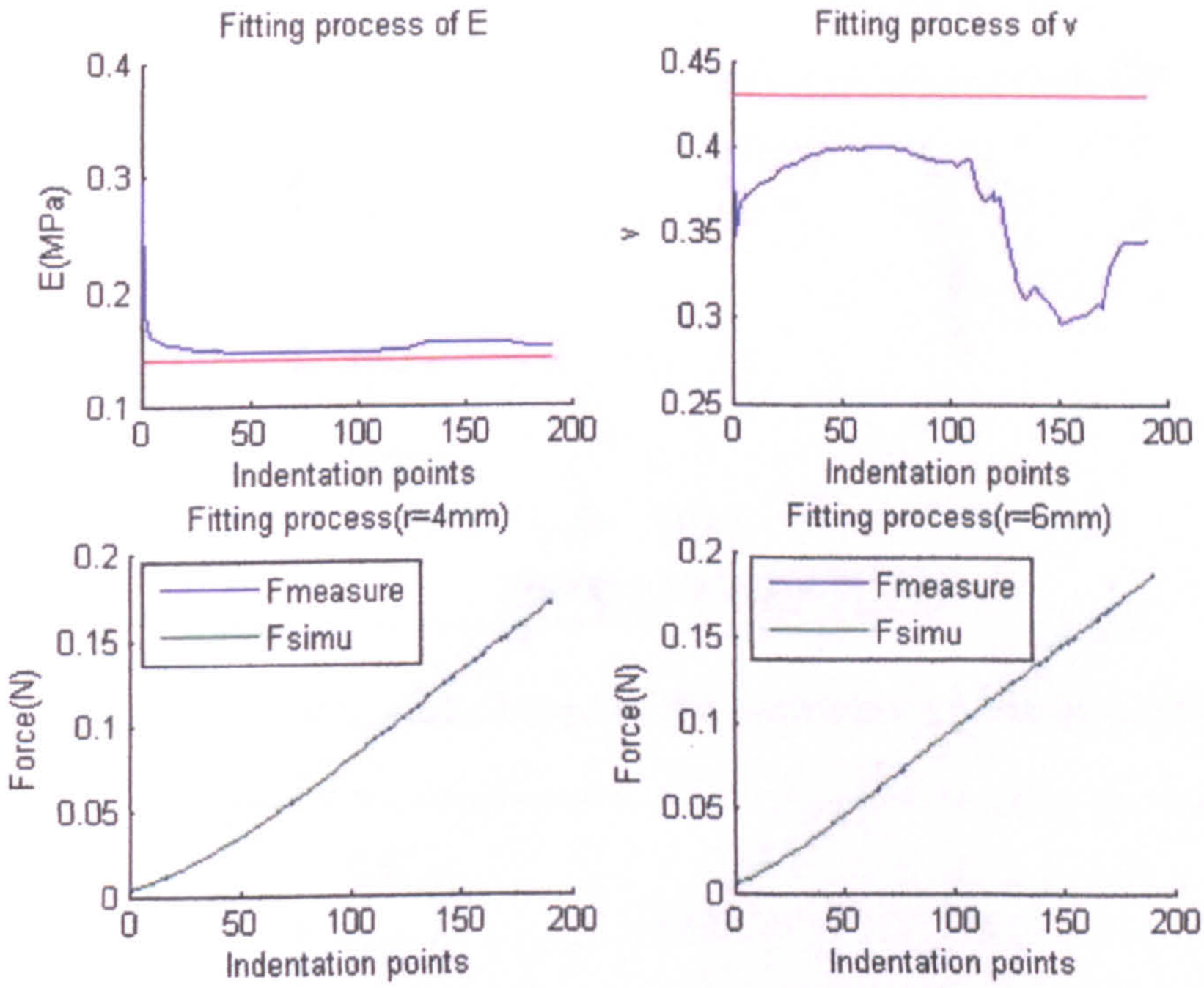


(a) Parameters searching process with a constant error (R=4mm, 6 mm).

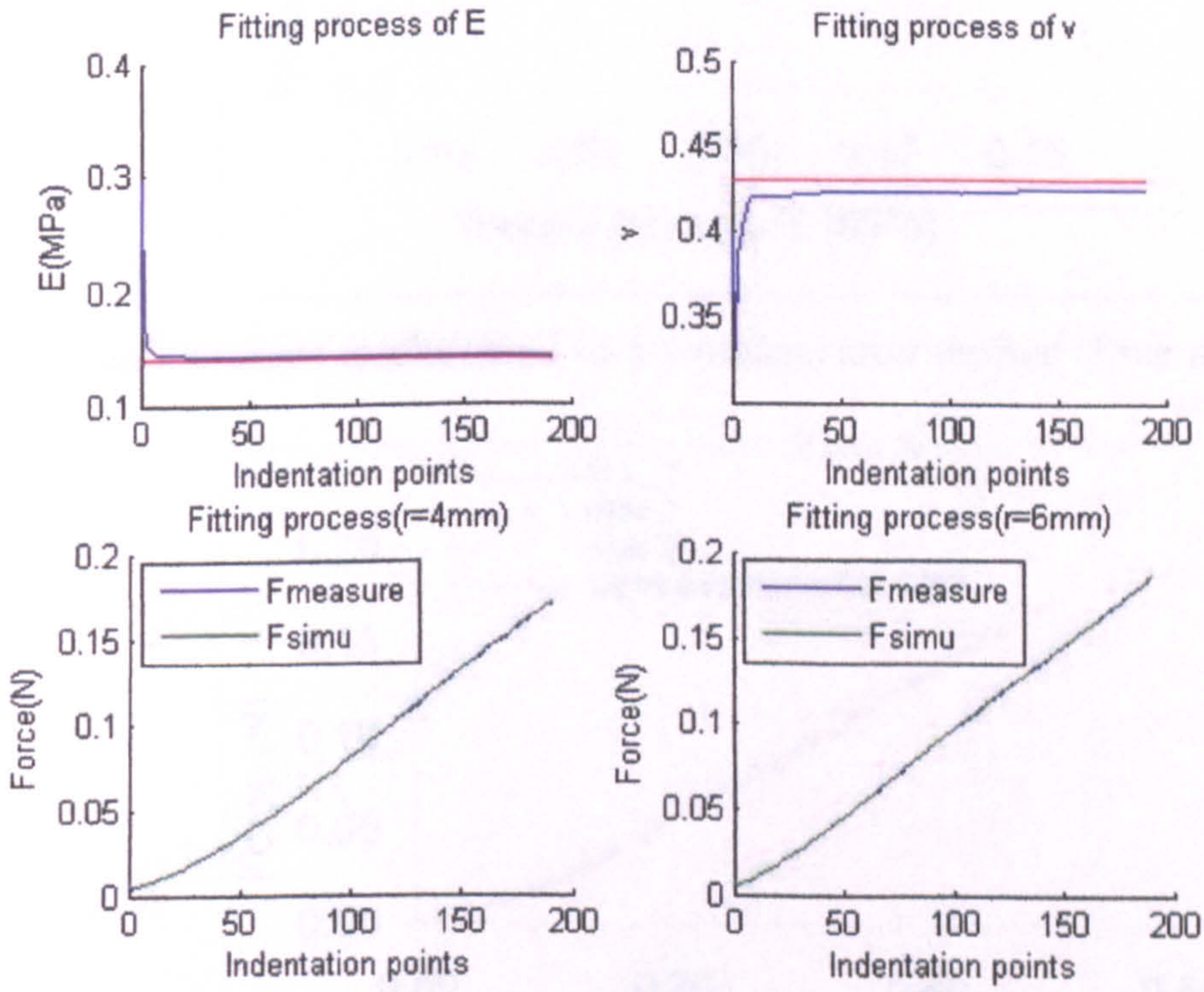


(b) Parameters searching process with Random error (R=4mm, 6 mm).

**Figure 3.14** Typical material parameter fitting curves for two indenters (a) Constant error method; (b) Random error method. (The true material properties are $E_T$=0.14, $v_T$=0.43; the initial guessed value are $E_0$=0.30 MPa and $v_0$=0.40).

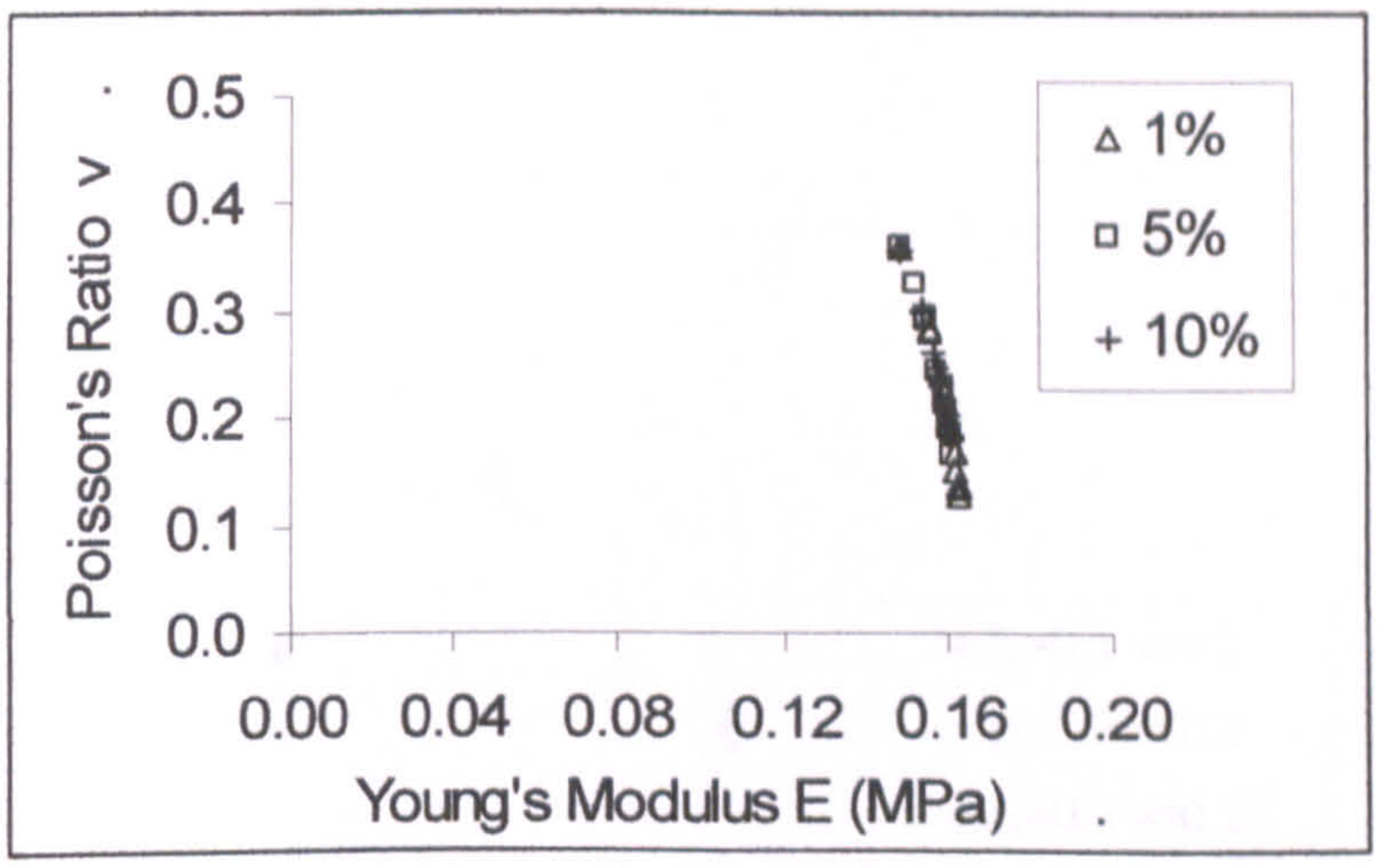


(a) Converged results based on the constant error method (Dual indenters).

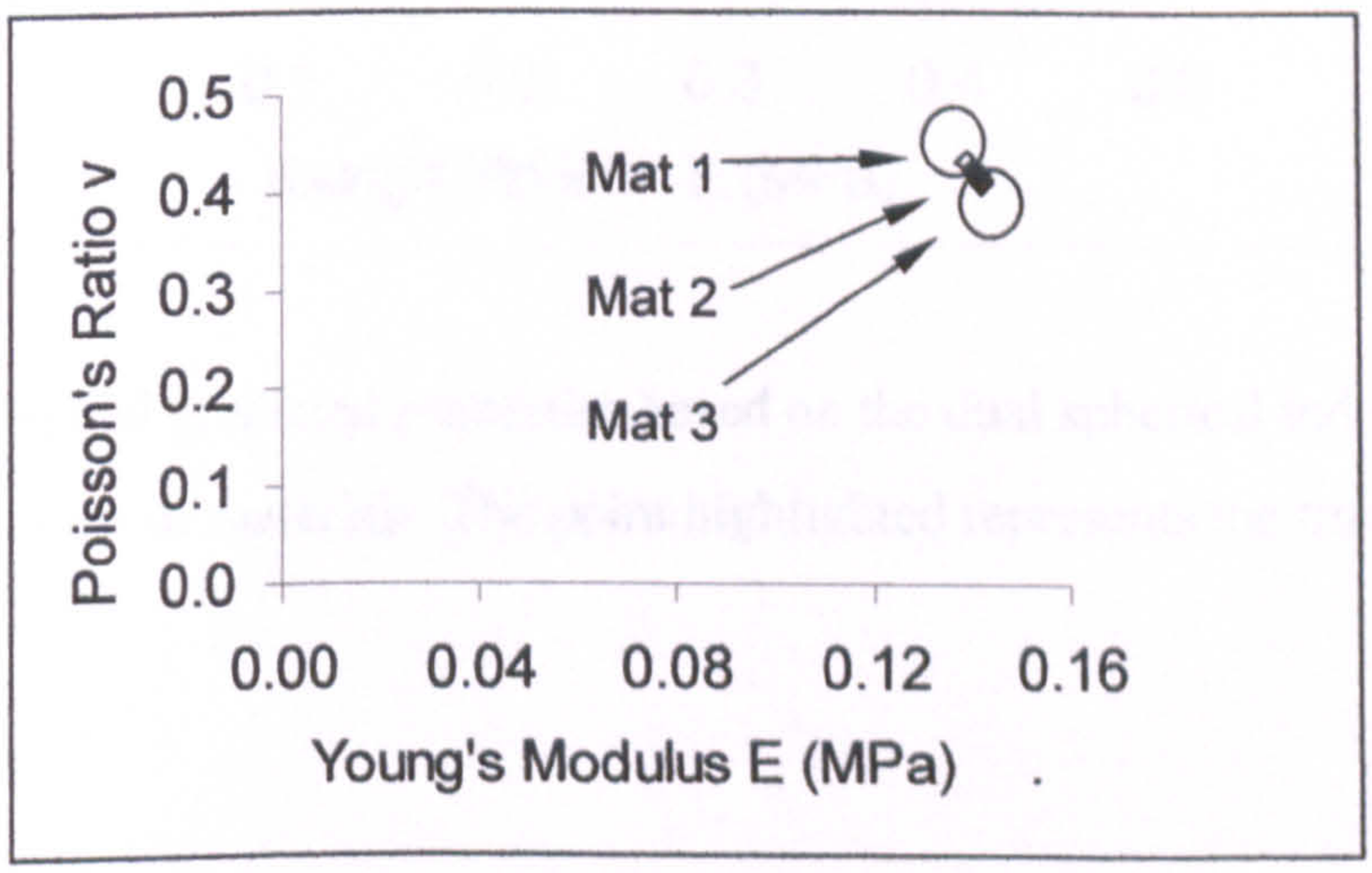


(b)Converged results based on the random error method (Dual indenters).

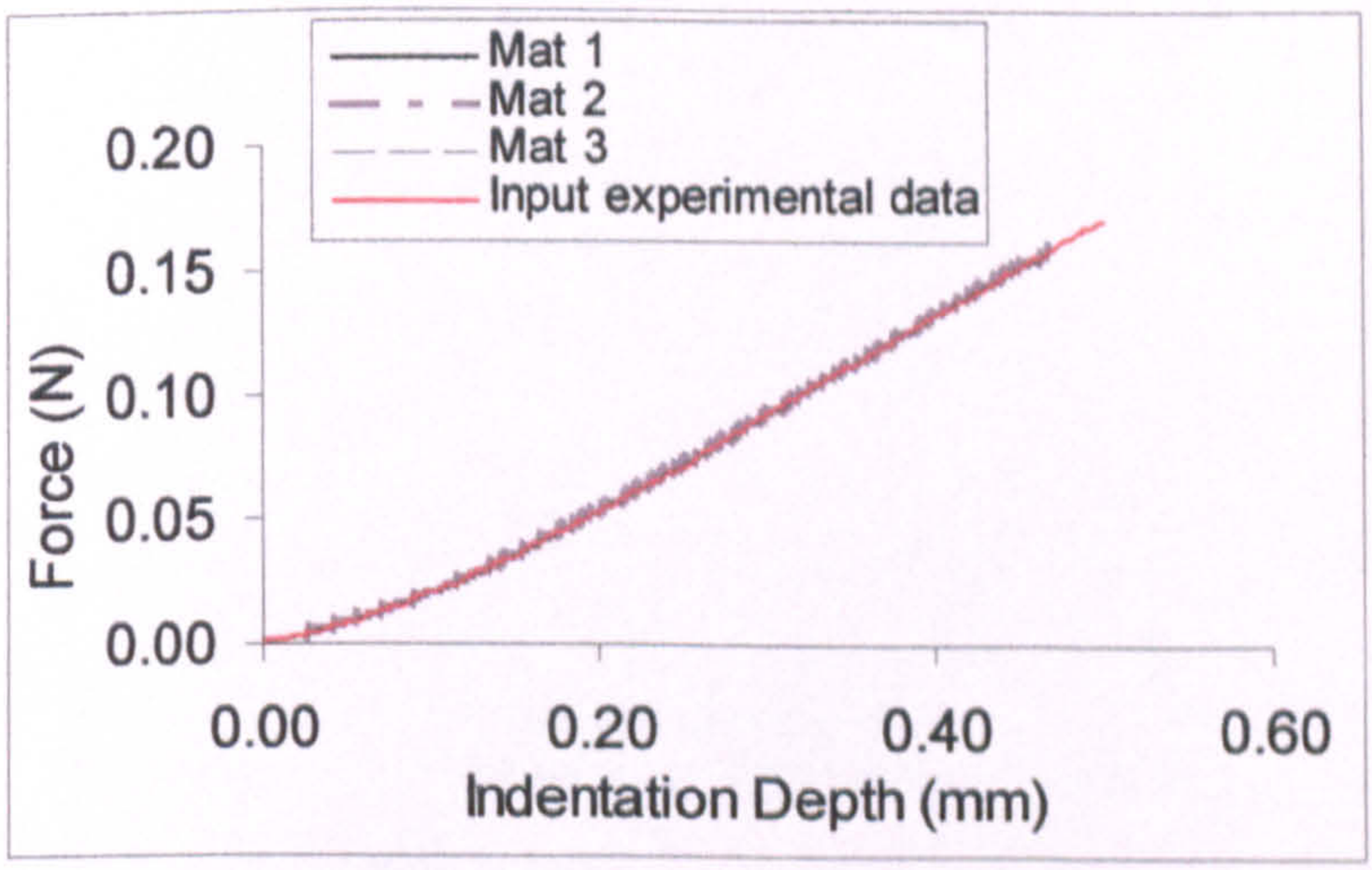


(c)Comparison between predicted indentation curves using converged parameters (Mat 1-3 in (b)) and the original input experimental data.

**Figure 3.15** Converged results with different initial values based on the dual indenters method.

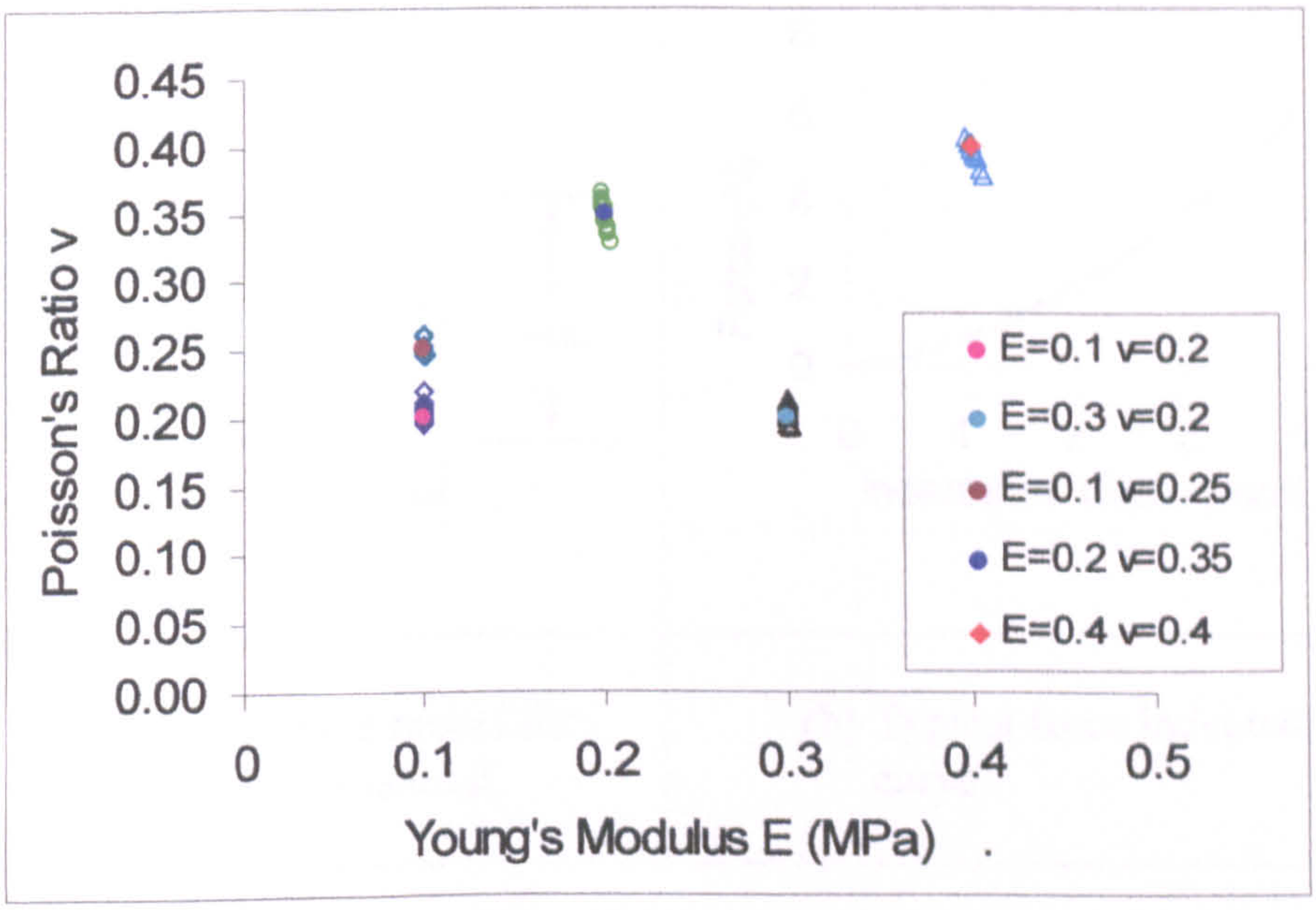


**Figure 3.16** Typical predicted properties based on the dual spherical indenters approach for a range of materials. The point highlighted represents the true material data.

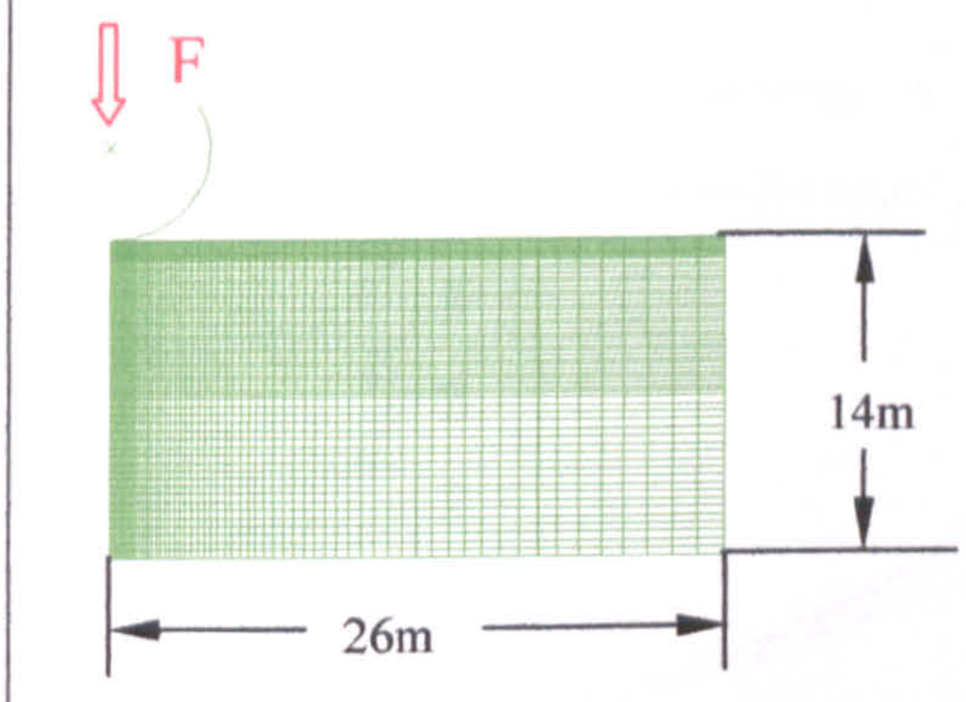


(a) FE indentation model for hyperelastic material.

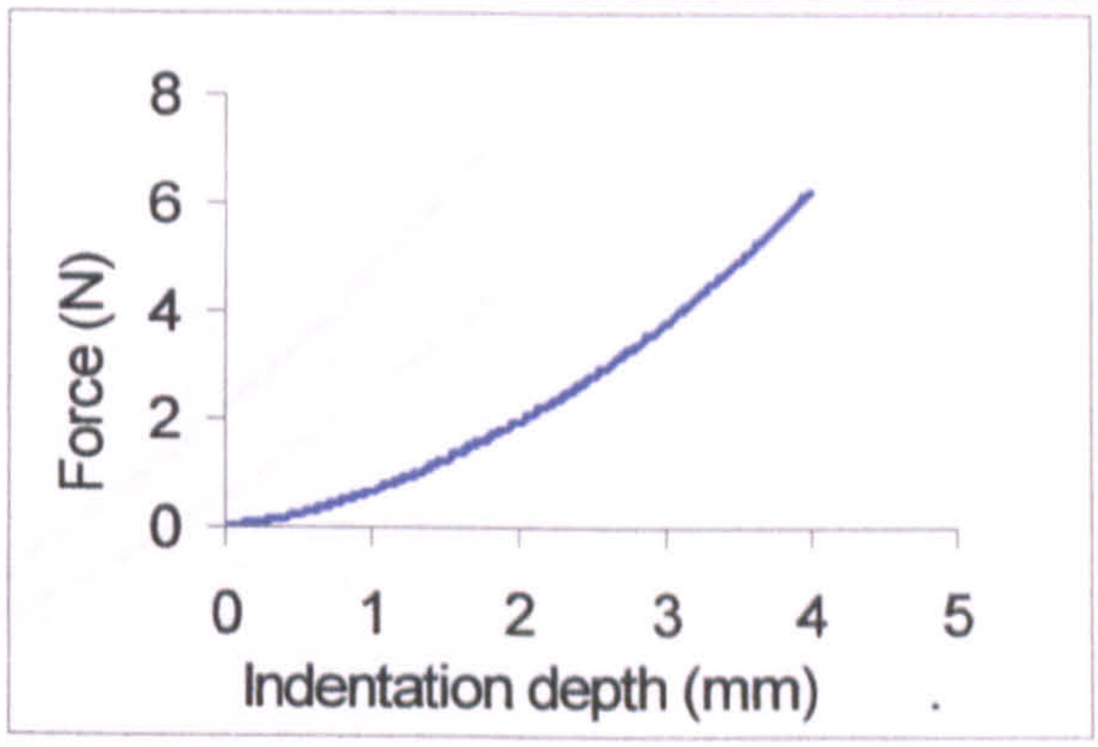


(b) Typical force indentation depth curve.

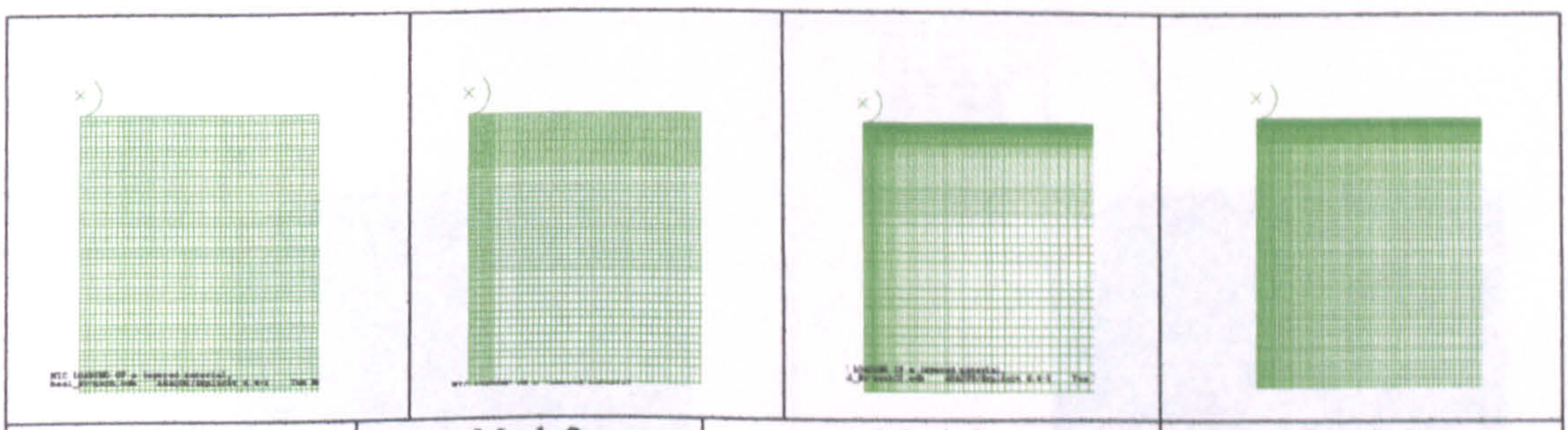

| Mesh 1 | Mesh 2 | Mesh 3 | Mesh 4 |
|---|---|---|---|

(c) FE model of indentation process with different mesh densities.

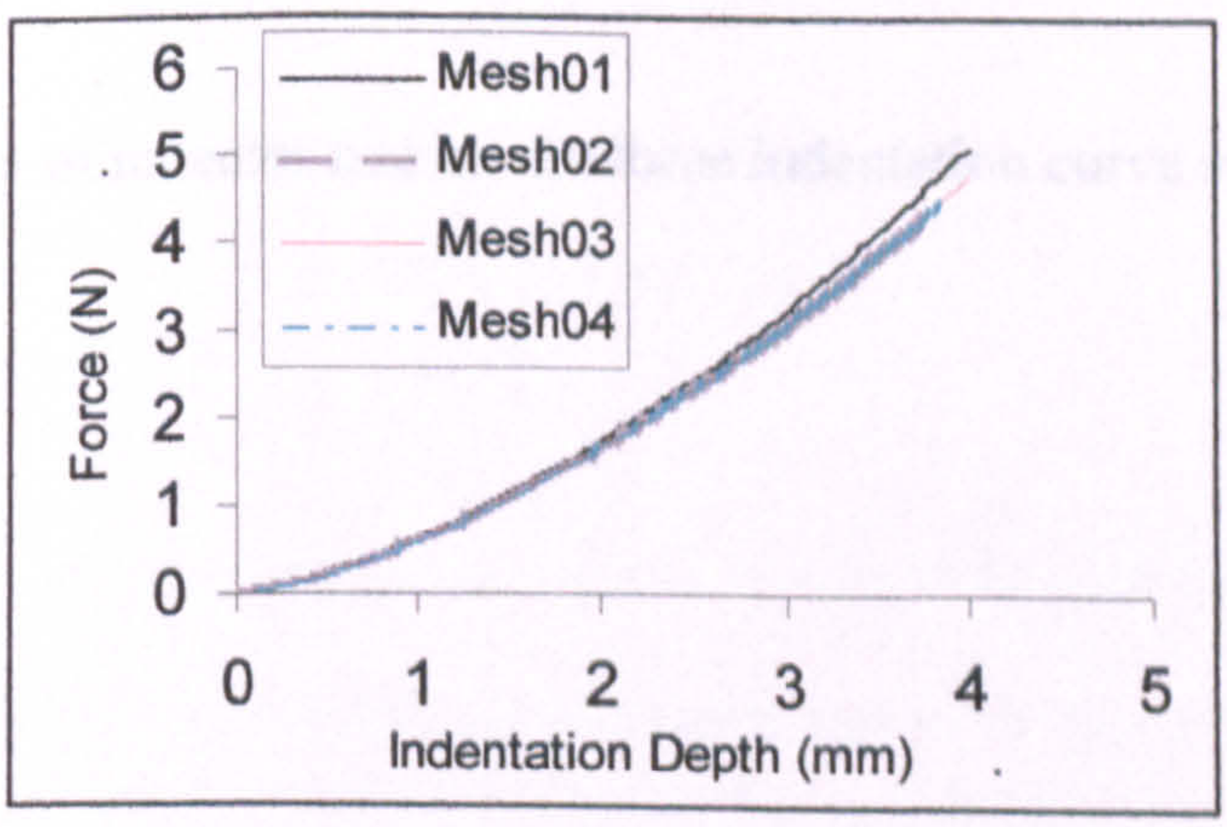


(d) Mesh density effects (R=4mm).

**Figure 3.17** FE indentation model of a hyperelastic material, typical force-indentation depth (*p*-*h*) curve and effect of meshing schemes.

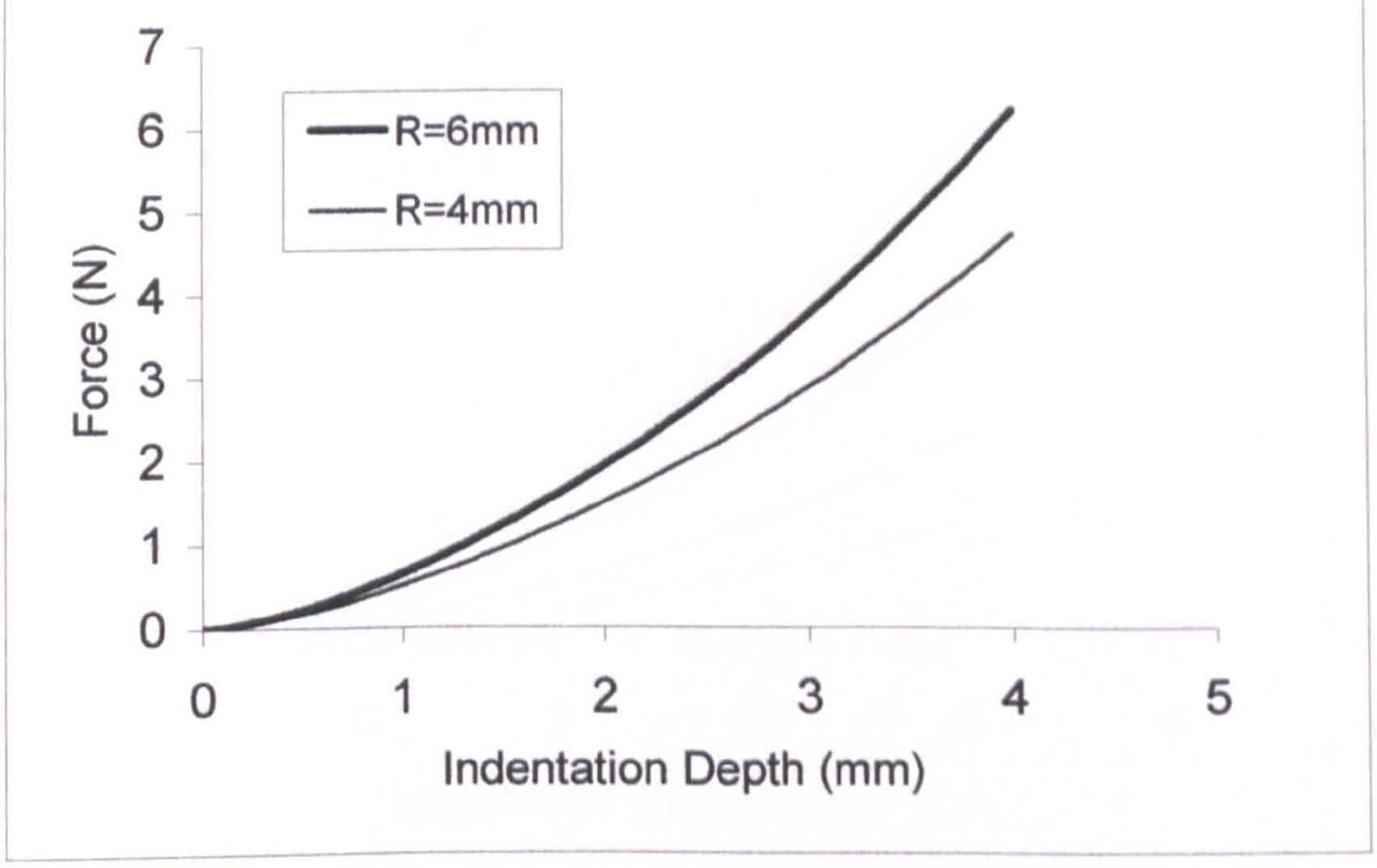


(a) Indentation curves for different indenter sizes. ($\mu$=0.07, $\alpha$=6.2)

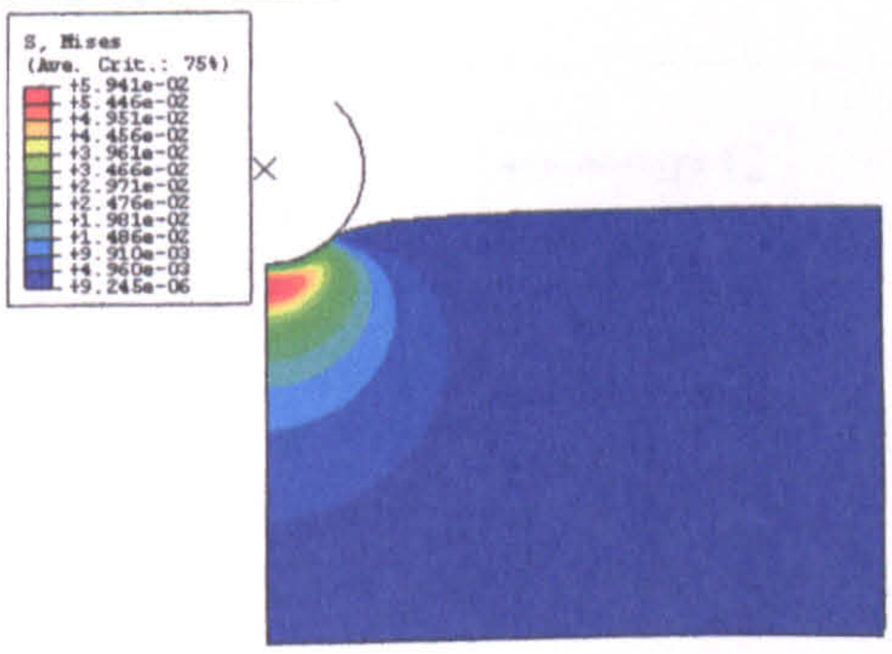


(b) R=4mm

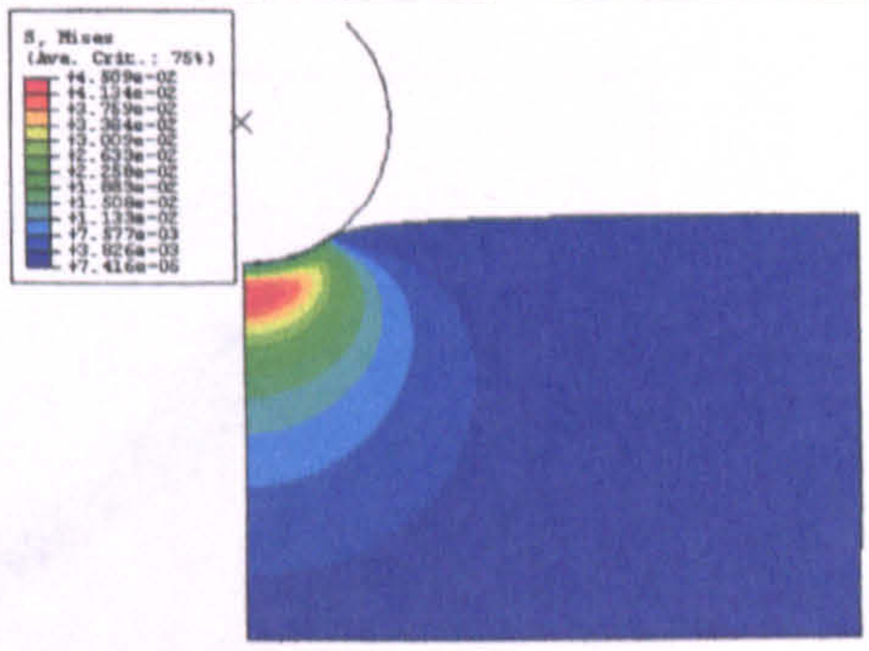


(c) R=6mm

**Figure 3.18** Effect of indenter size on the force indentation curve and stress distribution.

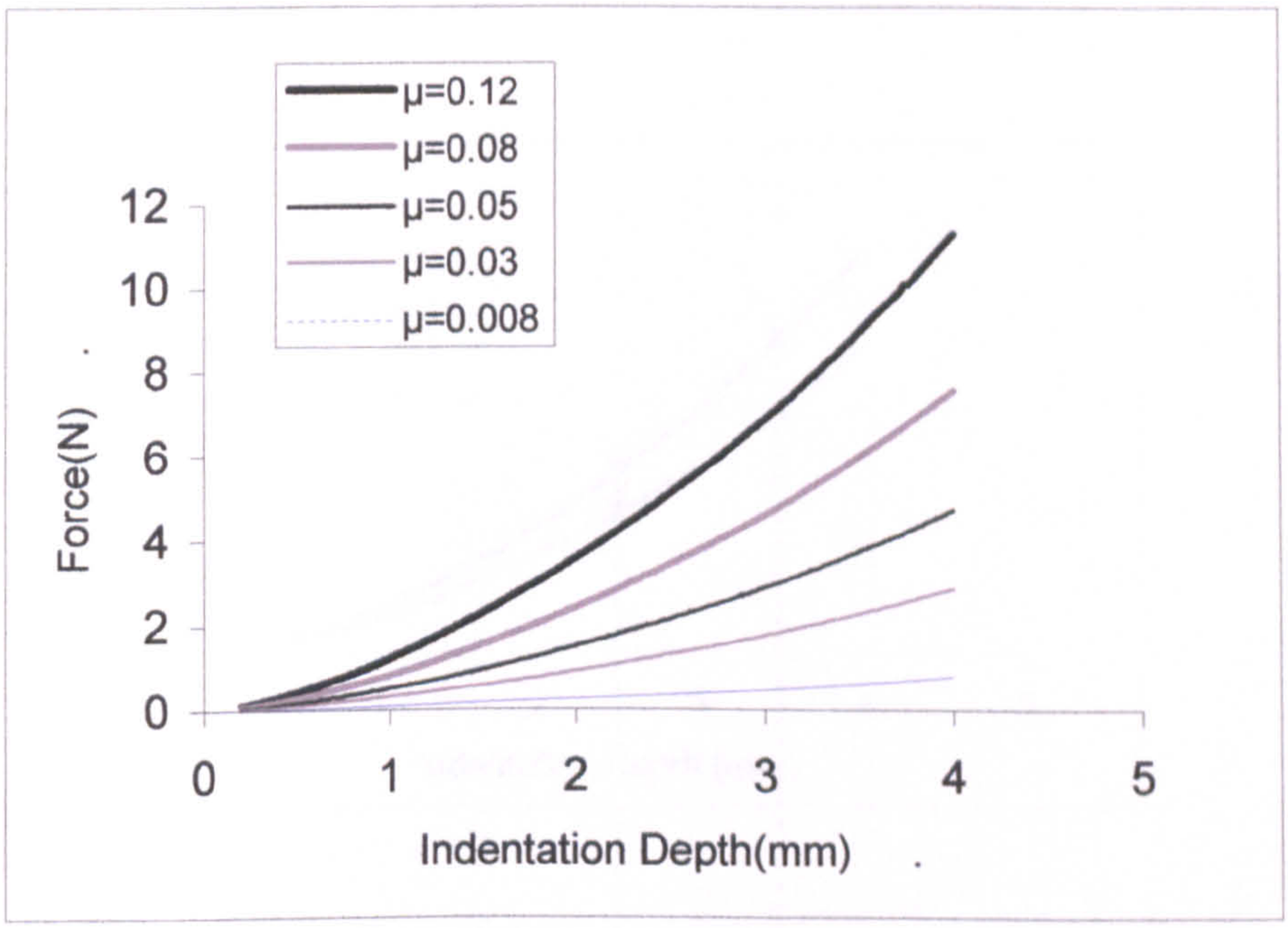


(a) Effect of the hyperelastic parameter 'μ' on the force-indentation depth data.

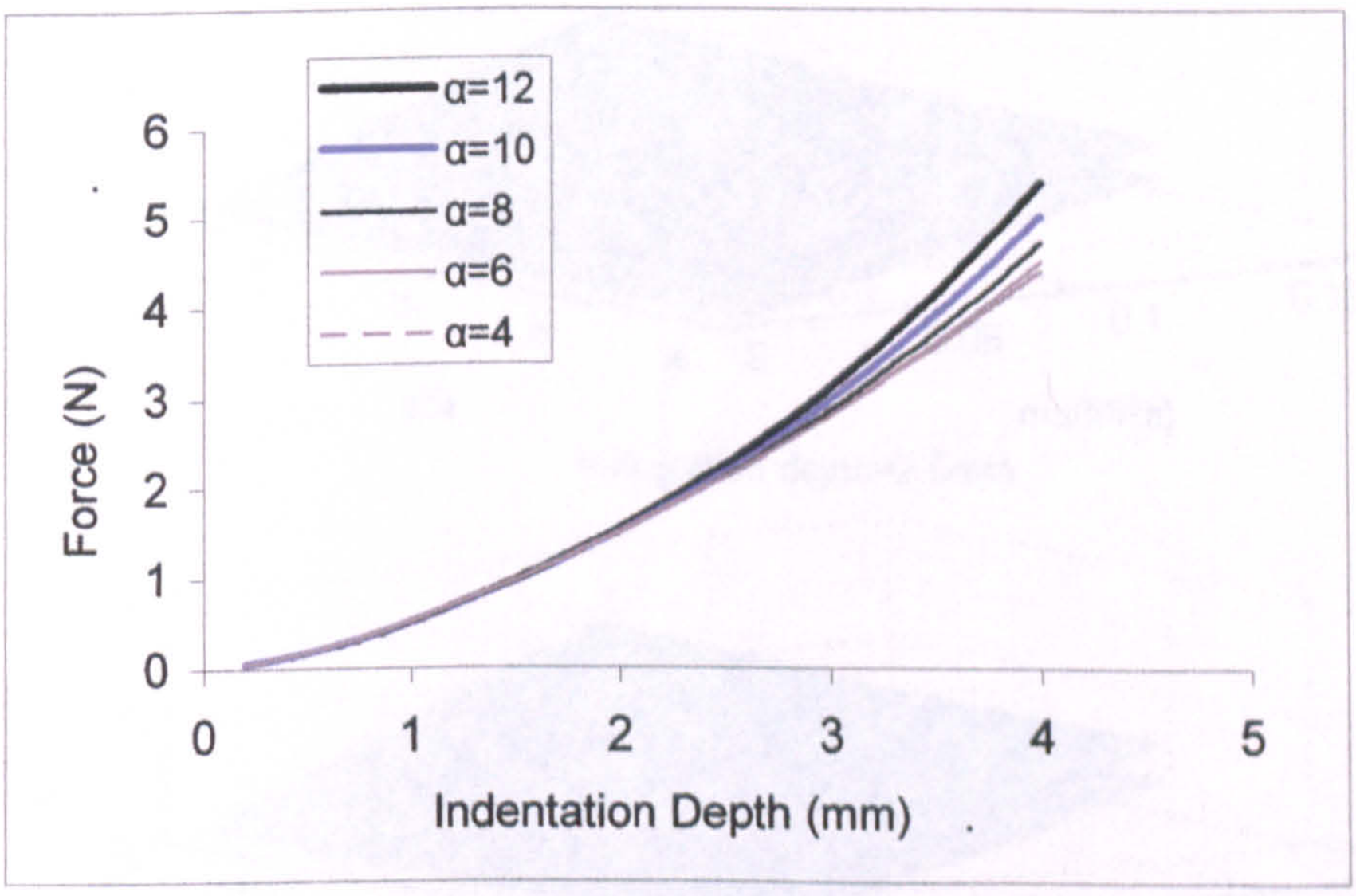


(b) Effect of the hyperelastic parameter 'α' on the force-indentation depth data.

**Figure 3.19** Effects of the material parameters (μ and α) on the force-indentation depth relationship.

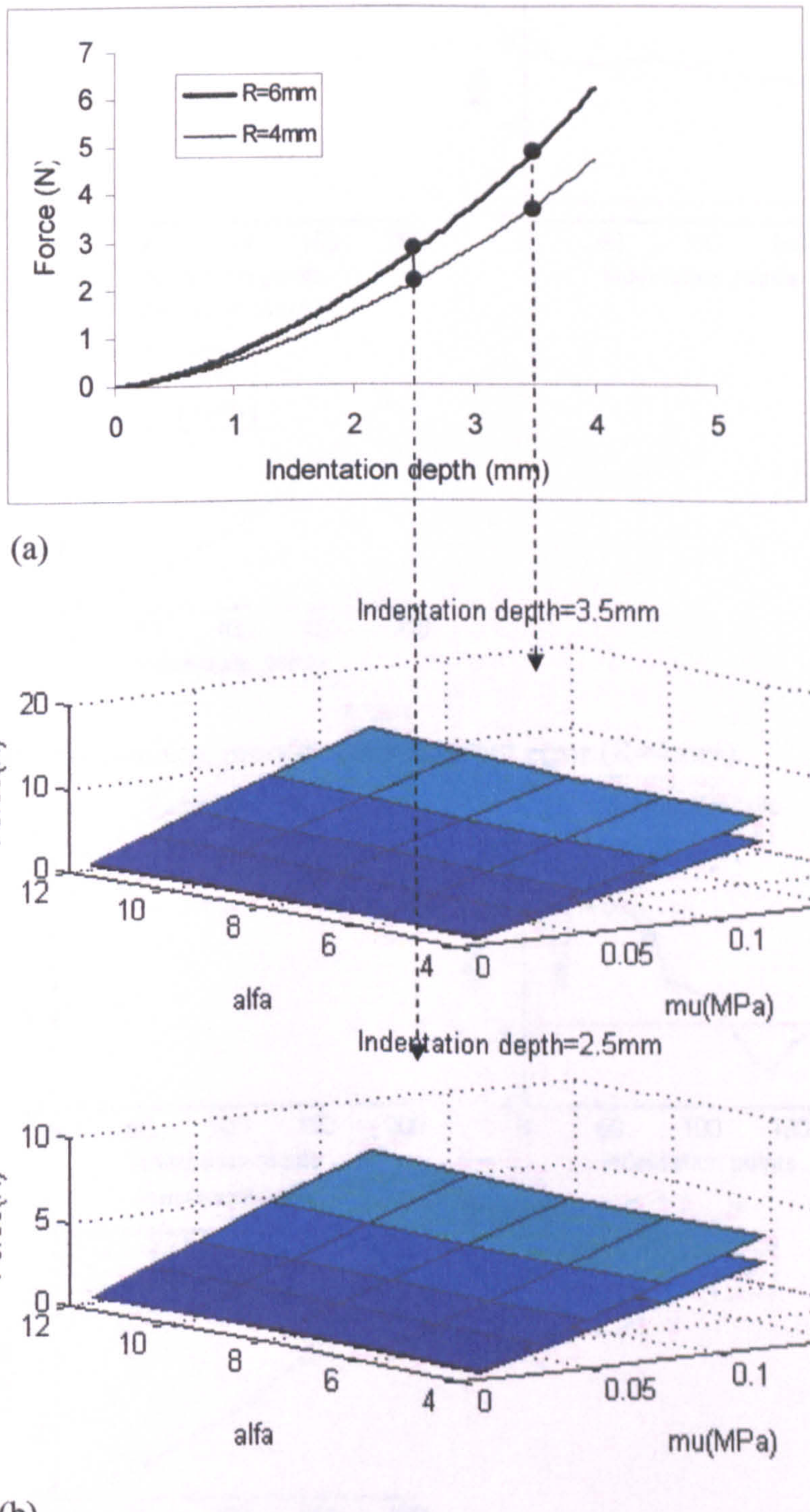


**Figure 3.20** Typical numerical experimental data with different indenter size and simulation surfaces at indentation depth of 2.5mm and 3.5mm.

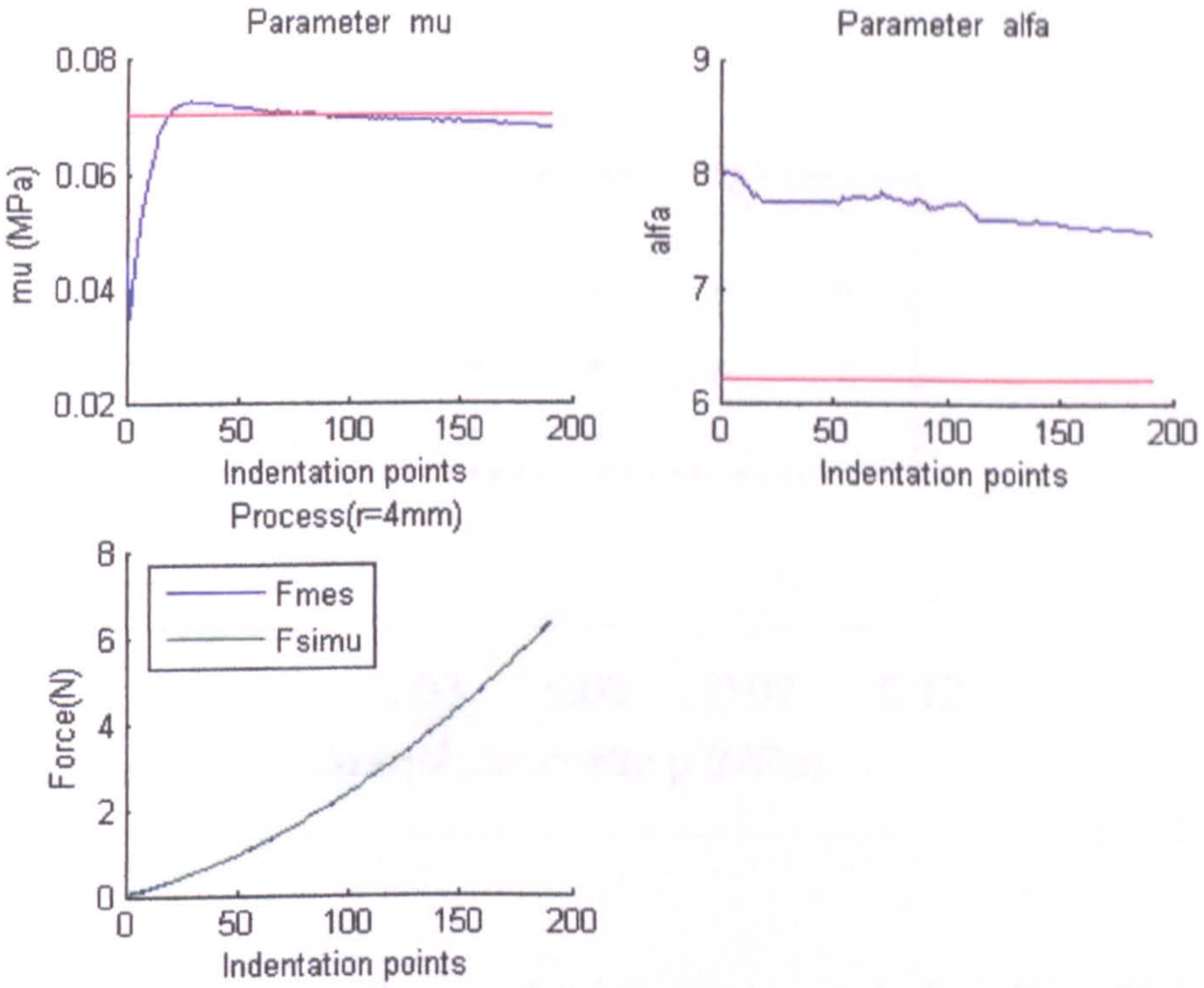


(a) Parameters searching process with constant error (R=4mm).

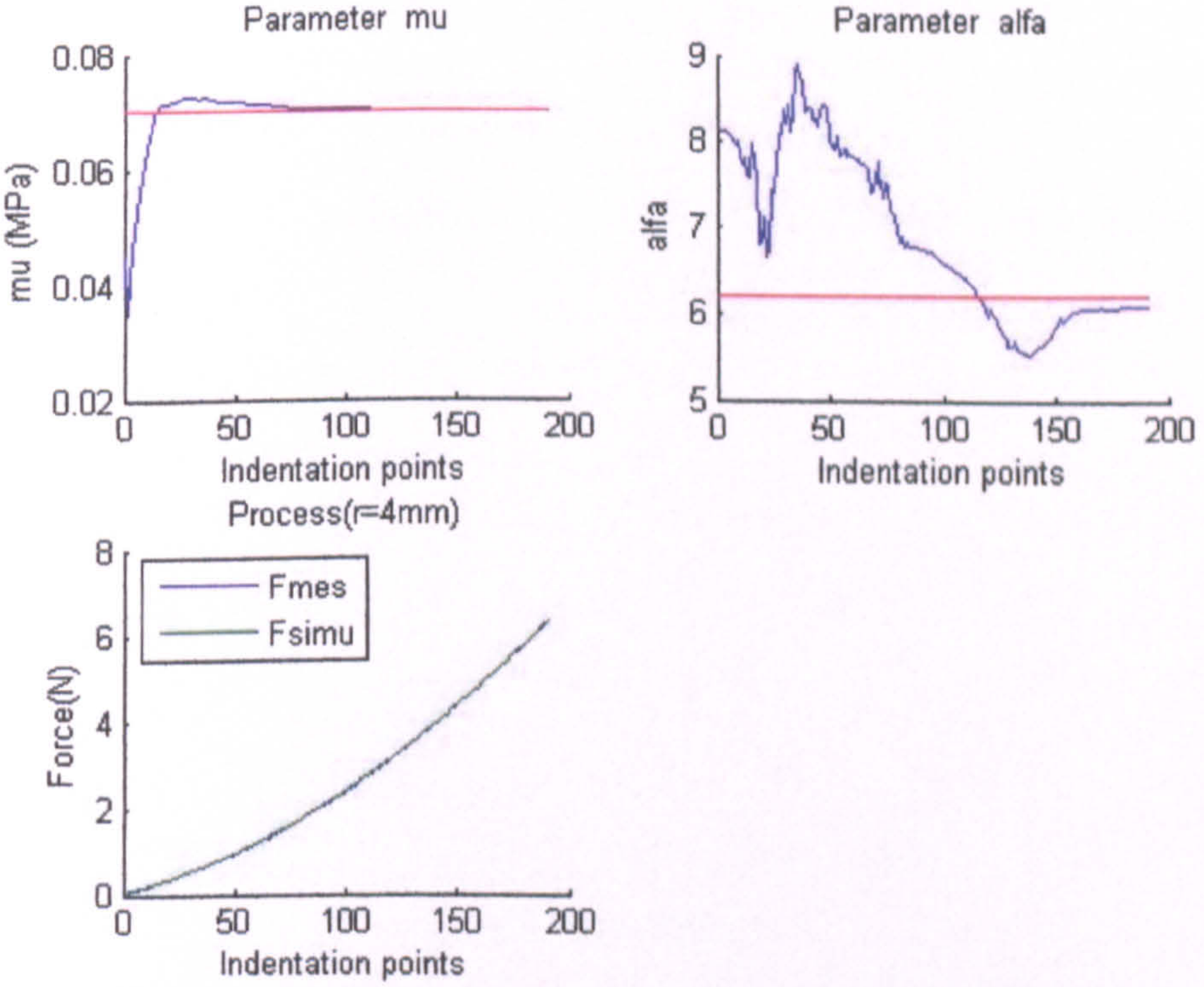


(b) Parameters searching process with random error (R=4mm).

**Figure 3.21** Typical material parameter fitting curves for the single indenter method. (Hyperelastic model, the true material properties are $\mu_T$=0.07, $\alpha_T$=6.2; the initial guessed value used are $\mu_0$=0.04 MPa and $\alpha_0$=8.0).

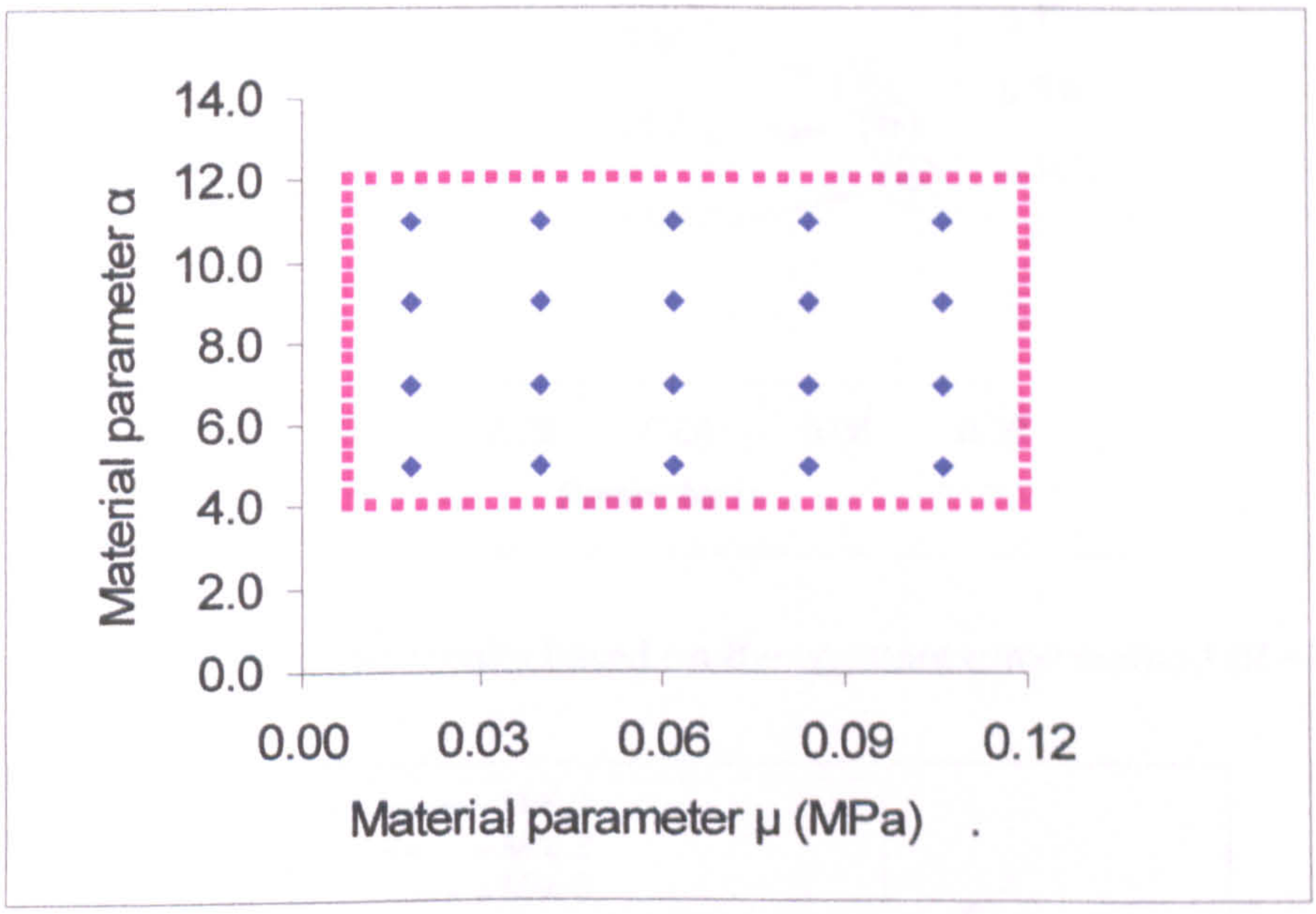


**Figure 3.22** Matrix of initial guessed values used to study the effect of initial value on the convergence of the program.

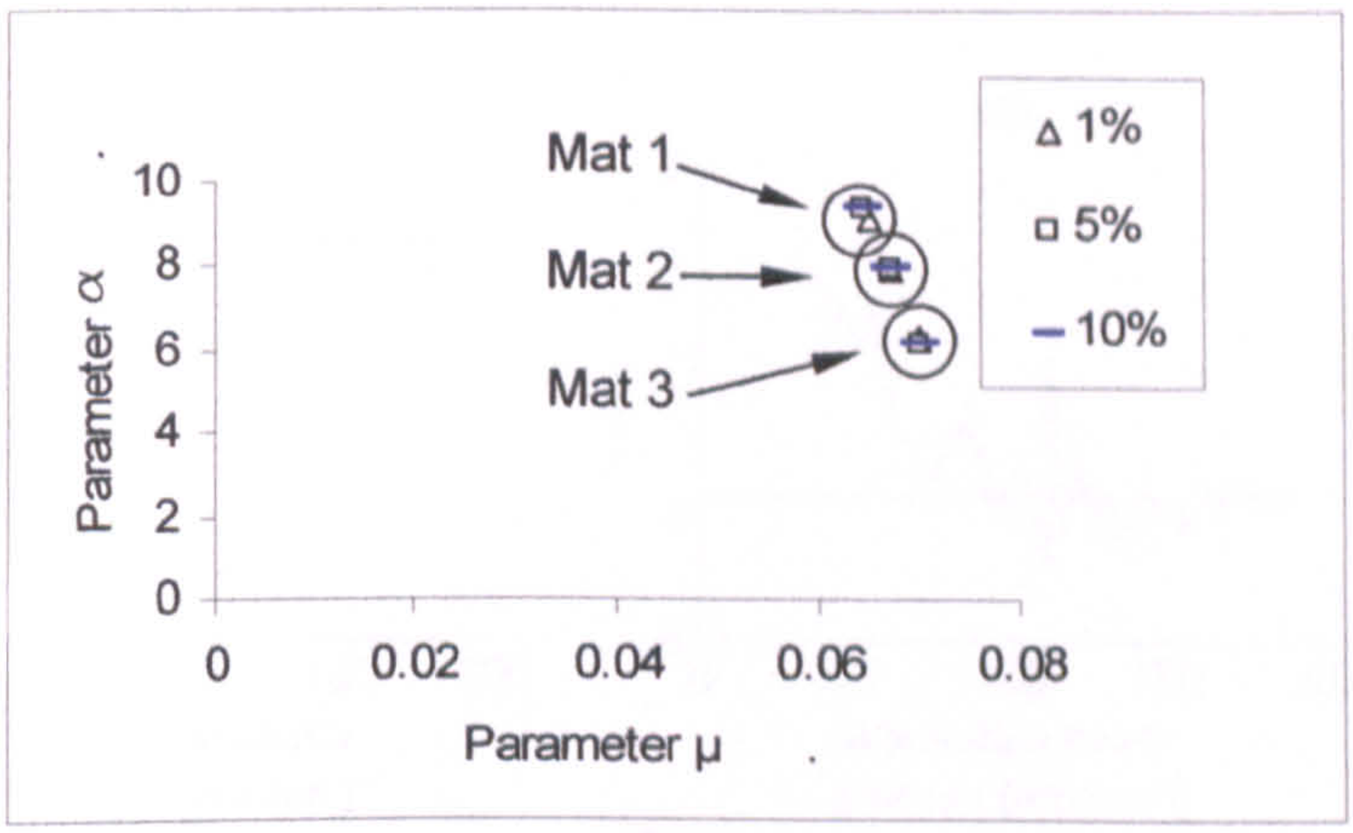


(a) Converged results based on the constant error method (R=4mm).

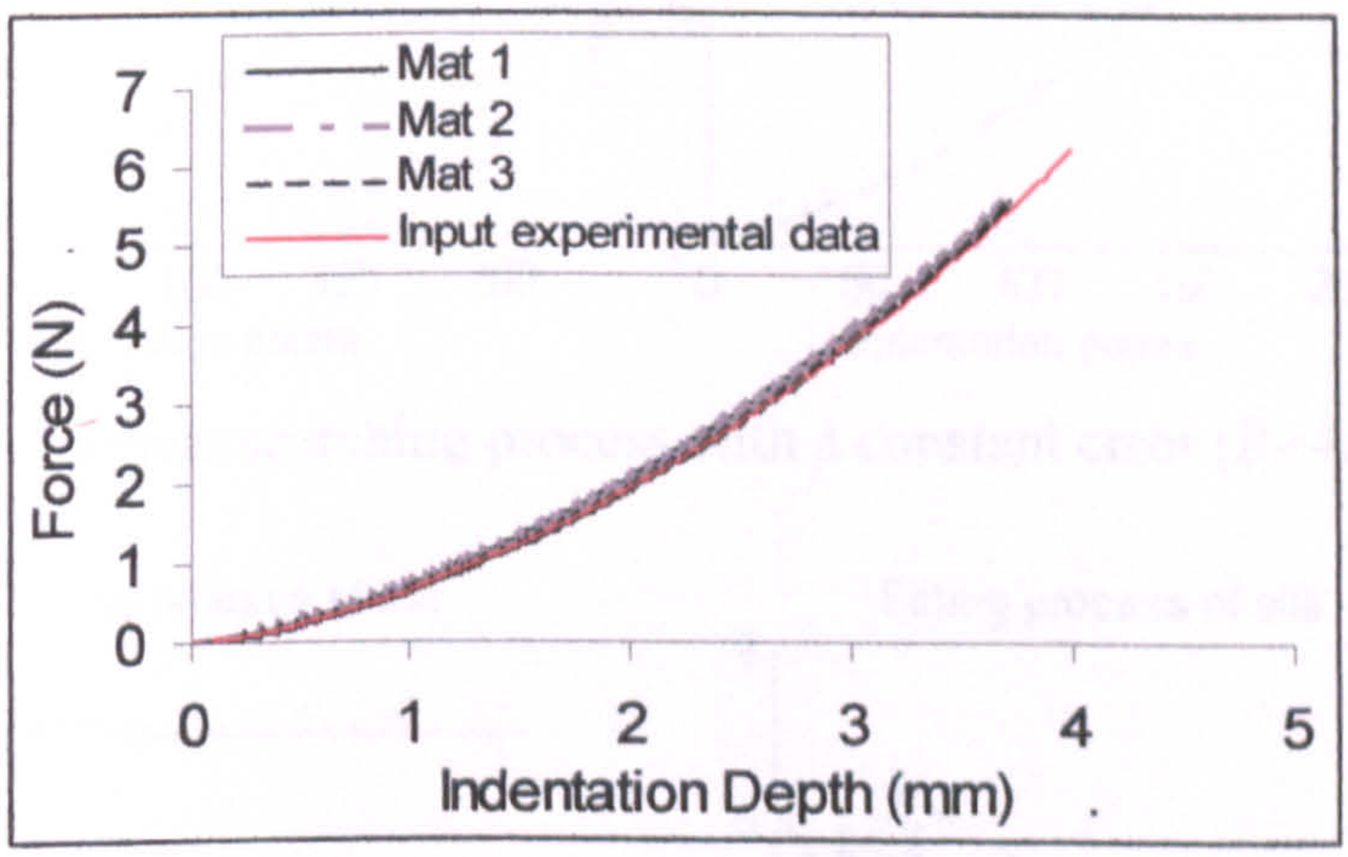


(b) Comparison between predicted indentation curves using converged parameters (Mat 1-3 in (a)) and the original input experimental data.

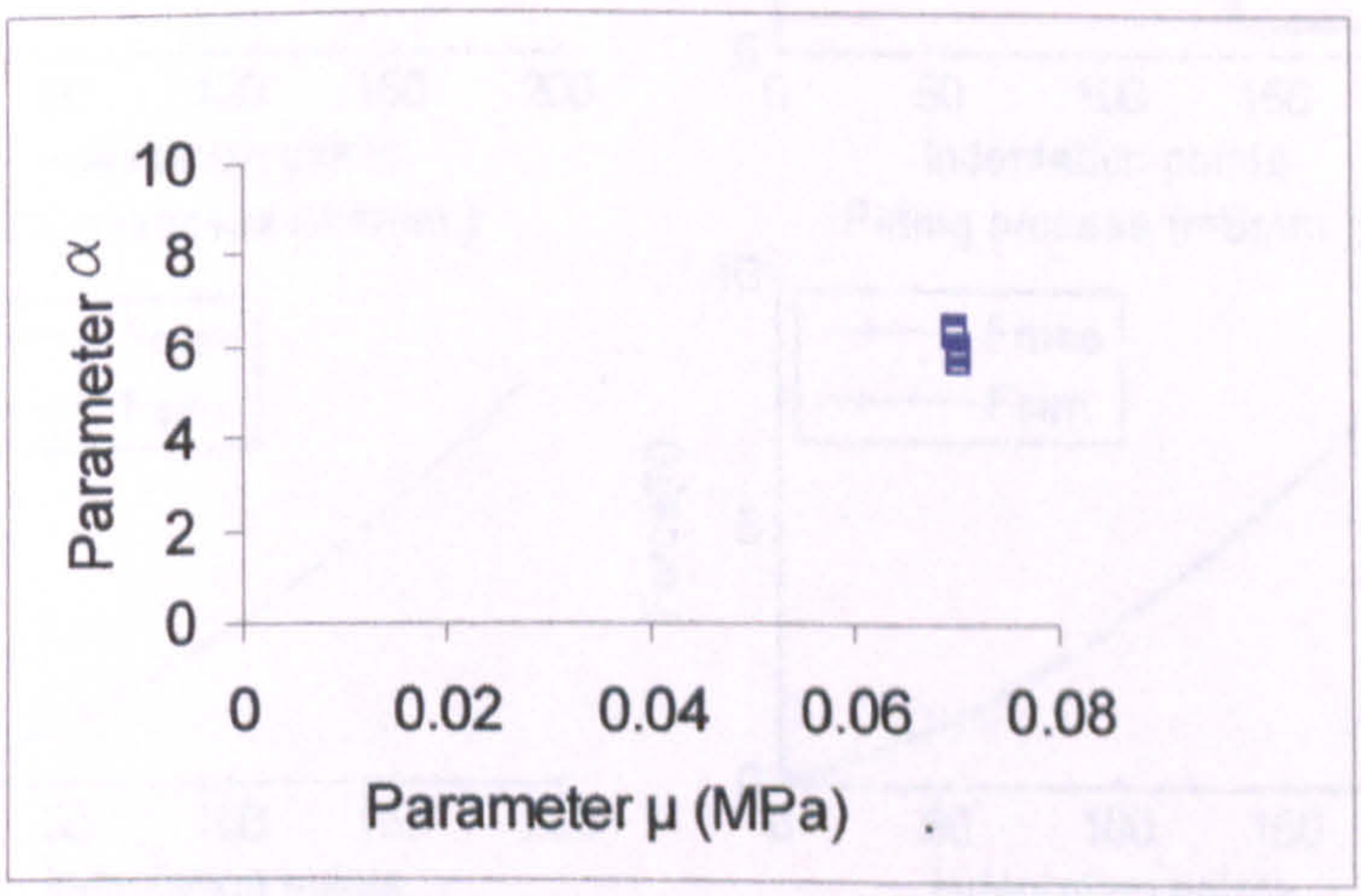


(c) Converged results based on the random error method (R=4mm).

**Figure 3.23** Converged results with different initial values based on the single indenter method for hyperelastic materials.

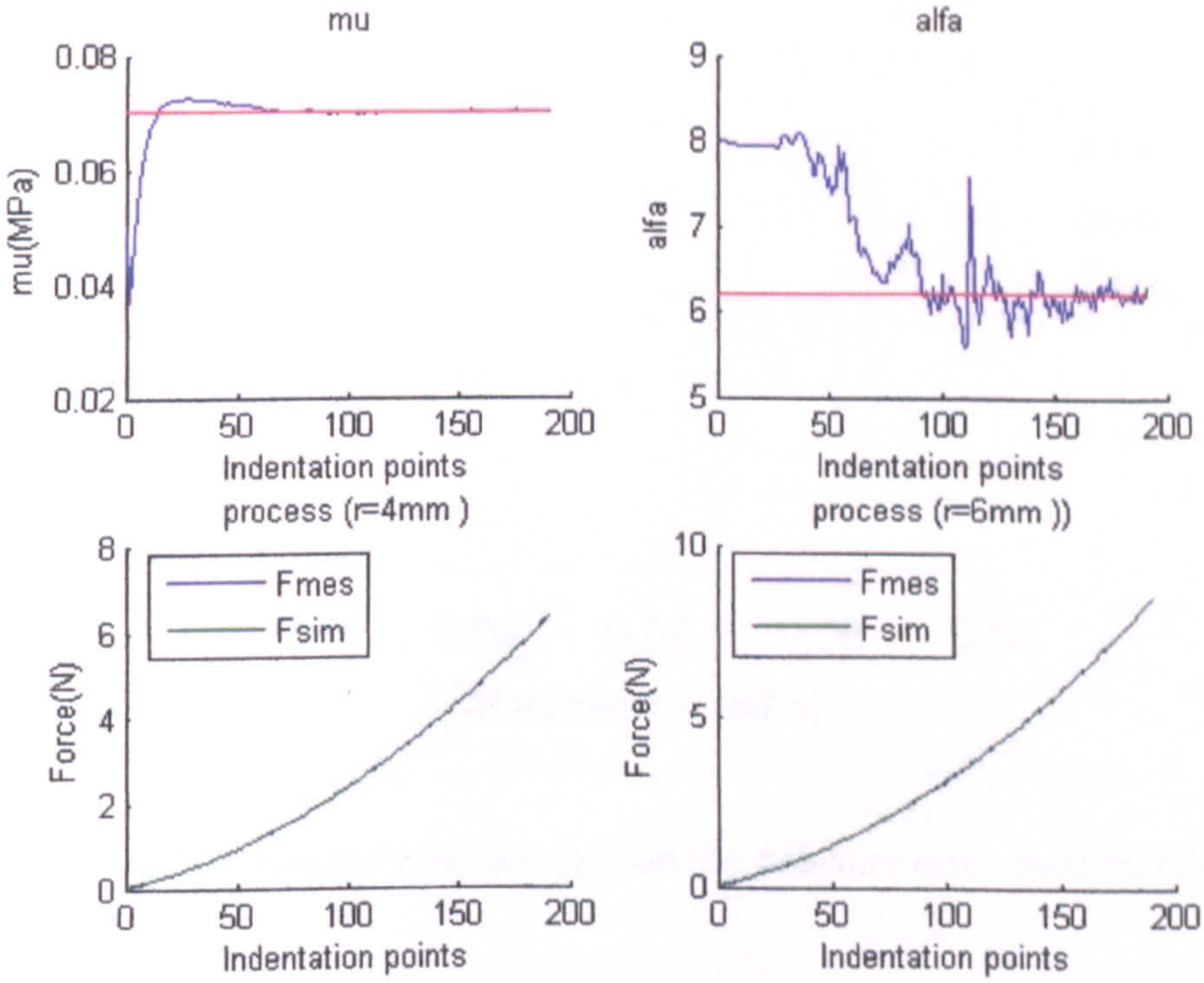


(a) Parameters searching process with a constant error (R=4mm, 6 mm).

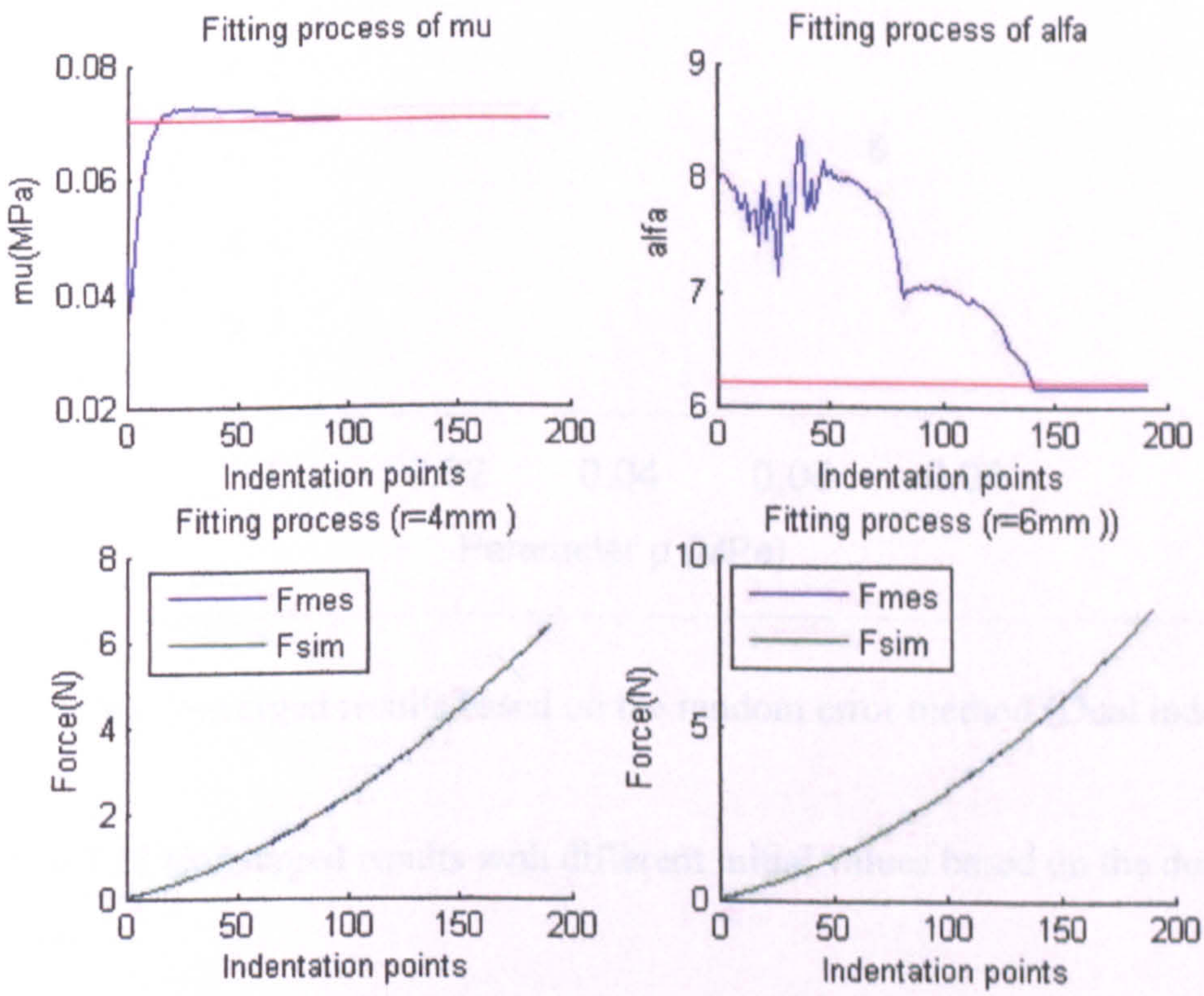


(b) Parameters searching process with a random error (R=4mm, 6 mm).

**Figure 3.24** Typical material parameter fitting curves for the double indenters method. (Hyperelastic model, the true material properties are $\mu_T$=0.07, $\alpha_T$=6.2; the initial guessed value used are $\mu_0$=0.08 MPa and $\alpha_0$=8.0).

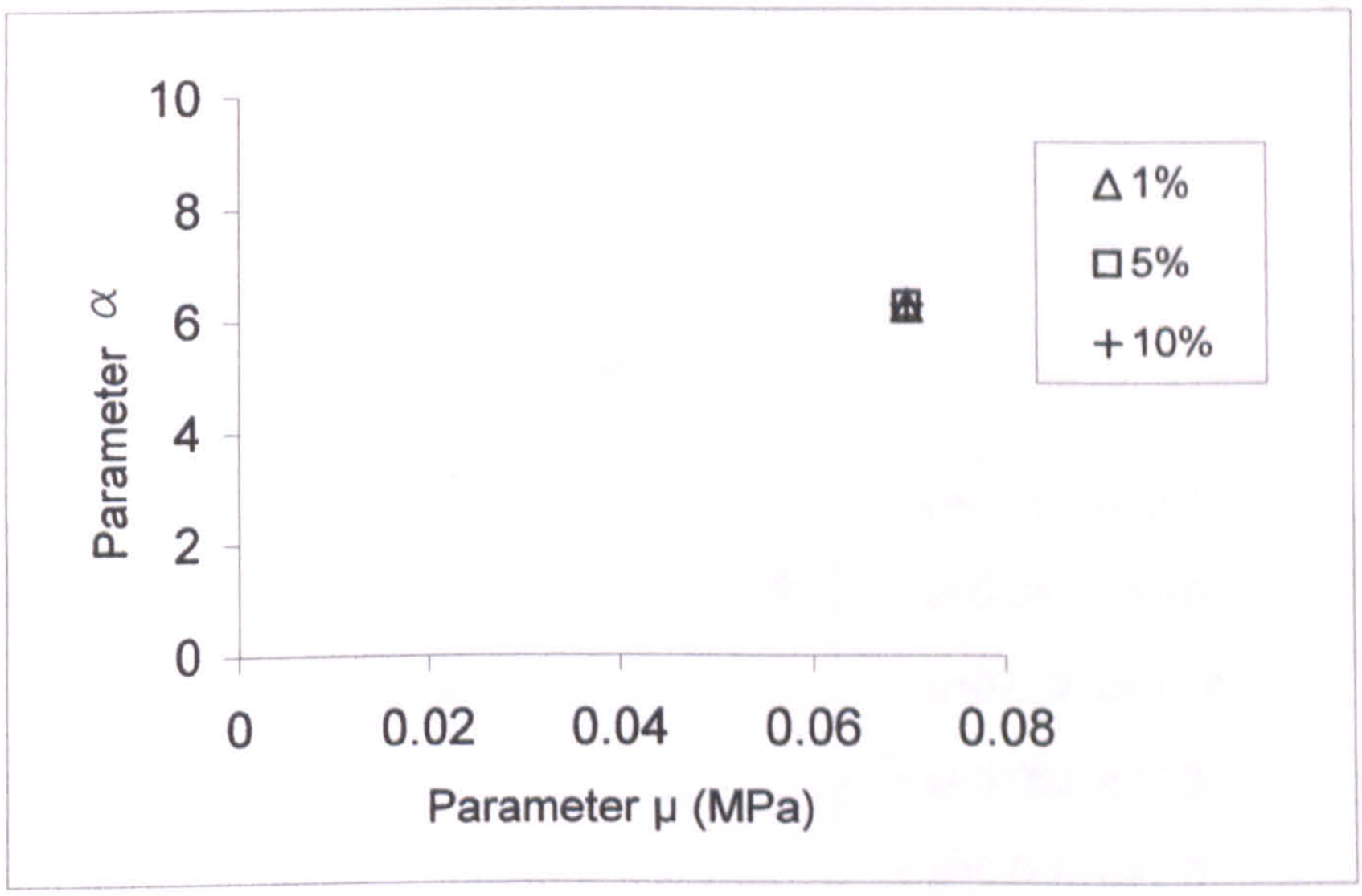


(a) Converged results based on the constant error method (Dual indenters)

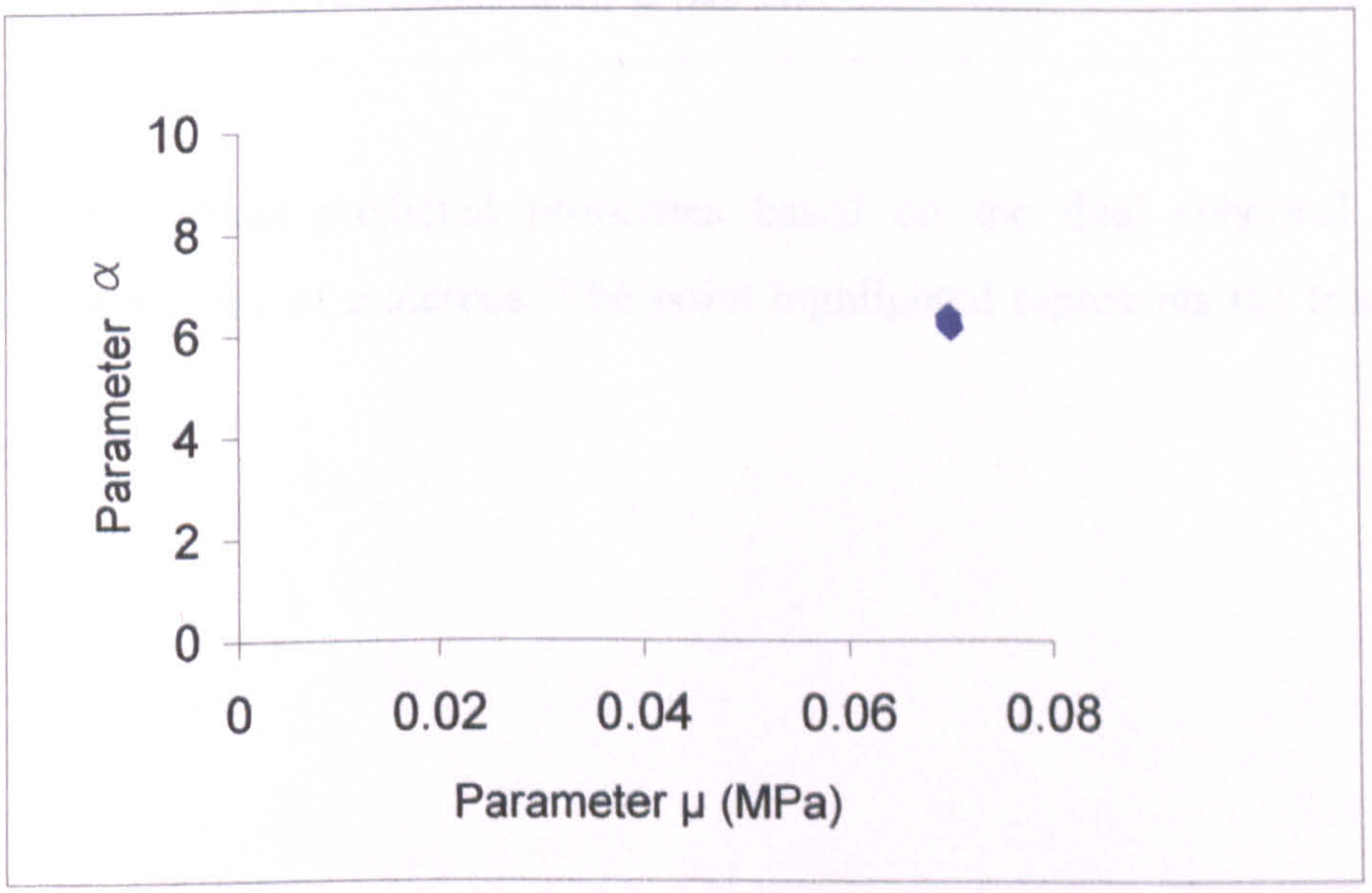


(b) Converged results based on the random error method (Dual indenters).

**Figure 3.25** Converged results with different initial values based on the dual indenters method.

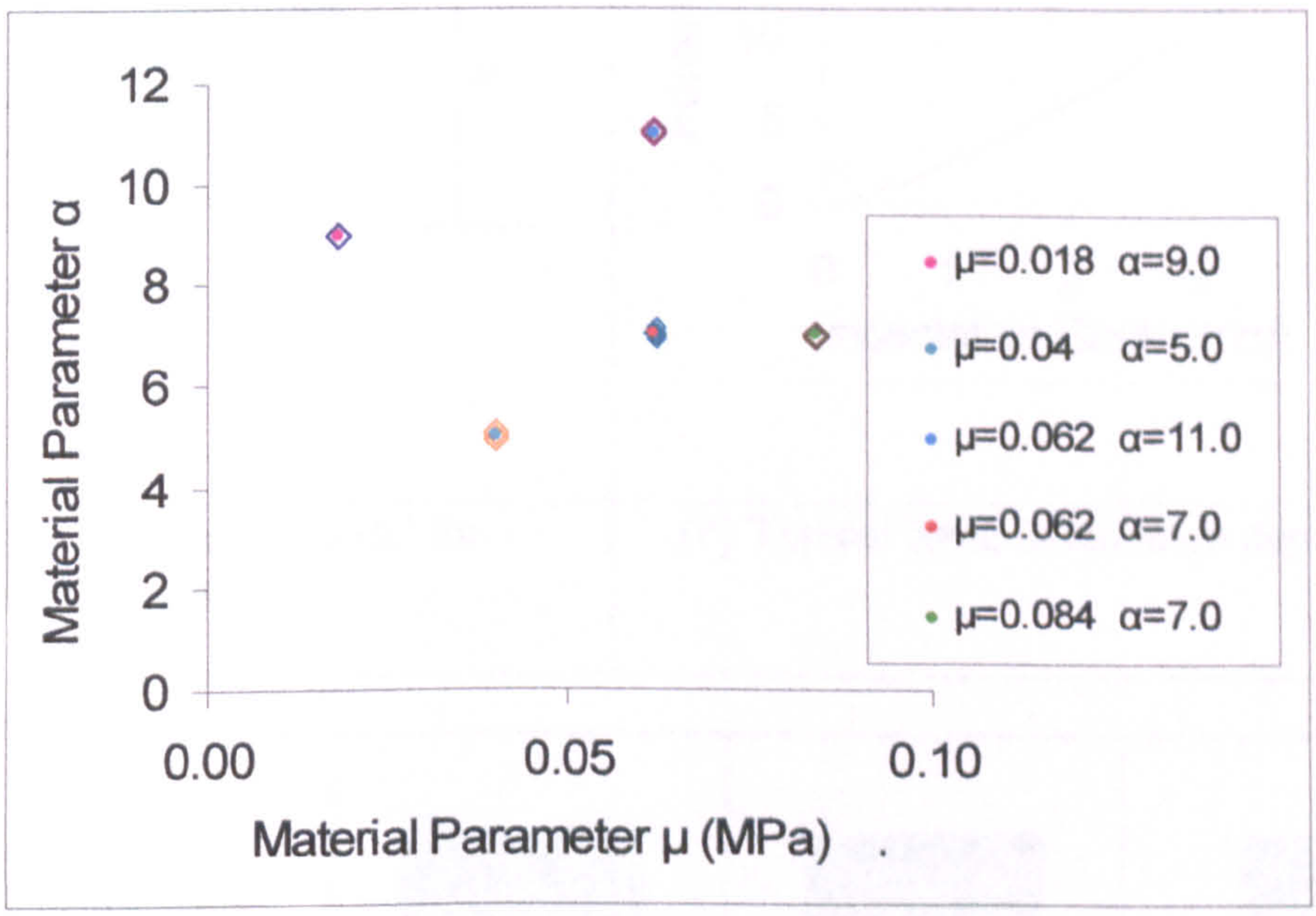


**Figure 3.26** Typical predicted properties based on the dual spherical indenters approach for a range of materials (The point highlighted represents the true material data).

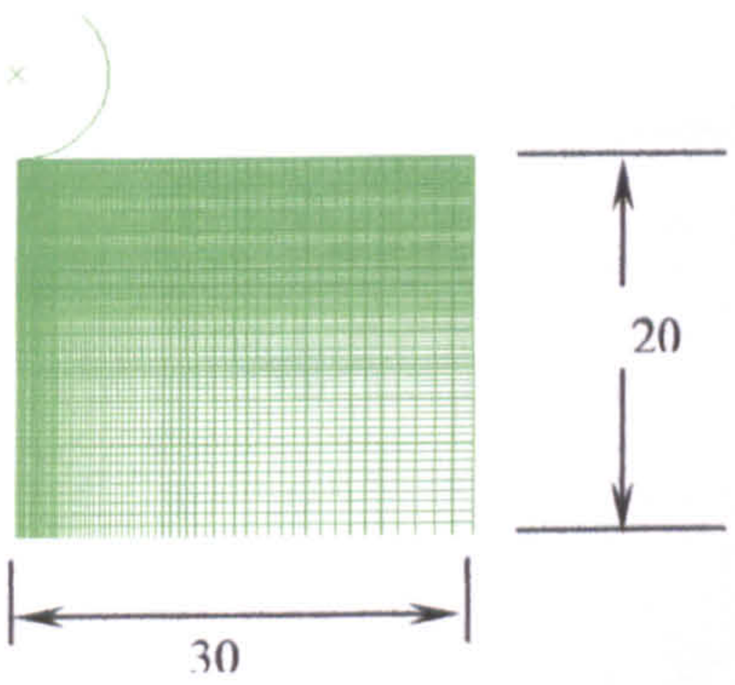


(a) FE indentation model for hyperfoam material.

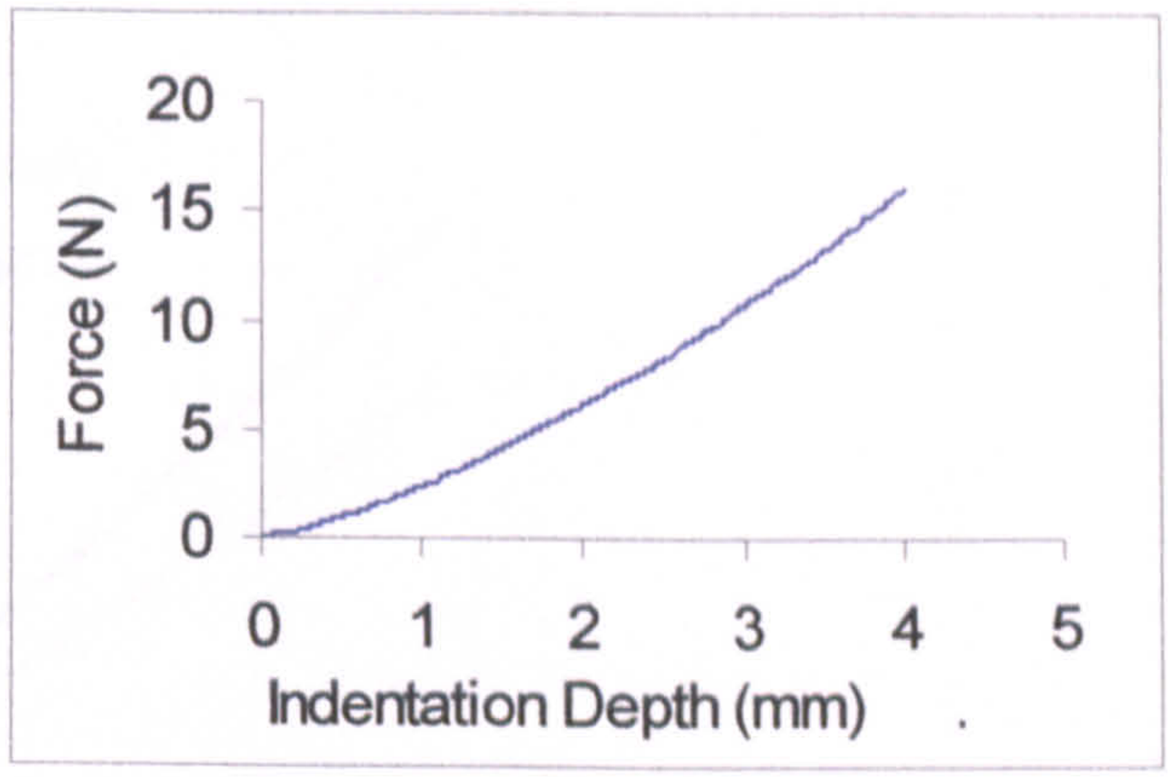


(b) Typical force indentation depth curve.

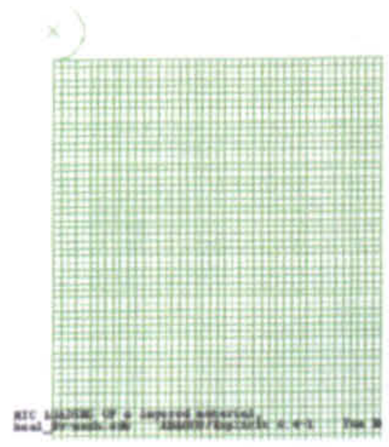

Mesh 1

Mesh 2

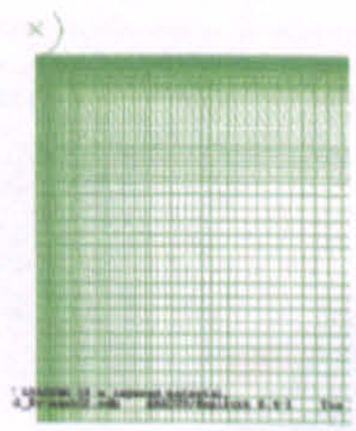

Mesh 3

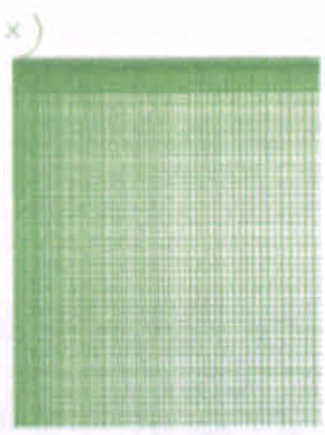

Mesh 4

(c) FE model with different mesh densities.

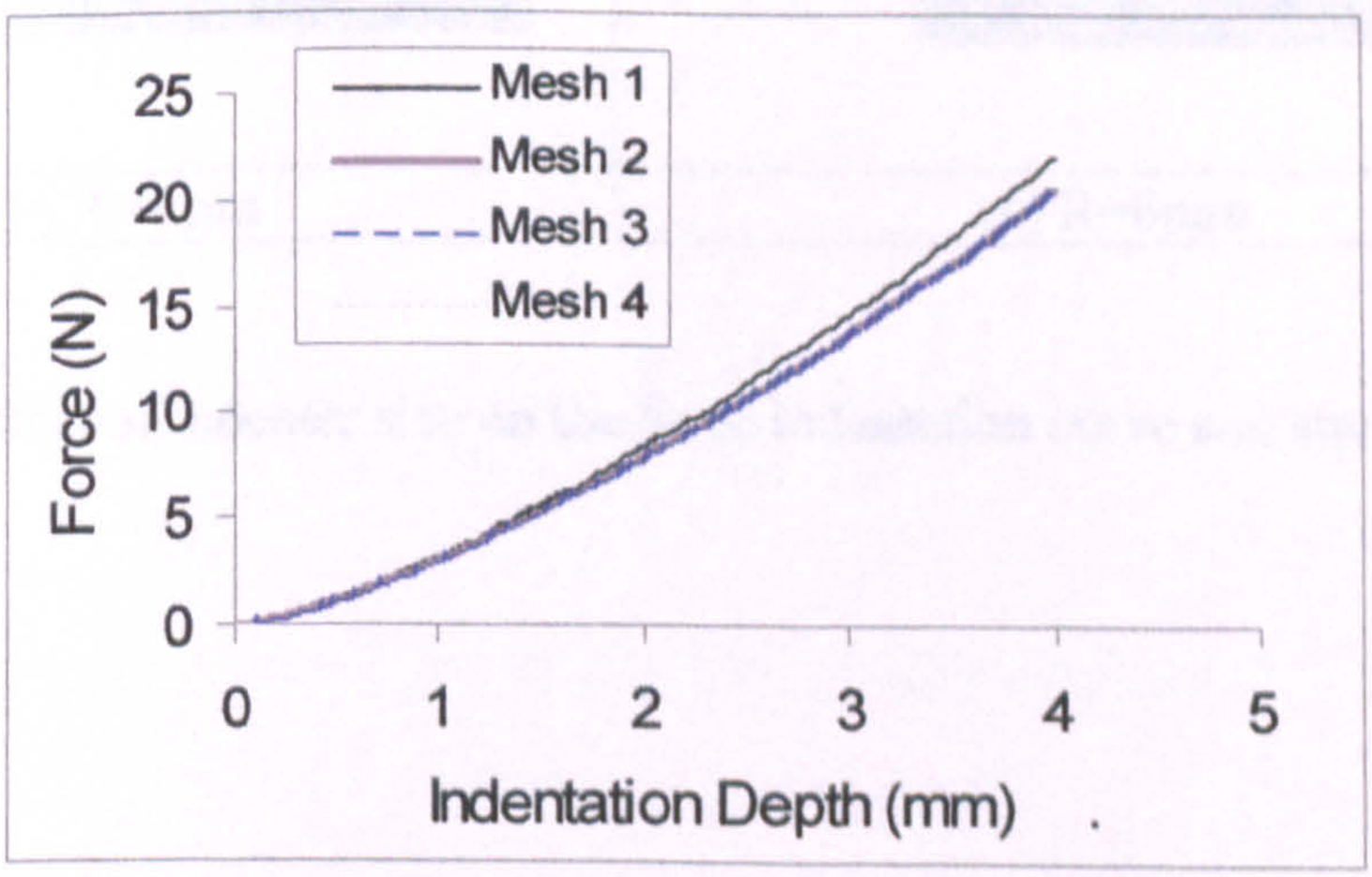


(d) Force indentation depth curves from FE models with different meshing schemes.

**Figure 3.27** FE indentation models of a hyperfoam material, typical force-indentation depth (*p-h*) curve and effect of meshing schemes.

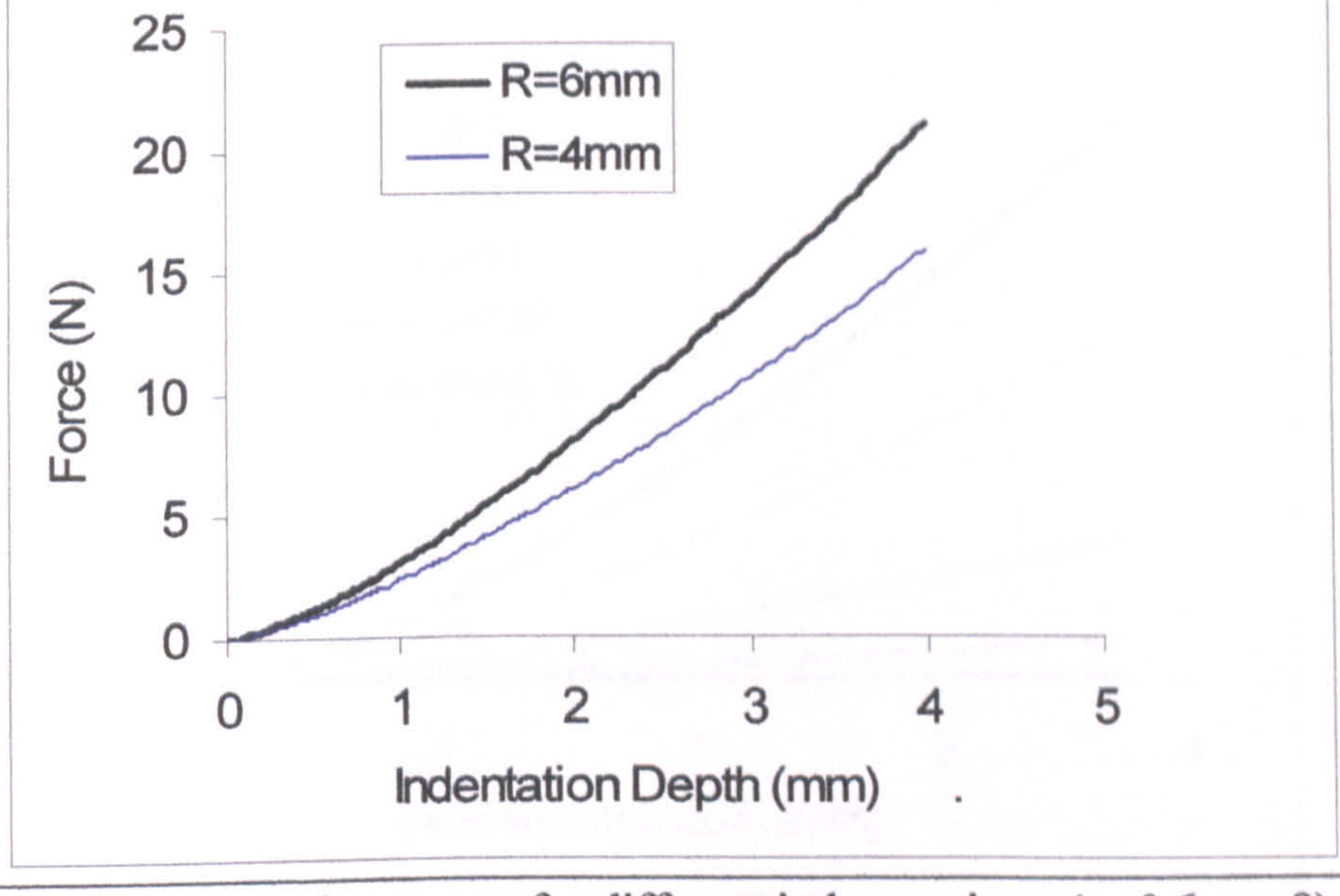


(a) Indentation curves for different indenter sizes. ($\mu$=0.6, $\alpha$ =8)

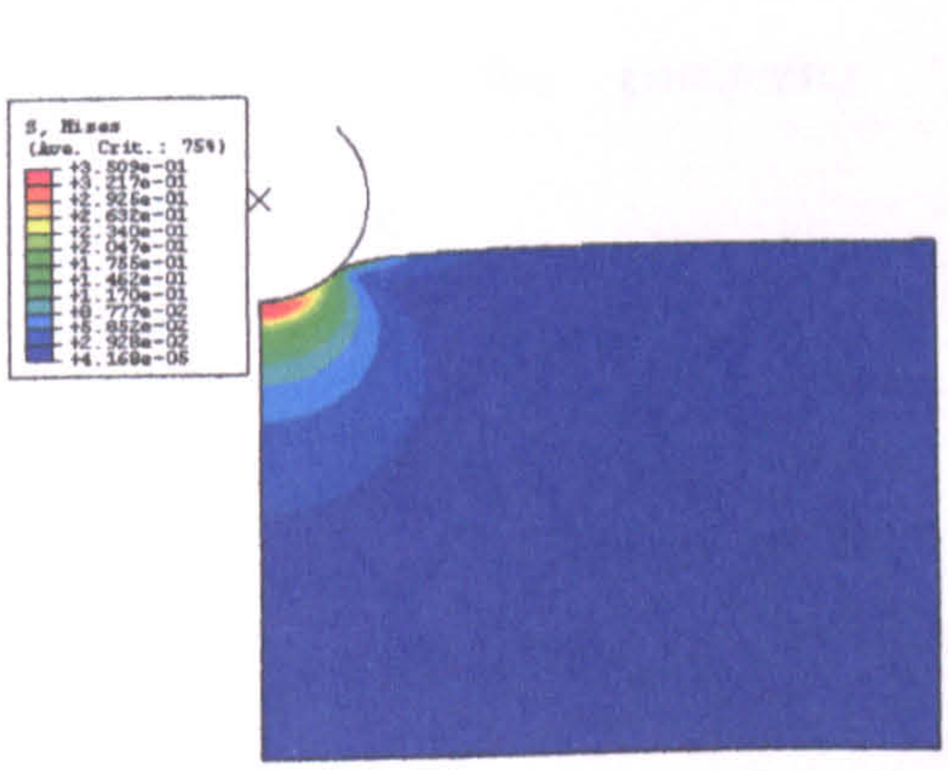


(b) R=4mm

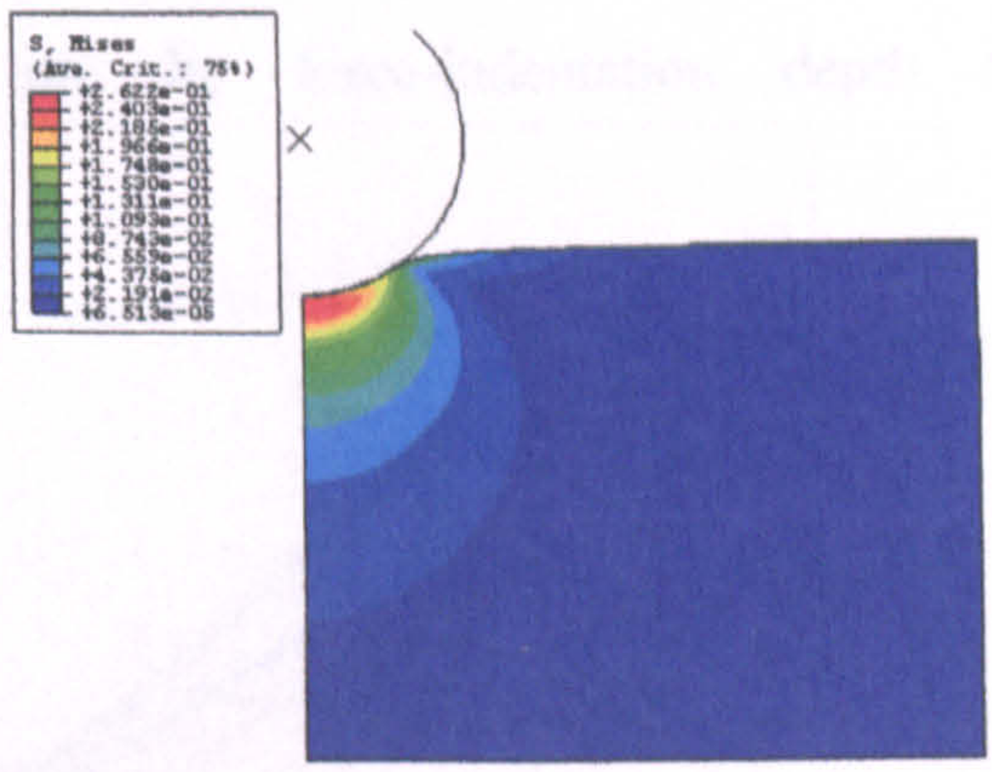


(c) R=6mm

**Figure 3.28** Effect of indenter size on the force indentation curve and stress distribution.

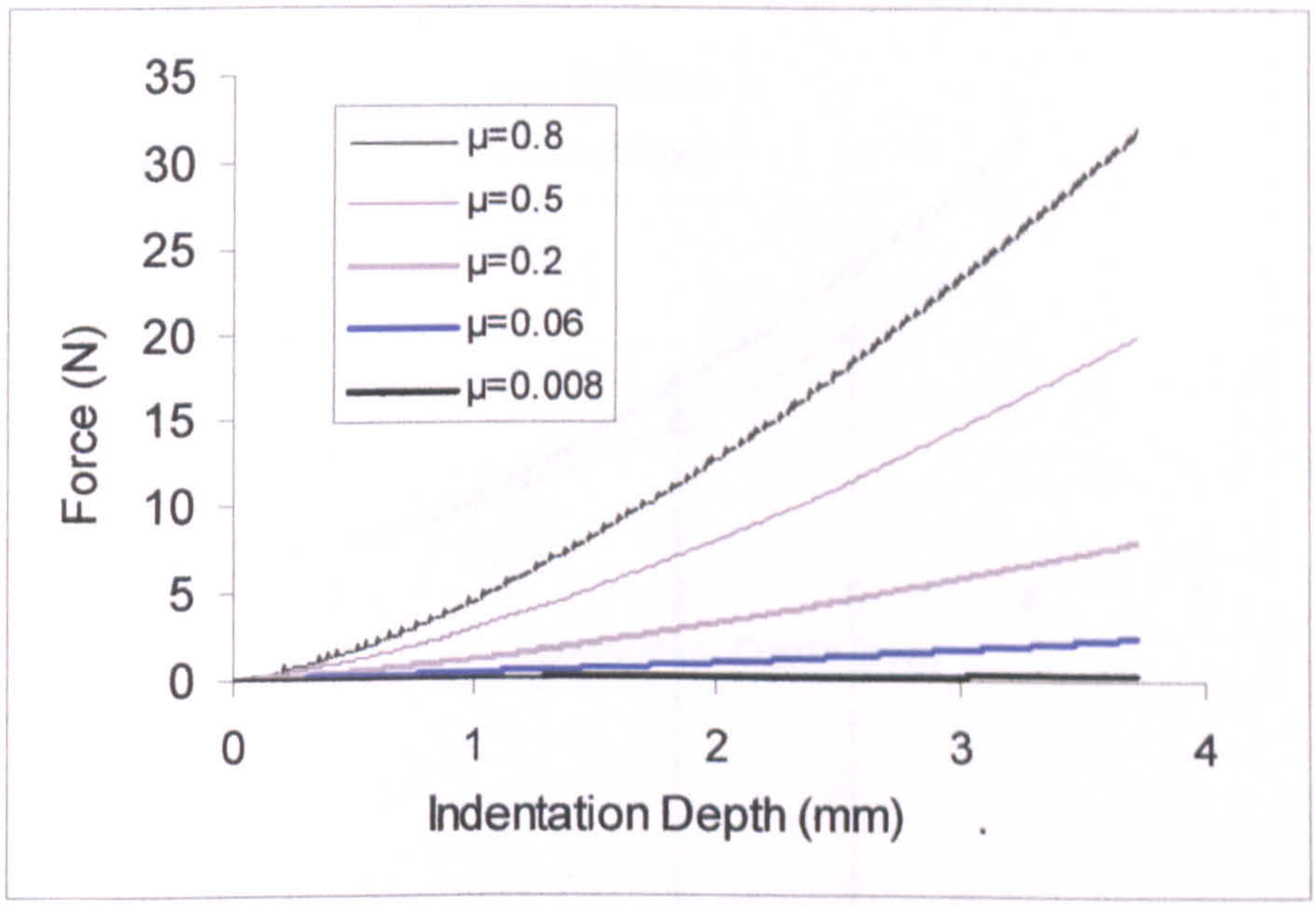


**(a)** Effect of the parameter 'μ' on the force-indentation depth data.

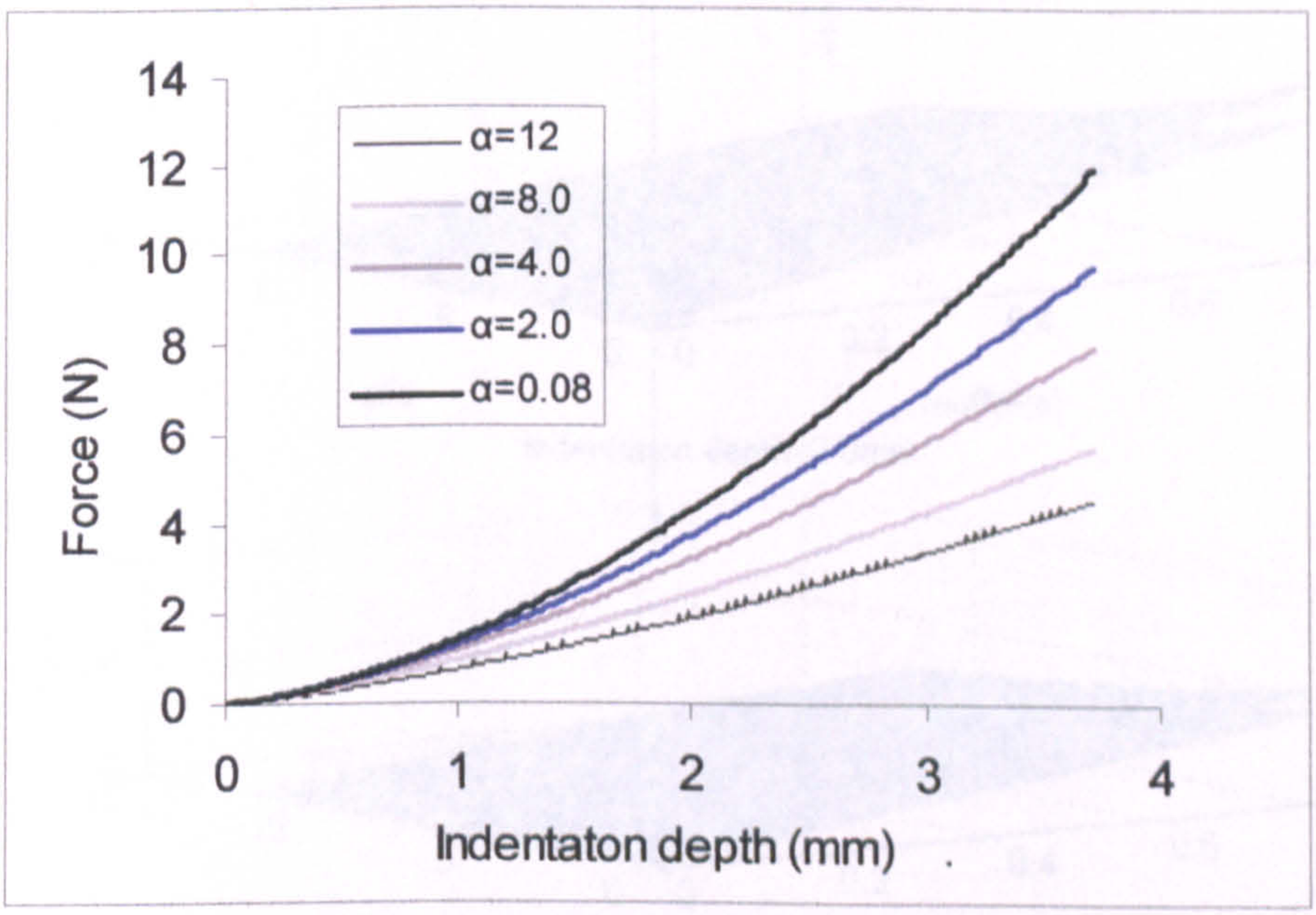


(b) Effect of the parameter 'α' on the force-indentation depth data.

**Figure 3.29** Effect of materials parameters on the force indentation curve for hyperfoam materials.

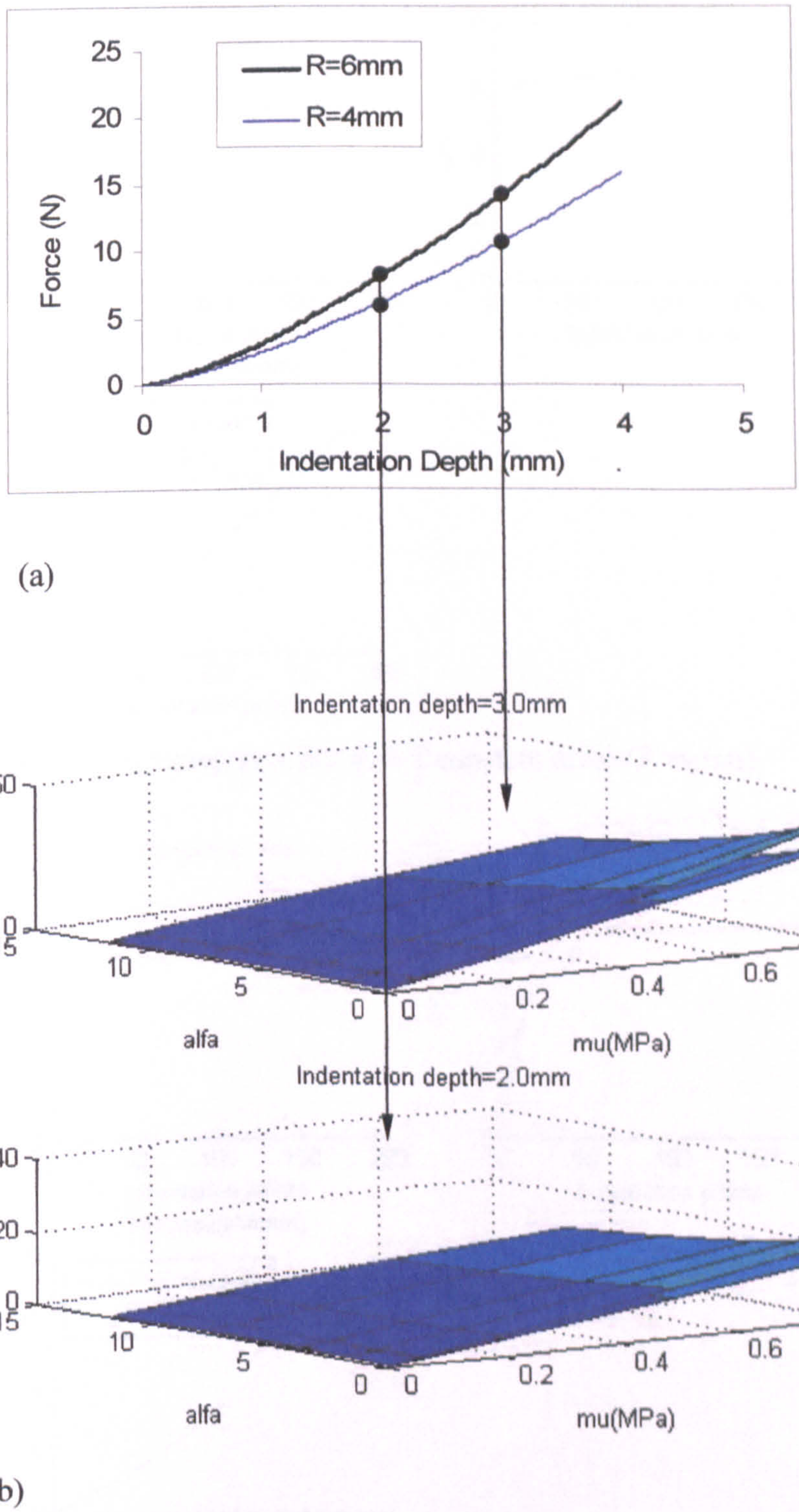


**Figure 3.30** Typical numerical experimental data with different indenter sizes (a) and simulation surfaces at indentation depth of 2mm and 3mm.

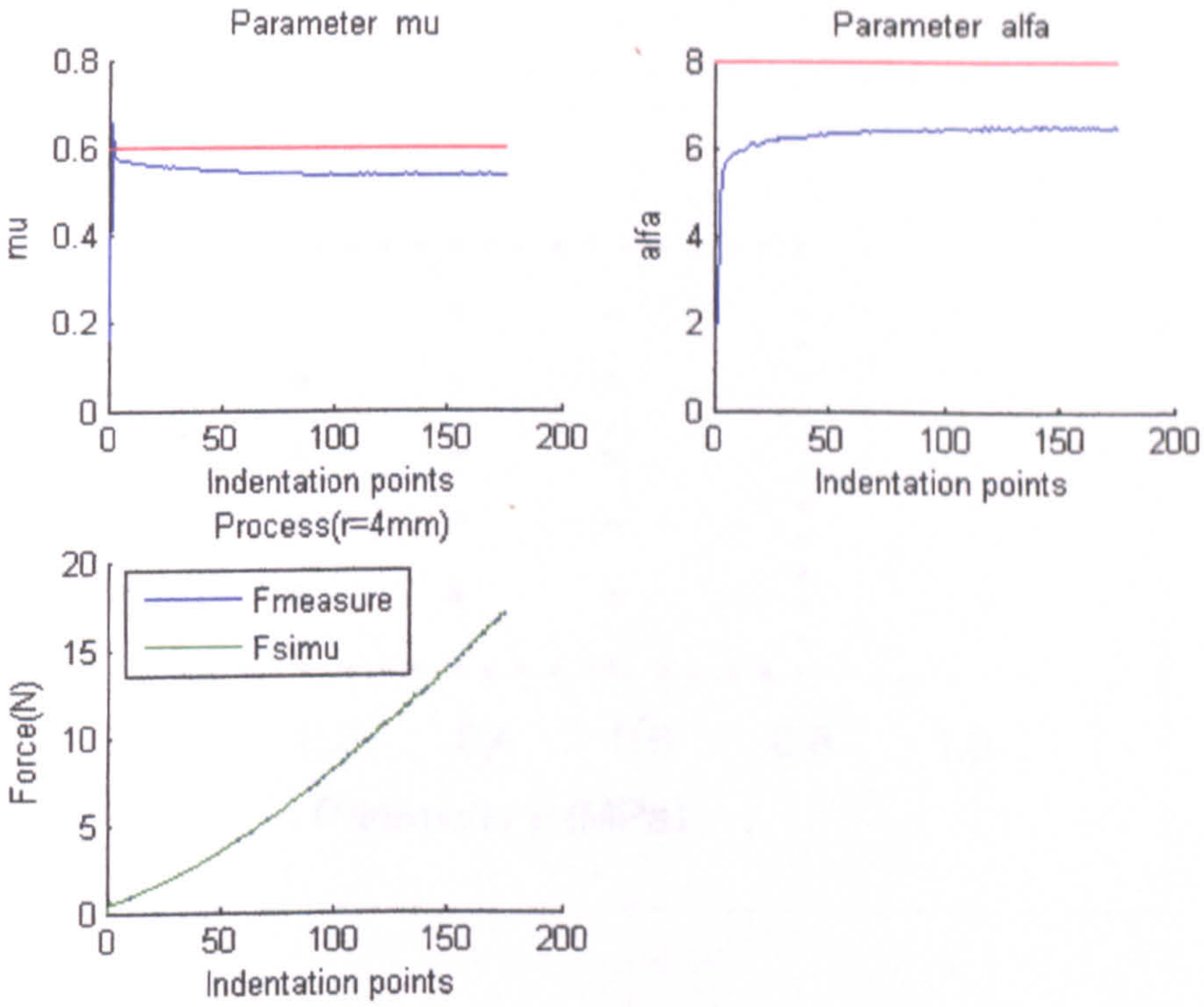


(a) Parameters searching process with a constant error (R=4mm).

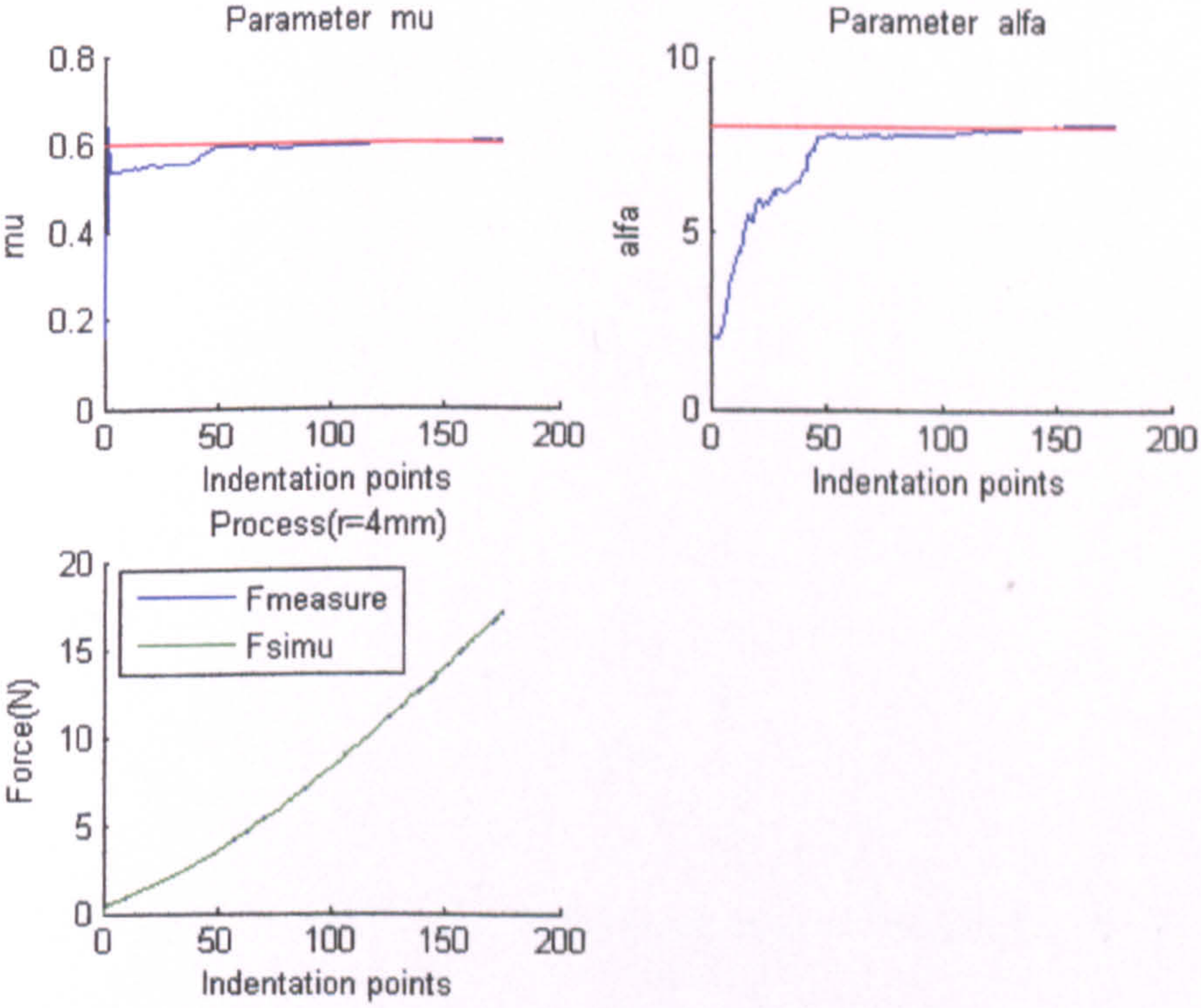


(b) Parameters searching process with random error (R=4mm).

**Figure 3.31** Typical material parameter fitting curves for the double indenter method. (The target material properties are $\mu_T$=0.6, $\alpha_T$=8; the initial guessed value used are $\mu_0$=0.16MPa and $\alpha_0$=2.0).

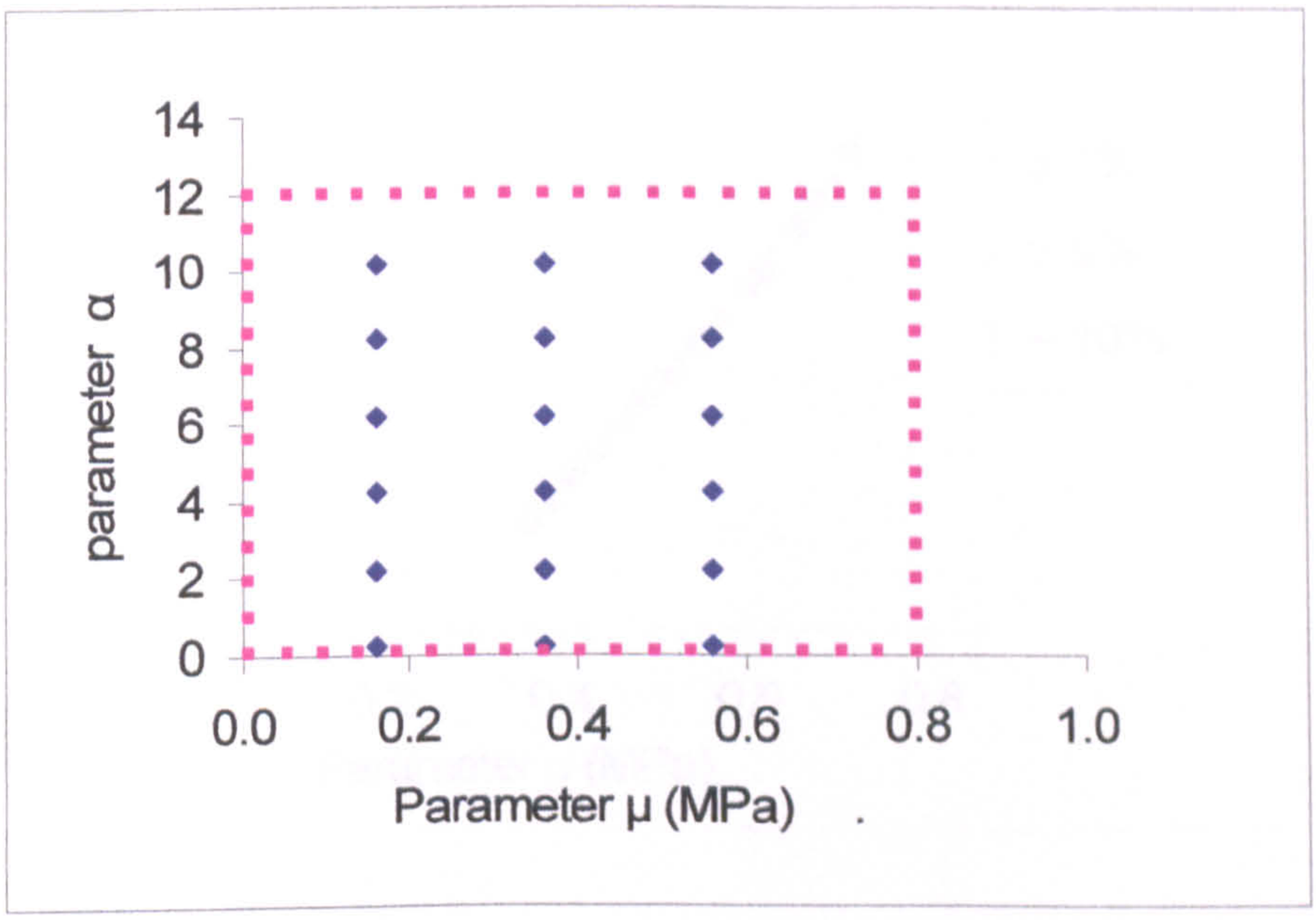


**Figure 3.32** Matrix of initial guessed values used to study the effect of initial value on the convergence of the program.

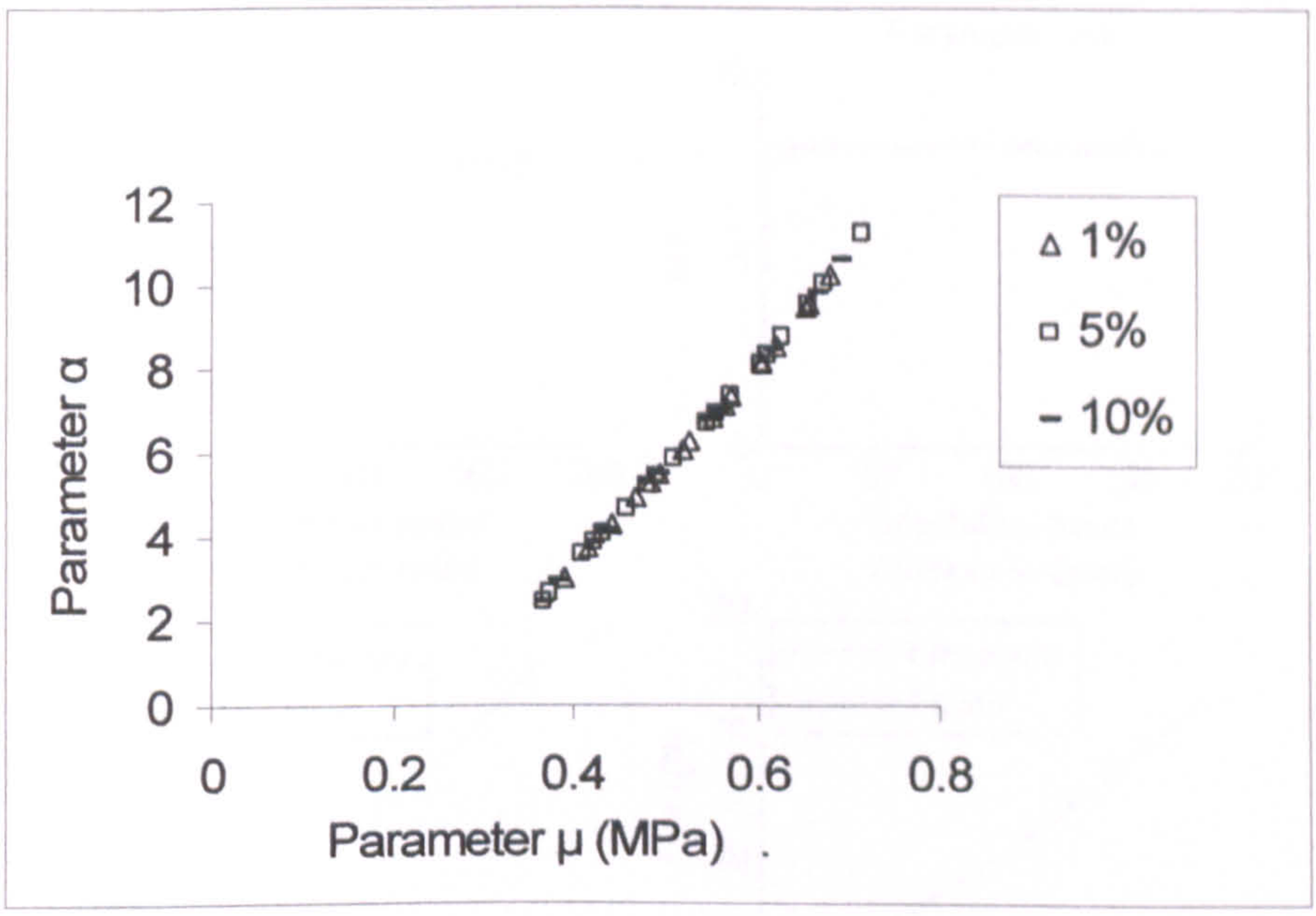


(a) Converged results based on the constant error method (R=4mm)

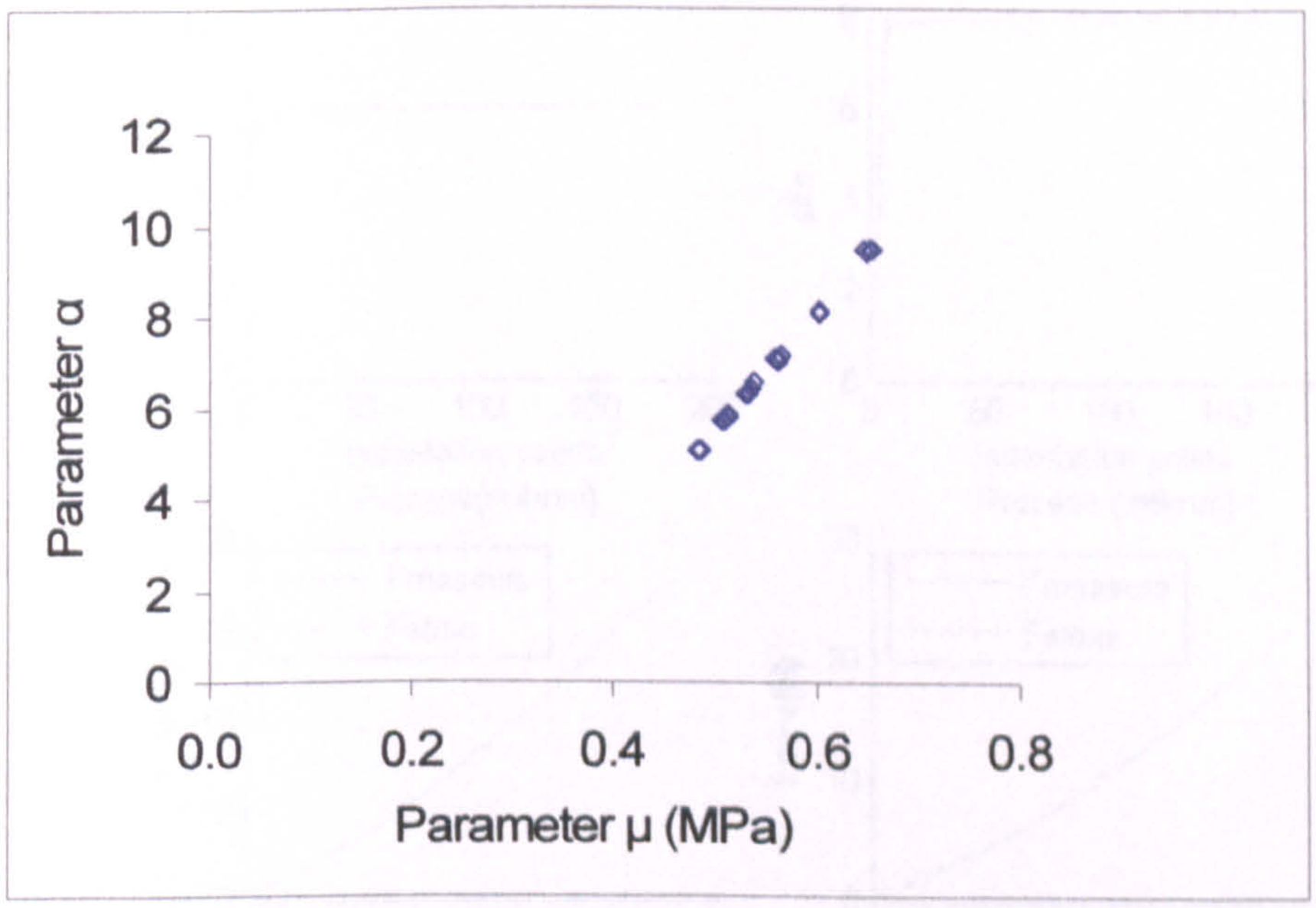


(b) Converged results based on the random error method (R=4mm)

**Figure 3.33** Converged results with different initial values based on the single indenter method.

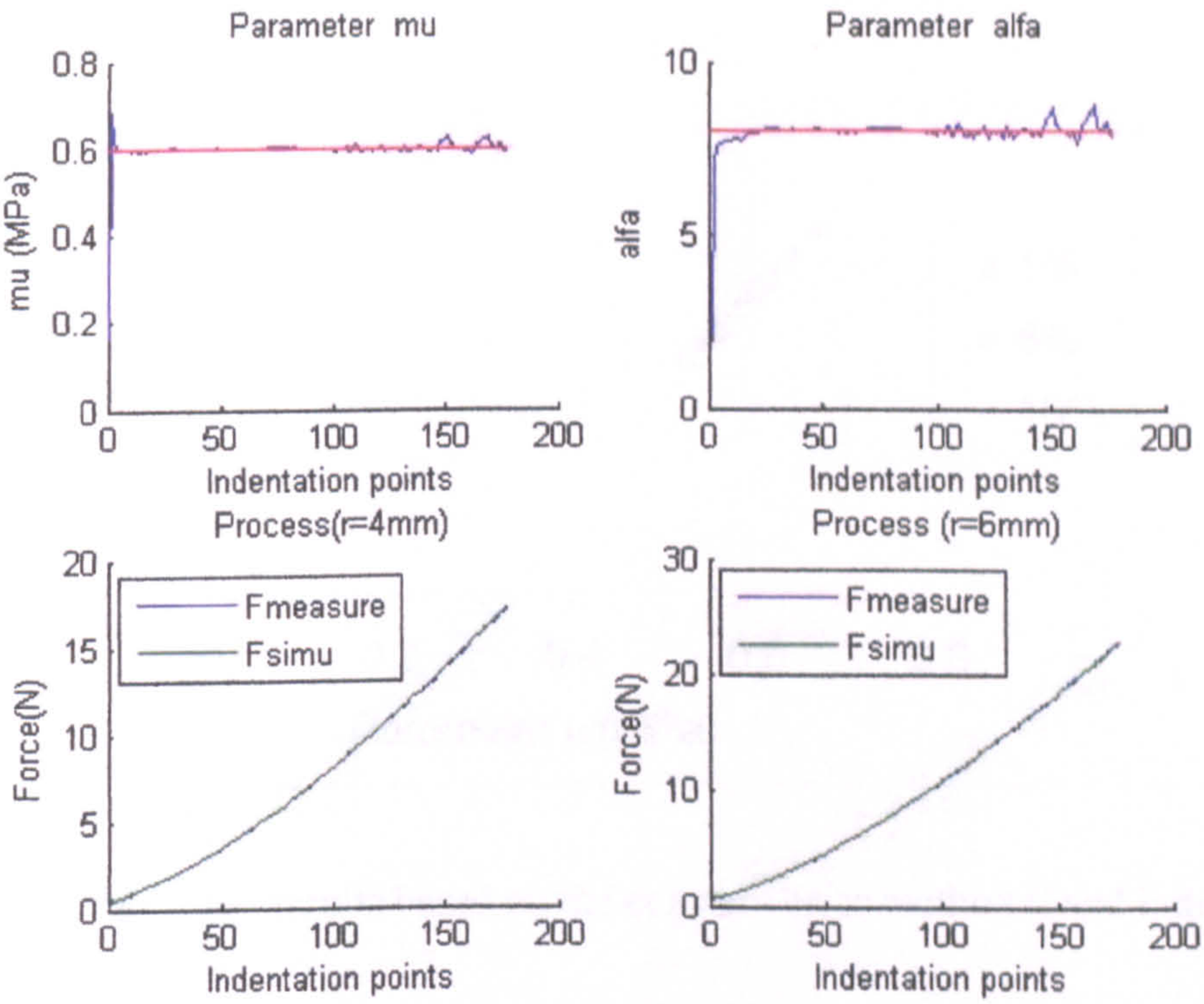


(a) Parameters searching process with a constant error (R=4mm, R=6mm).

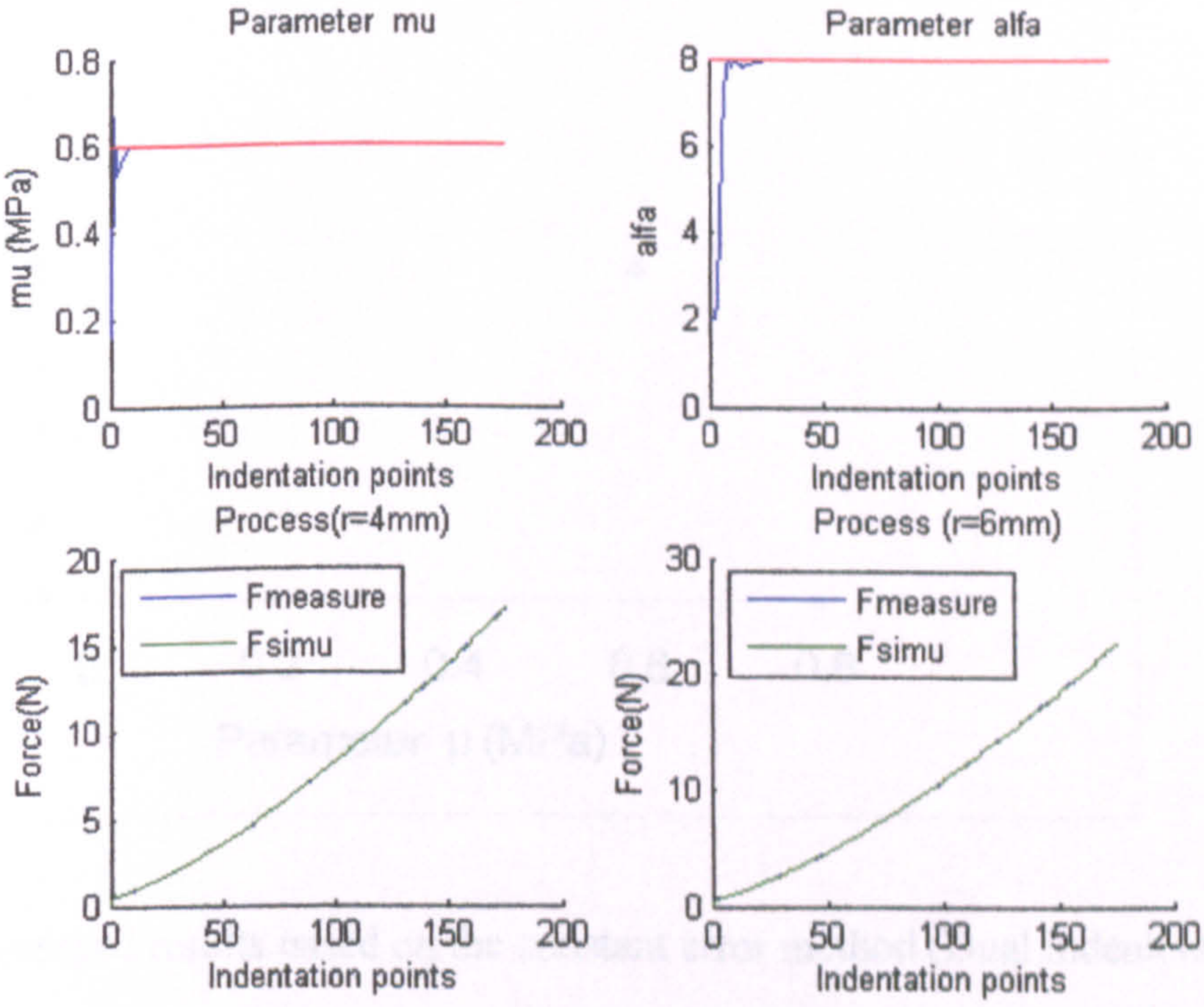


(b) Parameters searching process with random error (R=4mm, R=6mm).

**Figure 3.34** Typical material parameter fitting curves for the double indenter method (The target material properties are $\mu_T$=0.6, $\alpha_T$=8; the initial guessed value used are $\mu_0$=0.16 MPa and $\alpha_0$=2.0).

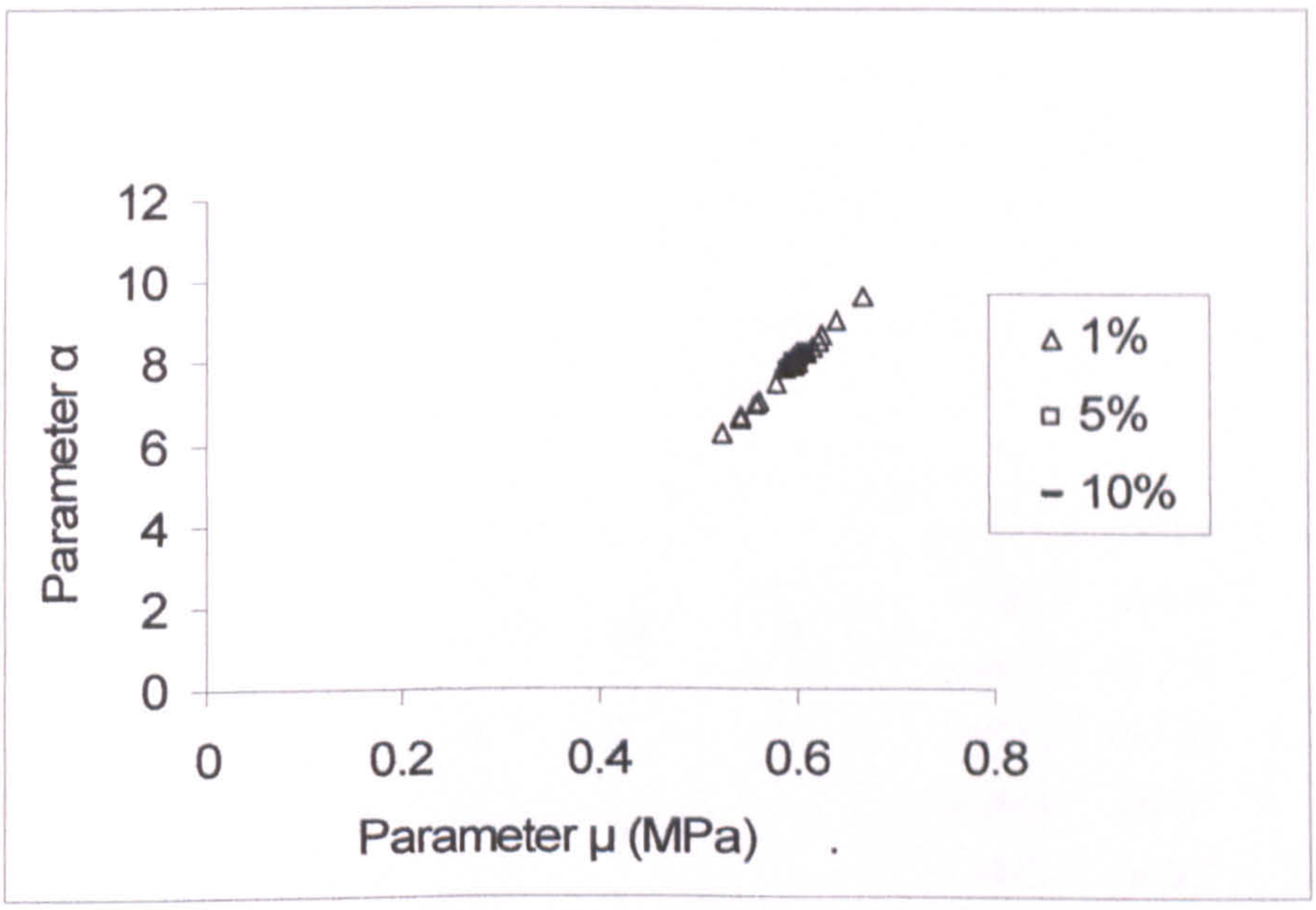


(a) Converged results based on the constant error method (Dual indenters)

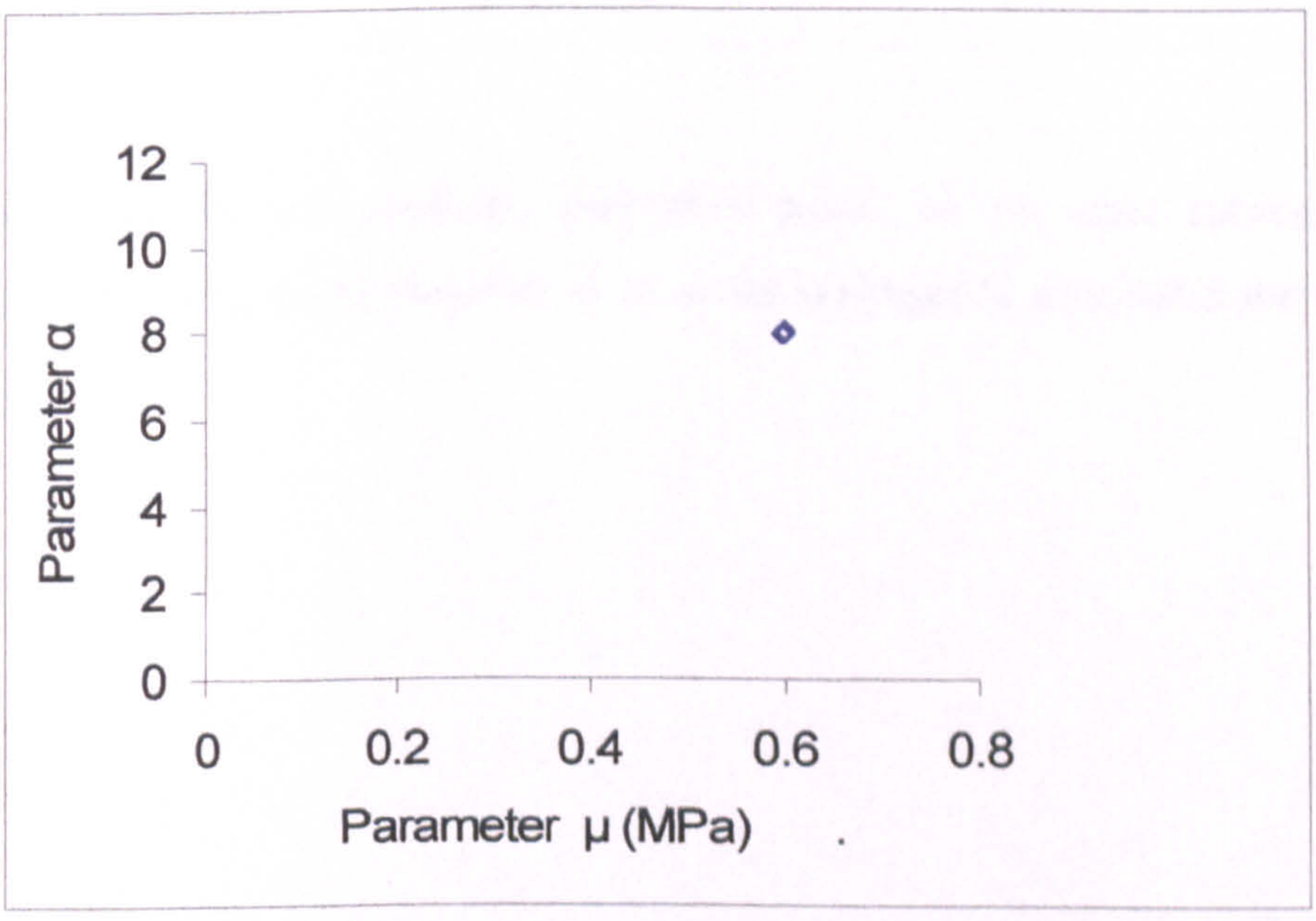


(b) Converged results based on the constant error method (Dual indenters)

**Figure 3.35** Converged results with different initial values based on the dual indenters method.

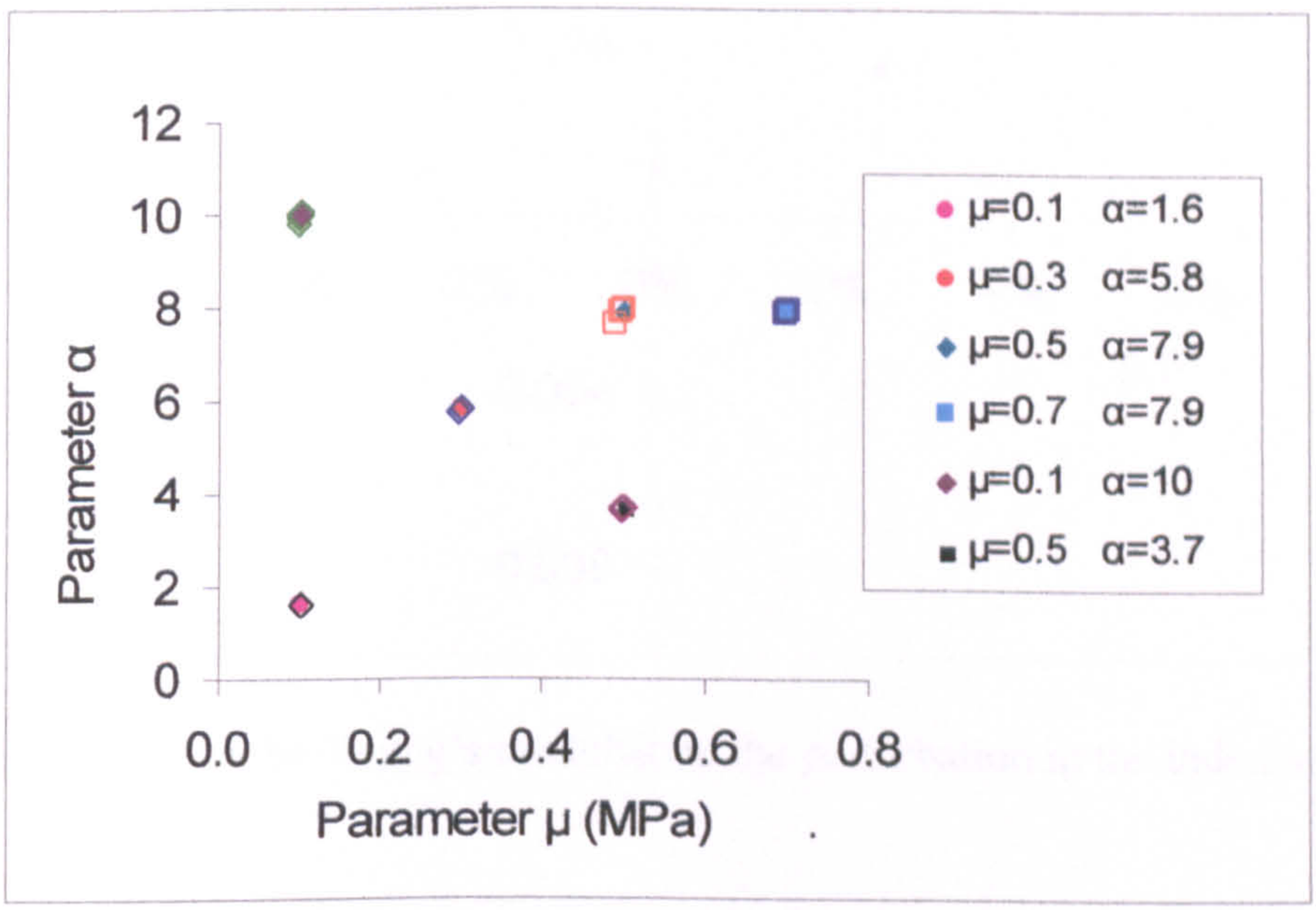


**Figure 3.36** Typical predicted properties based on the dual spherical indenters approach for a range of materials (The point highlighted represents the true material data).

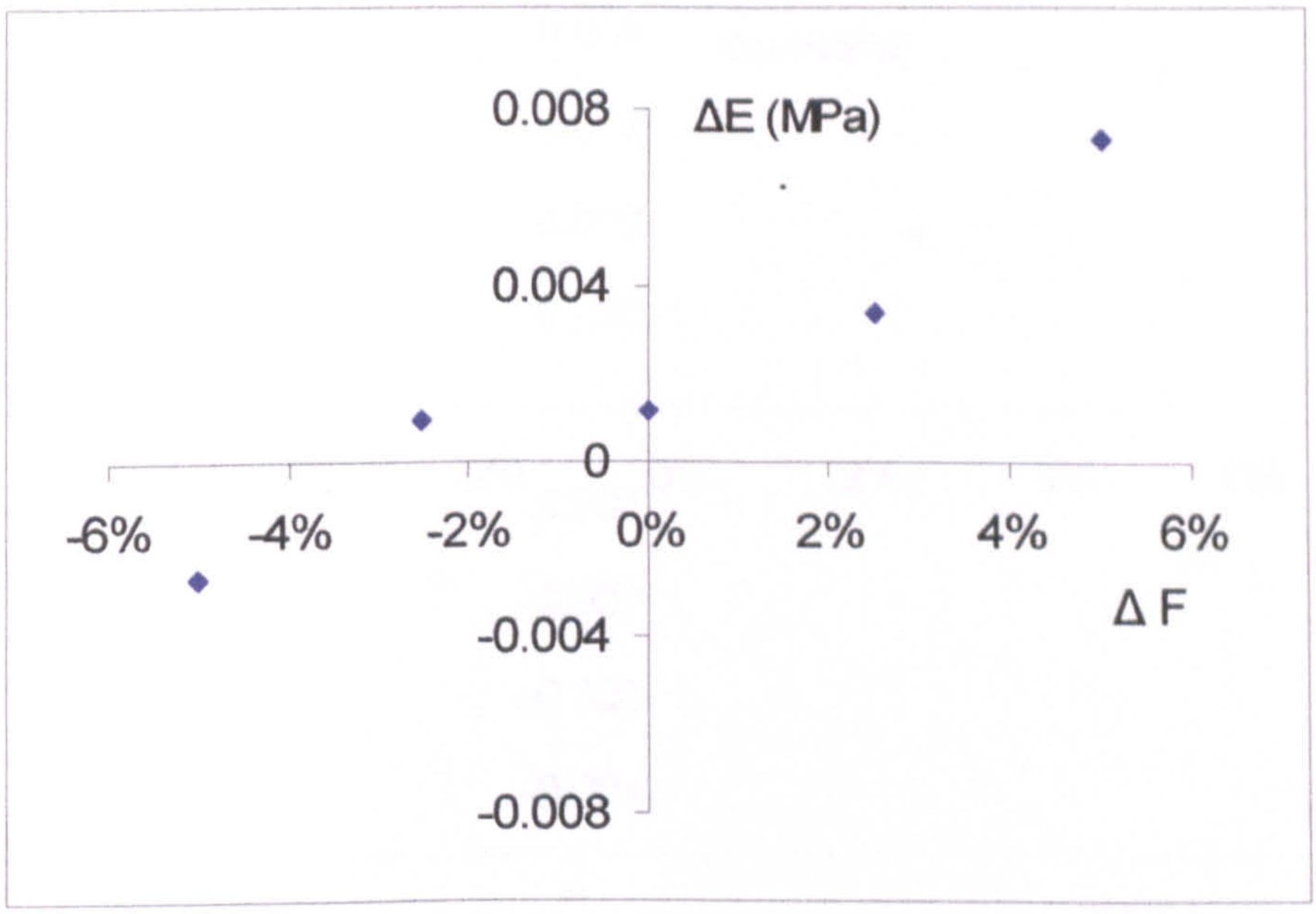


(a) Sensitivity of the Young's modulus on the perturbation in the indentation force.

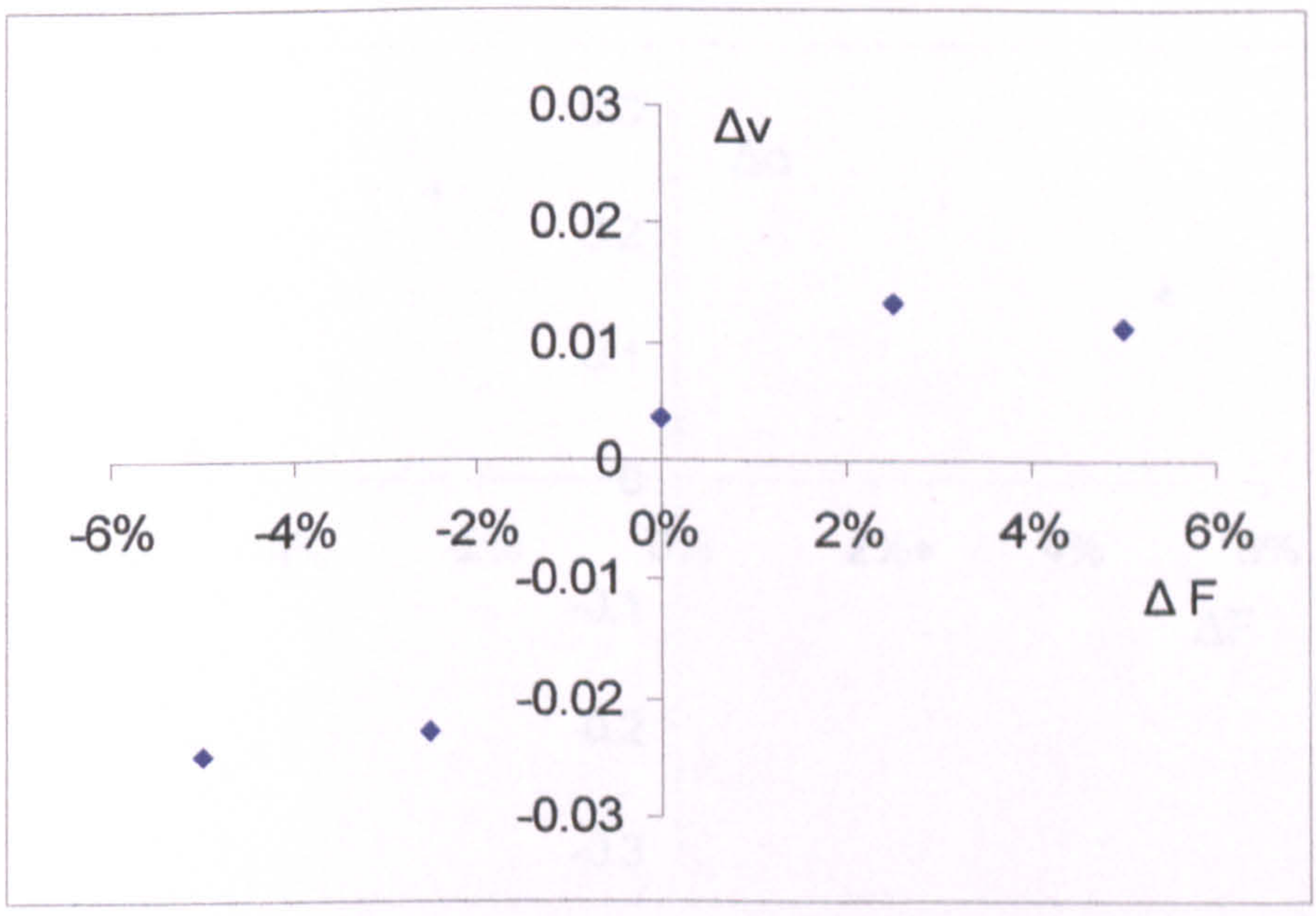


(b) Sensitivity of the Poisson's ratio on the perturbation in the indentation force.

**Figure 3.37** Typical sensitivity study results for the dual indenters method with an input material properties of E=0.14 and v=0.43.

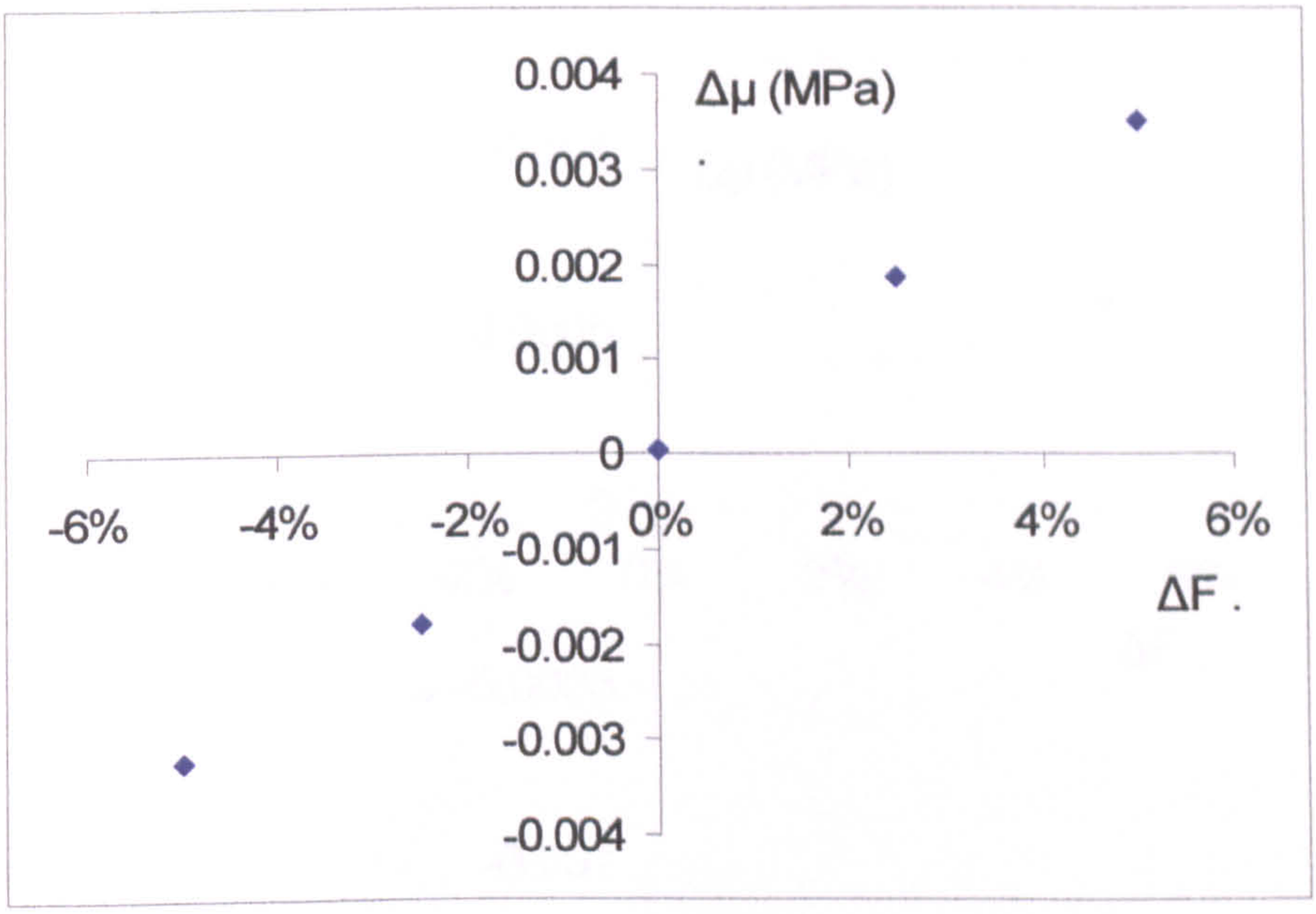


(a) Sensitivity of the hyperelastic parameter μ on the perturbation in the indentation force.

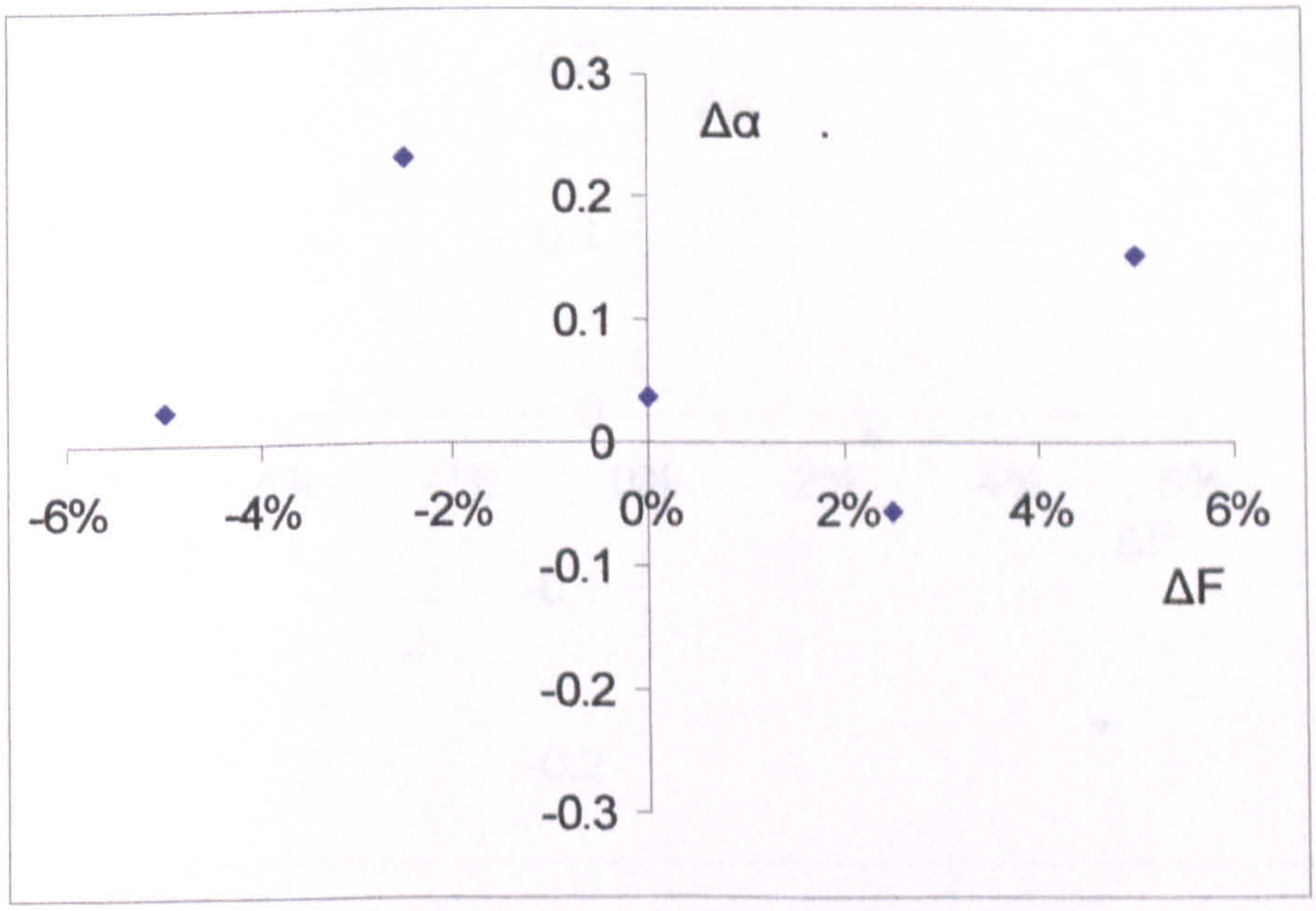


(b) Sensitivity of the hyperelastic parameter α on the perturbation in the indentation force.

**Figure 3.38** Typical sensitivity study results for the dual indenters method with an input material properties of $\mu$=0.07 and $\alpha$=6.2.

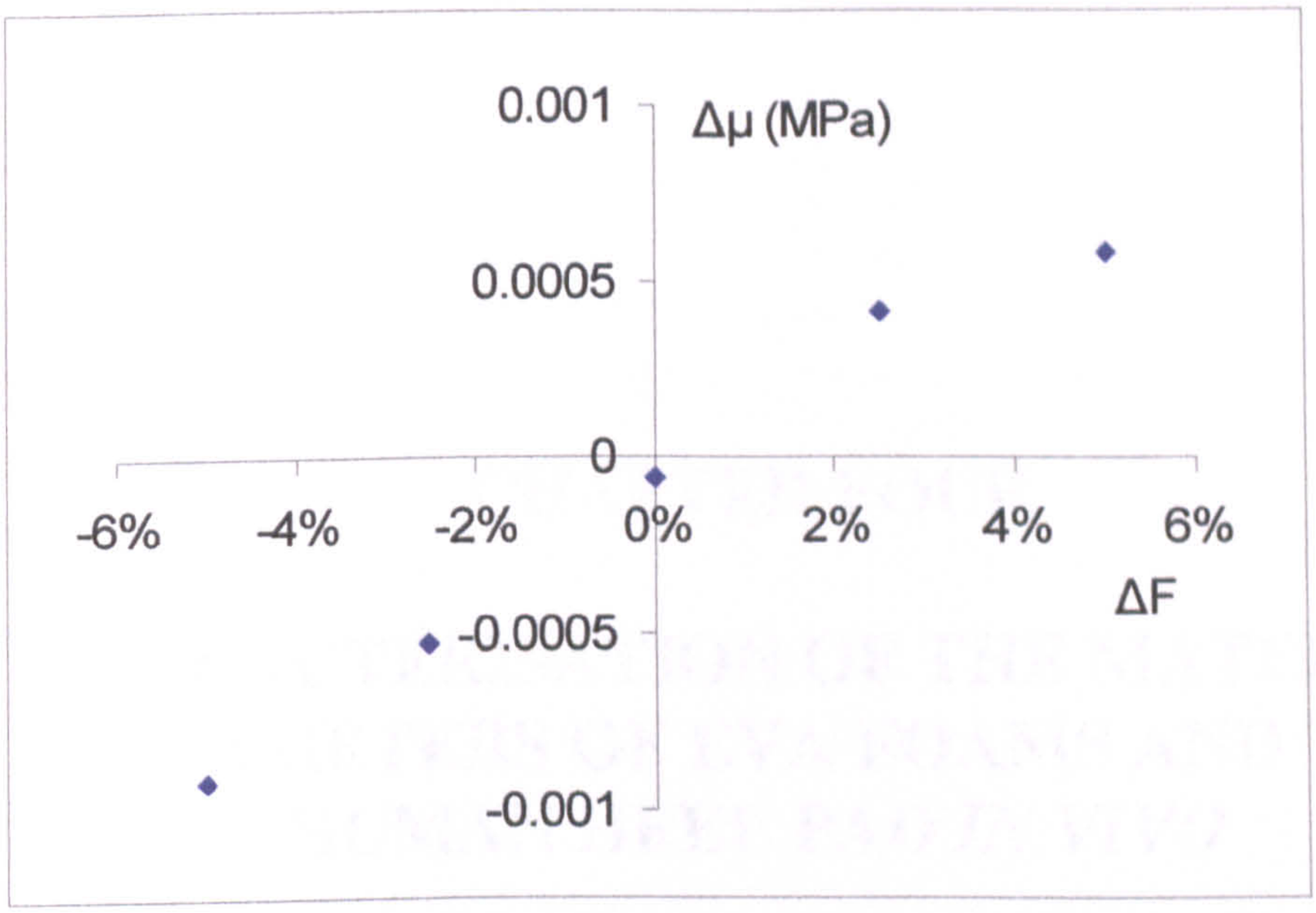


(a) Sensitivity of the hyperfoam parameter μ on the perturbation in the indentation force.

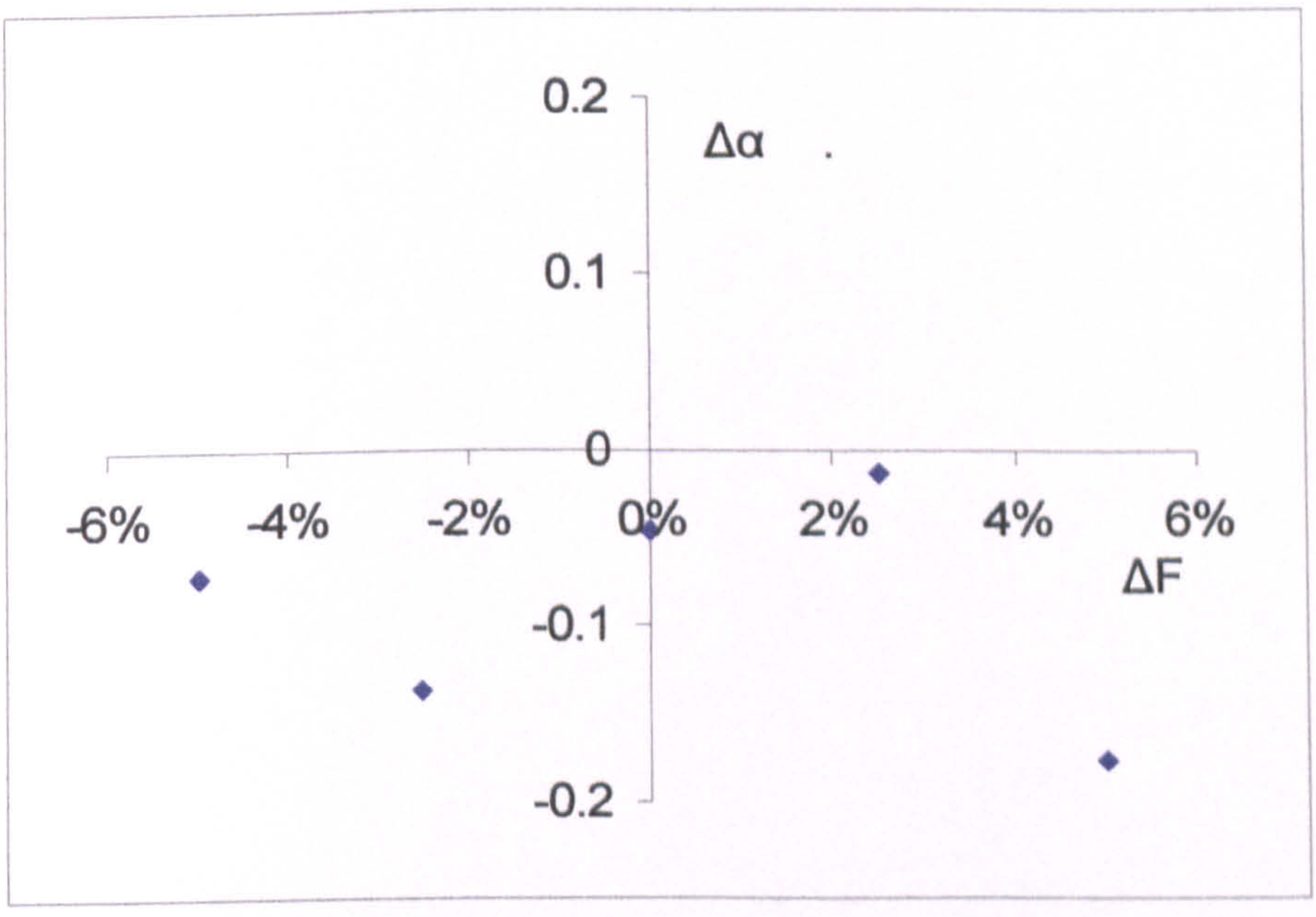


(b) Sensitivity of the hyperfoam parameter α on the perturbation in the indentation force.

**Figure 3.39** Typical sensitivity study results for the dual indenters method with an input material property of μ=0.0164 and α=6.82.

# CHAPTER FOUR

# CHARACTERISATION OF THE MATERIAL PARAMETERS OF EVA FOAMS AND THE HUMAN HEEL PAD *IN VIVO*

## 4.1 Introduction

In this chapter, the inverse FE program developed is applied to characterise the properties of the EVA foams and the human heel pad *in vivo*. In the first part, a new continuous testing system is designed and constructed. The accuracy of the system is validated on a rubber material with known material properties. The accuracy of the testing system is then further assessed by comparing the testing results on an EVA foam to that from a standard tensile testing machine. In the second part, indentation tests are performed on two EVA foams commonly used in sport equipments. The material parameters predicted from indentation tests using the framework for the hyperfoam model established in Chapter 3 are compared to that based the conventional compression and compression-shear test methods. The suitability of each method is systematically investigated. In the third part, the mechanical properties of the human heel pad are studied using the continuous indentation test and inverse FE modelling program. The repeatability and effect of experimental conditions on *in vivo* testing are established. Systematically tests with different indenter sizes are performed on human subjects, then the linear elastic and nonlinear elastic material parameters of the human heel pad were identified from the indentation test data.

## 4.2 Testing of EVA foams and Hyperfoam parameters identification

### 4.2.1 Experiments

Closed cell foams, such as EVA foam, are widely used in engineering, sport and biomedical fields. The properties of EVA foams are highly nonlinear and viscoelastic *(Verdejo and Mills, 2004; Ruiz-Herrero et al, 2005)*, and are best described by nonlinear material models. The mechanical behaviour of EVA foams is normally described using the Ogden hyperfoam model *(Mills et al, 2003; Petre et al, 2005)* which constitutes several material parameters. Determination of these parameters through foam testing is important to provide data for the simulation of their service performances, product design and quality control. However, many of these models involve materials constants without physical meaning and it is a challenging task to determine these parameters. Conventionally, the determination of material parameters is based on the use of test samples with a standardised geometry under simplified strain state, such that particular conditions on the stress and strain field are satisfied in the sample/or part of the sample. Then the unknown model parameters are obtained using curve fittings from experimental data. For foam materials, a wide range of tests have been used (e.g. compression test, shear test, volumetric test, etc.) in order to predict these parameters *(Mills et al, 2003; Moreu and Mills, 2004)*. These methods normally require large numbers of tests and samples with well-defined geometries. In some cases, such as the shear test, the assembly has to use adhesives to bond the sample to the loading plate, this limits the strain level that can be reached by the maximum strength of the adhesive bond *(Petre et al, 2005)*. In addition the method is inconvenient or even impossible where standard specimens are not readily available, or for *in situ* monitoring the mechanical strength of the materials. Indentation test represents a much more simple form of testing, which simulates conditions of variable pressures and deformation. However, conventional hardness tests, such as the Shore method, requires special samples (at least 6 mm thick) and the method only provides information about the hardness of a sample, which could not be directly used to model the detailed material behaviours in service.

As demonstrated in Chapter 3, using numerical experimental data, the hyperfoam parameters can be determined from indentation tests. It is important to directly compare the results with standard methods with experimental data.

As shown in Figure 4.1 the material was tested using continuous indentation, compression and shear tests. As a comparison to the indentation method, the second approach used the uniaxial compression test only (designated "Com" method). The third approach combined the compression and shear test (designated "Com-Shear" method). Both methods have been used by several works in characterizing foams *(Kim et al, 2002; Mills, et al, 2003).* In these approaches, the resulting data were analysed using standard data fitting procedure in the finite element analysis software ABAQUS (ABAQUS 6.5 User's Manual) and have been widely used in research or industrial applications. The foam parameters (i.e. $\mu$ and $\alpha$) from the three approaches based on experimental data of identical materials have been directly compared. This would provide a scheme to systematically evaluate and compare the feasibility and accuracy of these three approaches.

### 4.2.2 Materials

Specimens required for standard tests and indentation tests were cut from the same batch of EVA foams commonly used for making midsoles of footwear (Figure 4.2). Round specimens were used for the compression and indentation tests, while square specimens were used for the shear test. Two foams with different hardness have been used, and five samples of each material in different loading states were tested. Data used in the parameter determination reflect the average of these five trials. All tests were performed at room temperature with the sample preconditioned prior to final data collection (*Petre et al, 2005; Kim et al, 2002*). The data from each test were then used to extract foam parameters.

### 4.2.3 Compression, shear tests and testing results

The uniaxial compressive and shear test were performed on a standard tensile testing machine (Figure 4.3(a)) (model: Tinius Olsen, H50KS) with a 5kN (HTE-5000N) load cell. For the uniaxial compression tests, round samples were pressed between two parallel steel plates (Figure 4.3(b)). The shear tests were performed using a specially designed testing rig (Figure 4.3(d)). As shown in Figure 4.3(c&e), the uniaxial movement will result in a uniform strain within the material in the compression tests while in shearing test, the movement of the cross head results in a shearing load from both ends of the specimen. This ensures that the sample is aligned to the central line. Both ends of the specimen were glued to the plate to ensure uniform deformation. Trials with failure at the glued interface were repeated to determine the maximum strain for the shear test (Petre *et al*, 2005).

Figure 4.4 shows a typical foam stress-strain data of the uniaxial compression and shear test. The compression curves exhibits typical regions reflecting the bending, buckling and densification *(Gibson and Ashby, 1997; Ren and Silberschmidt, 2008).* In the compression test, the sample was deformed to a strain up to 50% of their original thickness. Lateral strain was not collected. In the shear test, the loading plate was displaced vertically by 50% of the sample thickness to obtain a maximum shear strain (NB: Trials with failure at the glued interface were repeated to determine the maximum displacement for the shear test.). FE modelling showed that the strain level in the compression and shear test was comparable to the indentation tests.

### 4.2.4 The indentation testing system, machine validation and results

The indentation test system (Figure 4.5) used an actuator as the driving system. Low friction and zero backlash due to the direct drive nature of the actuator provide an excellent positional repeatability and ideal for a range of positioning and localised testing. The indentation system was mounted on a strong supporting frame and allows tests in both vertical and horizontal directions. A sensitive load cell (model: LCMS-D12TC-10N) is attached to the moving head of the actuator to monitor the forces

during the test. The indentation tests were performed using a spherical indenter made of stainless steel. Indenters with different sizes have been used and the force indentation depth data were then used as the input to the FE inverse modelling program to determine the foam parameters.

Figure 4.6 shows the test result on a silicone rubber block in comparison to the analytical solution. The properties of the material are known with a Young's modulus of 0.134MPa and Poisson's ratio of 0.49 (*Ren et al, 2006*). In this figure, the analytical result follows the following equation (*Johnson, 1985*)

$$F_z = (\frac{16R}{9})^{\frac{1}{2}} * \frac{E}{1-\nu^2} * \delta^{\frac{3}{2}} \qquad (4.2.1)$$

Where '$F_Z$' is the reaction force, '$R$' is the indenter radius; '$E$' and '$\nu$' is the Young's modulus and Poisson's ratio of the material, respectively; 'δ' is the indentation depth. As shown in the figure, the two sets of data showed good agreement when the indentation depth is less than 1mm (i.e. within the linear elastic range).

Figure 4.7 compares the foam test results with the newly developed machine and results on a standard testing machine (LLOYD instruments LR30K, 100N load cell). The indentation tests were performed with the loading curves up to different depths. It is clearly shown that the loading curve from the new machine is comparable with that from the standard tensile test machine, this suggests that the new indentation machine is accurate. Figure 4.7 also shows the material had identical loading curves at different depths but different unloading curves. The unloading curve is associated with the viscoelasticicty of the material, which is to be studied in future works. The unloading curves of the standard testing machine was not presented since the machine is screw driven and could not accurately test the unloading curve. The experimental results were highly repeatable and tests on different materials, including rubber and open cell foams, showed similar level of repeatability (results not shown). Figure 4.8 shows the test results with different test rates. The test rate of 2mm/s, 4mm/s and 8mm/s were used. The strain level used is suitable in quasi-static modeling of footwear in walking and running conditions *(Petre et al, 2005)*. Sensitivity tests by varying the strain rate showed no significant effect on the force displacement data within the testing range. As shown in the curves, the material exhibits hysteresis under indentation, however,

only the loading part was used in the parameter identification representing the resistance of the materials during loading. The viscoelastic and hysteresis were not considered in this work.

Figure 4.9 shows the test results on foams with different indenter sizes (R = 2, 4, 6 mm). The force with larger indenter sizes is significantly higher but the loading and unloading cycle is very similar for the same material. The loading curve represents the indentation resistance of the materials, which is the main focus of this work; the viscoelasticicty is to be studied in future works. Figure 4.10 compares the loading curve of these two materials, and shows that Foam 1 is softer than Foams 2. All the curves showed similar trends with clear stiffening effect at higher indentation depth, but the curvature of the curves are different, which could provide data to predict the material parameters.

### 4.2.5 FE modelling of indentation tests on EVA foams and material parameters identification

The mechanical behaviour of EVA foams can be described by the hyperfoam model as detailed in Chapter 3. Figure 4.11 shows the inverse FE modelling approach process, which consists of three main parts — experimental works, FE modelling and the inverse program. The input of the experimental results was in the form of force-indentation depth data. Parametric finite element studies (*Ren et al, 2006*) were used to generate series of models with material properties varied over the potential range. The numerical data were then processed to form simulation surfaces for each indentation depth, which represents the variation of the foams' indentation resistance, for different combinations of material properties at a certain indentation depth. The inverse program will explore the simulation spaces, starting from a given initial guessed value, to determine the optimum material properties (a set of material parameters) which produce numerical indentation results that best match the experimental data. Material stability was evaluated for the predicted parameter set using the ABAQUS Drucker stability test, which ensures a positive definite material stiffness matrix *(ABAQUS)* preserving stability over the range of supplied strains. To

avoid ill-conditioning in the program, a wide range of starting points have been used and the average value of valid points with lower minima was used to represent the true material properties.

Figure 4.12 shows the FE models used mimicking the geometry, loading and boundary conditions of the indentation test. Preliminary numerical investigations showed limited difference between 2-D and 3-D results for the indentation depths employed in this work. The element type used is CAX4R (an axisymmetric element). Contact has been defined at the indenter and sample surface, with finer meshes used, in the regions underneath and around the indenter to increase the accuracy of the model. The friction between indenter and specimen is assumed to be 0.5. Sensitivity tests have been performed on the influence of mesh size, boundary conditions, and frictional condition, in order to ensure the FE model is accurate with an optimum requirement on computational resources. The experimental data was smoothed by using polynomial fitting method. Typical fitted data is shown in Figure 4.13 and Figure 4.14 for Foam 1 and Foam 2.

As described in section 3.4, the simulated force-indentation depth data has to be transformed into a discrete form. Figure 4.15 shows typical simulation surfaces at the indentation depth of 1.5mm and the indentation depth of 3.5mm. The parameter '$\mu$' ranged from 0.008 to 0.8 (MPa) and the parameter '$\alpha$' ranged from 0.08 to 12. Figure 4.16 illustrates the property searching process with initial values of $\mu_0$=0.50 MPa and $\alpha_0$=2.0. At each indentation point, the program searches for a combination of material properties which give the best fit to the target point (on the experimental curve). As shown in the Figure, the fitting process involved significant scatter in the initial stage starting from the initial value. In the later stage, the predicted results came closer to stable values. Similar to the method used in the blind test, a range of initial value and the average value of the predicted data was used to compare to the results fitted from conventional shear and com-shear tests.

Figure 4.17 compared the average value of $\mu$ and $\alpha$ of the two foams from the indentation method, compression, and combined compression-shear method for the same foam. The data from the indentation tests represents the average data from the

converged results. The prediction from the indentation methods showed comparable results to the combined com-shear tests and the results from the indentation tests were comparable. This suggests that indentation approach is a feasible approach. The result from uniaxial compression is significantly different from the indentation method and combined compression-shear method therefore it is not suitable for complex loading situations. Figure 4.18 shows the predicted force-indentation depth curves using parameters extracted from compression, compression-shear test and indentation (spherical indenter radius is 4 mm and 6mm) of foam 1. As shown in the figure, the simulated force-indentation depth curves with parameters from indentation and combined com-shear tests showed good agreement with the experimental results. To further assess the results and robustness of the approach to more complex loading condition, indenter of different size were employed. By changing the indenter size, the ratio between indenter size and indentation depth varies, so varied the strain condition underneath the indenters *(Johnson, 1985).* Typical results shown in figure 4.19 compare the results from indentation data, combined com-shear data and uniaxial data with an indenter radius of 2mm of two foams. Figure 4.20 plots the stress-strain curves with the material parameters from the two methods, that is indentation and com-shear. The uniaxial compression stress-strain curve of the foams showed good agreement. These results clearly showed that material parameters predicted from the indentation approach are comparable to the results from standard combined com-shear test. This could be a significant step forward in the testing method of polymer foams.

## 4.3 Indentation test of the human heel pad *in vivo* and inverse parameters identification

### 4.3.1 *In vivo* heel pad testing and results

Figure 4.21 shows the testing frame, the position of the indenter and the human heel. In the test, the subject put one foot on top of a rigid platform. The indenter is moved upward through a hole in the platform to compress the heel pad. An adjustable locking collar with a diameter much larger than the hole was used as one of the mechanical stopper to ensure the indenter will be stopped upon contact with the platform. The system used an actuator (LinMot PS01-23x160) as the driving system, which was mounted on a flexible supporting frame to allow tests in both vertical and horizontal directions. A sensitive load cell (model: LCMS-D12TC-10N) is attached to the moving head of the actuator to monitor the forces during the test. The indentation tests were performed using spherical indenter made of stainless steel. Indenters with different sizes have been used and the force indentation depth data was obtained, which was then used in the inverse analysis.

As shown in Figure 4.6 and 4.7, the tester were validated against testing on samples with standard compression and simple shear tests before testing on human subjects. Three subjects were aged from 20-40 years subjects with no known skin disease or lower lime injuries. Tests on the subjects with or without foot trap were compared and showed no significant effect. All the tests were performed under comparable ambient relative humidity (30-35 % RH) and temperature (20-23 °C).

Figure 4.22 shows a typical force indentation depth data of one subject with both the loading and unloading curves. The experimental results were highly repeatable and tests on different subject are comparable with similar level of repeatability (results not shown). The strain level used is suitable in quasi-static modeling of footwear in walking and running conditions (*Petre, 2007).* Sensitivity tests by varying the strain rate showed no significant effect on the force displacement data within the testing range. As show by the curve, the material exhibited clear hysteresis under indentation, however, only the loading part was used to evaluate the method in the parameter

identification for the study of the resistance of the materials during loading. The viscoelastic and hysteresis were not considered in this work. Figure 4.23 shows the repeated tests on the same subject. There is some discrepancy of the data but, in general the repeatability is reasonable. The averaged data of at least three tests has been used to represent the results. Figure 4.24 shows the test data with different indenter sizes (R = 4, 6 mm) on three subjects. All the curves showed a similar trend with clear stiffening effect at higher indentation depth, but the curvature ratios of the curves are different. The tests also clearly picked up the inter-person difference between the three subjects. The data gained were then used to predict the material parameters.

### 4.3.2 FE modelling of the heel pad tests

A numerical model mimicking the geometry, loading and boundary conditions of the indentation test was developed using the software 'ABAQUS' (ABAQUS 6.5 User's Manual). A 2-D axial symmetric model (Figure 4.25) was used due to the axisymmetry of the spherical indenter. The element type used is CAX4R (an axisymmetric element) and contact has been defined at the indenter and the sample surface, with finer meshes used, in the regions underneath and around the indenter to increase the accuracy of the model. The friction between indenter and specimen is assumed to be 0.5. Sensitivity tests have been performed on the influence of mesh size, boundary conditions, and frictional condition, in order to ensure the FE model is accurate with an optimum requirement on computational resources.

### 4.3.3 Inverse parameter identification of linear elastic properties of human heel pad *in vivo*

Figure 4.26 shows typical inverse searching process. During the data fitting process, the program automatically search for the optimum set of material properties until a convergence is reached. To assess the robustness of the program or to avoid ill conditioning, a range of initial guessed values has been used and final result was

shown in figure 4.27. It is clearly shown that the result was focused within a reasonable range. The result in agreement with some published data but there are clear inter-personal differences. The Poisson's ratio is comparable and close to 0.5 which represents incompressible materials.

### 4.3.4 Inverse parameter identification of hyperelastic properties of the heel pad

Figure 4.28 shows typical inverse searching processes for the hyperelastic parameters with one (a) and two indenters (b). During the data fitting process, the program automatically searches for the optimum set of material properties until a convergence was reached. The final material sets give minimum difference between the simulated indentation curve and the experimental data. The results for the subjects are shown in figure 4.29 (a) and (b). As shown in the figure, the predicted hyperelastic material parameters from the single indenter (r=4mm and R=6mm) is slightly different with the results from the dual indenter is in the middle. As shown by the error bar, the results from the single indenter is much more scattered than that based on the dual indenters, this showed that the dual indenter method is a better approach.

## 4.4 Summary

In this work, the inverse FE modelling program developed has been used to characterise the properties of EVA foams and the human heel pads *in vivo*. EVA foams were tested using indentation, compression and shear tests, and the material parameters determined were directly compared. The prediction from indentation tests showed comparable accuracy to the standard combined compression-shear tests, while only compression testing could not predict the parameters accurately describing the material at complex situations. Advantages and disadvantages of each method were discussed. The parameters inversely predicted can be directly used in the design and simulation process. The tests on the human heel pad showed that this is feasible method and the single indenter method produce results slightly depend on the indenter sizes, while the dual indenters method resulted in a value more representative to the material with a smaller error range.

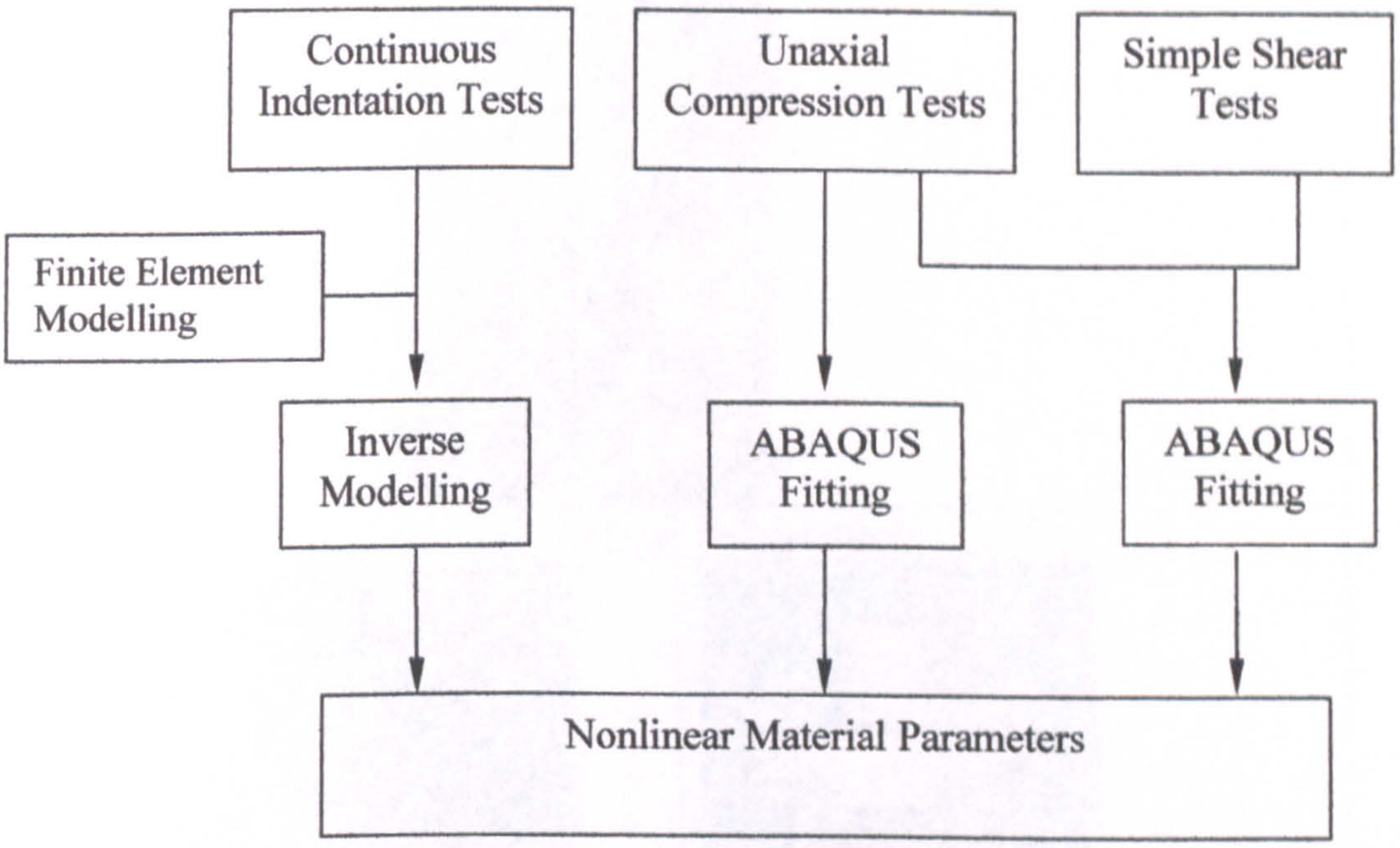


**Figure 4.1** Flow chart showing the three foam testing and data analysis approaches to determine the non linear material parameters of EVA foams (The approaches were designated as 'Inverse-Indentation method', 'Compression method' and Compression-Shear method, respectively)

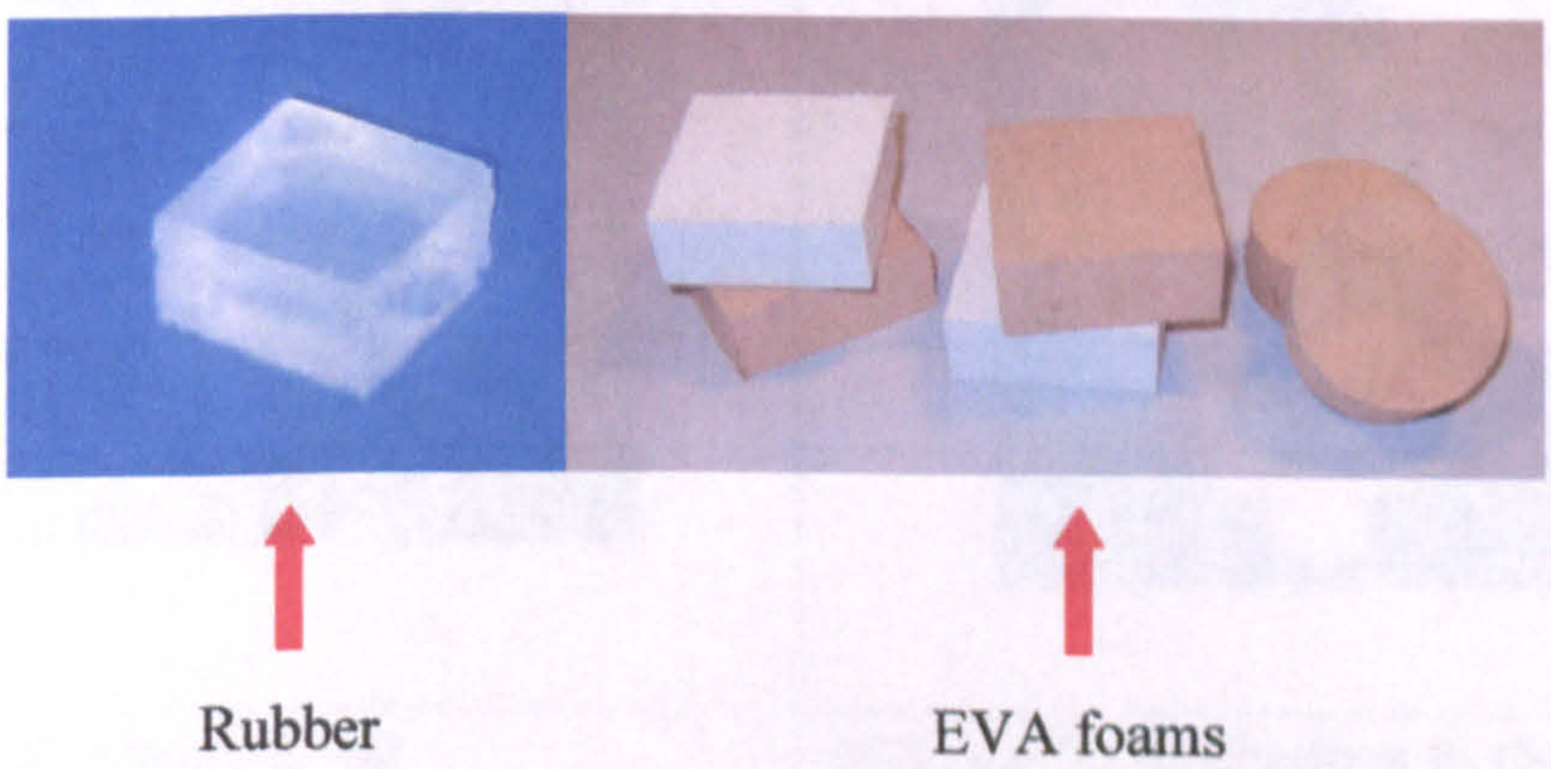


**Figure 4.2** Specimen of rubber and EVA foams.

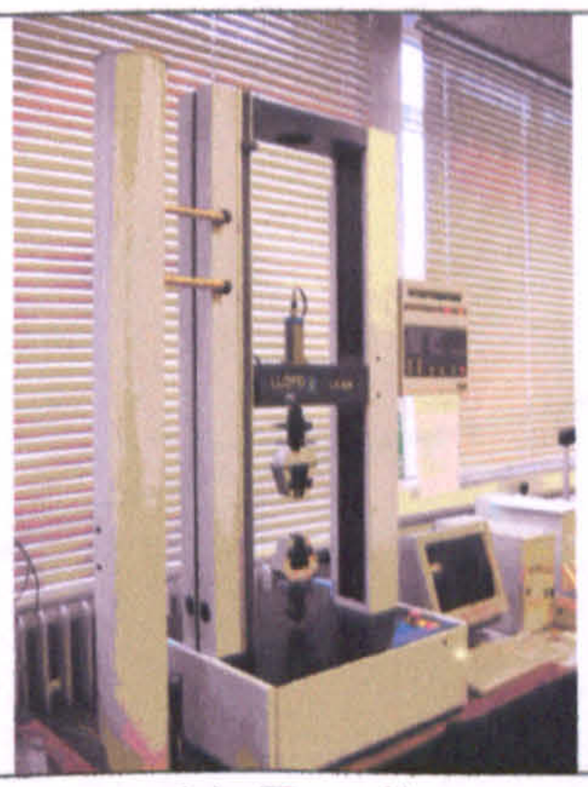

(a) Tensile test machine

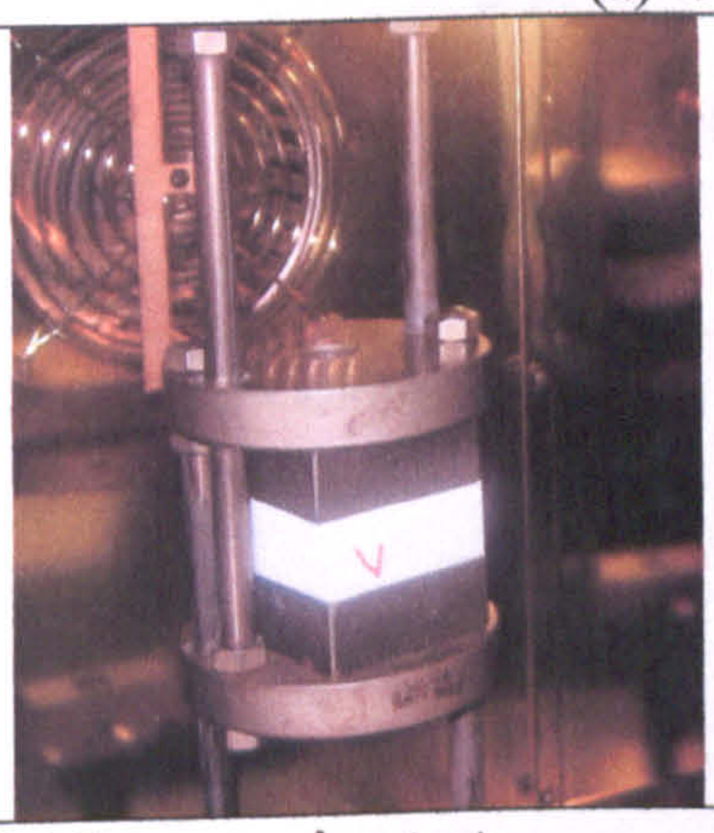

(b )Compression test

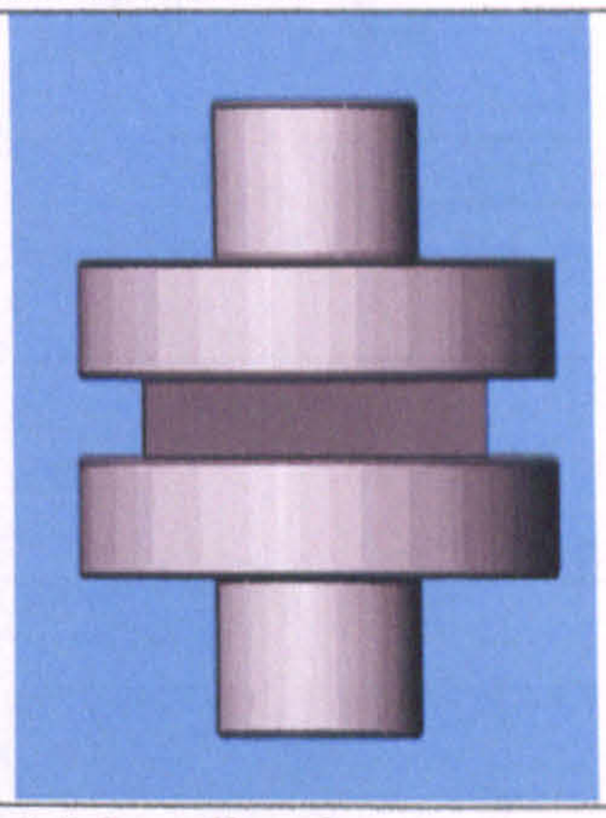

(c) Loading in compression tests

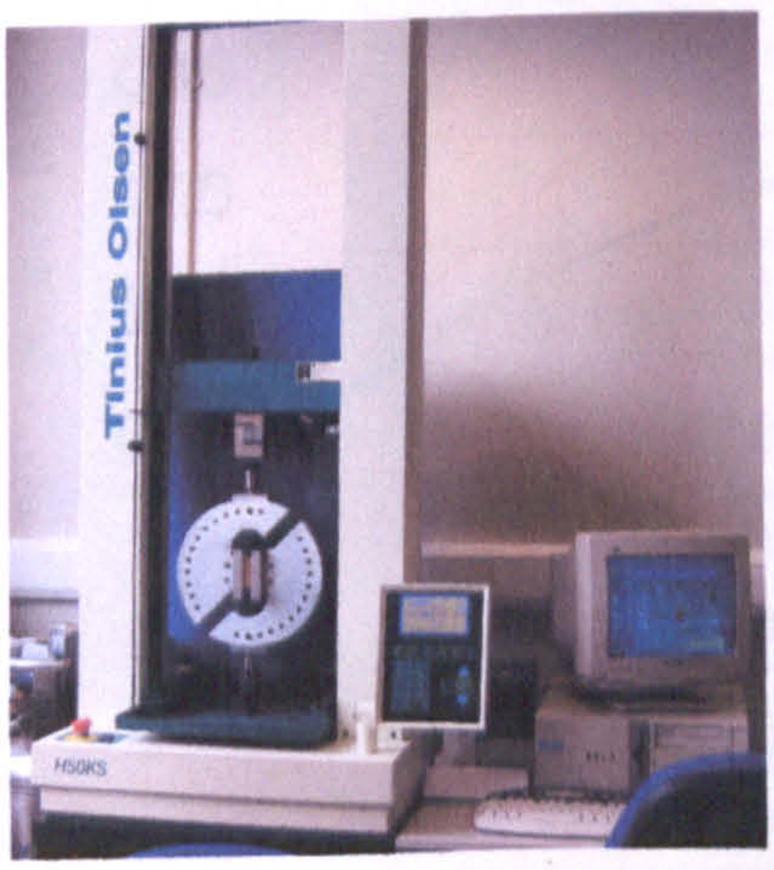


(d) Simple shearing test

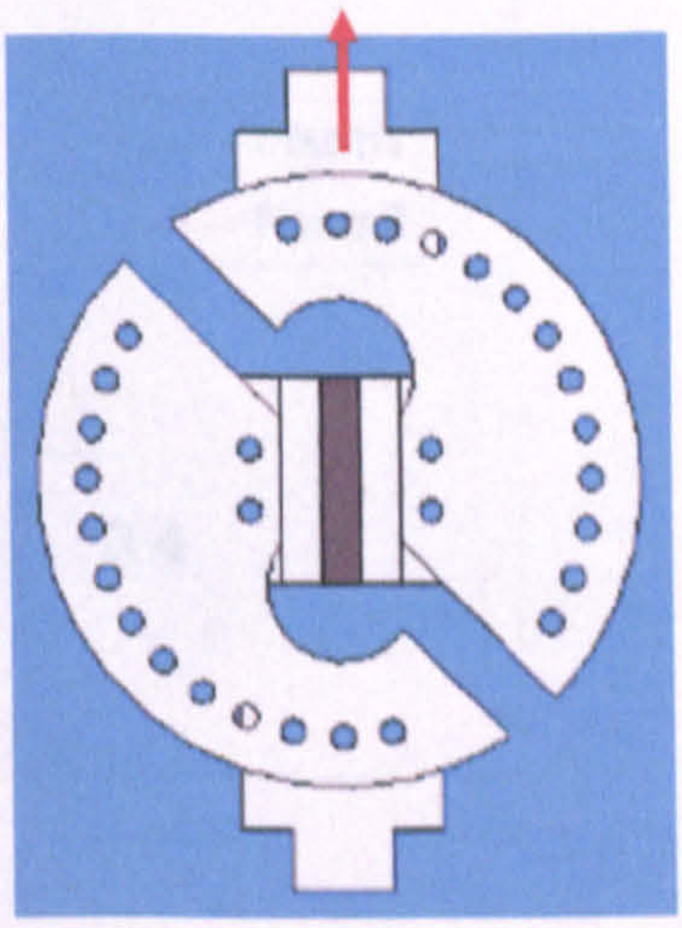

(e) Loading mechanism in the shear tests

**Figure 4.3** Set-up of the compression and simple shear tests.

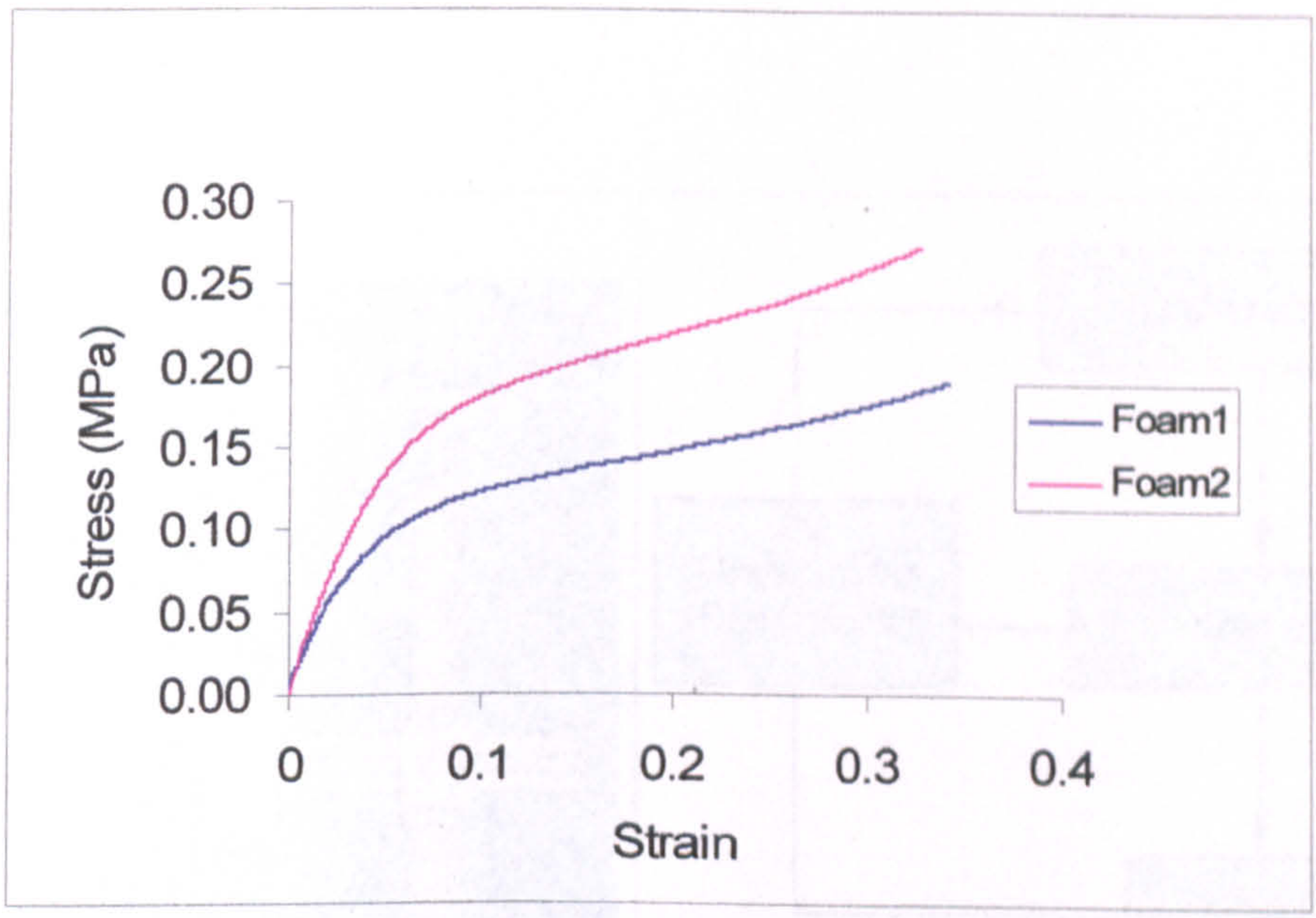


(a) Typical Compression Data

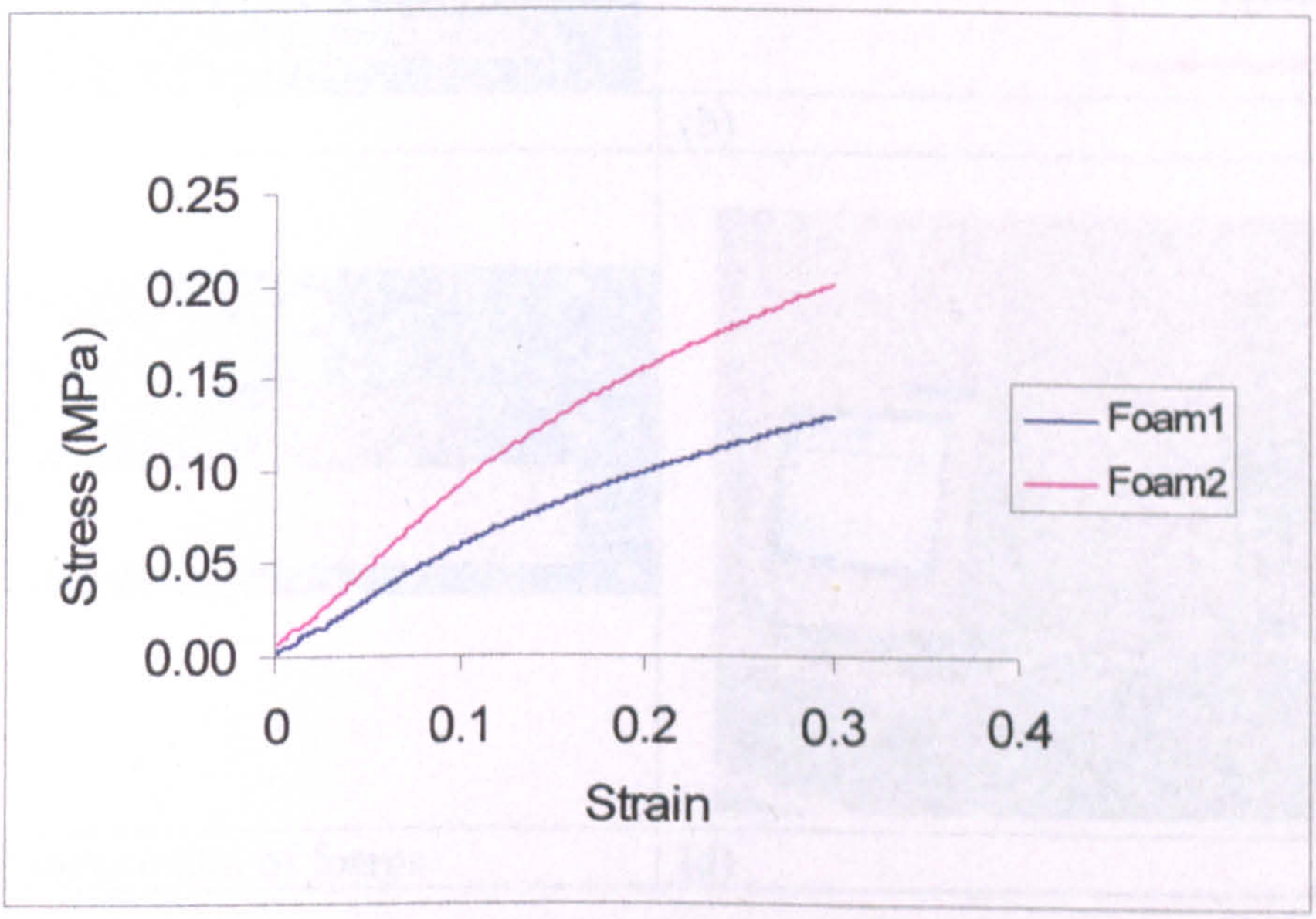


(b) Typical Shear data

**Figure 4.4** Typical stress-strain curves of EVA foams determined from compression test (a) and simple shear test (b).

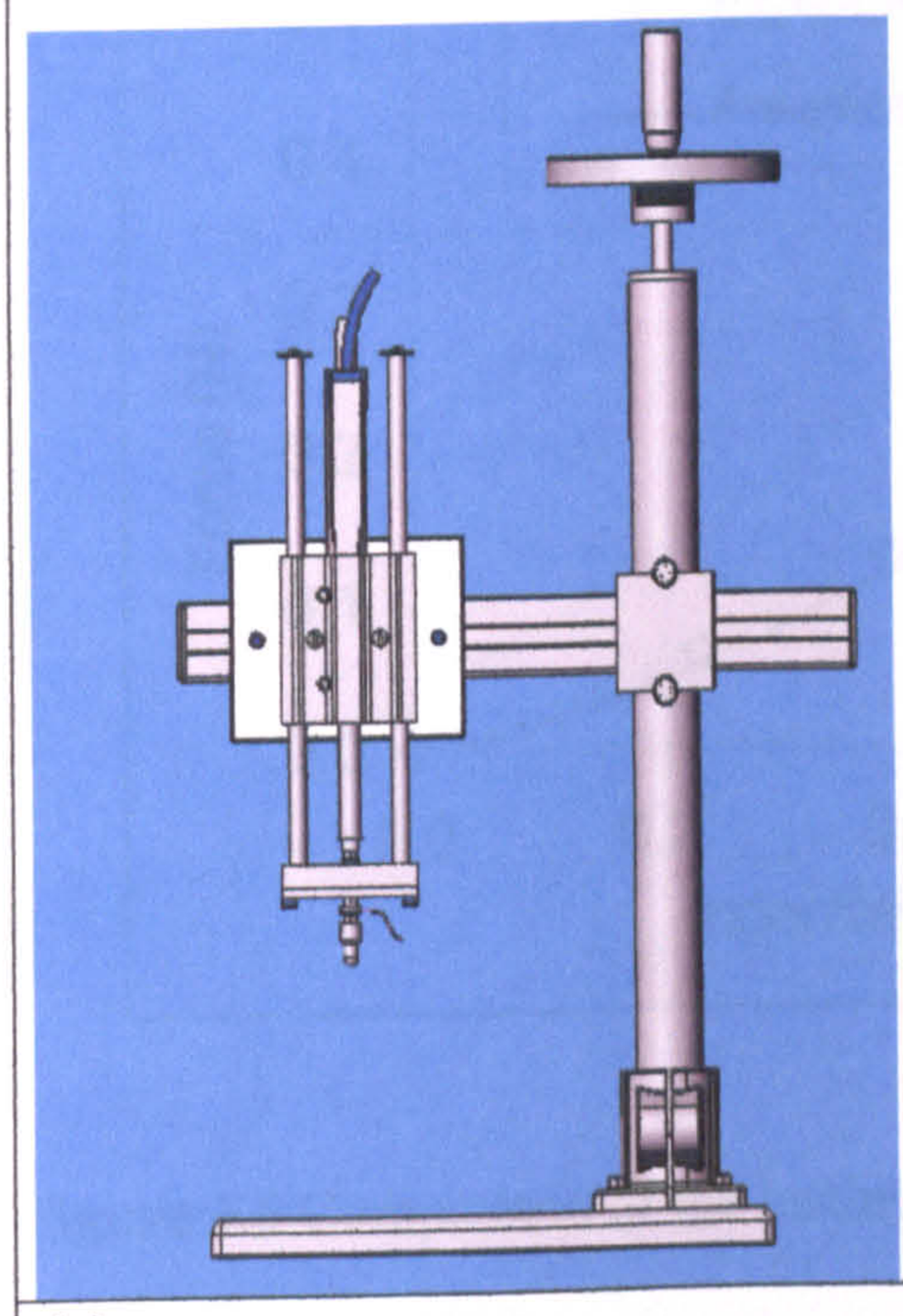

(a)

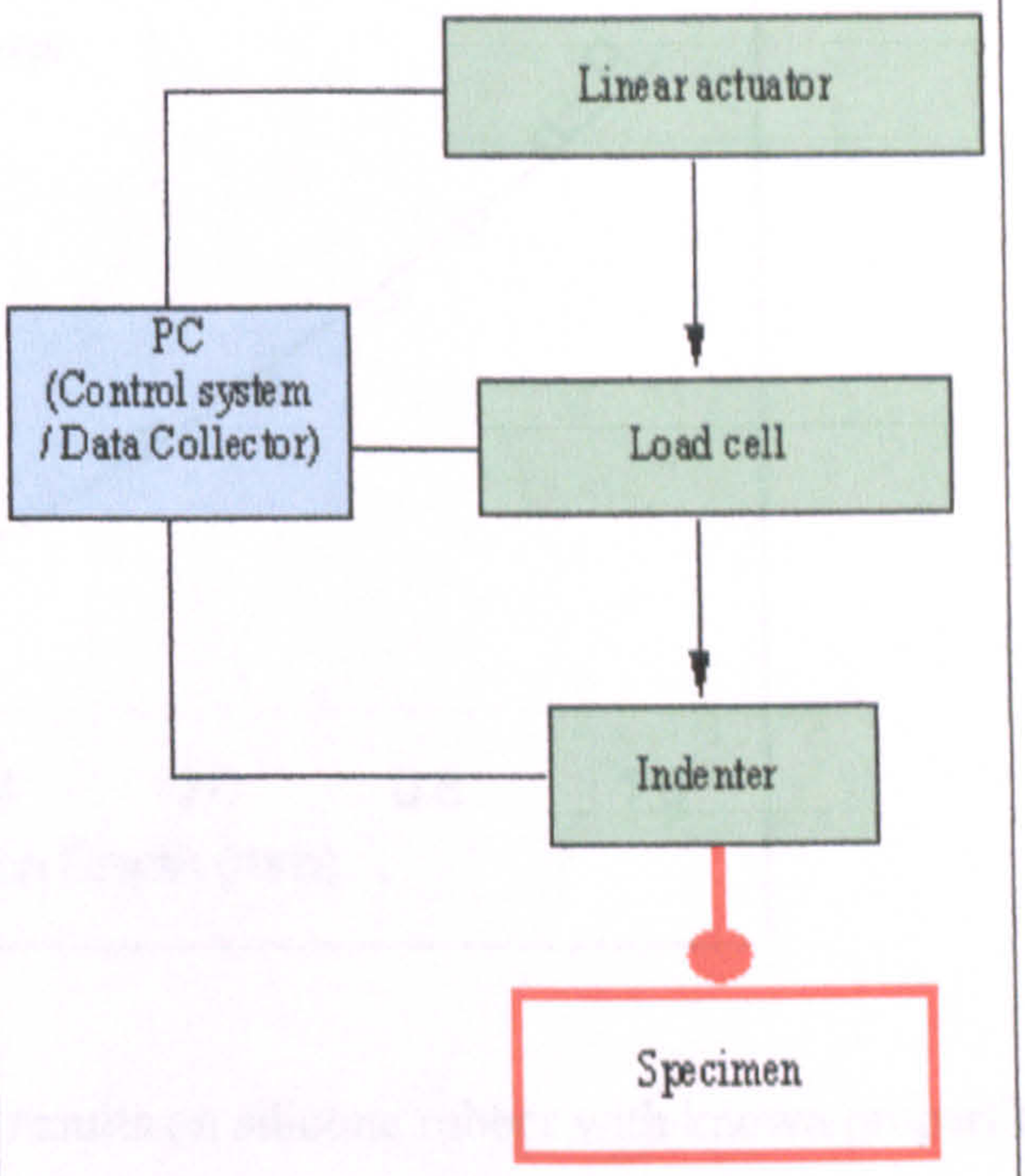


(b)

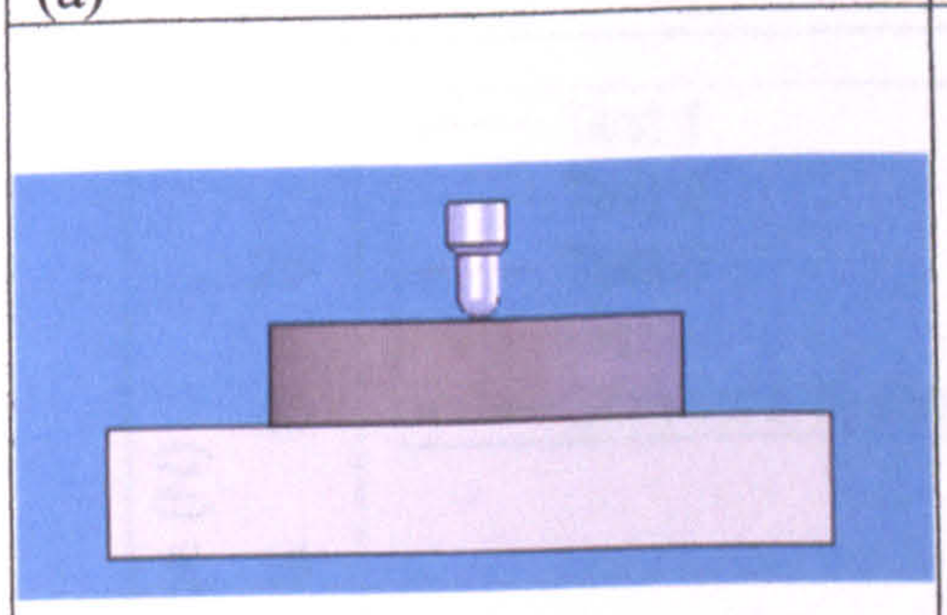

(c) Indentation of foams

(d)

**Figure 4.5** Structure of the continuous indentation testing system.

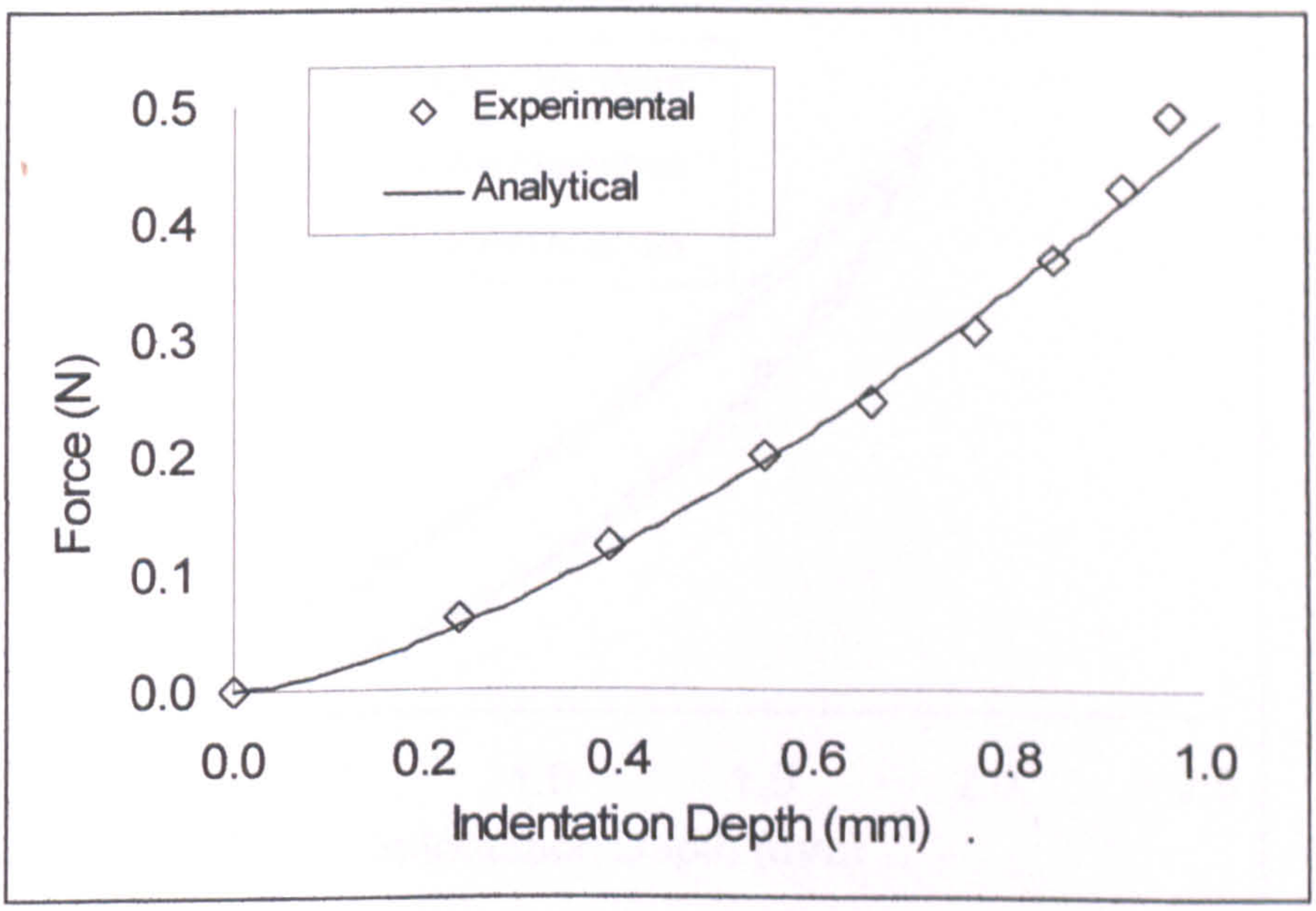


**Figure 4.6** Comparison of the testing results on silicone rubber with known properties and analytical results.

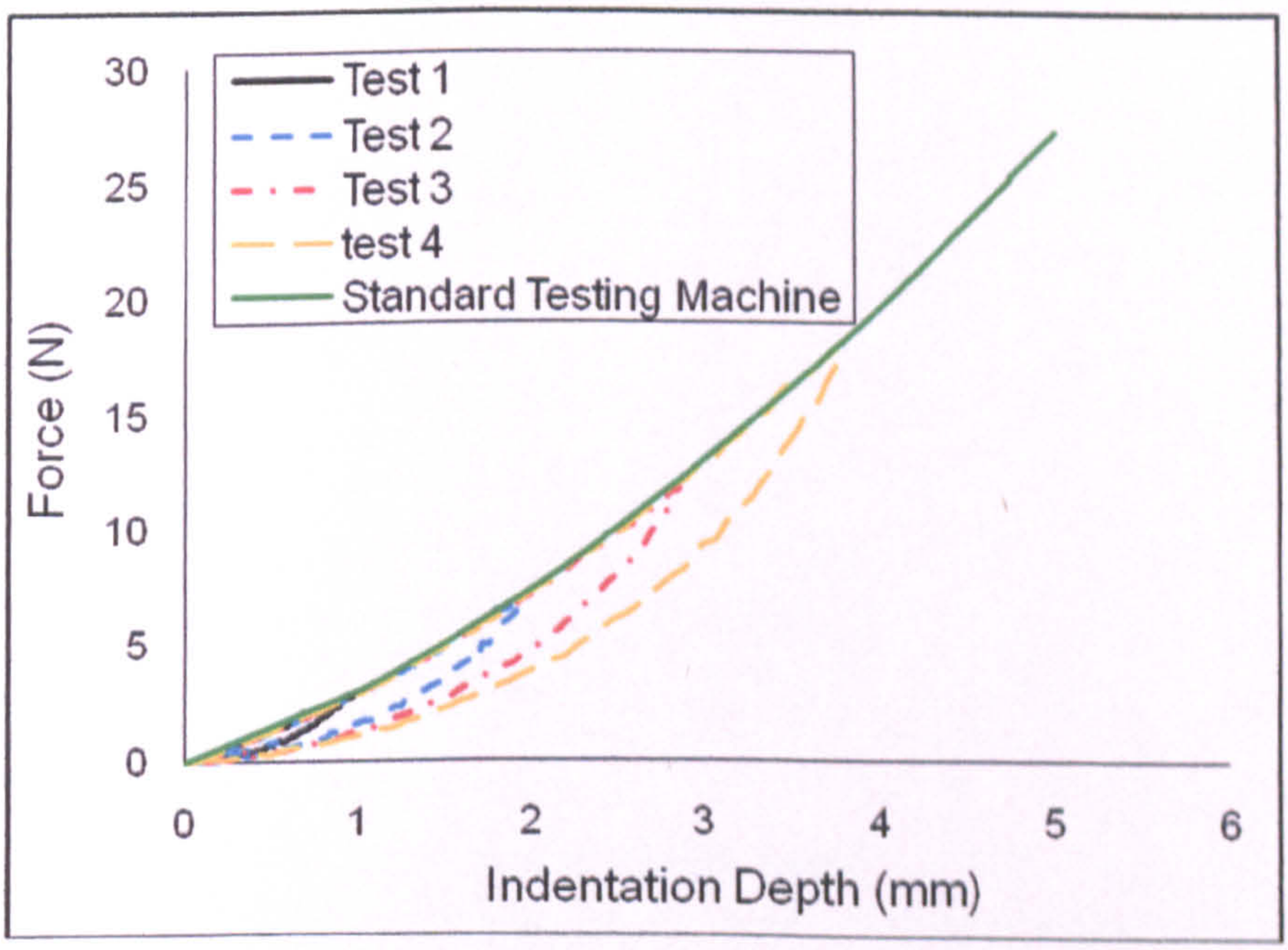


**Figure 4.7** Comparison of the testing results of EVA foams for different indentation depth using the newly developed machine and standard testing machine.

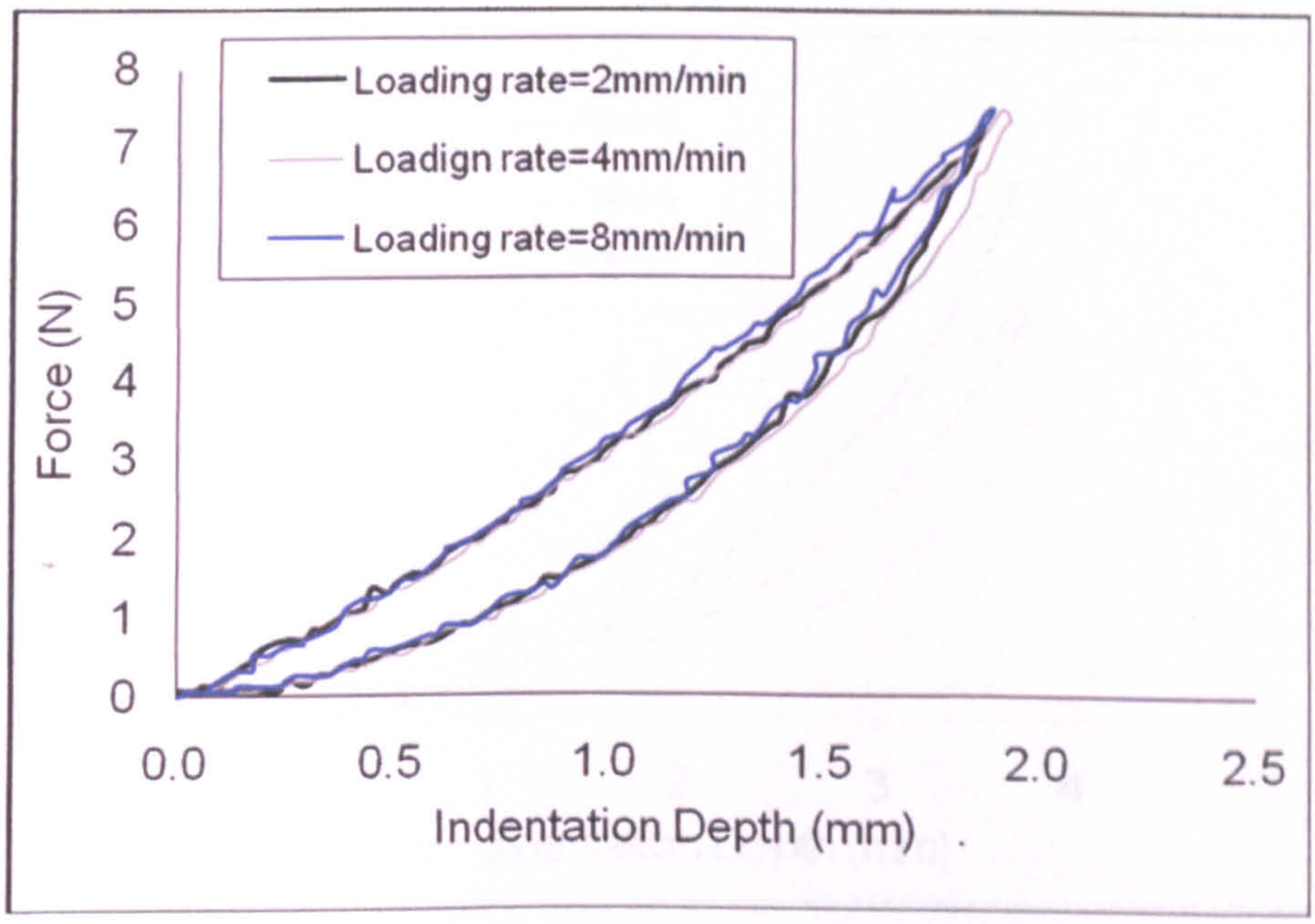


**Figure 4.8** Testing results on an EVA foam with different loading rates.

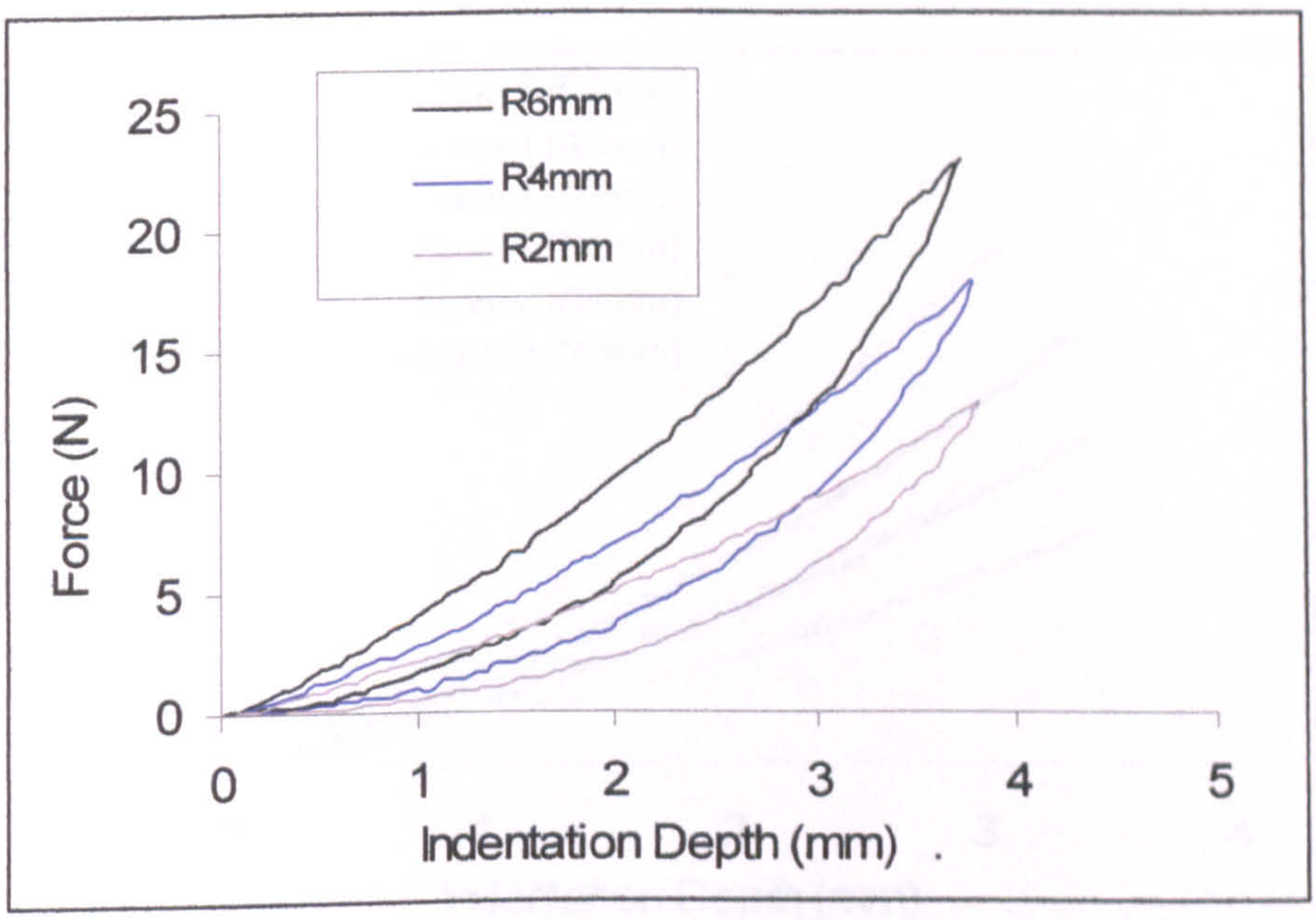


(a) Testing results with different indenter sizes for Foam 1.

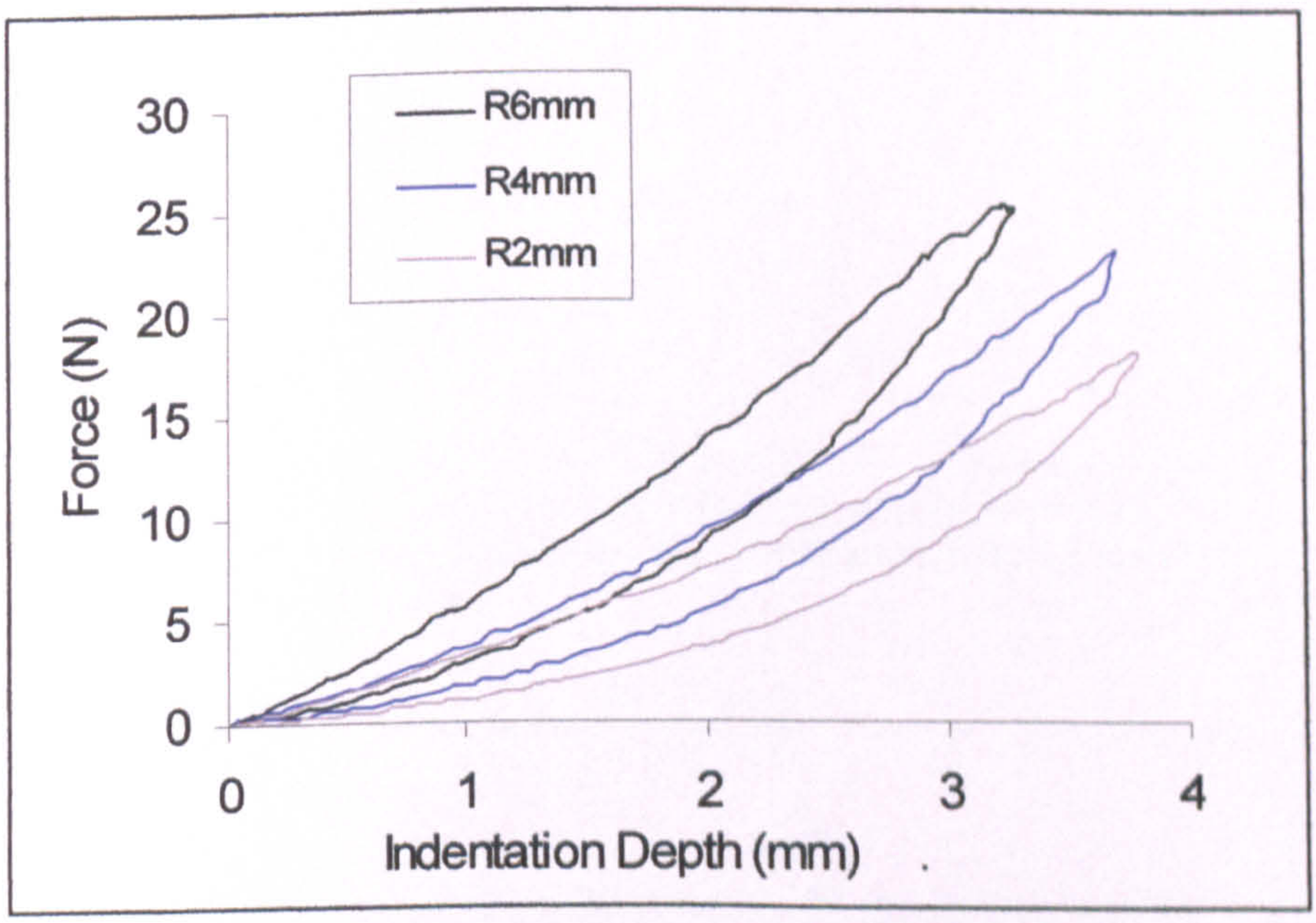


(b) Testing results with different indenter sizes for Foam 2.

**Figure 4.9** Test results with different indenter sizes on EVA foams (Loading rate =2mm/s).

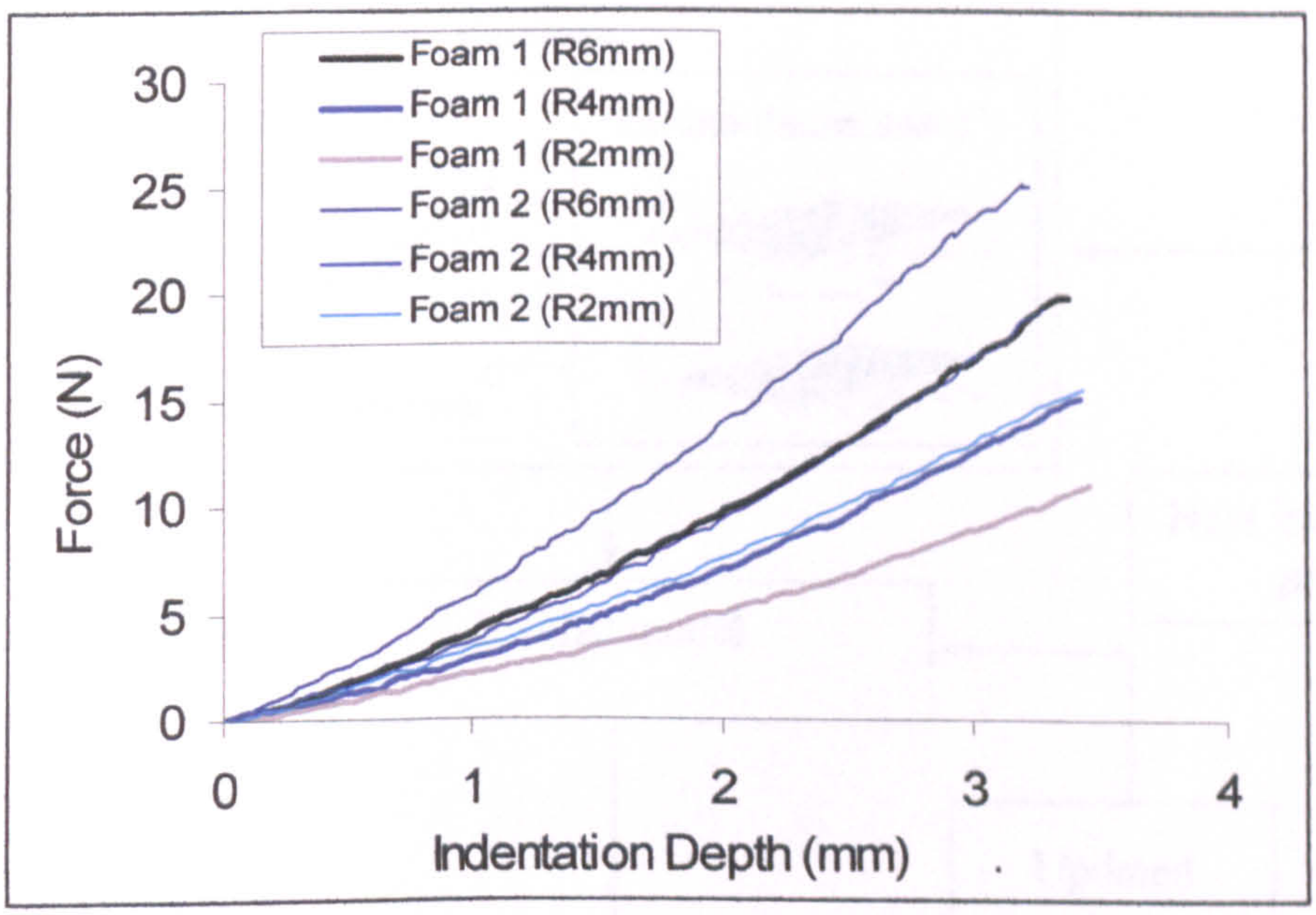


**Figure 4.10** Comparison of the loading curves of different EVA foams.

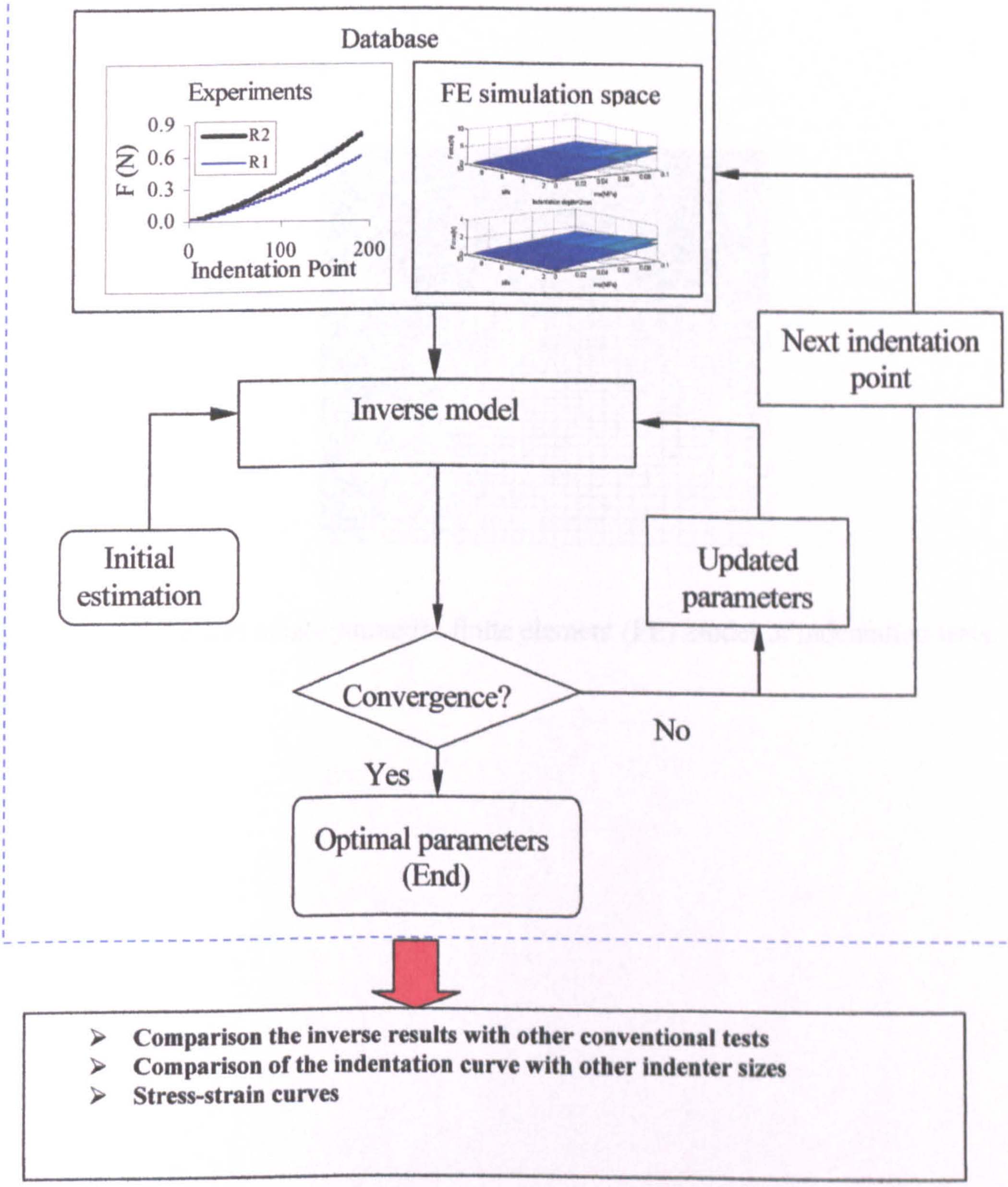


**Figure 4.11** Flow chart showing the inverse FE modelling approach to determine the foam parameters using loading curves of indentation tests and comparison of the results with other methods. .

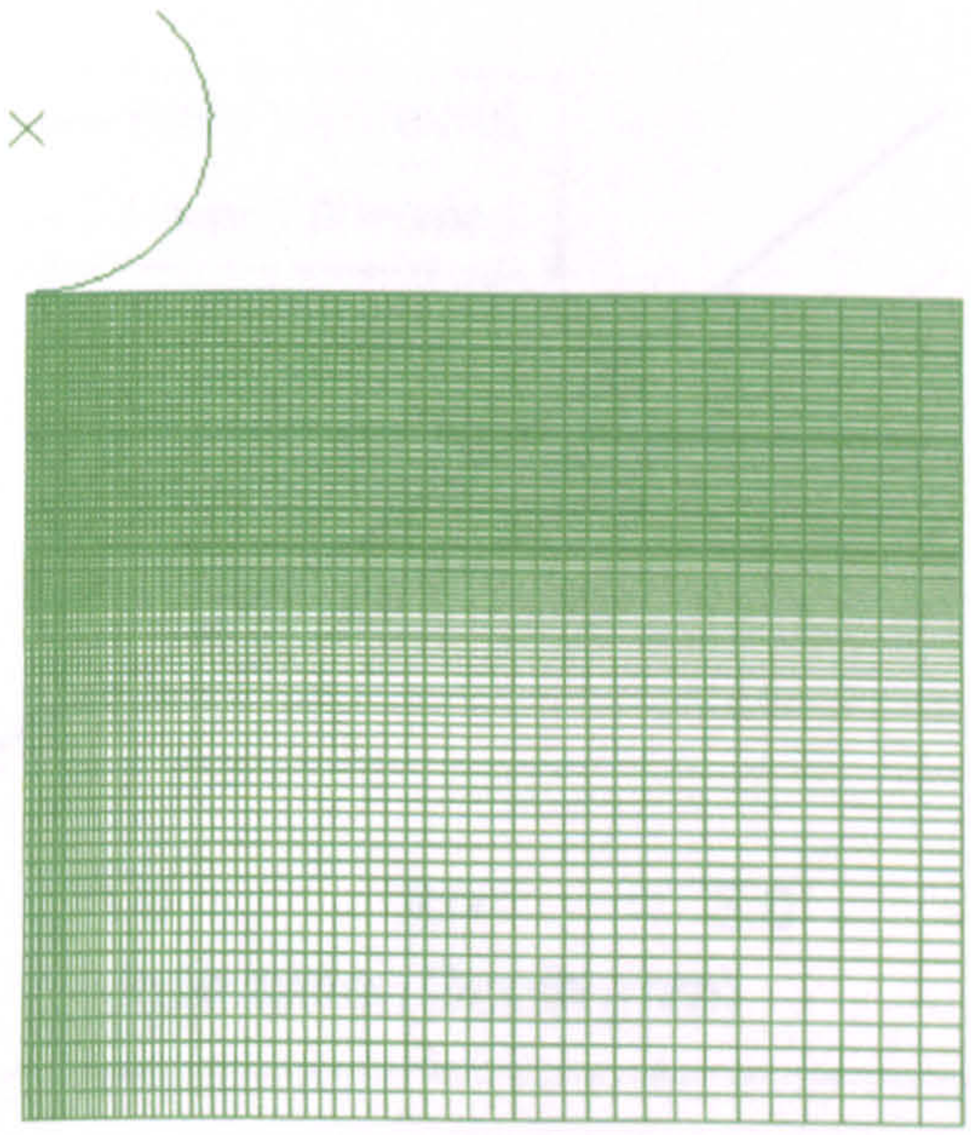

**Figure 4.12** Typical axial-symmetric finite element (FE) model of indentation tests.

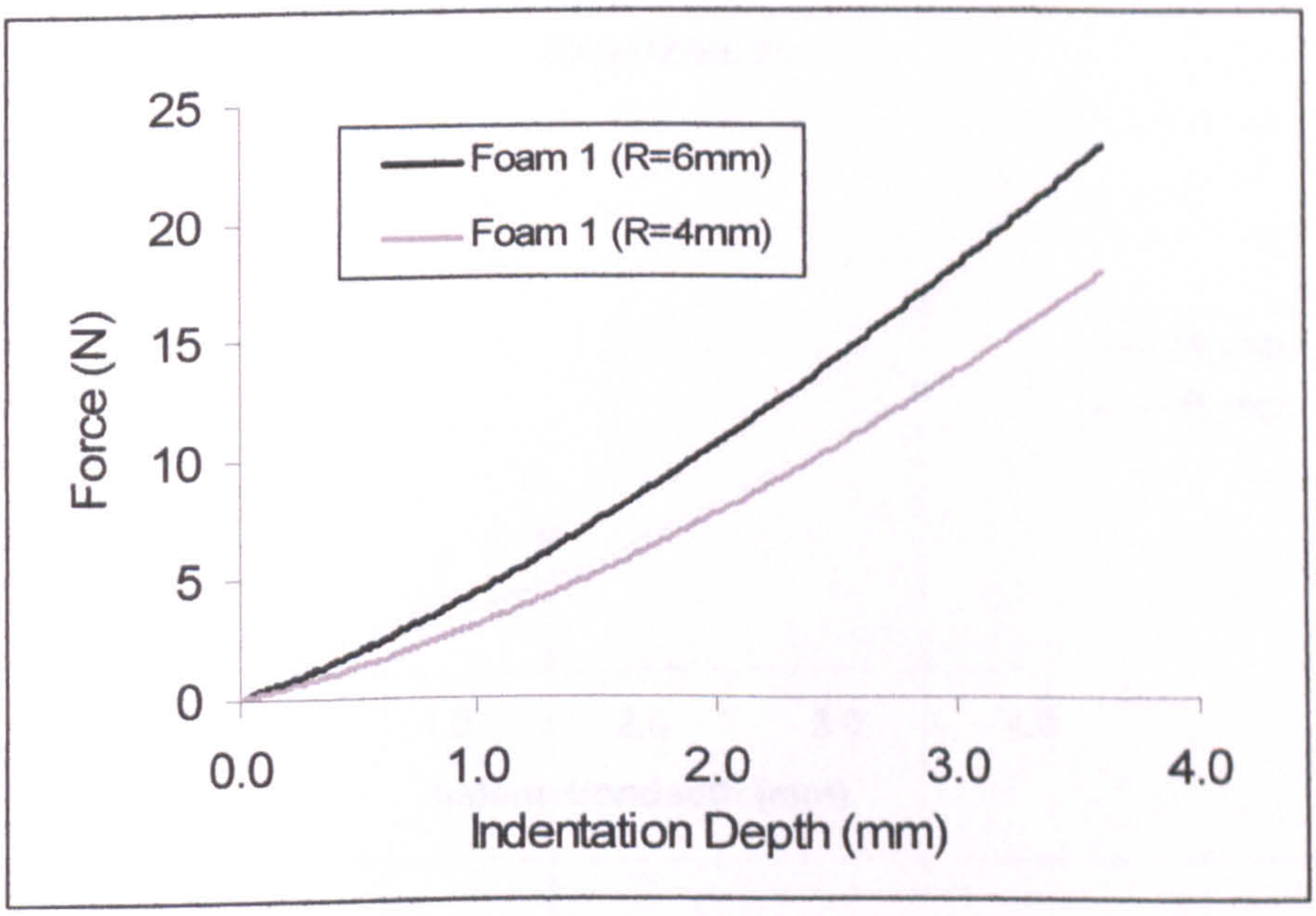


**Figure 4.13** Typical fitted force indentation depth data for different indenter sizes (Foam 1).

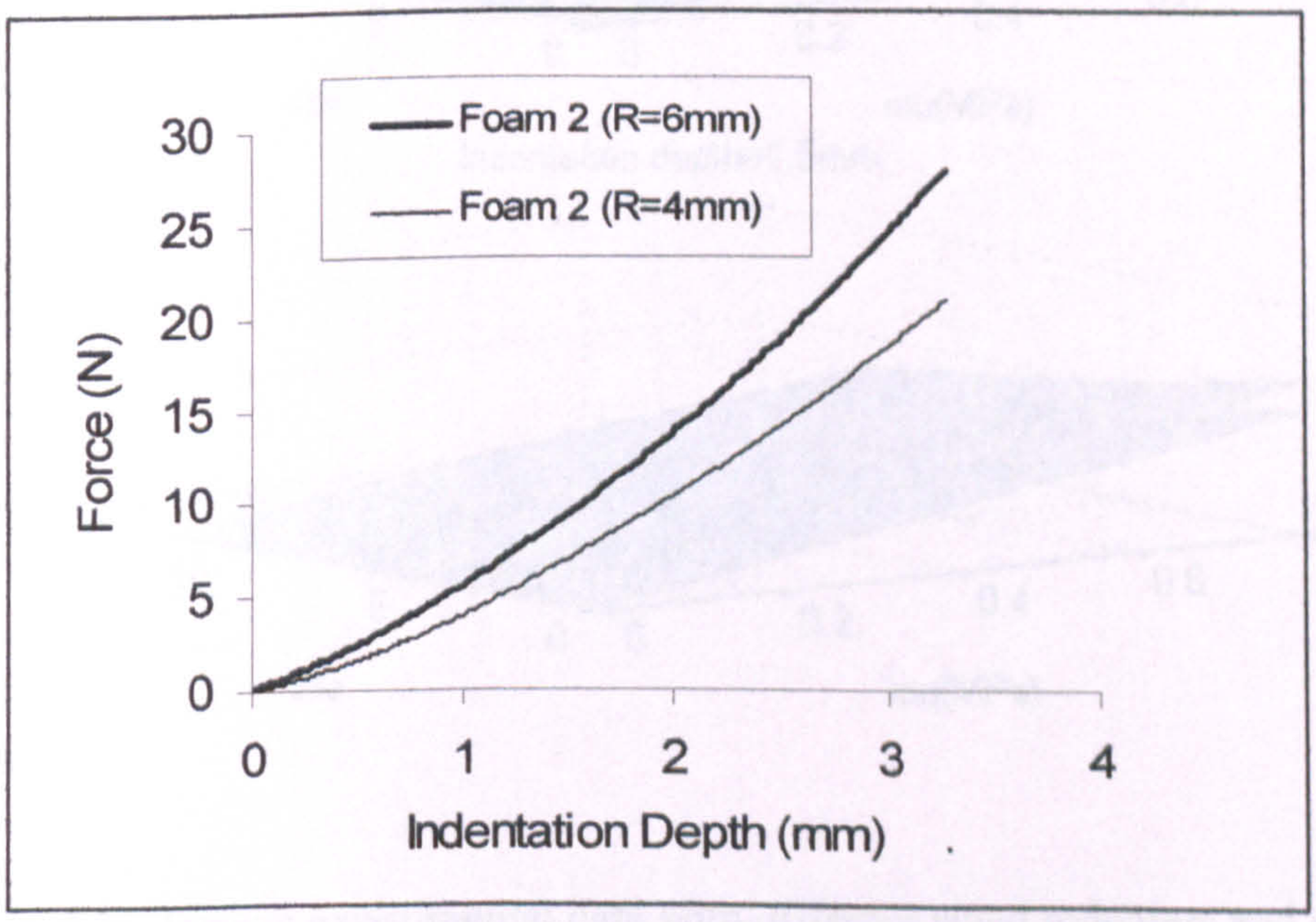


**Figure 4.14** Typical fitted force indentation depth data for different indenter sizes (Foam 2).

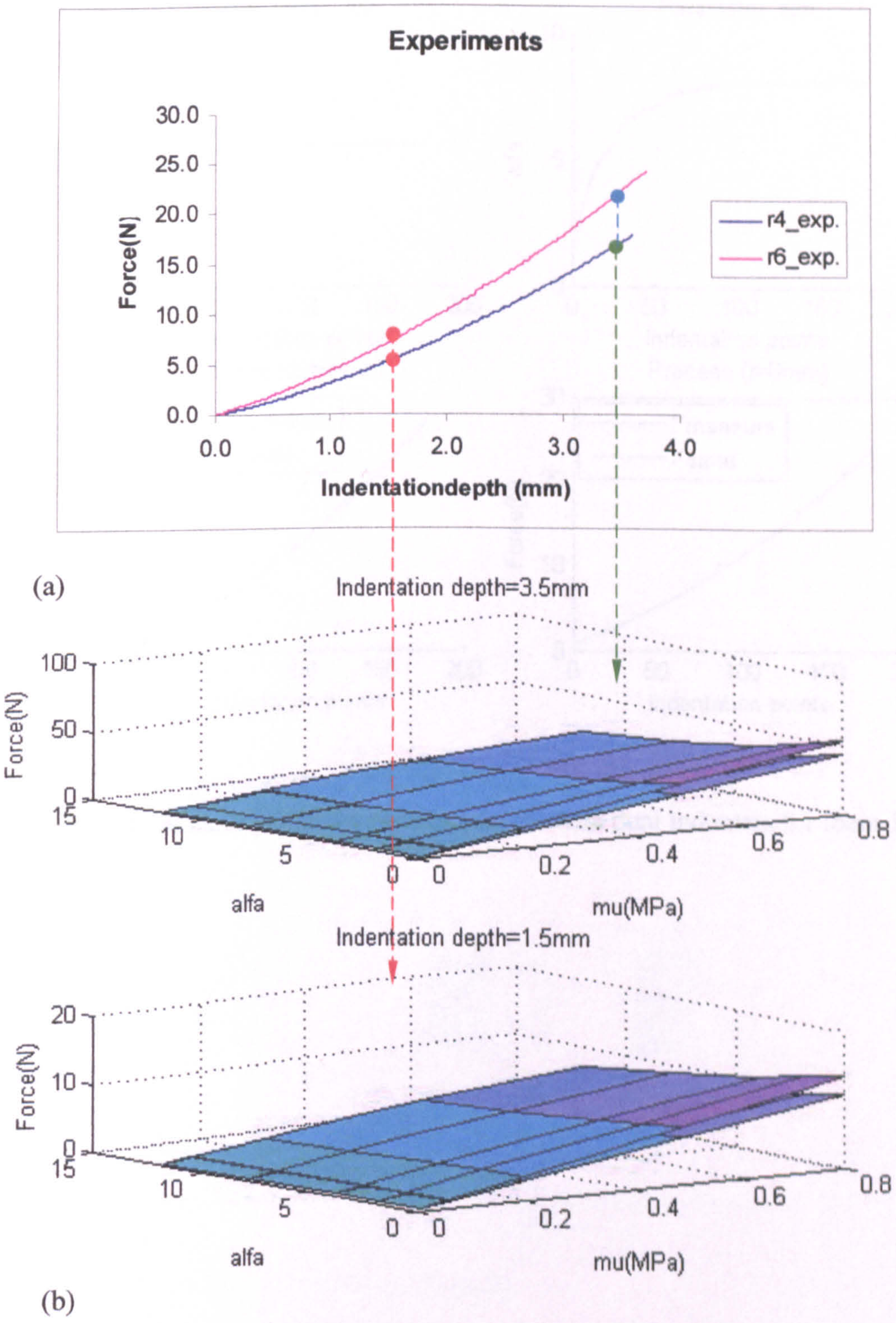


**Figure 4.15** Typical experimental data with different sized indenters and simulation surfaces at indentation depth of 1.5mm and 3.5 mm.

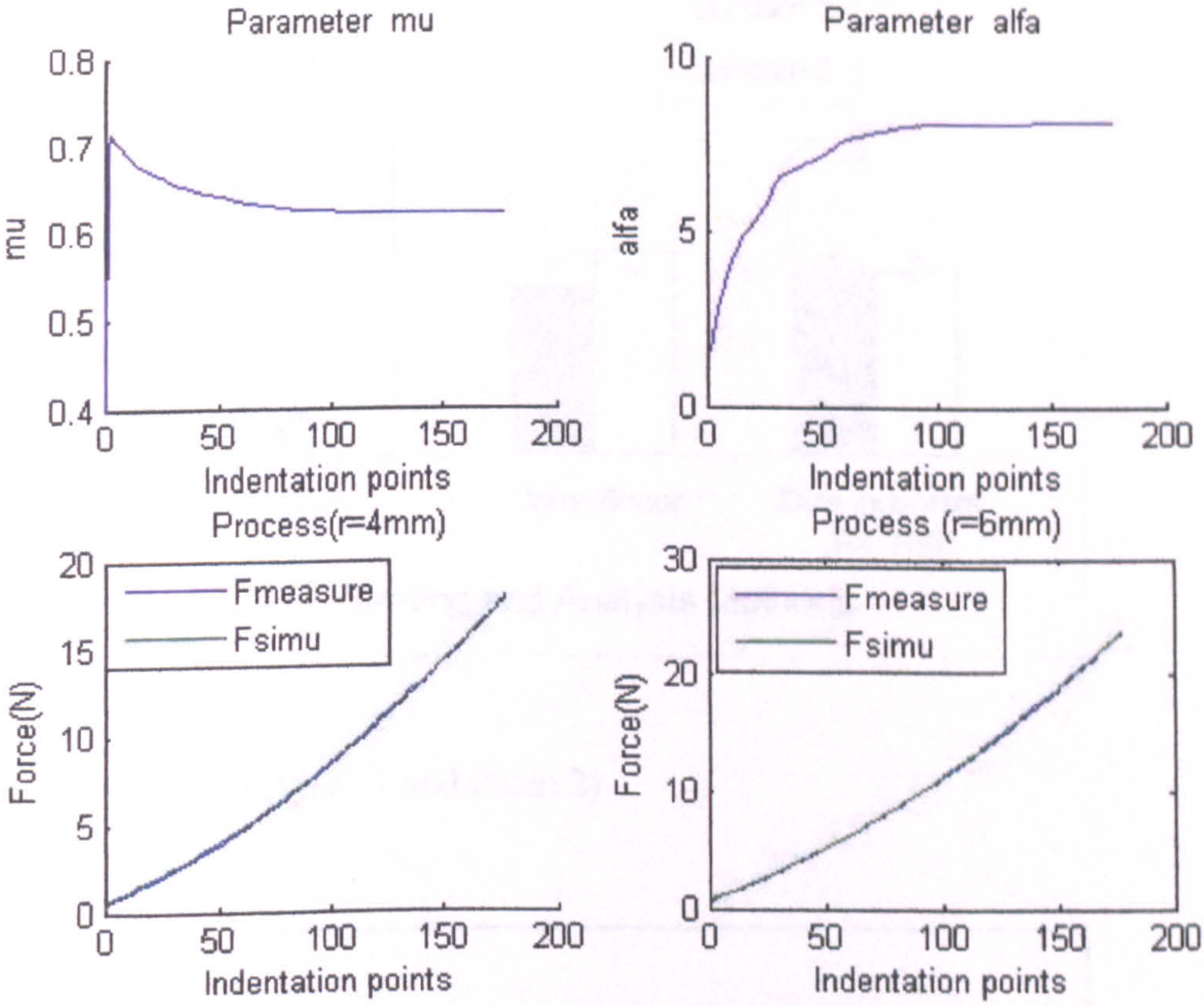


**Figure 4.16** Material parameters fitting process with dual indenters for foam 1.

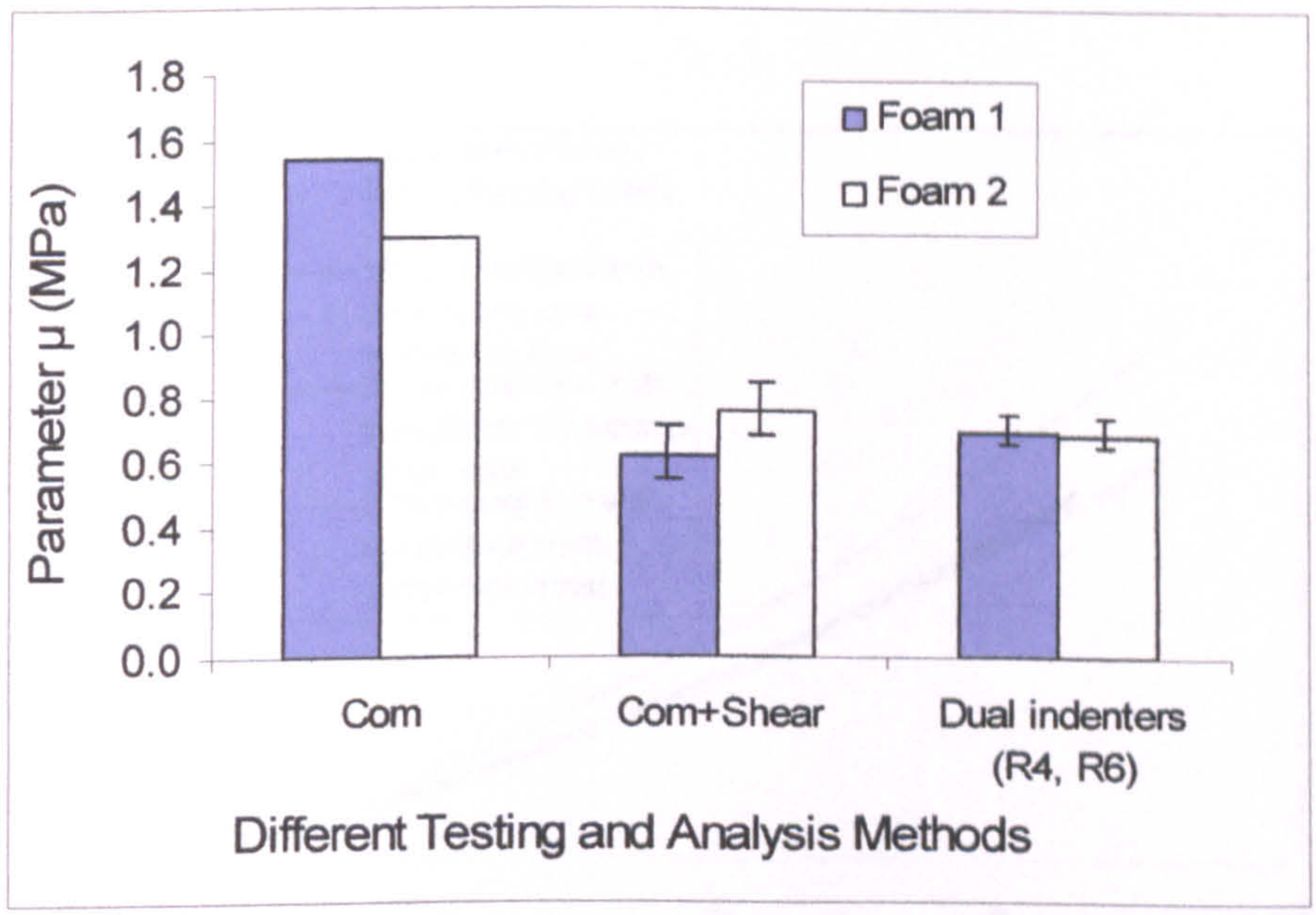


(a) Parameter μ (Foam 1 and Foam 2).

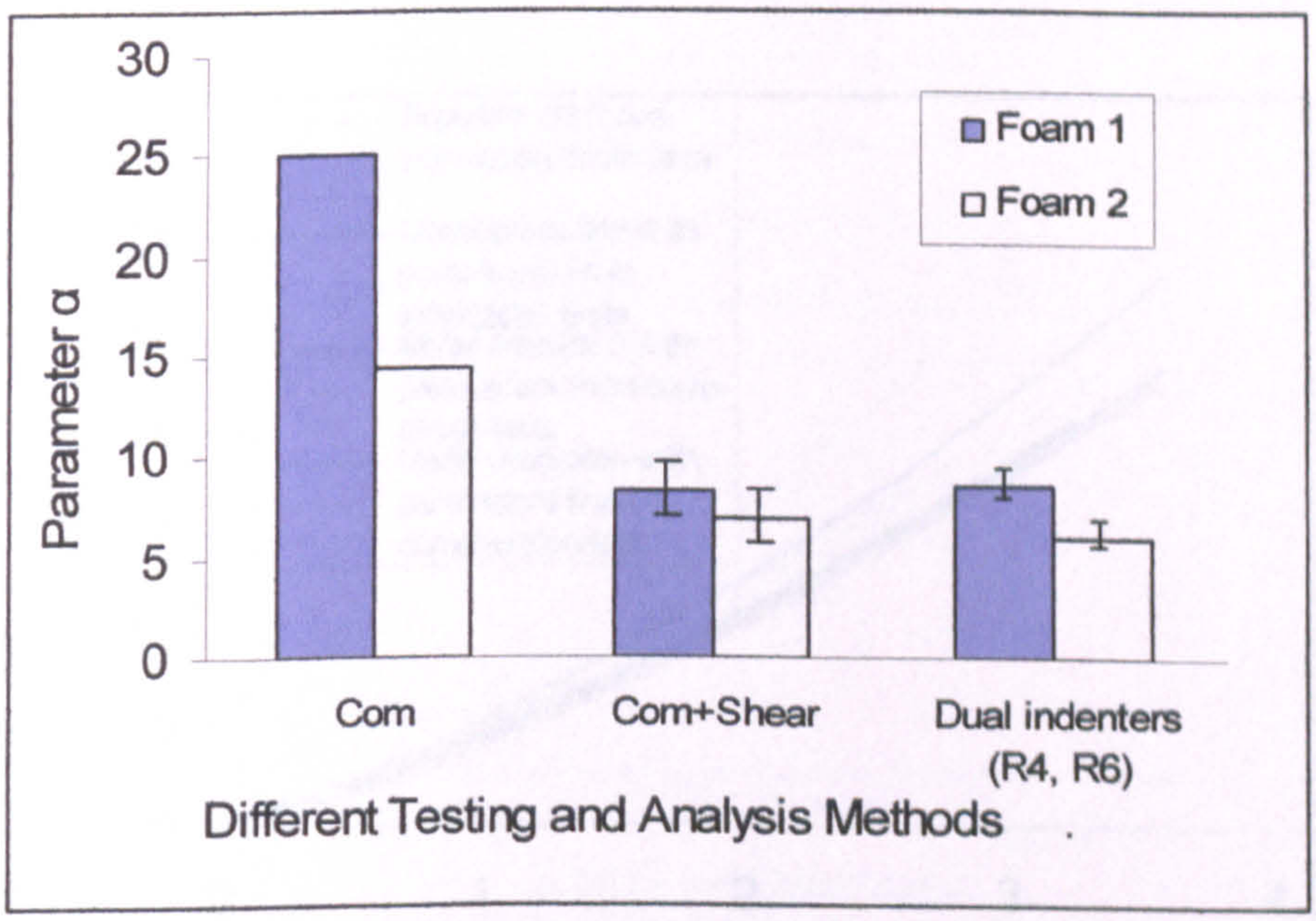


(b) Parameter α (Foam 1 and Foam 2).

**Figure 4. 17** Comparison of material parameters of EVA foams from the proposed inverse indentation approach, compression and com-shear methods.

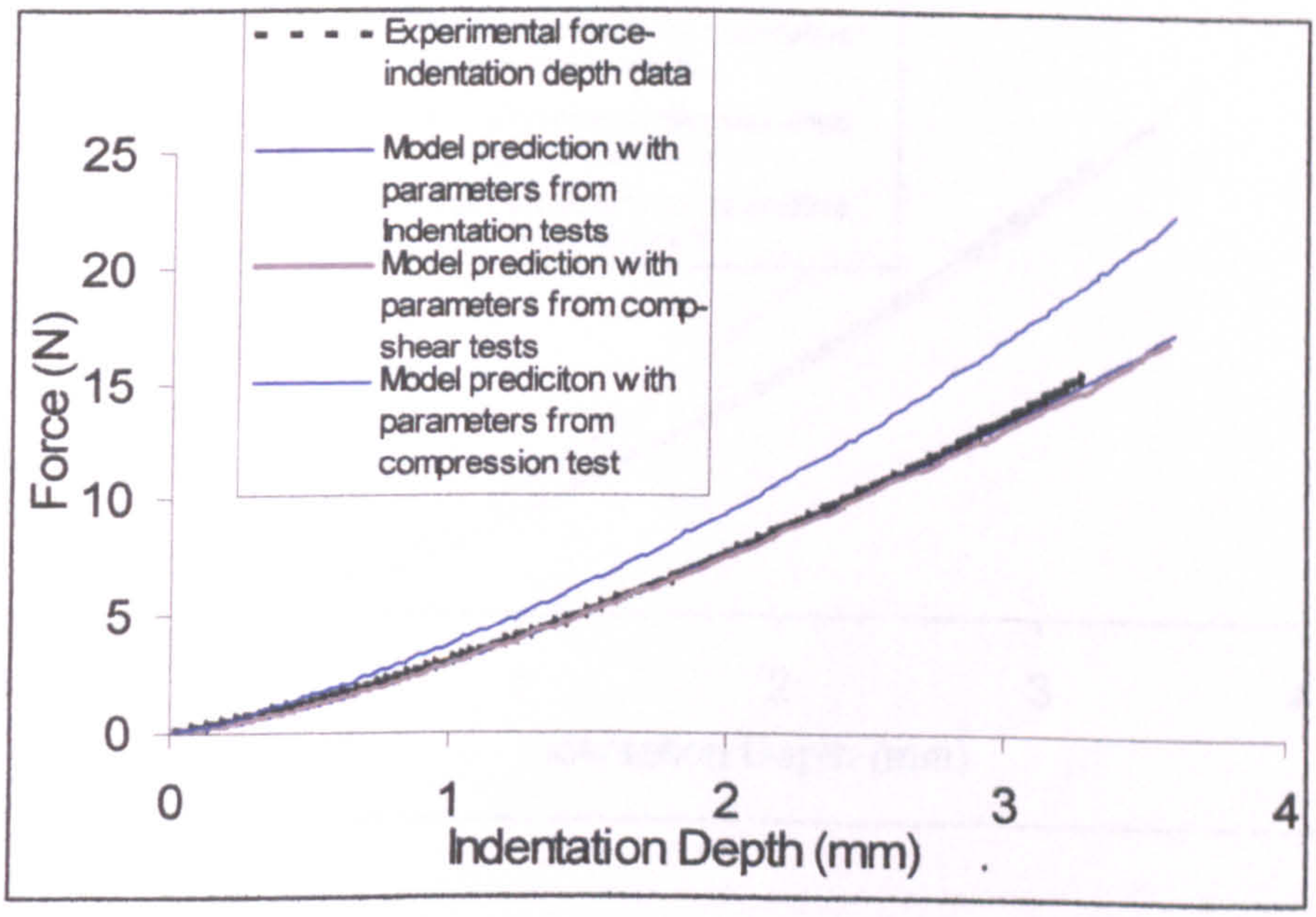


(a) Foam 1 (R=4mm)

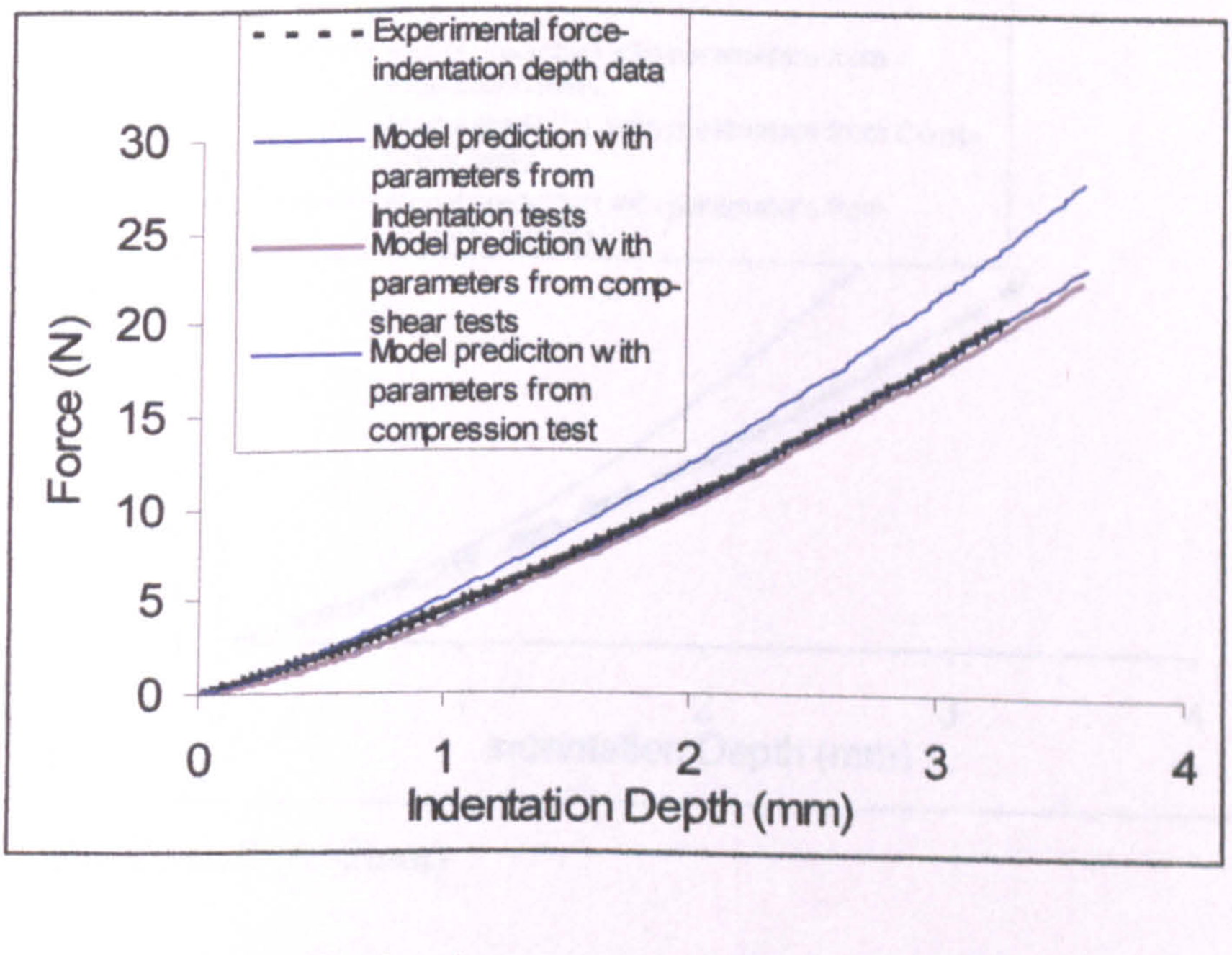


(b) Foam 1 (R=6mm)

**Figure 4. 18** The force-indentation depth curves with parameters extracted from different methods and the experimental results.

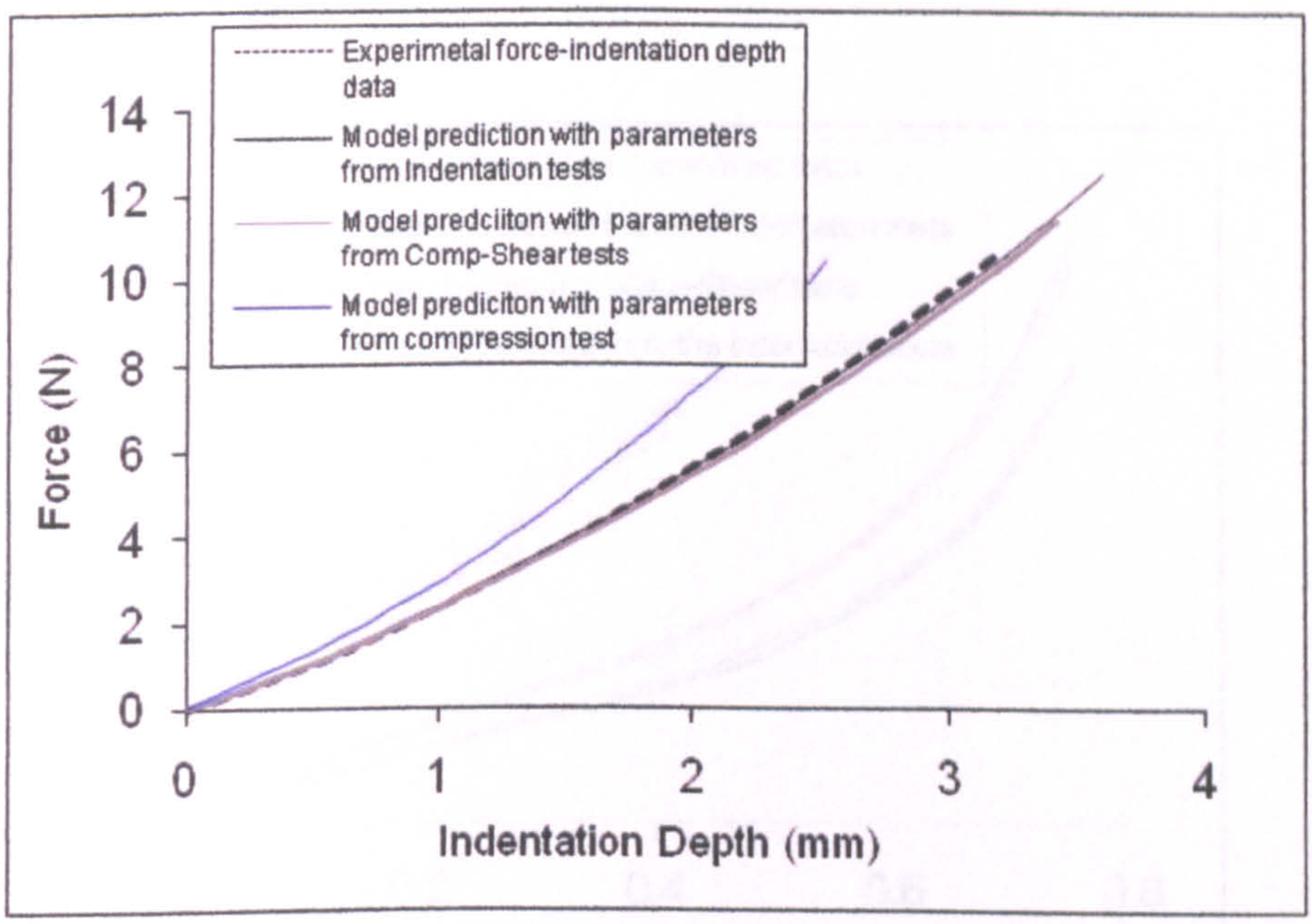


(a) Foam 1 (R=2mm)

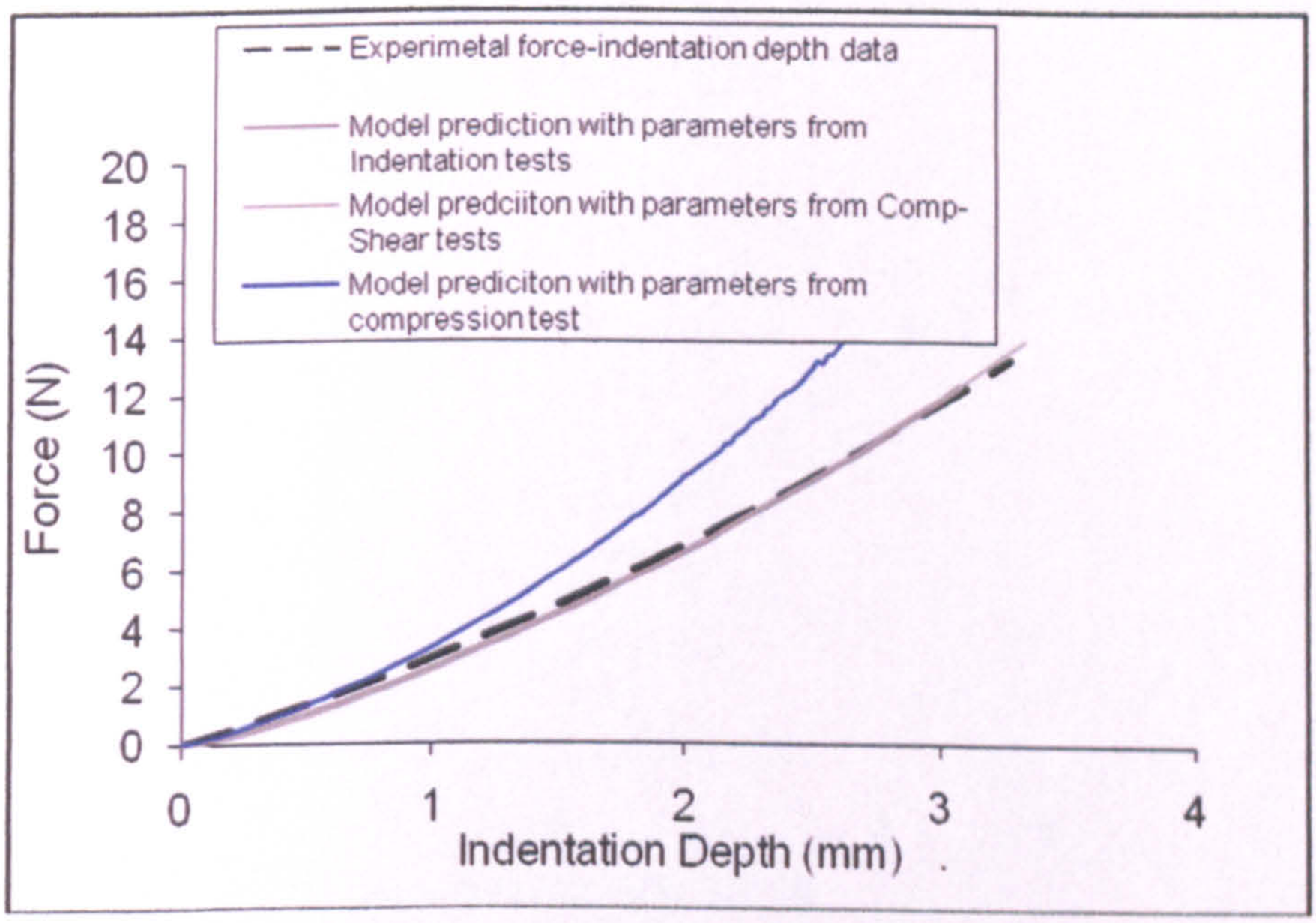


(b) Foam 2 (R=2mm)

**Figure 4. 19** Comparison of experimental and model predicted force-indentation depth curves with parameters extracted from indentation (with different indenter sizes), com-shear and compression data.

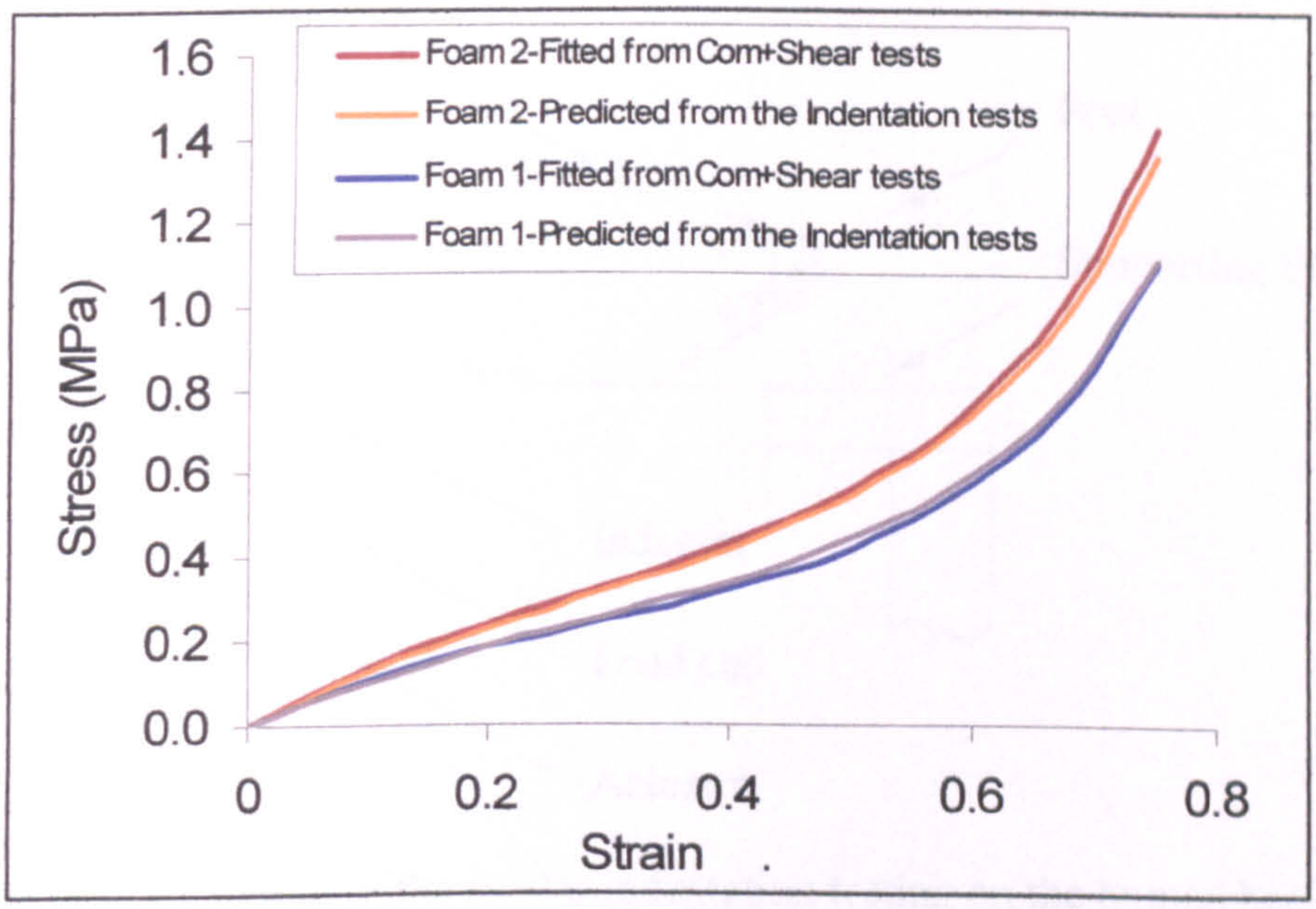


**Figure 4.20** Stress-strain curves of the two foams.

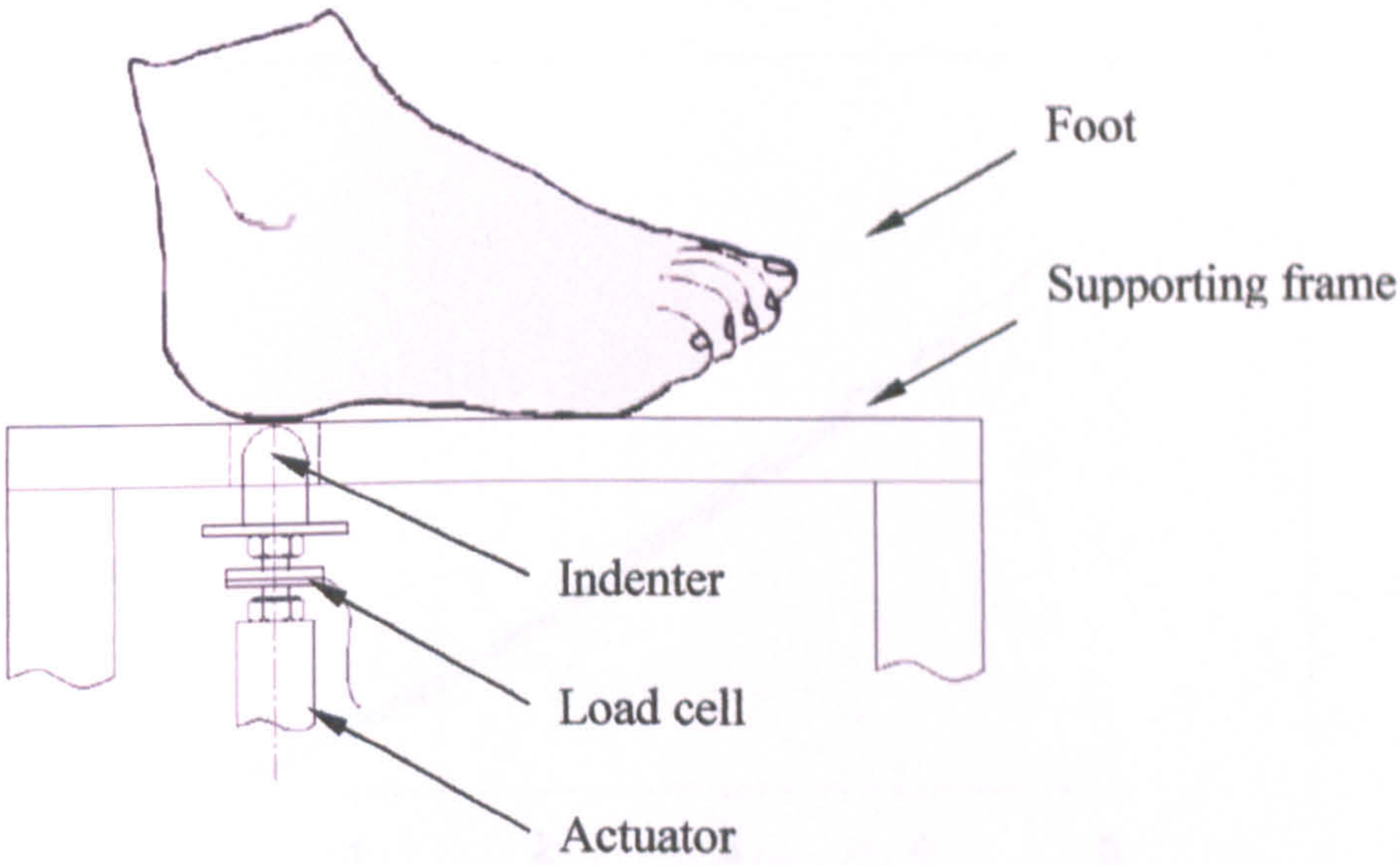


**Figure 4. 21** Set-up of the *in vivo* indentation testing on the human heel pad.

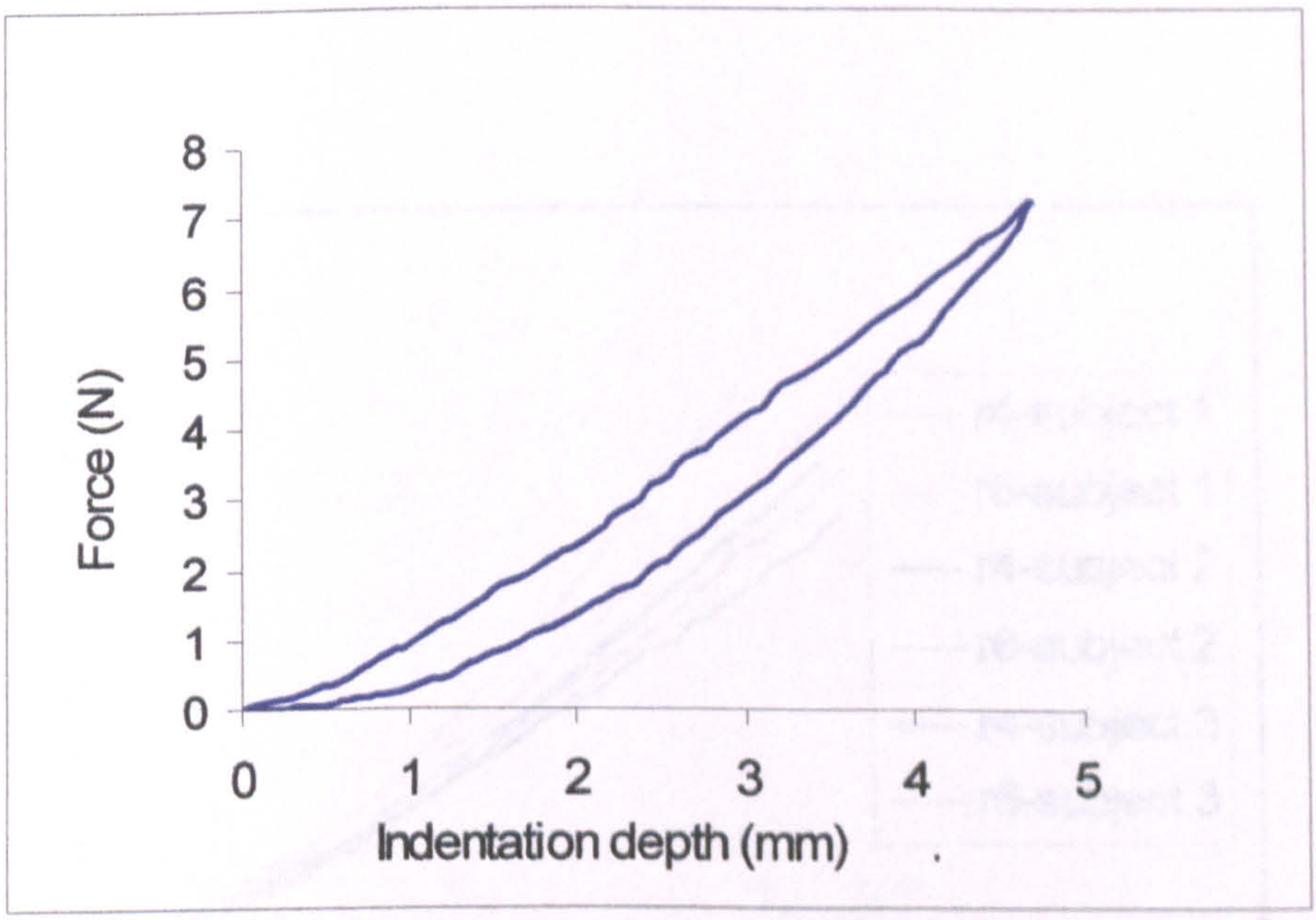


**Figure 4.22** Typical force indentation depth (*P*-*h*) curves.

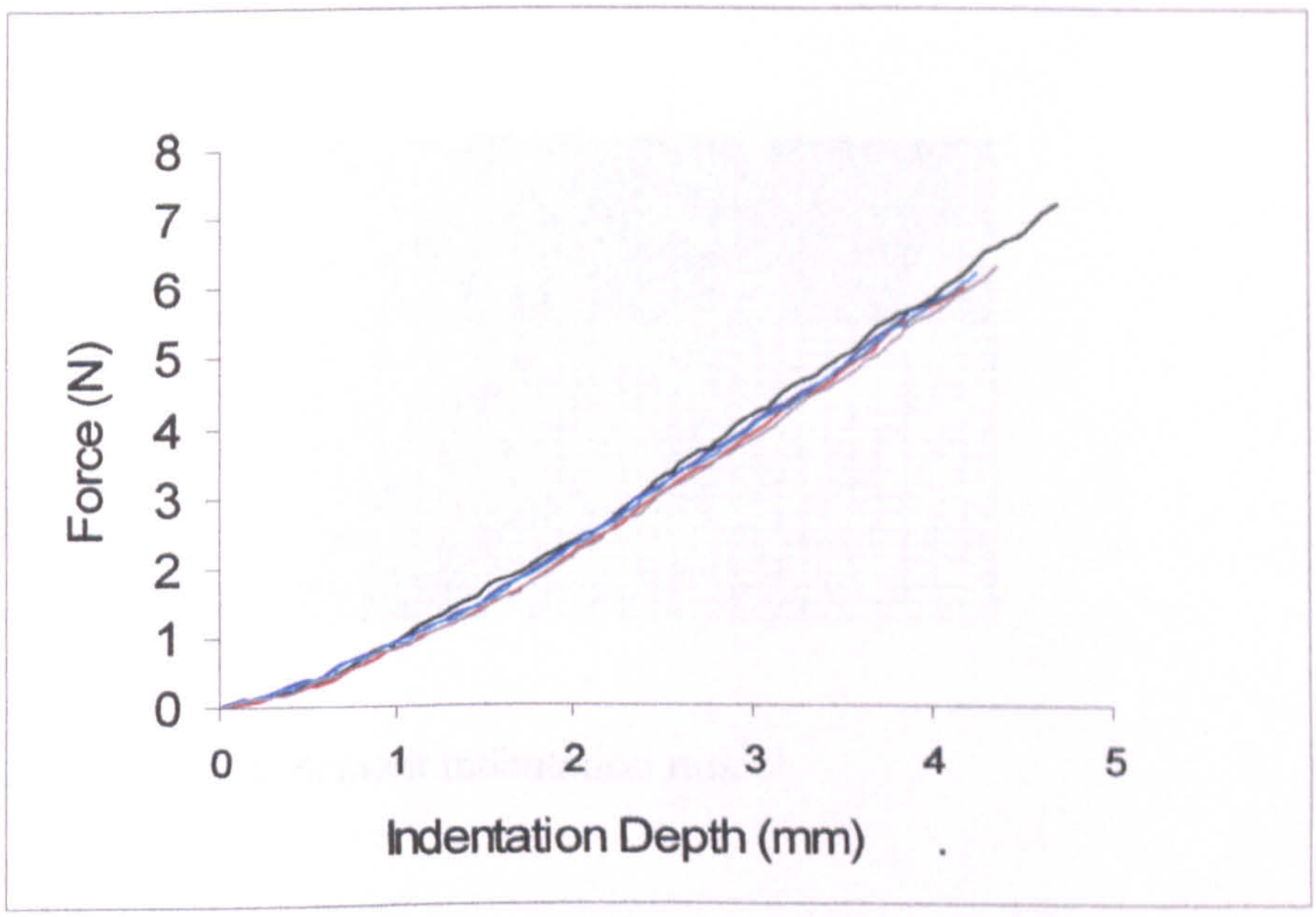


**Figure 4.23** Typical force indentation depth *(P-h)* curves on the same subject showing the repeatability.

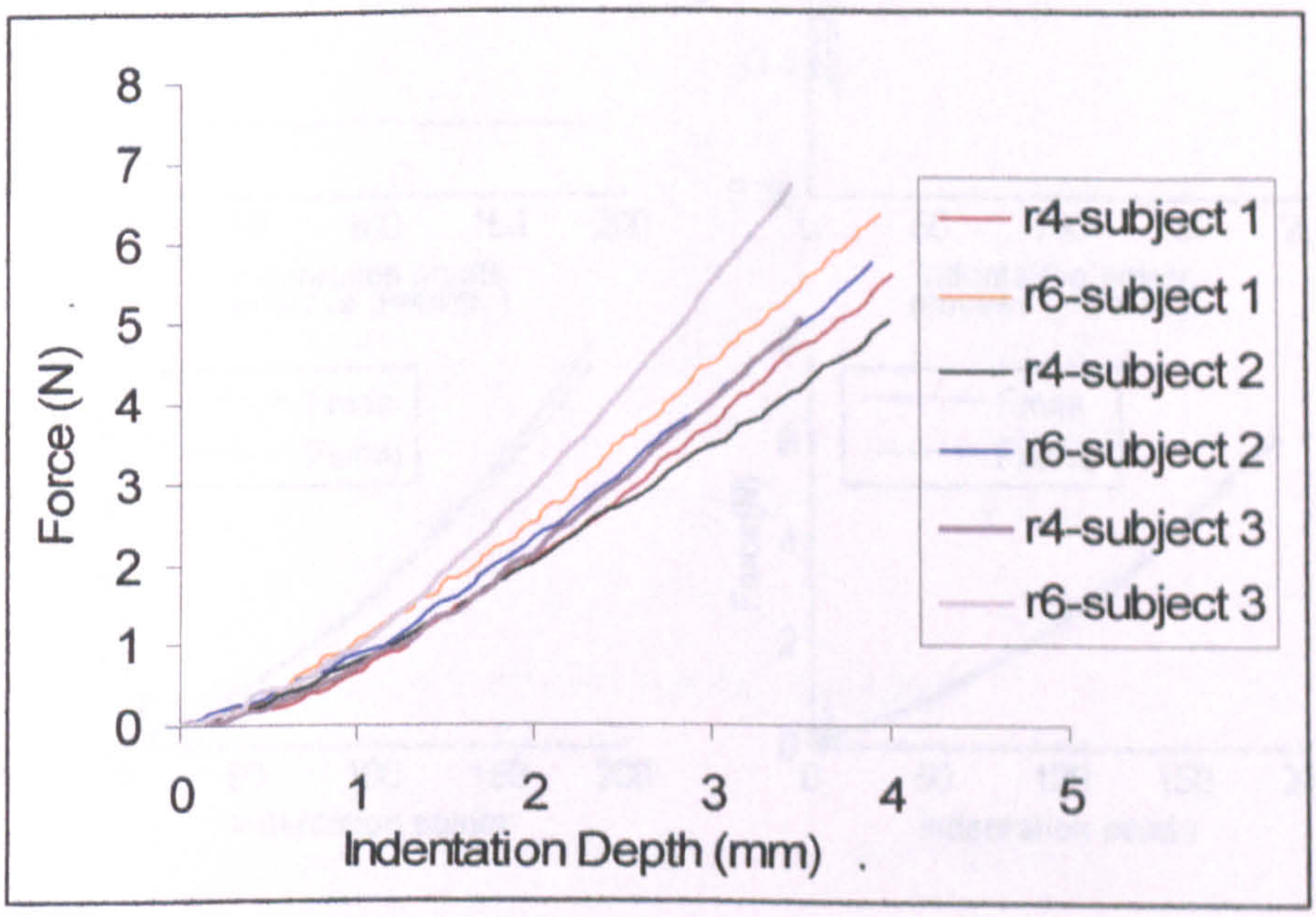


**Figure 4.24** The experimental loading curves on the three subjects.

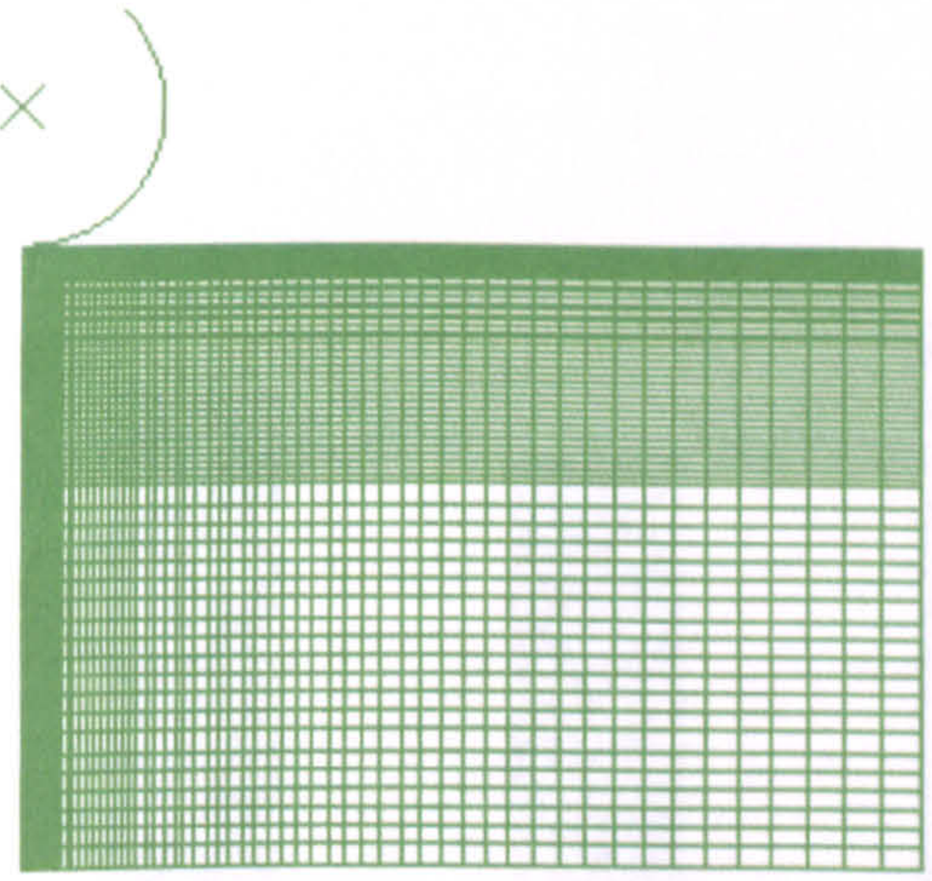

**Figure 4.25** Finite element indentation model.

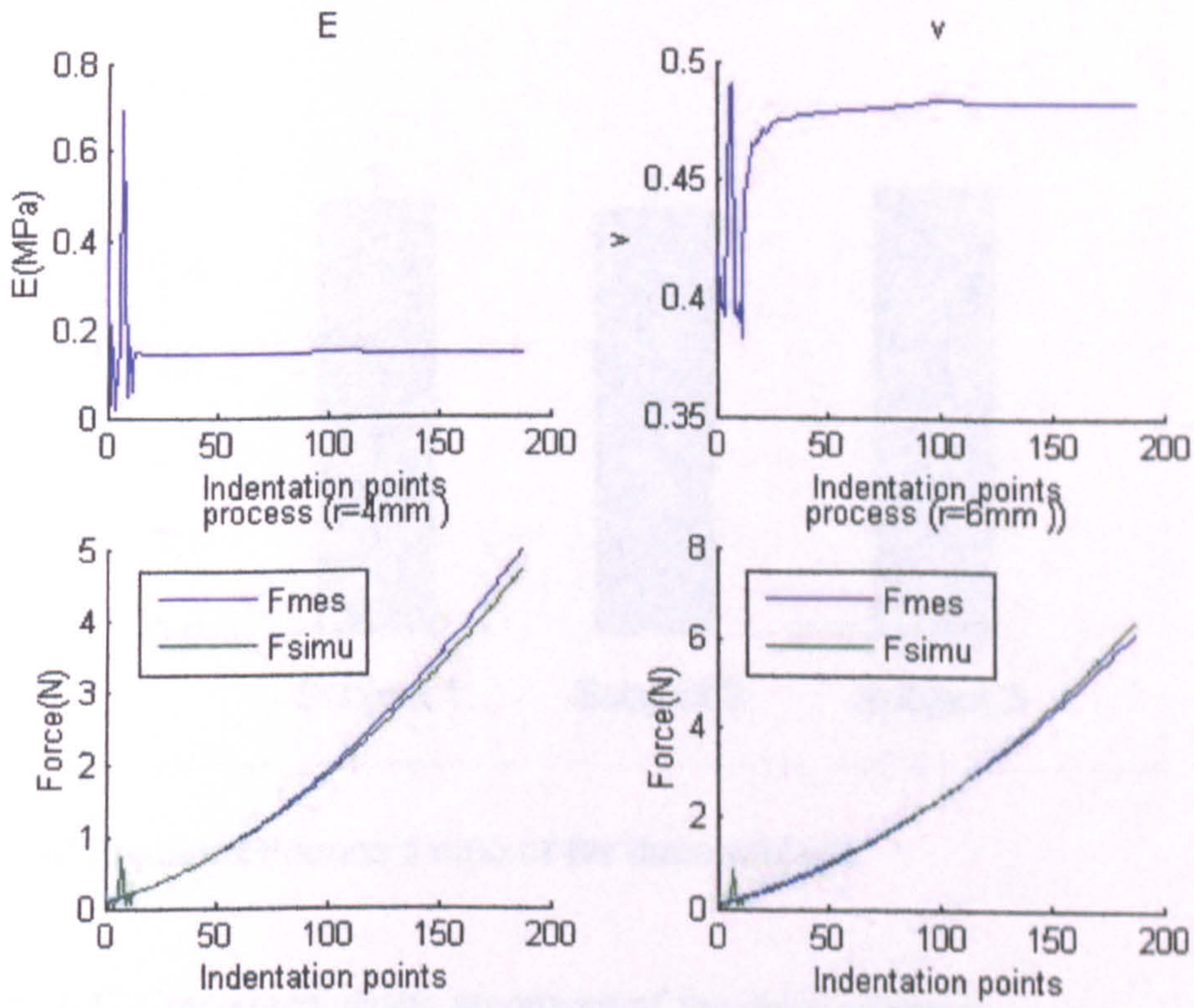


**Figure 4.26** Material parameters fitting process with dual indenters for the human heel pad (Linear elastic model).

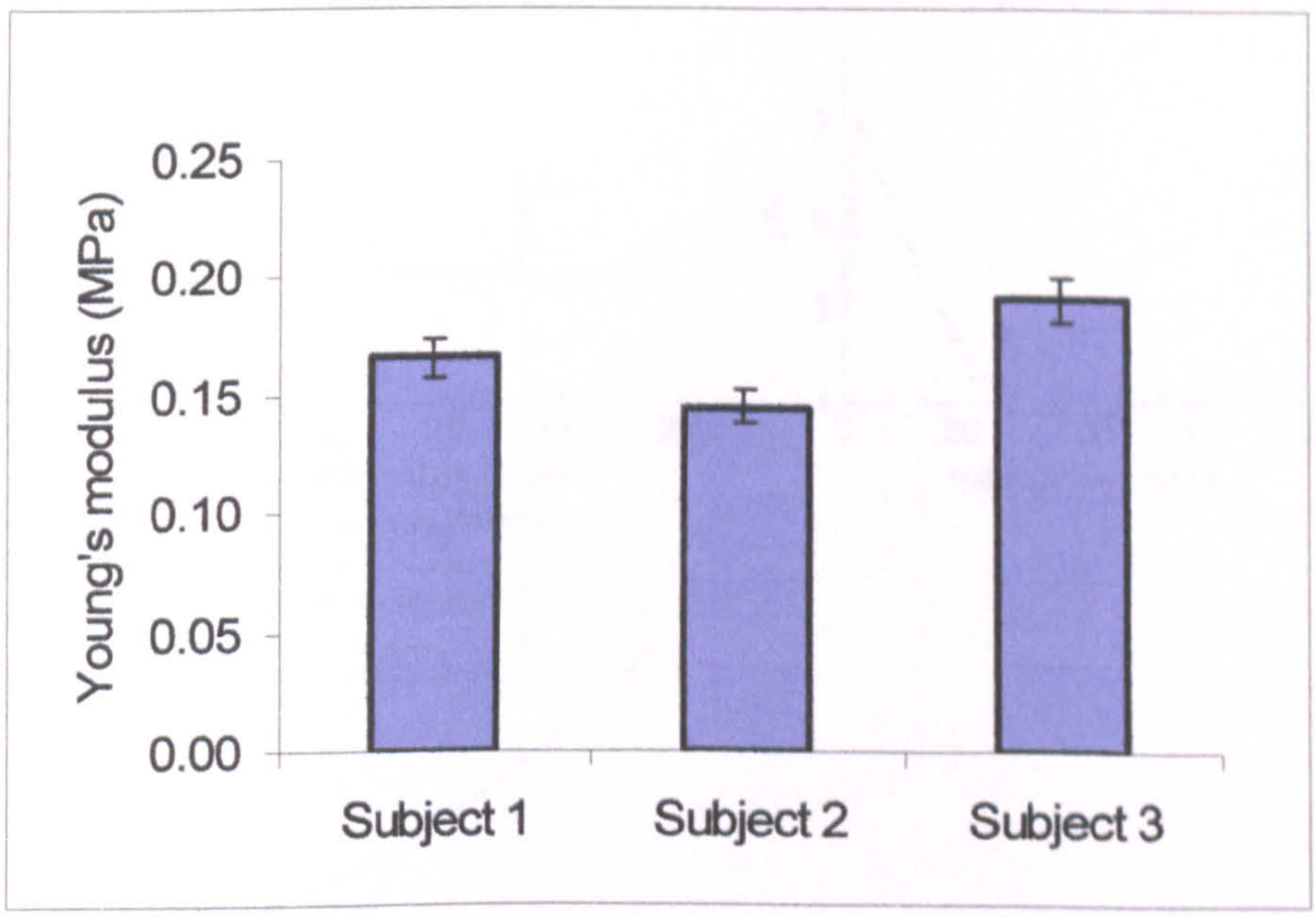


(a) Predicted linear elastic modulus of the three subjects

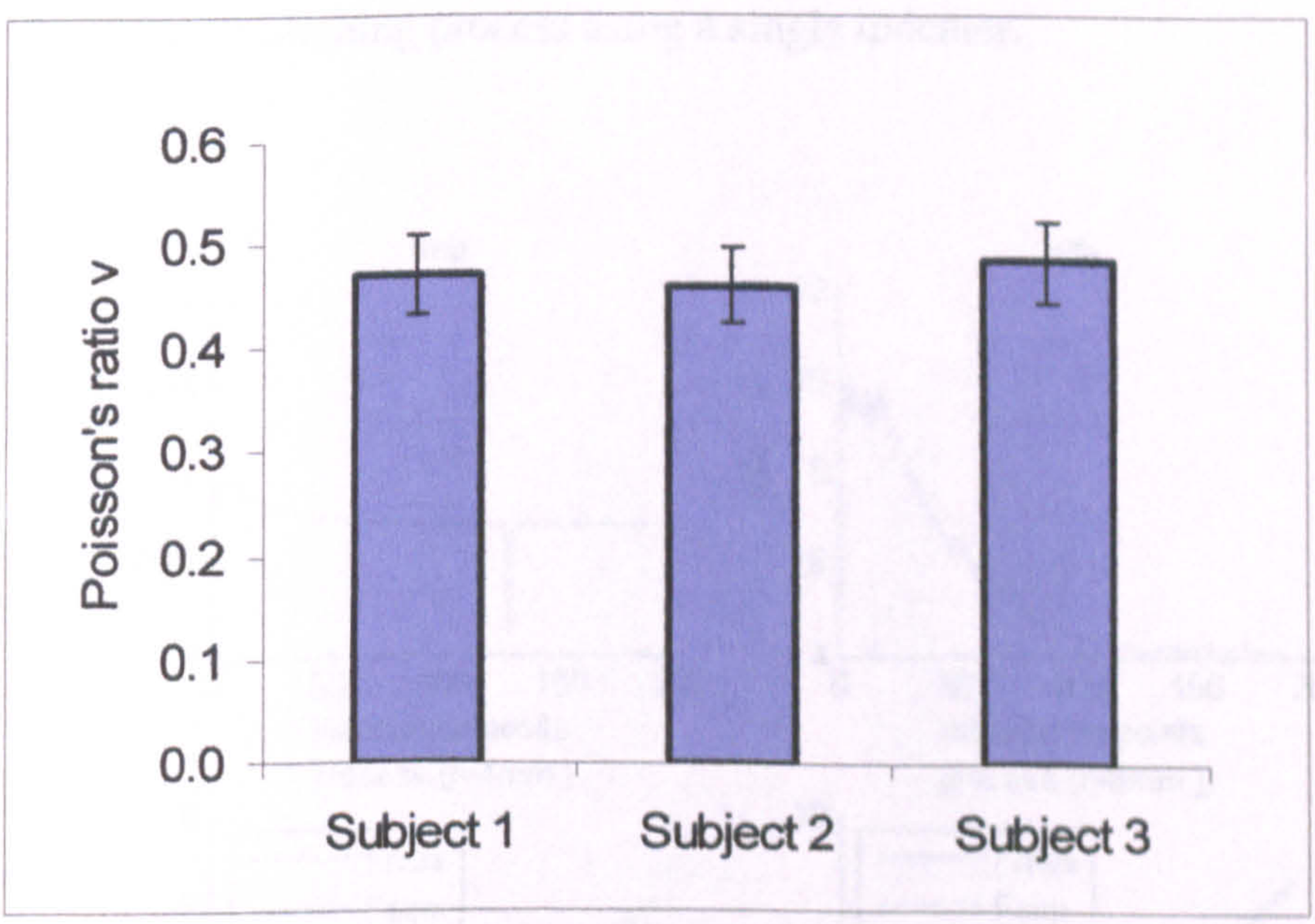


(b) Predicted Poisson's ratio of the three subjects

**Figure 4.27** Converged elastic properties of the three subjects.

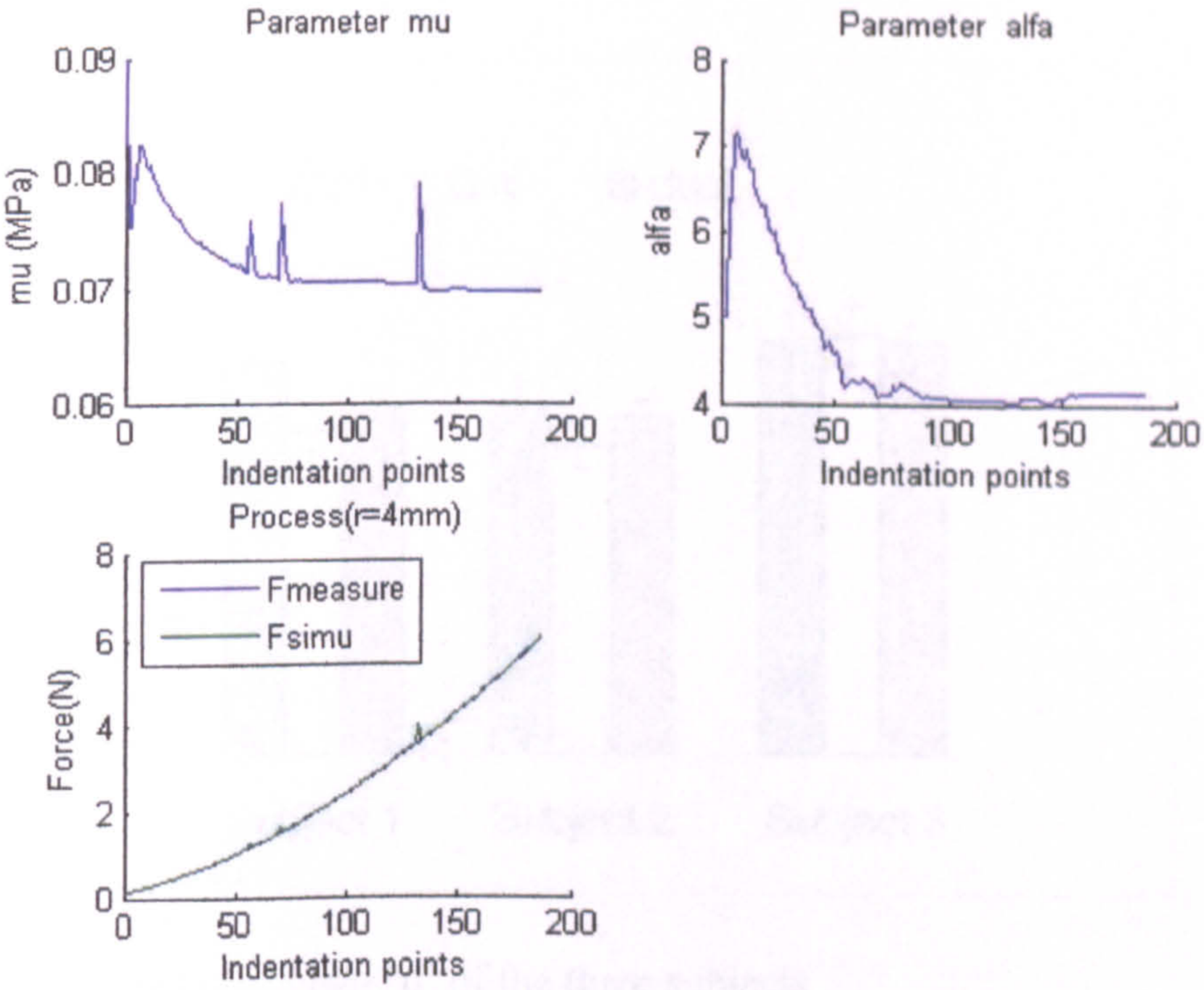


(a) Inverse searching process using a single indenter.

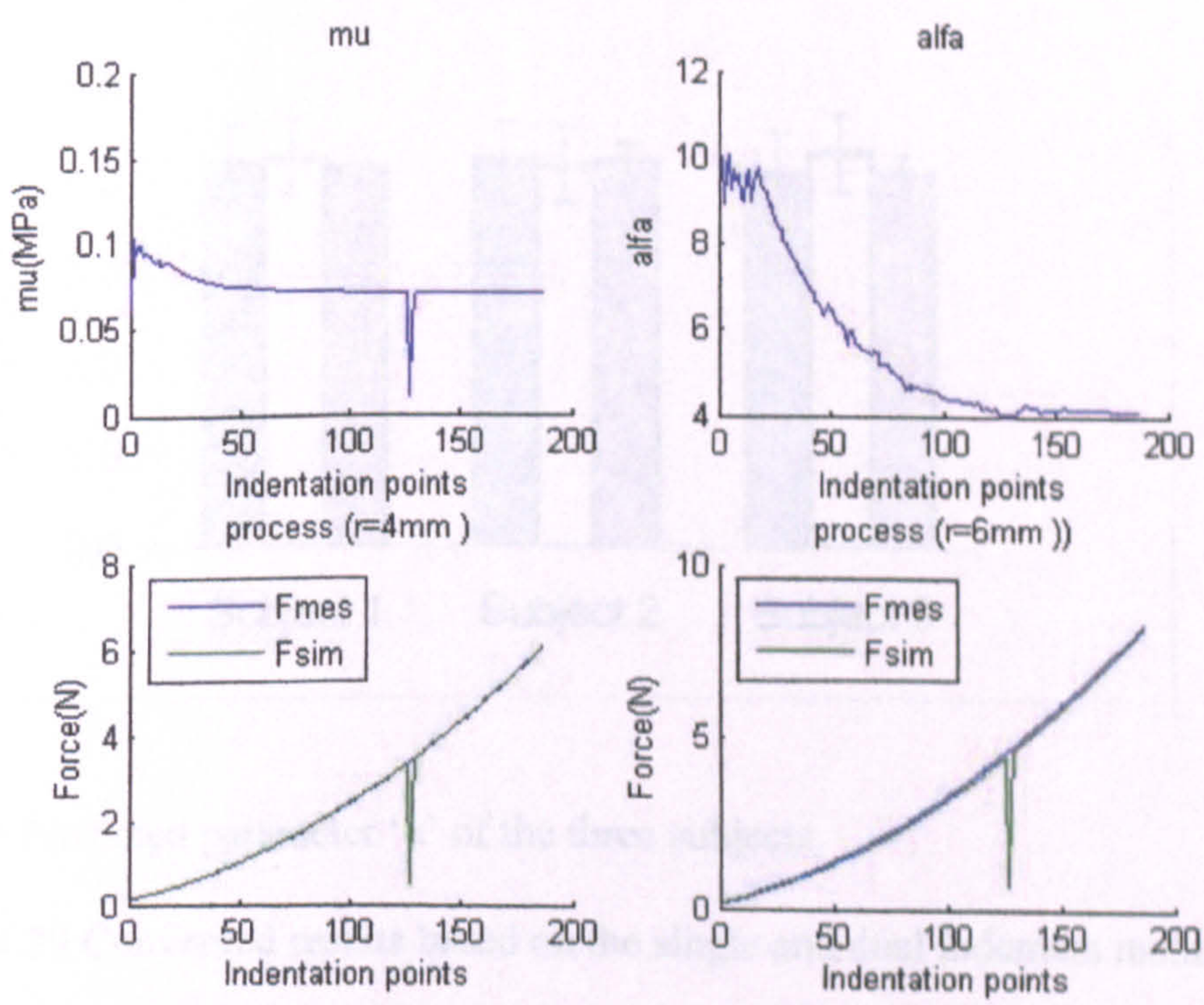


(b) Inverse searching process using dual indenters.

**Figure 4.28** Material parameter fitting process for the human heel pad based on the hyper-elastic model.

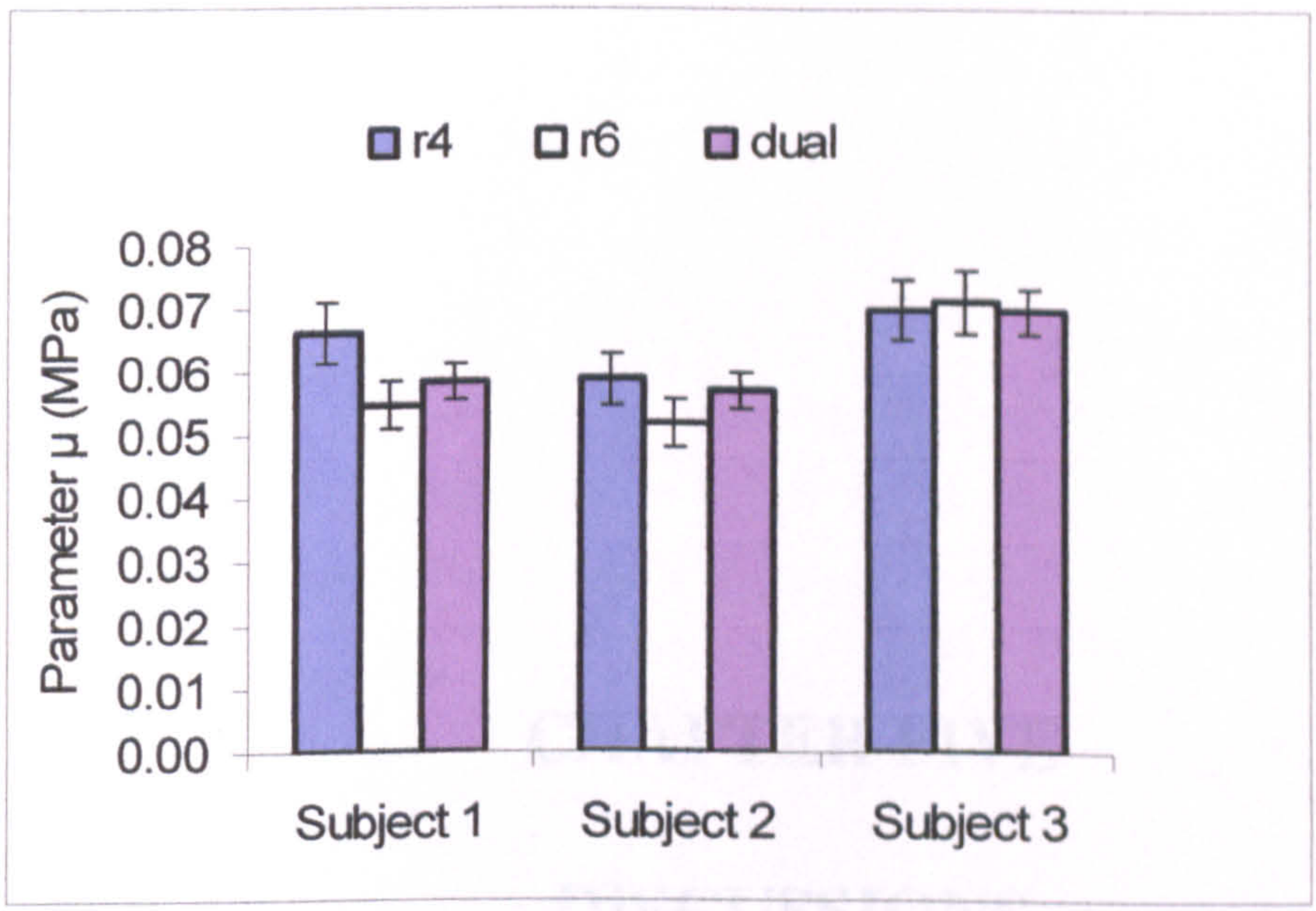


(a) Predicted parameter 'μ' of the three subjects

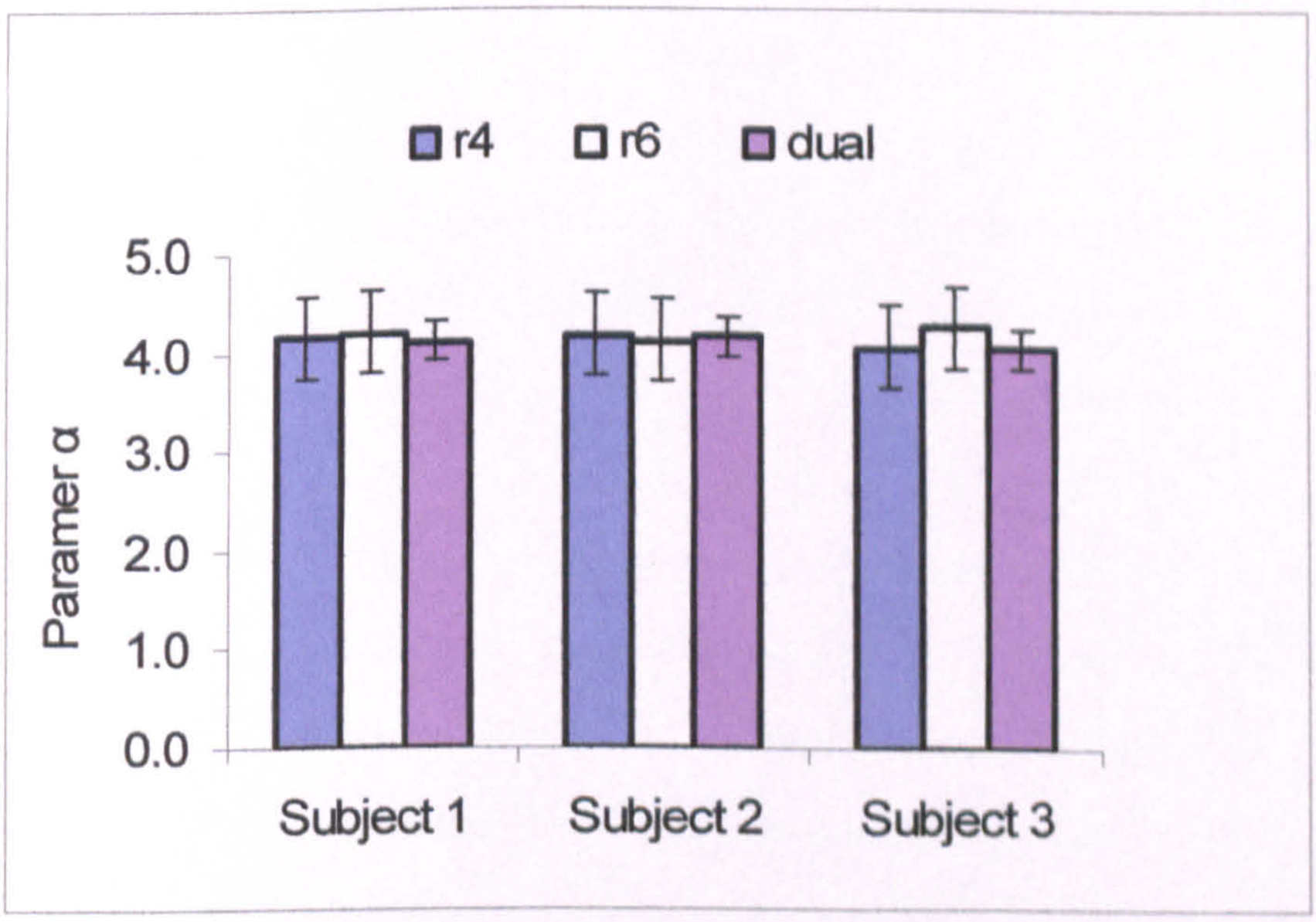


(b) Predicted parameter 'α' of the three subjects.

**Figure 4.29** Converged results based on the single and dual indenters method.

# CHAPTER FIVE

# DISCUSSIONS

## 5.1 Use of indentation tests and inverse FE modelling in characterising material properties

Indentation testing is an important materials testing method with either sharp or blunt indenter. It can be used to test different types of materials such as brittle (e.g. ceramics), elasto-plastic (e.g. metals) and soft materials (e.g. foams, rubbers, etc.) *(Ren et al, 2003)*. One significant advantage of the indentation lies that it only requires small amounts of material; this made it very attractive for the characterisation of material where standard specimen is not readily available such as *in situ* or *in vivo* tests *(Ren et al, 2004; 2006)*. With an inverse FE modelling technique, some important material parameters that could be obtained from indentation test directly. This would provide important materials data for design and materials development. The EVA foams test represents a typical case for such situations. As demonstrated in Chapter 4, the nonlinear materials for the EVA foams have been successfully predicted based on the indentation tests. The results showed a good agreement with the conventional compression-shear tests currently used. The values predicted are also comparable to some published data for EVA foams for similar applications *(Petre et al, 2006)*. Figure 5.1 compared the stress strain curves from this work and some published data on foams of different hardness. As it shown, the overall trend is comparable and it also shows that most of the EVA foams has different elastic part but very similar stiffening effect. The method developed represents a much simpler method in comparison to the conventional approach as detailed in Chapter 2. In the compression and shear tests, large sample size is required and the maximum strain applicable depends on the strength of the adhesive bond in the shear tests *(Petre et al, 2006)*. For continuous indentation tests, the sample size can be much smaller and can go into large deformations.

Another important field where inverse FE modelling is essential is *in vivo* tests, which involves tests on the human subject directly, where isolation of the sampling was not possible or the isolation process may change the natural state of the material. The accuracy of such approach depends on the robustness of the facilities and the inverse program. As evidence by the tests on different materials, the indentation tester developed achieved good accuracy and repeatability. The results on rubber have been

validated by comparing the results against the results of an established analytical solution (Figure 4.6). The result on foams also showed good agreement at different indentation depth with the standard materials testing machine (Figure 4.7). The test ensures the detection of properties of soft tissues in its nature state. The predicted results of the human heel pad showed good agreement with some published data *(Zheng et al, 2000)*. These suggest that the inverse program developed is accurate and could potentially used to detect some property change with treatment or medical conditions or ages.

The program developed has also been successfully used to other material systems including characterisation of the plastic properties of spot welded joints. Spot welding is widely used in automobile body assembly and each car body have over 4000-6000 spot welded joints. The plastic material properties for the different regions in a spot welded joint are crucial to the integrity of the structure. The program developed in this thesis has successfully been used to predict the plastic properties of the metal materials, which showed a good agreement with the standard tensile test results (Figure 5.2). These material properties were then used in a FE model to predict the performance of spot welded structure under tensile shear loading *(Kong et al, 2008)*. In the work to predict plastic properties, the indenter used is Knoop and Vickers indenter and indentation depth is much shallower (10 micrometer). These demonstrated that the framework development in this work is flexible and adaptable for many different materials types, which is very important for material characterisation.

## 5.2 The use of Kalman filter method in inverse material properties characterisation

As shown in Figure 3.3, the inverse FE modelling process developed consists of three main parts--experimental data, finite element modelling (FE) data and the inverse program. The validity and accuracy of this approach are influenced by factors associated with these processes such as accuracy of the experimental data, FE modelling, searching mechanism, etc. All these have been systematically investigated with blind tests before being applied to practical tests.

As shown in Chapter 3, numerical experimental data, i.e. numerical result with known material properties, were used as the experimental data for evaluation/identification purposes. This allows making direct evaluation of the estimated solutions, with respect to actual solutions, over a wide range of materials and systematically comparing the uniqueness, and accuracy of the results. It also allows the results from single and double spherical indenter method to be directly compared and their correlation established. Systematic study on different material models showed that the difference between single and dual indenters might vary with material properties (e.g. Figure 3.13, 3.15). For the elastic model, there is a clear effect; the single indenter approach could not uniquely predict the material parameters even with numerical experimental data. Similar results have been observed on other material properties such as plastic properties, where there were several combinations of the material properties which match the testing results *(Kong et al, 2008)*. This suggests the dual indenters method is a better approach to provide more robust solution.

The searching mechanism is another important factor in inverse FE modelling. The Kalman filter method was initially developed for optimization of electronic/control systems (signal-processing algorithm). Essentially the Kalman filter algorithm updates the previous estimates, through indirect measurements of unknown state variables, and covariance information of both the state and measurement variables, that may contain substantial error or noise and provides an efficient computational solution, based on the least-square theory. Its capacity for noise filtering made it potentially an important tool in dealing with materials testing data (as shown in the test results on

foams and human heel tissue), which normally associated with significant noise level. As detailed in section 3.2 and demonstrated in the results for different material models, the error treatment is a very important aspect of the inverse modelling process for material parameters characterisation. One is the measurement noise ($v_k$) while the other is the process noise ($w_k$) (equation 3.2.1-3.2.2). One conventional way to treat noise has been using constant normal error distribution. A major difficulty with this method lies that it is difficult to correctly estimate the error range since indentation may operate at different depth and type of materials. In addition, the work presented in this report clearly showed that the applicability of such an approach is material model dependent, i.e. it only works well for some material models. This could seriously limit the potential application of the approach as it requires in-depth knowledge to set the constant error. The new approach proposed in this work for this field is using normal distribution with different dispersion (Figure 3.4). i.e. both $R_k$ and $Q_k$ were treated as time dependent and varies from the true values following a normal distribution. With this method, the material properties are not required to be pre-known, which could be an significant advantage for the program for material characterisation in particular for the nonlinear material models. The results clearly showed that this approach is much more accurate and robust.

## 5.3 Factors affecting in the indentation test and inverse FE modelling process

FE modelling is an important part of an inverse modelling process, which provides data to form the simulation space. The inverse program explores the simulation space starting from a given initial guessed value to work out optimum material properties, which produce numerical results that match the testing results. The simulation space is normally constructed by using finite element models mimicking the testing and true boundary conditions. So, the FE model must be able to accurately represent the testing in order to predict the material properties accurately.

The indentation resistance of a material is commonly represented using the force indentation depth ($P$-$h$) curve, which can be affected by many factors (such as indenter shape and size, materials deformation around the indenter and experimental conditions, etc.). These factors have to be carefully considered when using indentation method and FE modelling process. As detailed in chapter 3 and chapter 4, for each material models studied, the effect of mesh size has been assessed by varying the meshing scheme. This ensured that the model is accurate and valid. The linear elastic model was directly compared to an analytical solution, which further validate the FE model. Friction is another important factor has to be studied. This has been assessed in the earlier stage of the work by comparing the indentation curves with different coefficients and showed no significant difference for the three material models with the indentation depth range used in this work (Figure 5.3). This could provide a significant advantage for inverse FE modelling as it could reduce the uncertainty of the results due to frictional condition, which is normally very difficult to be characterised.

## 5.4 Effect of indenter numbers and sensitivity studies

One crucial aspect of an inverse program lies that the input data must be able to provide sufficient material behaviour over different stress-strain conditions. In other words, there must be (or close to) one to one relationship between the stress-strain relationship and the experimental data. This may be effectively achieved by selecting suitable indentation testing conditions (types of indenter or combination of the indenters). This was evaluated in this work using comparative study approaches based on the single indenter and dual indenters method with different dimensions.

The results showed that the selection of the single and dual indenters could have significant effect on the influence of the initial values. As shown in Figure 3.13 and 3.33, the results from the single indenter method have scatter much more significant in particular in the case of linear elastic and hyperfoam models. This will require further measurements to refine the prediction if a single indenter method is used. For the dual indenters method, the results are not initial value dependent and focused on to a localised range around the true material value (Figure 3.15, 3.25, 3.35). This makes the dual indenter method a much better approach than the single indenter method in terms of convergence, in particular in situation where the material properties is not pre-known.

Sensitivity of the predicted material properties due to variations of the input data is essentially an intrinsic characteristic of inverse processes. In this work, the input data were taken from a numerical model, but, in a real testing situation, there can be potentially both system and random errors. Factors such as indenter angle, roundness of the tip, and accuracy of the recorded indentation force or depth all influence the measurement results *(Dao et al, 2001)*. This has been studied by adding a small percentage of perturbation to the indentation force, and then comparing the predicted properties with the original data. The results clearly showed that the method developed in this work is robust against potential errors in the experimental measurement.

## 5.5 Use of indentation test in *in vivo* testing

The human heel tissue consists of the fat pad surrounded by a thick subdermal layer of fibrous tissue and the skin *(Jahss et al, 1992)*. The structure is uniquely designed to enable pain-free weight bearing and locomotion *(Rome, 1998; Narvaez, et. al 2000)*. A detailed knowledge of its mechanics is indispensable to understand its roles as well as injury and medical conditions. It has been shown that the mechanical strength of the heel pad is associated with medical condition such as such as chronic lower back pain, plantar heel pain, muscle tears, degeneration of cartilage *(Volshin and Wosk, 1982; Pratt D J.1989)*. *In vivo* characterization of heel-pad deformation can also provide insight into tissue properties changes that may occur in diseases such as diabetes rheumatoid arthritis *(Rom, 1998; Hsu et al, 2000, 2002)*. With an accurate inverse approach, the clinical observation could be quantitatively assessed.

Theoretically the parameter $\mu$ in hyperelastic model represents the initial shear modulus. For an incompressible material, the initial elastic modulus can be calculated as $3\mu$ *(ABAQUS)*. Figure 5.4 compared the predicted elastic modulus from the linear elastic model and the estimated Young's modulus from the hyperelastic model of the three subjects. The predicted Young's modulus values from hyperelastic model are slightly higher than the predicted data from the elastic model. This is suggesting the nonlinear model is better in describing the properties of the heel pad. The predicted elastic properties were comparable to some published works. For example, Hsu et al *(2000)* has reported an E value of 168KPa; Wang *et al (1999)* has reported a value of 123KPa and Gefen reported a value of 105 KPa *(Gefen et al, 2001)*. As shown in Figure 5.4. The difference may be due to subject difference and the indenter shapes. The work clearly showed that the inverse method is applicable further work is to extend to more subjects and use the method to study the effect of medical or treatment to the properties change.

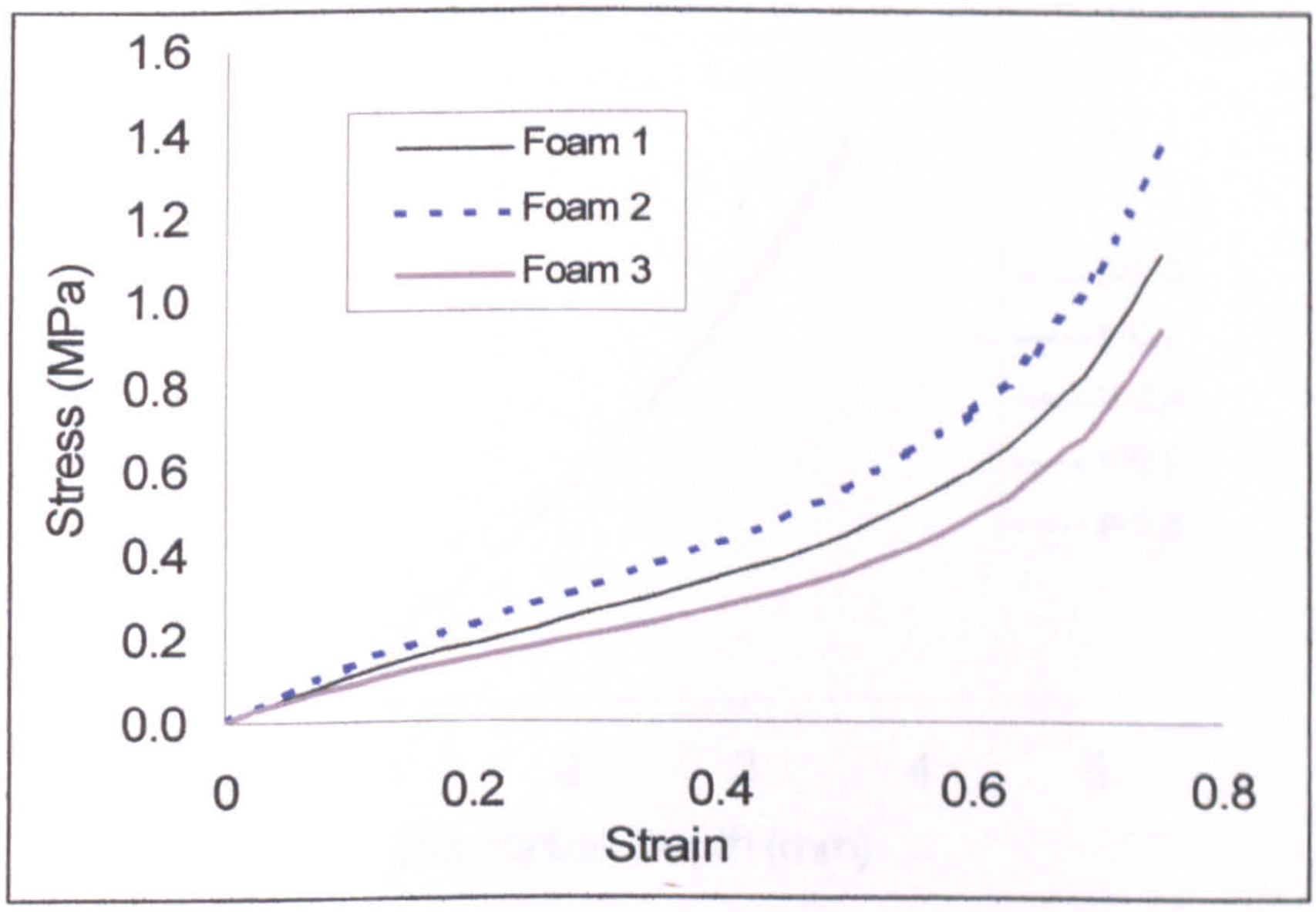


**Figure 5.1** Typical stress-strain curves for midsole EVA foams.

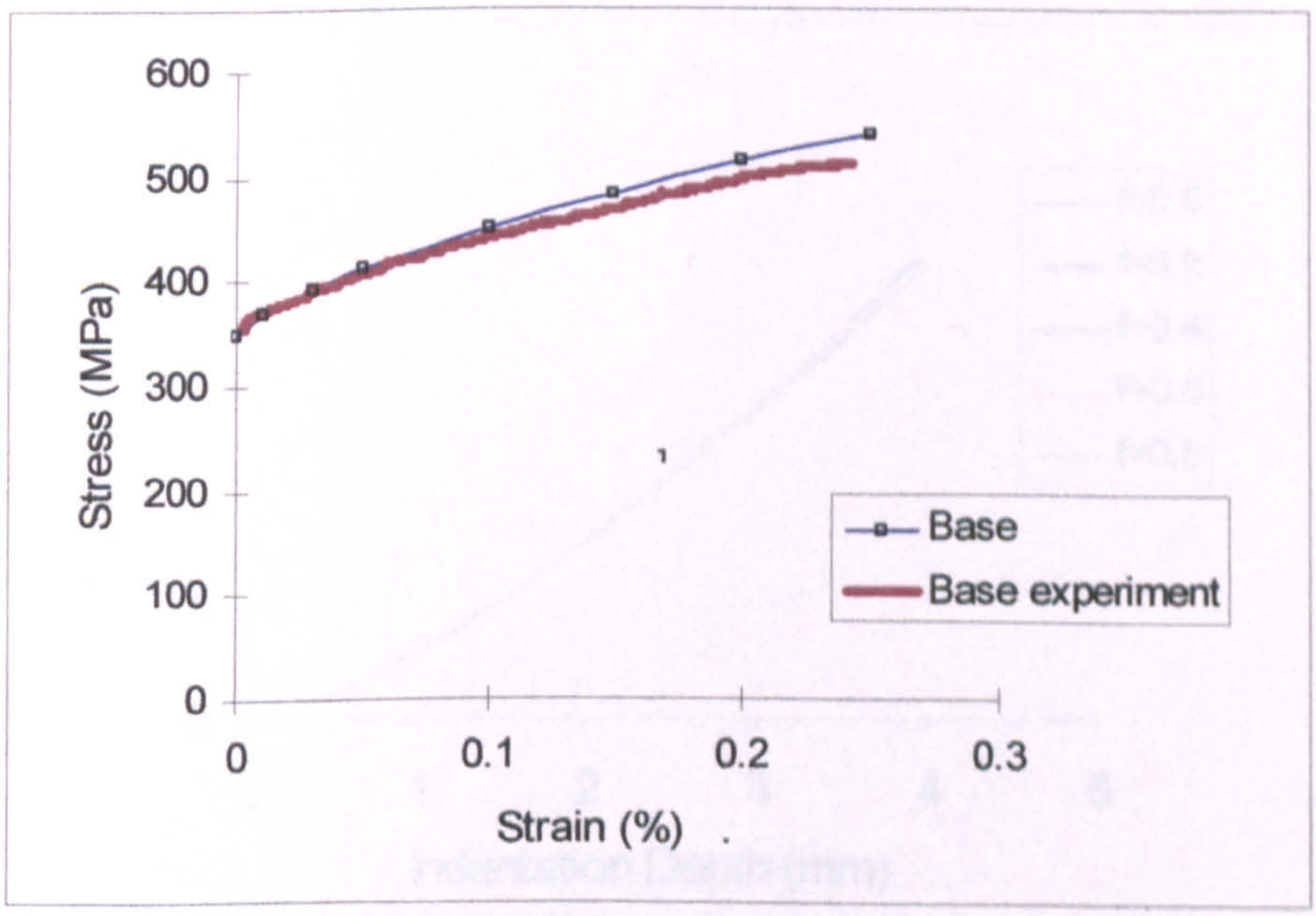


**Figure 5.2** The true stress-strain curve of a steel predicted from indentation tests using the program developed in this work.

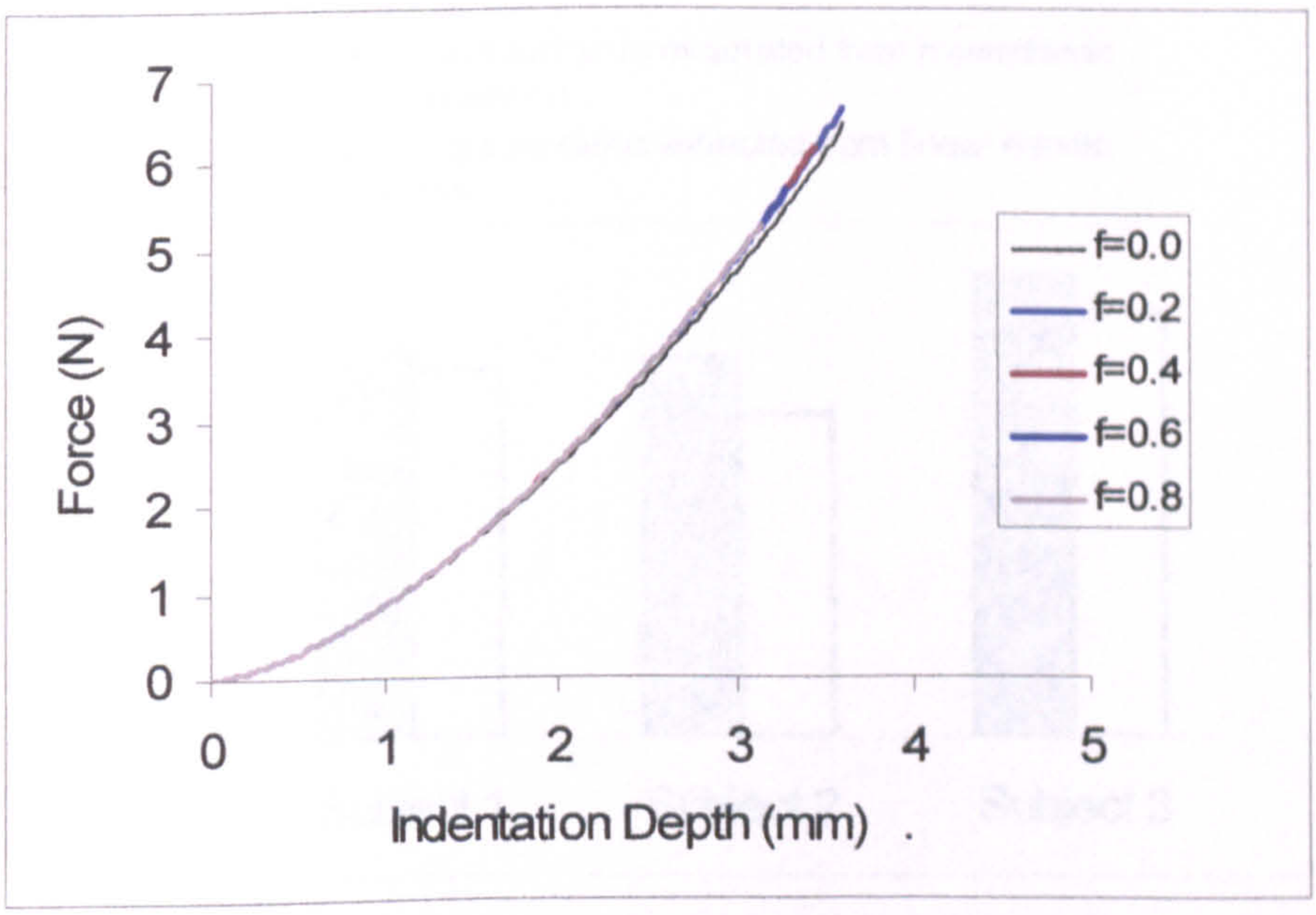


(a) Indentation curve with different friction coefficients (Hyperelastic model, R=4mm).

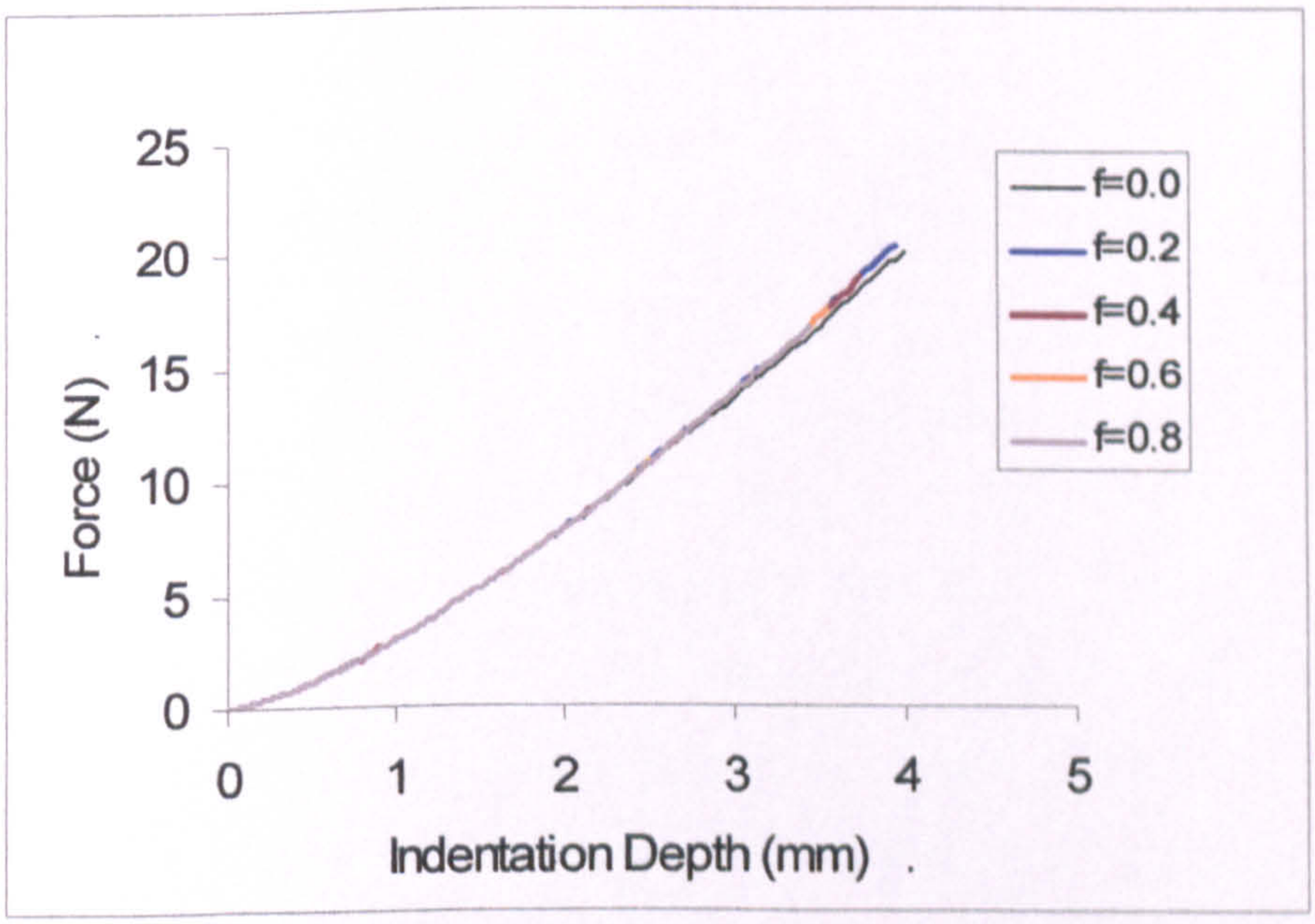


(b) Indentation curves with different friction coefficients (Hyperfoam model, R=4mm).

**Figure 5.3** Friction effect on the indentation process showing the friction coefficient has no significant effect on the indentation curves.

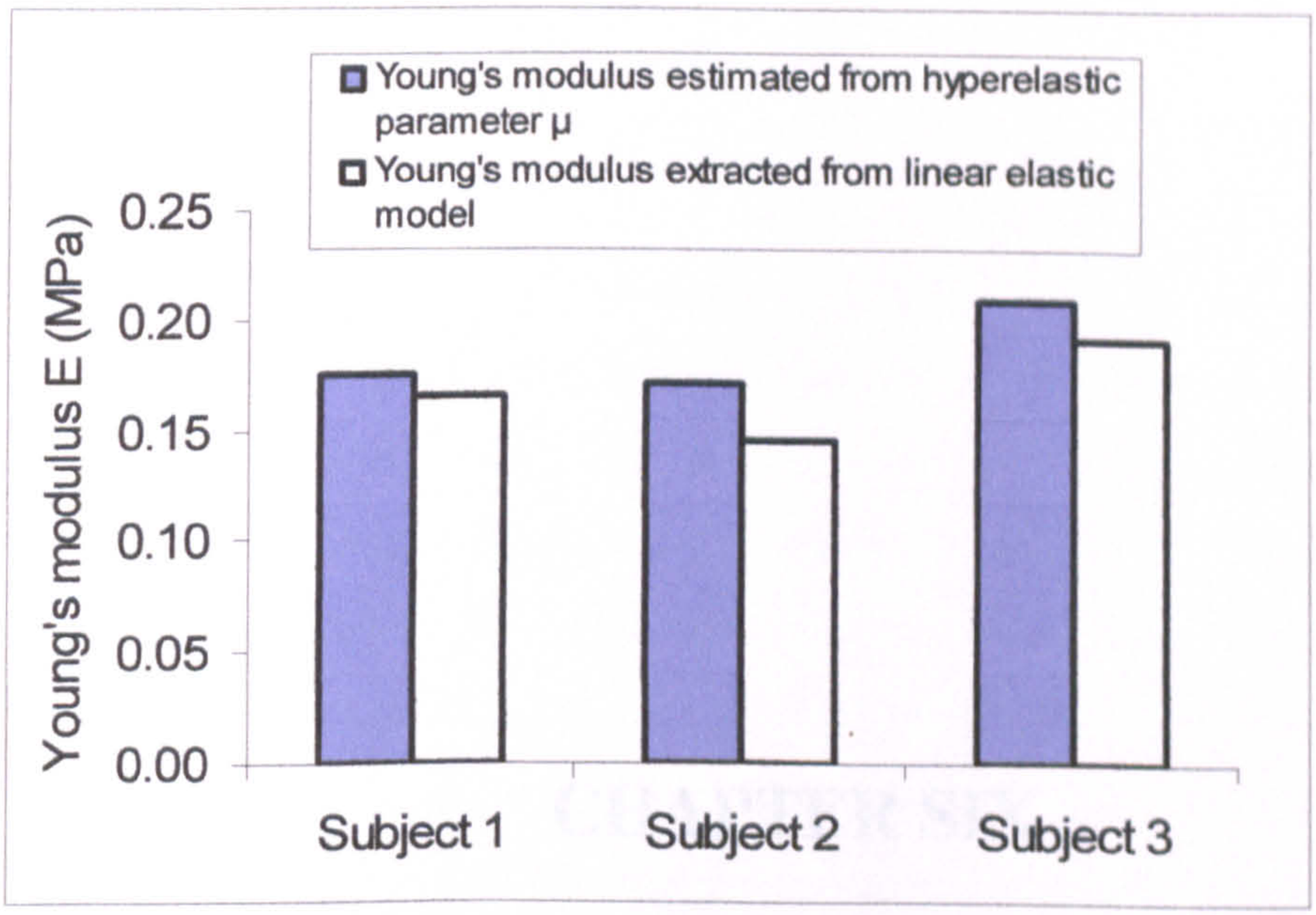


**Figure 5.4** Comparison of the Young's Modulus of the human heel pad from the elastic models and estimated from the nonlinear model.

# CHAPTER SIX

# CONCLUSIONS AND FUTURE WORKS

## 6.1 Summary and conclusions

In this work, an inverse FE modelling program based on the Kalman filter technique has been developed and applied to study three typical material models (elastic, hyperelastic and hyper foam) suitable for rubbers, biological materials and foams. Two error treatment methods have been developed and implemented in the program and their feasibilities for different material systems was systematically studied and established. FE models simulating indentation tests of three typical material behaviours have been developed and factors such as mesh sensitivity, material properties were systematically studied to validate the FE models. Simulation spaces over a wide range of material properties have been developed for each material model, which successfully provided the data for the material properties prediction. The use of single indenter and dual indenters has been comparatively studied in terms of accuracy, convergence and robustness, which are important for materials characterisation

The program was evaluated using blind tests with numerical experimental data including their validity, efficiency and robustness for different material models. The results showed that the single indenter method is initial guessed value dependent with scattered converged results, while the dual indenter method is much more robust with improved accuracy. The results also demonstrated that the new random error treatment method was applicable to all the three material models while the program with the constant error treatment was initial value dependent in some cases. The results showed that Kalman filter is a feasible method and the random error treatment is more practical approach for material characterisation. It is not initial value dependent and can be universally applied to different materials models.

The framework established has been successfully used to characterise complex material systems including EVA foams and human heel pad *in vivo*. EVA foams were tested using indentation, compression and shear tests, and the material parameters determined were directly compared. The prediction from indentation tests showed comparable accuracy to the standard combined compression-shear tests, while pure compression test failed to predict the parameters accurately to describe the material

under complex situations. Providing better information than simple hardness values these parameters can be directly used in the design and simulation process.

A new *in vivo* test machine has been developed and tests performed on three human subjects showed good accuracy and repeatability. The elastic and nonlinear parameters of the heel pad have been successfully predicted based on the indentation tests. The predict results showed good agreement with some published data, and the predict elastic and hyperelastic properties showed good correlation for all the subjects. However the nonlinear model is more accurate in describing the stiffening effect of the heel pad. This method would potentially provide a practical way for detecting the property change of the heel pad with differed conditions.

## 6.2 Recommendations for future works

This work has developed a framework for characterising materials properties based on indentation tests. The program and the results on EVA foams and the human heel pad *in vivo* have laid a solid platform for future works in the following areas:

1. Use the approach to study the environmental effect such as temperature and humidity on foams or other plastic materials. The methodology developed represents a general approach which can be used in many other material systems.
2. To model the heel pad in a multilayered structure. FE model developed represent a simply model and it has sufficiently represent the material behaviour within the indentation depth. It will be of great importance to develop a program for layered structure. A layered model will use much higher computational resources but potentially can be used try to distinguish the contribution of different layers to the indentation resistance.
3. Use the method to characterise the effect of treatment or sport on the properties of the heel pad such as diabetic, aging, etc; another area is to characterise the regional material parameters difference in the planner tissue of foot and use the data in modelling the foot shoe interaction.

## References


**ABAQUS,** User's Manual, version 6.5, Hibbitt, Karlsson & Sorensen.Inc.

**Aerts P., Ker R.F., De Clercq D., Ilsley D.W., McN R.A.,** 1995, 'The mechanical properties of the human heel pad: A paradox resolved'. Journal of Biomchanics. Vol.28, No.11, pp.1299-1308.

**Aoki S., Amaya K., Sahashi M., Nakamura T.,** 1997, 'Identification of Gurson's Material Constants by Using Kalman Filter'. Computational Mechanics. Vol.19, No.6, pp.501-506.

**Araujo A.L., Lopes H.M.R., Vaz M.A.P., Mota Soares C.M., Herskovits J., Pedersen P.,** 2006, 'Parameter estimation in active plate structures'. Computers and Structures. Vol.84, pp.1471-1479.

**Atkin R.J., Fox N.,** 1980, *An Introduction to the Theory of Elasticity.* ISBN: 0-582-44283-4. Longman Inc. New York.

**Bader D.L., Bowker P.,** 1983, 'Mechanical characteristics of skin and underlying tissues in vivo'. Biomaterials. Vol.4, pp.305-308.

**Beck J.V., Blackwell B., St. Clair Jr C.R.,** 1985, *Inverse Heat Conduction: Ill-Posed Problems.* John Wiley & Sons , Newyork.

**Berardesca E., Borroni G., Gabba P., Borlone R., Rabbiosi G.,** 1986, 'Evidence for elastic changes in aged skin revealed in an *in vivo* extensometeic study at low loads'. Bioeng Skin. Vol.2, pp.261-270.

**Blatz P.J., Ko W.L.,** 1962, 'Application of finite elasticity theory to deformation of rubbery materials'. Trans. Soc. Rheology, Vol. 6, pp.223-51.

**Bolzon G., Maier G., Panico M.,** 2004, 'Material model calibration by indentation, imprint mapping and inverse analysis'. International Journal of Solids and Structures Vol.41, pp.2957-2975.

**Callinan, T.,** 2003, 'Artificial Neural Network identification and control of the inverted pendulum'. PhD Thesis, Dublin City University.

**Clark J.A., Cheng J.C.Y., Leung K.S.,** 1996, 'Mechanical properties of normal skin and hypertrophic scars'. Burns. Vol. 22, No. 6, pp.443-446.

**Dao M., Chollacoop N., Van Vliet K. J., Venatesh T. A., Suresh S.,** 2001, 'Computational modelling of the forward and reverse problems in instrumented sharp indentation'. Acta materialia. Vol.49, pp.3899-3918.

**De Campos Velho H.F., Ramos F.M., Chalhoub E.S., Stephany S., Carvalho J.C., De Sousa F.L.,** 2007, 'Inverse problems in space science and technology'. Inverse Problems in Science and Engineering. Vol.15, No.4, pp.359-372.

**Delalleau A., Josse G., Lagarde J.M., Zahouani H., Bergheau J.M.,** 2006, 'Characterization of the mechanical properties of skin by inverse analysis combined with the indentation test.' Journal of Biomechanics. Vol.39, N0.9, pp.1603-1610.

**Diridollou S., Berson M., Vabre V., Black D., Karlsson B., Auriol F., Gregoire J.M., Yvon C., Vaillant L., Gall Y., Patat F.,** 1998, 'An *in vivo* method for measuring the mechanical properties of the skin using ultrasound'. Ultrasound in Medicine & Biology. Vol.24, no.2, pp.215-224.

**Diridollou S., Patat F., Gens F., Vaillant L., Black D., Lagarde J.M., Gall Y., Berson M.,** 2000, '*In vivo* model of the mechanical properties of the human skin under suction'. Skin Research and Technology. Vol.6, pp.214–221.

**Elsner P., Berardesca E., Wilhelm K.P., Maibach H.I.,** (eds). 2002, *Bioengineerinng of the Skin: Skin Biomechanics.* ISBN: 0-8493-7521-5. London, CRC Press LLC

**Erdemir A., Viveiros M.L., Ulbrecht J.S., Cavanagh P.R,** 2006, 'An inverse finite-element model of heel pad indentation'. Journal of Biomechanics. Vol.39, No.7, 1279-1286.

**Gefen A., Megido-Ravid M., Azariah M., Itzchak Y., Arcan M.,** 2001, 'Integration of plantar soft tissue stiffness measurements in routine MRI of the diabetic foot'. Clinical Biomechanics. Vol.16, pp.921-925.

**Gerard J.M., Ohayon J., Luboz V., Perrier P., Payan Y.,** 2005, 'Non-linear elastic properties of the lingual and facial tissues assessed by indentation technique Application to the biomechanics of speech production'. Medical Engineering & Physics. Vol.27, pp.884–892.

**Giannakopoulos A.E.,** 2006, 'Elastic and viscoelastic indentation of flat surfaces by pyramid indentors', Journal of the Mechanics and Physics of Solids. Vol.54, pp.1305-1332.

**Gibson L.J., Ashby M.F.,** 1997, *Cellular Solids: Structures and Properties* (2edn), ISBN: 10-0521499119.Cambridge University Press, Cambridge, UK.

**Gouldstone A., Chollacoop N., Dao M., Li J. Minor A. M., Shen Y.,** 2007, 'Indentation across size scales and disciplines: Recent developments in experimentation and modelling'. Acta Materialia. Vol.55, pp.4015–4039.

**Grewal M.S., Andrews A.P.,** 2001. *Kalman Filtering: Theory and Practice using MATLAB.* ISBN: 978-0-470-17366-4. John Wiley & Sons, Inc., New York.

**Gu Y., Nakamura T., Prchlik L., Sampath S., Wallace J.,** 2003, 'Micro-indentation and inverse analysis to characterize elastic-plastic graded materials'. Materials science and Engineering. Vol.A345, pp.223-233.

**Gunner C.W., Hutton W.C., Burlin T.E.,** 1979, 'The mechanical properties of skin *in vivo*- a portable hand-held extensometer'. British Journal of Dermatology. Vol.100, pp.161-163.

**Hendriks F.M., Brokken D., Oomens C.W.J., Bader D.J., Baaijens F.P.T.,** 2006, 'The relative contributions of different skin layers to the mechanical behavior of human skin in vivo using suction experiments'. Medical Engineering & Physics. Vol.28, pp.259-266.

**Hertz H.,** 1881, 'On the elastic contact of elastic solids'. J. Reine Angew. Math. Vol.92, pp.156-171. (in Elsner et al 2002)

**Hoshiya M., Saito E.,** 1984, 'Nonlinear structural identification using extended Kalman filter'. *Computers and Structures.* Vol.52, No.4, pp.1757-1770.

**Hsu T.C., Wang C.L., Shau Y.W., Tang F.T., Li K.L., Chen C.Y.,** 2000, 'Altered heel-pad mechanical properties in type 2 diabetic patients'. Diabetic Med. Vol.17, pp.854–859.

**Hsu T.C., Lee Y.S., Shau Y.W.,** 2002, 'Biomechanics of the heel pad for type 2 diabetic patients'. Clinical Biomechanics. Vol.17, pp.291– 296.

**Huber N., Tsakmakis C.,** 1999, 'Determination of constitutive properties from spherical indentation data using neural networks[Part I] the case of pure kinematic hardening in plasticity laws'. Journal of the Mechanics and Physics of Solids. Vol.47, pp.1569-1588.

**Huber N., Tsagrakis I., Tsakmakis C.H.,** 2000, 'Determination of constitutive properties of thin metallic films on substrates by spherical indentation using neural networks'. International Journal of Solids and Structures. Vol.37, pp.6499–516.

**Huber N., Nix W.D., Gao H.,** 2002, 'Identification of elastic–plastic material parameters from pyramidal indentation of thin films' Proceedings of the Royal Society.Vol.A458, pp.1593-620.

**Ishida R.,** 1994, 'Strongest Column Design by Constructive Algorithm'. Transactions of the JSME, Part A, Vol.80, No.579, pp.2672–2677.

**Jahss M.H., Michelson J.D.,Desai P., Kaye R., Kummer F., Buschman W., Watkins F., Reich S.,** 1992, 'Investigations into the fat pads of the sole of the foot: anatomy and histology'. Foot & Ankle. Vol.13, pp.233-42.

**Johnson K.L.,** 1985, *Contact Mechanics.* ISBN 0521347963. Cambridge University Press.

**Kalman R. E.,** 1960, 'A new approach to linear filtering and prediction problems'. Trans. ASME, Ser. D, J. Basic Eng., Vol.82D, pp.35-45.

**Kapoor R., Pal D., Chakravartty J.K.,** 2005, 'Use of artificial neural networks to predict the deformation behavior of Zr–2.5Nb–0.5Cu'. Journal of Materials Processing Technology. Vol.169, pp.199–205.

**Kauer M.,** 2001, 'Inverse finite element characterization of soft tissue with aspiration experiments'. Degree of Doctor of Technical Sciences, Swiss Federal Institute of Technology

**Kauer M. , Vuskovic V., Dual J., Szekely G., Bajka M.,** 2002, 'Inverse finite element characterization of soft tissues'. Medical Image Analysis, Vol.6, pp.275–287.

**Keeve E., Girod S., Kikinis R., Girod B.,** 1998, 'Deformable modelling of facial tissue for craniofacial surgery simulation'. Computer Aided Surgery. Vol.3, pp.228-238.

**Ker R.F.,** 1996, 'The time dependent mechanical properties of the human heel pad in the context of locomotion'. The Journal of Experimental Biology. Vol.199, No.7, pp.1501–1508.

**Kim J.S., Walter M.E., Lee J.K.,** 2002, 'Modelling mechanical response of intumescent mat material at room temperature'. International Journal of Mechanical Sciences. Vol.44, pp.2285–2315.

**Klaesner J.W., Commean P.K., Hastings M.K., Zou D., Mueller M. J.,** 2001, 'Accuracy and reliability testing of a portable soft tissue indenter'. IEEE Transactions on neural systems and rehabilitation engineering. Vol.9, No.2, pp.232-240

**Knight L.R., Smeathers J.E., Isdale A.H., Helliwell P.S.,** 2001, 'Evaluating the cutaneous involvement in scleroderma: torsional stiffness revisited'. Rheumatology. Vol.40, pp.128-132.

**Kong X., Yang Q., Li B., Rothwell G., English R., Ren X.J.,** 2008, 'Numerical study of strengths of spot-welded joints of steel'. Materials and Design. Vol.29, pp.1554– 1561

**Lanir Y.,** 1979, 'A structural theory for the homogeneous bixial stress-strain relationships in flat collagenous tissues'. Journal of Biomechanics. Vol.12, pp.423-436.

**Leustean L.,Rosu G.,** 2003, 'Certifying Kalman Filters'. RIACS technical report.

**Mattei C.P., Zahouani H.,** 2004, 'Study of adhesion forces and mechanical properties of human skin in vivo'. Journal of Adhesion Science and Technology. Vol 18, No.15-16, pp.1739-1758.

**Metropolis N., Rosenbluth A., Rosenbluth M., Teller A., Teller E.,** 1953, 'Equation of state calculations by fast computing machines'. Journal of Chemical Physics. Vol.21, pp.1087-1092.

**Meuwissen M.H.H., Oomens C.W.J., Baaijens F.P.T., Petterson R., Janssen J.D.,** 1998, 'Determination of the elasto-plastic properties of aluminum using a mixed numerical-experimental method'. Journal of Materials Processing Technology. Vol.75, pp.204–211.

**Mills N.J., Fitzgerald C., Gilchrist A., Verdejo R.,** 2003, 'Polymer foams for personal protection: cushions, shoes and helmets'. Composites Science and Technology. Vol.63, pp.2389–2400.

**Mills N., Zhu H.,** 1999, 'The high strain compression of closed cell polymer foam'. Journal of the Mechanics and Physics of Solids. Vol.47, pp. 669-695.

**Mooney,M.,** 1940, 'A theory of large elastic deformation'. J.Appl. Phys. Vol.11, pp.582-592. (in Atkin and Fox, 1980)

**Moreu Y. M., Mills N.J.,** 2004, 'Test Method-Rapid hydrostatic compression of low-density polymeric foams'. Polymer Testing. Vol.23, pp.313-322.

**Nakamura T., Wang T., Sampath S.,** 2000, 'Determination of properties of graded materials by inverse analysis and instrumented indentation'. Acta materialia. Vol.48, No.17, pp.4293-4306.

**Narvaez J.A., Narvaez J., Ortega R., Aquilera C., Sanchez A., Andia E.** 2000, 'Painful heel: MR imaging findings'. Radiographics. Vol.20, No. 2, pp.333–352.

**Neaupane K.M., Sugimoto M.,** 2003, 'An inverse boundary value problem using the extended Kalman filter'. Science Asia. Vol.29, pp.121-126.

**Noe D.A., Voto S.J., Hoffmann M.S., Askew M.J., Gradisar I.A.,** 1993, 'Role of the calcaneal heel pad and polymeric shock absorbers in attenuation of heel strike impact'. Journal Biomedical Engineering. Vol.15, No.1, pp.23–26.

**Ogden, R.W.,** 1972a, 'Large deformation isotropic elasticity-on the correlation of theory and experiment for incompressible rubber like solids'. Proceedings of the Royal Society Lond. Vol.A326, pp.565-84.

**Ogden R.W.,** 1972b, 'Large deformation isotropic elasticity-on the correlation of theory and experiment for compressible rubberlike solids'. Proceedings of the Royal Society Lond. Vol.A328, pp.567-83.

**Ohura T., Sugihara T., Honda K.,** 1980, 'Postoperative evaluation in plastic surgery using the Bio-skin tension meter'. Annals of Plastic Surgery. Vol.5, pp.74-82.

**Oomens C., van Campen D., Grootenboer H.,** 1987, 'A mixture approach to the mechanics of skin'. Journal of Biomechanics. Vol.20, No.9, pp.877-885.

**Pailler-Mattei C., Zahouani H.,** 2006, 'Analysis of adhesive behaviour of human skin in vivo by an indentation test'. Tribology International. Vol.39, pp.12–21

**Payne P. A.,** 1991, 'Measurement of properties and function of skin'. Clinical Physics and Physiological Measurement. Vol.12, No.2, pp.105-129

**Petre M.T., Erdemir A., Cavanagh P.R.,** 2007, 'Determination of elastomeric foam parameters for simulations of complex loading'. Computer Methods in Biomechanics and Biomedical Engineering. Vol.9, No.4, pp.231-242.

**Petre R.E, Quaile M.P., Rossman E.I., Ratcliffe S.J., Bailey B.A., Houser S.R., Margulies K.B.,** 2006, 'Sex-Based Differences in Myocardial Contractile Reserve'. American Journal of Physiol Regulatorl Integativer and Comparative Physiology. Vol.292, pp.810-818.

**Petre M.T., Ahmet E.E., Peter C.R.,** 2005, 'Determining Foam Parameters For Complex Biomechanical Loading Simulations'. *Summer Bioengineering Conference, Vail, Colorado.*

**Pratt D. J.,** 1989, 'Mechanisms of shock attenuation *via* the lower extremity during running'. Clinical Biomechanics. Vol.4 pp.51-57.

**Press W.H., Teukolsky S.A., Vetterling W.T., Flannery B.P.,** 1996, *Numerical Recipes in Fortran 77 - The Art of Scientific Computing.* (2nd Eds) ISBN: 9780521430647. Cambridge University Press, Cambridge, MA .

**Ren X.J., Hooper R.M., Griffths C. and Henshall L.J.,** 2001, 'The effect of indenter heating on the indentation creep behaviour of single crystal MgO'. Journal of Materials Science Letters. Vol.20, pp.1819-1821.

**Ren X.J., Hooper R.M., Griffths C. and Henshall L.J.,** 2002, 'Indentation size effect (ISE) in single crystal MgO'. Philosophical Magazine A, Vol.82, No.10, pp.2113-2120.

**Ren X.J., Hooper R.M. and Henshall L.J.,** 2005, 'Indentation creep in Zirconia ceramics under variable loads'. Key Engineering Materials. Vol.1-2, pp.280-283.

**Ren X.J., Smith, C.W., Evans, K.E., Dooling, P.J., Burgess, A. and Wiechers, J.W.,** 2005, 'Experimental testing and numerical modelling of mechanical properties of the human skin'. International Foundation of Society of Cosmetic Chemists (IFSCC), Vol.1, pp.95-98.

**Ren X.J., Smith C.W., Evans K.E., Dooling P., Burgess A., Wiechers J., Zahlan N.,** 2006, 'Experimental and numerical investigations of the deformation of soft materials under tangential loading'. International Journal of Solids and Structure. Vol.43, pp.2364-2377.

**Ren X.J., Silberschmidt V.V.,** 2008, 'Numerical modelling of low-density cellular materials'. Computational Materials Science. Vol.43, pp.65–74.

**Rome K.,** 1998, 'Mechanical properties of the heel pad: current theory and review of the literature'. The Foot. Vol.8, pp.179-185

**Ruiz-Herrero J.L., Rodriguez-Perez M.A., de Saja J.A.,** 2005, 'Effective diffusion coefficient for the gas contained in closed cell polyethylene-based foams subjected to compressive creep tests'. Polymer. Vol.46, pp.3105-3110

**Schwefel H. P.,** 1981, *Numerical Optimization of Computer Models.* Wiley, Chichester.

**Seifert T.,** 2003, *Identification of Material Parameters Using Instrumented Indentation Test Data.* COMMAS Master Thesis. Fraunhofer Institute for Mechanics of Materials (IWM), Freiburg.

**Serup J., Jemec G.,** 1999, *Hand book of non-invasive methods and the skin*, CRC Press, London.

**Spencer,A.J.M.,** 1980. *Continuum Mechanics.* ISBN: 10-0582442826. Longman New York.

**Stoer J., Burlisch R.,** 1980, *Introduction to Numerical Analysis,* ISBN: 10-038795452X. Springer Verlag.

**Sugihara T., Ohura T., Homman K., Igawa H.H.,** 1991, 'The extensibility in human skin: variation according to age and site'. British Journal of Plastic Surgery. Vol.44, pp.418-422.

**Szeliga D., Gawad J., Pietrzyk M.,** 2004, 'Parameters identification of materials based on the inverse analysis'. International Journal of Applied Mathematics and Computer Science. Vol.14, No.4, pp.549–556.

**Taljat B., Zacharia T.,** 1998, 'New analytical procedure to determine stress-strain curve from spherical indentation data'. International Journal of Solids and Structures. Vol.35, No.33, pp. 4411~426

**Tanaka M., Dulikravick G.S.,** 2000, *Inverse problems in engineering mechanics II.* ISBN: 10-0080436935. Elsevier Science.

**Tho K.K., Swaddiwudhipong S., Liu Z.S., Hua J.,** 2004, 'Artificial neural network model for material characterization by indentation'. Modelling and Simulation in Materials Science and Engineering. Vol.12, pp.1055–1062.

**Tikhonov A.N., Arsenin V.Y.,** 1977, *Solutions of ill-Posed Problems.* ISBN: 0898710502. Winston and Sons , Washington, DC.

**Tong J., Lim C.S., Goh O.L.,** 2003, 'Technique to study the biomechanical properties of the human calcaneal heel pad'. The Foot. Vol.13, pp.83–91.

**Twizell E.H., Ogden R.H.,** 1986, 'Non-linear optimization of the material constants in Ogden's stress-deformation function for incompressible isotropic elastomers'. Journal of the Australian Mathematical Society Series. Vol.B24, pp.424– 444.

**Tyulyukovskiy E., Huber N.,** 2007, 'Neural networks for tip correction of spherical indentation curves from bulk metals and thin metal films'. Journal of the Mechanics and Physics of Solids. Vol.55, pp.391–418.

**Vandamme M., Ulm F.J.,** 2006, 'Viscoelastic solutions for conical indentation'. International Journal of Solids and Structures. Vol.43, pp.3142-3165.

**Vannah W.M., Childress D.S.,** 1996, 'Indenter tests and finite element modeling of bulk muscular tissue *in vivo'*. Journal of Rehabilitation Research and Development. Vol.33 No. 3, pp.239-252.

**Venkatesh T.A., Van Vliet K.J., Giannakopoulos A.E, Suresh S.,** 2000, 'Determination of elasto-plastic properties by instrumented sharp indentation: Guidelines for property extraction'. Scripta materialia. Vol.42, pp.833–839.

**Verdejo R., Mills N.J.,** 2004, 'Heel-shoe interactions and the durability of EVA foam running-shoe midsoles', Journal of Biomechanics. Vol.37, pp.1379-1386.

**Vescovo P., Varchon D., Humbert P.,** 2002, 'In vivo tensile tests on human skin: the extensometers'. in *Bioengineering of the Skin: Skin* Biomechanics. (Elsner, P., Berardesca E., Wilhelm K.P. Maibach H. I., eds) London, CRS Press LLC

**Volshin A, Wosk J.,** 1982, 'An *in-vitro* study of low back pain and shock absorption in the human locomotor system'. Journal of Biomechanics. Vol.15, pp.21-27.

**Warren R., Garstein V., Kligman A.M., Montagna W., Allendorf R.A., Ridder G.M.,** 1991, 'Age, sunlight, and facial skin: a histologic and quantitative study'. Journal of the American Academy Dermatology. Vol.25, pp.751-760.

**Wang C.L., Shau Y.W., Hsu T.C., Chen H.C., Chien S.H.,** 1999, 'Mechanical properties of heel pads reconstructed with flaps'. Journal of Bone and Joint Surgery. Vol.81B, pp.207–211.

**Wasserman P.D.,** 1989, *Neural Computing: Theory and Practice*, Van Nostrand Reinhold.

**Weiss J.A., Gardiner J.C.,** 2001, 'Computational Modeling of Ligament Mechanics'. Critical Reviews in Biomedical Engineering. Vol.29, No. 4, pp.1-70.

**Wijn P.,** 1980, *The linear viscoelastic properties of human skin in vivo for small deformations*. PhD Thesis. University of Nijmegen, Nijimegen, The Netherlands.

**Zahouani H, Asserin J., Humbert P.,** 2002, 'Mechanical properties of the skin during friction assessment'. in *Bioengineering of the Skin: Skin* Biomechanics. (Elsner, P., Berardesca E., Wilhelm K.P. Maibach H. I., eds) London, CRS Press LLC

**Zheng Y.P., Mak A.F., Lue B.,** 1999, 'Objective assessment of limb tissue elasticity: Development of a manual indentation procedure'. Journal of Rehabilitation Research and Development. Vol.36, No. 2, pp.71–85.

**Zheng Y.P., Choi Y.K.C., Wong K., Chan S., Mak A.F.T.,** 2000, 'Biomechanical assessment of plantar foot tissue in diabetic patients using an ultrasound indentation system'. Ultrasound in Medicine & Biology. Vol.26, No.3, pp.451-456

**Publication list**

**Li B., Gu Y.D., Rothwell G., English R., Ren X.J.,** 2008, 'Characterisation of Nonlinear Material Parameters of Foams Based on Indentation Tests'. *Materials & Design.* (in press)

**Li B., Ren X.J., English R., Rothwell G.,** 2008, 'Inverse Finite Element characterisation of Biological Tissues *in vivo* Based on Indentation Tests', European Medical and Biology Engineering Conference

**Kong P. X., Li B., Yang Q., English R., Rothwell G., Ren X. J.,** 2008, 'Numerical modelling of the strength of spot welded joints of steels', *Materials and Design.* Vol. 29(8), pp. 1554 -1561.

**Kong P. X., Li B., Yang Q., English R., Rothwell G., Ren X. J.,** 2008, 'Numerical study of the effect of welding parameters on the strength of spot-welded joints'. *Applied Mechanics and Materials.* Vol.10, No.12, pp.322-326.

**Kong P. X., Li B., Ren X. J., English R., Rothwell G.,** 2007, 'Determination of plastic properties of materials by combined numerical and experimental method', *3rd Int. Indentation Workshop*, Cambridge.